NASA CR-54703
FR-056-968

DESIGN AND DEVELOPMENT OF A THERMO-IONIC ELECTRIC THRUSTOR

by

A. C. Ducati, R. G. Jahn, E. Muehlberger and R. P. Treat

prepared for

NATIONAL AERONAUTICS AND SPACE ADMINISTRATION

CONTRACT NAS w-968

FACILITY FORM 602
N68-26981 (ACCESSION NUMBER)
(THRU)
402 (PAGES)
1 (CODE)
CR-54703 (NASA CR OR TMX OR AD NUMBER)
28 (CATEGORY)

JUL 1968
RECEIVED
NASA STI FACILITY
INPUT BRANCH

GIANNINI SCIENTIFIC CORPORATION

NOTICE

This report was prepared as an account of Government sponsored work. Neither the United States, nor the National Aeronautics and Space Administration (NASA), nor any person acting on behalf of NASA:

A.) Makes any warranty or representation, expressed or implied, with respect to the accuracy, completeness, or usefulness of the information contained in this report, or that the use of any information, apparatus, method, or process disclosed in this report may not infringe privately owned rights; or

B.) Assumes any liabilities with respect to the use of, or for damages resulting from the use of any information, apparatus, method or process disclosed in this report.

As used above, "person acting on behalf of NASA" includes any employee or contractor of NASA, or employee of such contractor, to the extent that such employee or contractor of NASA, or employee of such contractor prepares, disseminates, or provides access to, any information pursuant to his employment or contract with NASA, or his employment with such contractor.

Requests for copies of this report should be referred to

National Aeronautics and Space Administration
Office of Scientific and Technical Information
Attention: AFSS-A
Washington, D.C. 20546

NASA CR-54703
FR-056-968

FINAL REPORT

DESIGN AND DEVELOPMENT OF A THERMO-IONIC ELECTRIC THRUSTOR

by

A. C. Ducati, R. G. Jahn, E. Muehlberger and R. P. Treat

prepared for

NATIONAL AERONAUTICS AND SPACE ADMINISTRATION

May 1966

CONTRACT NAS w-968

Technical Management
NASA Lewis Research Center
Cleveland, Ohio
Spacecraft Technology Division
Henry R. Hunczak

GIANNINI SCIENTIFIC CORPORATION
Special Projects Group
3839 South Main Street
Santa Ana, California 92702

PRECEDING PAGE BLANK NOT FILMED.

FOREWORD

This is the final report of work carried out by Giannini Scientific Corporation on the program entitled "Design and Development of a Thermo-Ionic Electric Thrustor." The work has been conducted under Contract NAS w-968 with NASA Lewis Research Center during the period from 30 April 1964 to 11 January 1966. Mr. Henry R. Hunczak of the Electric Propulsion Office was Project Manager.

Adriano C. Ducati was Principal Investigator in charge of the overall direction of the work. Principal participants in the performance of the investigation and preparation of the report were Erich Muehlberger, R. G. Jahn and R. P. Treat. Significant contributors and their areas of work were B. Podolsky, theoretical analysis; W. A. Stoner, preparation of the experimental portion of the report; J. P. Todd, technical liaison; A. S. Aguinaga, R. J. Bregozzo, and E. C. Dageford, propulsion performance testing.

ABSTRACT

An experimental and theoretical investigation of propulsion performance and basic physical processes of thermo-ionic electric thrustors has been conducted. Fifty-hour continuous operation has been achieved with H_2 at 3000, 6000 and 10,000 seconds with very little degradation in performance. The results of these tests have yielded extensive information on life properties. Efficiencies have been measured over a wide range of arc parameters. One of the significant results was the very weak dependence of efficiency on magnetic field strength in the 1 to 16 kilogauss range. For sufficiently high mass flows the thrust efficiencies of H_2 and D_2 follow the frozen flow efficiencies over a wide range of specific impulse. The thermal efficiency was above 60 percent for optimum operating conditions. Thermal efficiencies of various other propellants were considerably lower.

A study of the effect of the test environment on performance has been initiated. The goal of this investigation is the definition, and possibly the construction, of a test environment that would permit a reliable extrapolation of terrestrial tests to deep space conditions.

The distribution of arc currents has been studied theoretically in some detail. Energy transfer by ohmic heating and energy equipartition have been investigated. The transfer of energy from electrons to heavy particles by collisions appears to be effective under some conditions. Elementary aspects of a continuum model of an axisymmetric, fully ionized, rotational flow in a strong magnetic field have been considered.

TABLE OF CONTENTS

		Page
1.0	INTRODUCTION	1
2.0	EXPERIMENTAL INVESTIGATION	3
2.1	Life Behavior of the Thermo-Ionic Thrustor	5
2.1.1	General	5
2.1.2	Effect of Geometry on Thrustor Life	7
2.1.3	Effect of Propellant on Thrustor Life	17
2.1.4	Effect of the Arc Chamber Pressure on Thrustor Life	37
2.1.5	Effect of Power, Current, and Voltage on Thrustor Life	45
2.1.6	Effect of the External Magnetic Field on Thrustor Life	59
2.1.7	Effect of External Environment on Thrustor Life	79
2.2	Efficiency of the Thermo-Ionic Thrustor	89
2.2.1	General	89
2.2.2	Effect of Geometry on Efficiency	91
2.2.3	Effect of Propellant on Efficiency	129
2.2.4	Effect of Pressure on Efficiency	150
2.2.5	Effect of Power, Current and Voltage on Efficiency	161
2.2.6	Effect of External Magnetic Field on Efficiency	180
2.2.7	Effect of External Environment on Efficiency	191

TABLE OF CONTENTS (cont.)

		Page
2.3	Testing Anomalies With Thermo-Ionic Thrustor	207
2.3.1	General	207
2.3.2	Effect of Geometry on Anomalies	208
2.3.3	Effect of Propellant on Anomalies	224
2.3.4	Effect of Pressure on Anomalies	230
2.3.5	Effect of Power, Current, and Voltage on Anomalies	236
2.3.6	Effect of External Magnetic Field on Anomalies	247
2.3.7	Effect of External Environment on Anomalies	257
3.0	ANALYTICAL INVESTIGATION	272
3.1	An Electron's View of the MPD Arc Jet	273
3.1.1	Hall Parameter and Gyro Radii	276
3.1.2	Conduction Processes	279
3.1.3	Thrust Mechanisms	285
3.1.4	Density, Temperatures, and Field Patterns in the MPD Arcs	289
3.1.5	Application to Arc Jet Without External B Field	295
3.1.6	Application With External B Field and Low Current	305
3.1.7	Application to Arc Jet With External B Field and High Current	314
3.1.8	Extension and Improvement of the Analysis	316

TABLE OF CONTENTS (cont.)

		Page
3.2	Energy Transfer and Acceleration Processes	319
3.2.1	Electron Energy Gain in the Arc and Thermalization of the Plasma	319
3.2.2	Elementary Aspects of an Axisymmetric Rotational Flow in a Strong Magnetic Field	330
3.2.3	A Thrust Formula Showing the Effects of Magnetic Compression	337
3.3	Interpretation of Experimental Results	345
3.3.1	Efficiency of Operation	345
3.3.2	Discussion of Anomalies in Thrust and Specific Impulse Measurements	357
4.0	SUMMARY AND CONCLUSIONS	361
	REFERENCES	368

ILLUSTRATIONS

Figure		Page
1	Typical Coaxial Electrode Configuration	8
2	View of Cathode Tip Showing Even Distribution of the Arc Discharge	9
3	First Appearance of Cathode Build-up After 75 Hours of Operation	10
4	Build-up of Tungsten Cathode After 2 Hours of Operation Without Propellant Throughput	12
5	Anode Arc Termination Stabilized in a Single Spot at High Current Operation	13
6	Anode Erosion During Life Test Due to Localized Arc Termination	14
7	Magnetic Field Coil in Series With Anode Avoids Localized Arc Termination	15
8	Hot Hydrogen or Metal Vapors Can Reduce Insulators to Metal Form	19
9	Electrodes After Long Operation With Deuterium at 5000 Seconds Isp and 2000 Amperes Arc Current	21
10	Electrodes After Two Hours of Operation With Lithium 3 Mg/Sec, 300 Amperes	22
11	Micrograph Showing Deep Carburization of Tungsten Electrode Material	25
12	Erosion of Tungsten Anode Material Under Action of Carbon Vapor	26

ILLUSTRATIONS (cont.)

Figure		Page
13	Thrust Versus Input Power for Radiation-Cooled Thermo-Ionic Thrustors Without Propellant Throughput	30
14	Condensation of Lithium Vapor on Engine Components and Vacuum Chamber	31
15	Deposit of Lithium on Tank Window (opacity in one hour at 1 mg/sec mass flow)	32
16	Lithium Condensed From Vapor in Vacuum Tank	33
17	Lithium Condensed in Vacuum Pump Baffle (20 Feet From Vapor Jet)	34
18	Lithium Deposit in Vacuum Switch Connected to Tank Through 1/2-Inch Pipe 20 Feet Long	35
19	Potassium Deposited in Vacuum Tank, One Hour Operation at 30 Mg/Sec Propellant Flow Rate	36
20	Melted Cathode Spot Operating at High Pressure and Low Power	38
21	Increased Cathode Crater Operating at Hihg Pressure and High Power	39
22	Destruction of Cathode When Operating at Very High Pressure and Very High Power Input	40
23	First Thermo-Ionic Cathode After Operation at Low Arc Chamber Pressure and 3500 Amperes	41
24	At Low Pressure Operation the Arc Attachment is Spreading on the Cathode Surface	42

ILLUSTRATIONS (cont.)

Figure		Page
25	At Very Low Arc Chamber Pressure the Spreading of the Arc Attachment Reaches the Cathode Base	43
26	Power Density for Effective Cathode Surface Area Used During 50-Hour Life Tests at 3000, 6000, and 10,000 Seconds Isp	46
27	Variation of Power Density in Effective Anode Surface Area at 3000 Seconds Isp Without External Magnetic Field	47
28	Power Density for Effective Anode Surface Area With Applied External Magnetic Field at 3000, 6000, and 10,000 Seconds Isp	48
29	Variation of Current and Voltage With the Intensity of External Magnetic Field	50
30	Jet Operating Normally Without Anode Luminous Spots	51
31	First Appearance of Luminous Anode Spots at Increasing Voltage	52
32	Anode Spots Increase Both in Number and Intensity as Voltage is Further Increased	53
33	Unexpected Pinhole Erosion After a Long Period of Operation	55
34	Destructive Effects With Complete Anode Melting. Power Input is Increased After Reaching Dangerous Voltage Level	56
35	Cathode of Thermo-Ionic Thrustor After Operation at 4000 Amperes Arc Current Without Externally Applied Magnetic Field	58

ILLUSTRATIONS (cont.)

Figure		Page
36	Photograph of Various Water-Cooled Magnetic Field Coils Used During Experimental Investigation	61
37	Specific Coil Power Loss Versus Magnetic Field Strength	62
38	Degradation of Arc Chamber Pressure Due to Anode Throat Erosion With and Without Externally Applied Magnetic Field at 3000 Seconds Isp	63
39	Arc Exhaust of Thermo-Ionic Thrustor Without (Top) and With (Bottom) Externally Applied Magnetic Field	64
40	Cathode Tip After Operation at 3000 Amperes Arc Current and Moderate External Applied Magnetic Field	66
41	Deep Cross-Like Crack on Cathode Tip After Operation at 2500 Amperes Arc Current and Strong External Applied Magnetic Field	67
42	Schematic of Artificially Heated Cathode for Studies of Magneto-Mechanical Forces on Its Surface	68
43	Photograph of Swirl Effect of Molten Cathode Material Caused by the Externally Applied Magnetic Field	69
44	Photograph of Cathode Showing Increased Swirl Effect of Molten Cathode Material at Moderate Externally Applied Magnetic Field Strength	70
45	Cathode Showing Strong Swirl Effect on Molten Cathode Material at Increased Externally Applied Magnetic Field Strength	71

ILLUSTRATIONS (cont.)

Figure		Page
46	Cathode Showing Heavy Swirl Type Erosion at Very Strong Externally Applied Magnetic Field Strength and Increased Cathode Temperature	72
47	Series of Cathodes Showing Swirl Type Erosion at Gradually Increased Arc Current and Externally Applied Magnetic Field Strength	74
48	Face of Water-Cooled Copper Anode Showing Swirl of Molten Material Due to Influence of the External Magnetic Field	75
49	Excessive External Magnetic Fields and Large Anode Throat Diameters Result in Destructive Electron Bombardment on the Anode	76
50	Increased Anode Throat Length or Decreased Anode Throat Diameter or Decreased Magnetic Field Help to Eliminate Anode Erosion Due to Electron Bombardment	77
51	Pressure at Various Altitudes From Earth's Surface	80
52	Variation of Vapor Pressure With Temperature for Various Materials (From R. E. Honig, "Vapor Pressure Data for the Solid and Liquid Elements," RCA Review, XXIII, No. 4 (1962), pp. 567-586)	81
53	Volume of Evaporated Solids Versus Deposition Area for a Skin Depth of 10^{-5} MM	84
54	Spacecraft Components Whose Functions can be Degraded by Deposition of Metal Films From Thrustor Exhaust	85

ILLUSTRATIONS (cont.)

Figure		Page
55	Possible Envelope of Plasma Exhaust From Thermo-Ionic Electric Thrustor During Space Operation	86
56	Thermo-Ionic Jet at Environmental Pressure of 10^{-1} Torr	87
57	Thermo-Ionic Jet at Environmental Pressure of 5×10^{-2} Torr	87
58	Thermo-Ionic Jet of Figure 57 at Decreased Environmental Pressure	87
59	Thermo-Ionic Jet of Figure 58 at Further Decreased Environmental Pressure	87
60	Ratios of Throat Length to Throat Diameter for Electrode Configurations Used During Testing	93
61	Photograph of the Various Interchangeable Testing Heads Used During the Experimental Investigation	94
62	Dimensions of Interchangeable Testing Head (No. 1 - 4) for Hydrogen Operation	95
63	Dimensions of Interchangeable Testing Head (No. 5 - 8) for Hydrogen Operation	96
64	Dimensions of Interchangeable Testing Head (No. 9 - 12) for Hydrogen Operation	97
65	Dimensions of Interchangeable Testing Head (No. 13 - 16) for Hydrogen Operation	98
66	Dimensions of Interchangeable Testing Head (No. 17 - 20) for Hydrogen Operation	99

ILLUSTRATIONS (cont.)

Figure		Page
67	Dimensions of Interchangeable Testing Head (No. 21 - 24) for Hydrogen Operation	100
68	Photograph of Typical Interchangeable Radiation-Cooled Testing Head for Operation With Lithium and Potassium	101
69	Dimensions of Interchangeable Testing Head for Lithium - Potassium Operation (Anode Throat Diameter 0.250 Inches)	102
70	Dimensions of Interchangeable Testing Head for Lithium - Potassium Operation (Anode Throat Diameter 0.350 Inches)	103
71	Dimensions of Interchangeable Testing Head for Lithium - Potassium Operation (Anode Throat Diameter 0.440 Inches)	104
72	Photograph of Interchangeable Radiation-Cooled Testing Head for Operation Without Propellant Throughput	105
73	Dimensions of Interchangeable Radiation-Cooled Testing Head for Operation Without Propellant Throughput (Anode Throat Diameter 0.250 Inches)	106
74	Dimensions of Interchangeable Radiation-Cooled Testing Head for Operation Without Propellant Throughput (Anode Throat Diameter 0.375 Inches)	107
75	Dimensions of Interchangeable Prototype Testing Head With Reversed Polarity Electrode Configuration for Operation Without Propellant Throughput	108

ILLUSTRATIONS (cont.)

Figure		Page
76	5 KW Interchangeable Water-Cooled Head With Anode and Cathode	110
77	Design of a 5 KW Water-Cooled Thermo-Ionic Thrustor for High Specific Impulse Operation	111
78	Photograph of Interchangeable Prototype Testing Head With Reversed Polarity Electrode Configuration for Operation Without Propellant Throughput	112
79	Photograph of Interchangeable Testing Head With Pressure Regulated Cathode for Stability Study	113
80	Schematic of Heat Exchanger System for Measuring Thermal Efficiency and Jet Power of a Water-Cooled Thermo-Ionic Thrustor	115
81	Thermal Efficiency Versus Anode Throat Diameter (Throat Length/Throat Diameter = 1.5)	116
82	Thermal Efficiency Versus Anode Throat Diameter (Throat Length/Throat Diameter = 1.5)	117
83	Thermal Efficiency Versus Anode Throat Diameter (Throat Length/Throat Diameter = 1.5)	118
84	Schematic of Heat Exchanger System for Measuring Thermal Efficiency and Jet Power of a Radiation-Cooled Thermo-Ionic Thrustor	119
85	Typical Radiation-Cooled Testing Head With Water-Cooled Radiation Shield	120

ILLUSTRATIONS (cont.)

Figure		Page
86	Thermal Efficiency Versus Anode Throat Diameter for Radiation-Cooled Thermo-Ionic Thrustor (Throat Length/Throat Diameter = 1.5)	121
87	Thermal Efficiency Versus Anode Throat Diameter (Throat Length/Throat Diameter = 1.5)	123
88	Thrust Efficiency Versus Anode Throat Diameter (Throat Length/Throat Diameter = 1.5)	124
89	Thrust Efficiency Versus Anode Throat Diameter (Throat Length/Throat Diameter = 1.5)	125
90	Overall Efficiency Versus Anode Throat Diameter (Throat Length/Throat Diameter = 1.5)	126
91	Overall Efficiency Versus Anode Throat Diameter (Throat Length/Throat Diameter = 1.5)	127
92	Dimensions of Electrode Geometry Used for Comparative Test With H_2 and D_2 Propellants	134
93	Average Reported Overall Efficiency Versus Specific Impulse for Thermo-Ionic Thrustors Operating With Hydrogen Propellant	135
94	Thermal Efficiency Versus Specific Impulse for Various Thrustors Using H_2 Propellant	136
95	Thrust Efficiency Versus Specific Impulse for Various Thrustors Using H_2 Propellant	138
96	Thermal Efficiency Versus Specific Impulse for Thermo-Ionic Thrustor Using D_2 Propellant	139

ILLUSTRATIONS (cont.)

Figure		Page
97	Thrust Efficiency Versus Specific Impulse for Thermo-Ionic Thrustor Using D_2 Propellant	140
98	Thermal Efficiency Versus Specific Impulse for Thermo-Ionic Thrustor Using He Propellant	141
99	Thrust Efficiency Versus Specific Impulse for Thermo-Ionic Thrustor Using D_2 Propellant	142
100	Thermal Efficiency Versus Specific Impulse for Thermo-Ionic Thrustor Using NH_3 Propellant	144
101	Thrust Efficiency Versus Specific Impulse for Thermo-Ionic Thrustor Using NH_3 Propellant	145
102	Thermal Efficiency Versus Arc Input Power for Thermo-Ionic Thrustor Using Lithium Propellant	146
103	Thermal Efficiency Versus Arc Input Power for Thermo-Ionic Thrustor Using Potassium Propellant	147
104	Thermal Efficiency Versus Arc Input Power for Thermo-Ionic Thrustor Without Propellant Throughput	148
105	Thermal Efficiency Versus Arc Input Power for Thermo-Ionic Thrustor Operating With Electrode Vapor and H_2 Seeded Propellant	149
106	Variation of Arc Chamber Pressure With Arc Current at Different Locations	153
107	Thermal Efficiency Versus Arc Chamber Pressure for Thermo-Ionic Thrustor Using H_2 at 1000 Seconds Isp	154

ILLUSTRATIONS (cont.)

Figure		Page
108	Thermal Efficiency Versus Arc Chamber Pressure for Thermo-Ionic Thrustor Using H_2 at 4000 Seconds Isp	155
109	Thermal Efficiency Versus Arc Chamber Pressure for Thermo-Ionic Thrustor Using H_2 and D_2 Propellants	156
110	Thermal Efficiency Versus Arc Chamber Pressure for Thermo-Ionic Thrustor Using He Propellant	157
111	Thermal Efficiency Versus Arc Chamber Pressure for Thermo-Ionic Thrustor Using NH_3 Propellant	158
112	Thermal Efficiency Versus Arc Chamber Pressure for Thermo-Ionic Thrustor Using Argon Propellant	159
113	Thrust Efficiency Versus Arc Chamber Pressure for Thermo-Ionic Thrustor Using H_2 Propellant	160
114	Thermal Efficiency Versus Arc Input Power for Thermo-Ionic Thrustor Using H_2 Propellant	162
115	Thermal Efficiency Versus Power Density in Throat Cross-Section for Thermo-Ionic Thrustor Using H_2 Propellant	163
116	Thermal Efficiency Versus Arc Input Power at Constant Isp for Thermo-Ionic Thrustors Using H_2 Propellant	164
117	Thermal Efficiency Versus Power in Gas at Constant Isp for Thermo-Ionic Thrustor Using H_2 Propellant	165
118	Increased Rate of Change in Thermal Efficiency With Increased Arc Input Power at Constant Propellant Mass Flow Using Hydrogen	167

ILLUSTRATIONS (cont.)

Figure		Page
119	Increased Rate of Change in Thermal Efficiency With Increased Arc Input Power at Constant Propellant Mass Flow Using Deuterium	168
120	Increased Rate of Change in Thermal Efficiency With Increased Arc Input Power at Constant Propellant Mass Flow Using Lithium	169
121	Increased Rate of Change in Thermal Efficiency With Increased Arc Input Power at Constant Propellant Mass Flow Using Potassium	170
122	Variation of Arc Voltage at Different Throat Diameters and Magnetic Fields and Constant Input Power	171
123	Variation of Arc Current at Different Throat Diameters and Magnetic Fields and Constant Input Power	172
124	Thermal Efficiency Versus Arc Current Using H_2 at Constant Specific Impulse, Mass Flow Rate and External Magnetic Field	173
125	Thermal Efficiency Versus Arc Voltage Using H_2 at Constant Specific Impulse, Mass Flow Rate and External Magnetic Field	174
126	Thrust Efficiency Versus Arc Current for H_2 at Constant Power, Mass Flow Rate and Magnetic Field	175
127	Thrust Efficiency Versus Arc Voltage for Hydrogen at Constant Power, Mass Flow Rate and Magnetic Field	177
128	Overall Efficiency Versus Arc Current for Hydrogen at Constant Power, Mass Flow Rate and Magnetic Field	178

ILLUSTRATIONS (cont.)

Figure		Page
129	Overall Efficiency Versus Arc Voltage for Hydrogen at Constant Power, Mass Flow Rate and Magnetic Field	179
130	Photograph of Water-Cooled 32 Turn External Magnetic Field Coil Used During Testing	182
131	Magnetic Field Strength Versus Coil Current for External Field Coil Used During Testing	183
132	Thermal Efficiency Versus External Magnetic Field Strength for H_2 at Various Anode Throat Diameters and Constant Isp	184
133	Thermal Efficiency Versus External Magnetic Field Strength for H_2 at Various Specific Impulse Levels and Constant Anode Throat Diameter	185
134	Thrust Efficiency Versus External Magnetic Field Strength for H_2 at Various Anode Throat Diameters and Constant Isp	187
135	Thrust Efficiency Versus External Magnetic Field Strength for H_2 at Two Specific Impulse Levels and Constant Anode Throat Diameter	188
136	Thermal Efficiency Versus External Magnetic Field Strength for D_2 at Various Specific Impulse Levels and Constant Anode Throat Diameter	189
137	Thrust Efficiency Versus External Magnetic Field Strength for D_2 at Various Anode Throat Diameters and Constant Isp	190
138	Dimensions of Vacuum Chamber With Thrust Stand Used During Early Experiments With Thermo-Ionic Thrustor	192

ILLUSTRATIONS (cont.)

Figure		Page
139	Enlarged Vacuum Tank Used During Most of the Experimental Investigation	194
140	Vacuum Chamber Used at the Electro-Optical Systems Inc. Laboratory[4]	195
141	Large Vacuum Test Tank Used at NASA Lewis Laboratories	196
142	Design of Very Large Metal Vacuum Tank Lined With Insulation for Future Experiments	197
143	Design of High Vacuum Test Facility Constructed Entirely of Insulating Materials	198
144	Dimension of High Vacuum Chamber Constructed of Plexiglas at Princeton University[9]	199
145	Photograph of Metal Vacuum Tank With Insulating Refractory Lining for Preliminary Experiments	201
146	Thermal Efficiency Versus Vacuum Tank Diameter for Hydrogen at Various Test Conditions	202
147	Overall Efficiency Versus Vacuum Tank Diameter for Hydrogen at Various Test Conditions	203
148	Visual Expansion of Thrustor Exhaust Plume at Gradually Decreased Test Chamber Pressure	205
149	Preliminary Test Results of Thrust Variation Versus Vacuum Tank Pressure	206
150	Parasitic Zero Shift Produced by Nonuniform Heat Load on Thrust Balance Components	210

GIANNINI SCIENTIFIC CORPORATION

ILLUSTRATIONS (cont.)

Figure		Page
151	Schematic of Thrust Balance With and Without Compensation of Thermal Expansion	211
152	Schematic of Thrust Killer Attached to Suspended Platform on Thrust Beam	212
153	Photograph of Prototype Thrust Killer Attached to Thermo-Ionic Thrustor	213
154	Photograph of Enlarged Thrust Killer Attached to Thermo-Ionic Thrustor With Extended Electrodes (Out Position)	214
155	Photograph of Enlarged Thrust Killer Attached to Thermo-Ionic Thrustor With Extended Electrodes (In Position)	215
156	Schematic of Enlarged Fully Insulated Thrust Stagnator	217
157	Schematic of Mechanism for Thrust Cancellation by Changing the Thrust Axis	218
158	Illustration of Coil Movement on Thrustor Producing Center of Gravity Shift	219
159	Schematic of Completely Insulated Thrustor Suspension System	221
160	Photograph of Thermo-Ionic Thrustor Totally Insulated With a Thick Layer of Silicone Rubber	222
161	Photograph of Complete Thrustor Suspension System Insulated With a Thick Layer of Silicone Rubber	223

ILLUSTRATIONS (cont.)

Figure		Page
162	General Trend of Decrease in Thermal Efficiency Versus Decrease of Propellant Mass Flow Rate at Constant Isp	227
163	General Trend of Increase in Thrust Efficiency Versus Decrease of Propellant Mass Flow Rate at Constant Isp	228
164	Schematic of Location of Pressure Sensors in Close Proximity of Arc Chamber	231
165	Schematic of Arc Chamber Pressure Sensing Apparatus for Alkali Metal Propellants	233
166	Comparison of Arc Chamber Pressure Variation at Two Locations With Increased Arc Input Power and Constant Mass Flow Rate	235
167	Average Total Input Power Versus Specific Impulse at Constant Propellant Mass Flow Rate	237
168	Average Total Input Power and Theoretical Thrust Power Versus Specific Impulse at Constant Propellant Mass Flow Rate	238
169	Average Total Input Power and Power in Gas Versus Specific Impulse at Constant Propellant Mass Flow Rate	239
170	Average Power in Gas and Theoretical Thrust Power Versus Specific Impulse at Constant Propellant Mass Flow Rate	240
171	Schematic of Improved Heat Exchanger System for Precise Determination of the Thermal Efficiency of Thermo-Ionic Thrustors	242

ILLUSTRATIONS (cont.)

Figure		Page
172	Photograph of Anode Front Surface (Conventional Polarity) After Short Operation Showing Distinct Zones of Arc Discharge Pattern	244
173	Photograph of Cathode Front Plate (Reversed Polarity) After Short Operation Showing Distinct Marks of Current Discharge Path	245
174	Schematic of Experimental Reversed Polarity Arc Chamber for Short Tests	246
175	Variation of Arc Chamber Pressure Versus External Magnetic Field Strength at Various Anode Throat Diameters and Constant Propellant Mass Flow Rate	248
176	Variation of Arc Voltage Versus External Magnetic Field Strength at Various Anode Throat Diameters and Constant Propellant Mass Flow Rate	249
177	Variation of Arc Current Versus External Magnetic Field Strength at Various Anode Throat Diameters and Constant Propellant Mass Flow Rate	250
178	Variation of Arc Input Power Versus External Magnetic Field Strength at Constant Anode Throat Diameter, Specific Impulse and Propellant Mass Flow Rate	251
179	Variation of Power in Gas Versus External Magnetic Field Strength at Constant Anode Throat Diameter, Specific Impulse and Propellant Mass Flow Rate	252
180	Anode Throat Diameter Versus Magnetic Field Strength for H_2 Propellant at Constant Voltage Operation	253

ILLUSTRATIONS (cont.)

Figure		Page
181	Increased Plasma Plume With Increased External Magnetic Field Strength or Increased Anode Throat Diameter	254
182	Assumed Typical External Arc Current Path for Various Operating Conditions	256
183	Dimensions of the Vacuum Tank Used for Testing Gaseous Propellants	258
184	Dimensions of the Vacuum Tank Used to Test Alkali Metal Propellants	259
185	Dimensions of the Vacuum Tank Used to Study Vaporization of Lithium and Potassium	260
186	Photograph of Vacuum Tank Used for Studies of Vaporization Characteristics of Lithium and Potassium Propellants	261
187	At Very Low Magnetic Field and Low Power, Beam-Like Jet is Formed	263
188	Increasing the Magnetic Field and the Power, A Regular Jet Appears	263
189	Increasing the Power at Constant Magnetic Field the Jet Remains Regular	263
190	At Still Higher Power and the Same Magnetic Field the Jet is Still Regular	263
191	Increasing the Power and the Magnetic Field of Figure 190 an External Coaxial Anodic Path Appears	265

ILLUSTRATIONS (cont.)

Figure		Page
192	Increasing the Magnetic Field of Figure 191 the Jet Lengthens Conserving Its Shape	265
193	Increasing the Power of Figure 192 the Jet Fattens and the External Anodic Path Increases	265
194	Increasing the Magnetic Field of Figure 193 the Jet Lengthens Conserving Its Shape	265
195	Increasing the Magnetic Field of Figure 194 the Anodic Coaxial Path Separates From the Central Beam	266
196	Decreasing the Power of Figure 195 at the Same High Magnetic Field the Separation is Improved	266
197	At the Lower Power of Figure 196 and the Same Magnetic Field the Separation is Very Sharp	266
198	At Still Lower Power of Figure 197 and Higher Magnetic Field the Central Jet Extends Toward the End of the Tank	266
199	At Very High Magnetic Fields the Jet Discharges to the Vacuum Tank in Two Points	268
200	Applying an External Current to the Vacuum Tank Interaction With the Magnetic Coil has Been Detected	269
201	A Partial Discharge to the Tank May Apparently Decrease the Thermal Losses	270
202	Schematic of Totally Insulated Thrust Stand Facility With Attached Thrustor Suggested for Improved Future Experimentation	271

ILLUSTRATIONS (cont.)

Figure		Page
203	Contours of Constant Hall Parameter in the r - z Plane in the Self-Field of the Arc	296
204	Contours of Constant Hall Parameter in the r - z Plane in the Self-Field of the Arc	297
205	Ion Gyro Radii as a Function of Radial and Axial Position in the Self-Field of the Arc	301
206	Hall Parameter as a Function of Axial Position in an External Magnetic Field	306
207	Ion Gyro Radii as a Function of Axial Position in an External Magnetic Field	311
208	Electrode Configuration Showing Control Surface and Imagined Current Distribution	337
209	Comparison of Hydrogen Thrust-Power Efficiency With Frozen Flow Efficiency	351
210	Comparison of Deuterium Thrust-Power Efficiency With Frozen Flow Efficiency	353
211	Comparison of Measured Thrust Power Efficiency With Frozen Flow Efficiencies for Operation With and Without an External Magnetic Field	354
212	Comparison of Measured Efficiency With Frozen Flow Efficiency	358

TABLES

Table		Page
1	Chemical Activity of Various Propellants and Electrode Materials at High Temperatures	18
2	Erosion of Boron Nitride Insulation Using Lithium and Potassium Propellants	24
3	Weight Loss of Radiation-Cooled Tungsten Anodes at Different Operating Temperatures With no Propellant Throughput	27
4	Weight Increase of Radiation-Cooled Tungsten Cathode at Different Operating Temperatures With no Propellant Throughput	28
5	Approximate Temperatures Versus Specific Impulse for Propellants of Various Atomic Weights	131
6	Ratio of Useful Energy to Total Energy in Various Propellants at Several Isp	132
7	Ionization Potentials for Common Propellants	225
8	Average Working Voltage Ranges for Various Propellants	226
9	Cold Flow Arc Chamber Pressures at Various Anode Throat Diameters and Propellant Mass Flow Rates for H_2 and D_2	232

1.0 INTRODUCTION

The thermo-ionic thrustor is a steady-state device that adds electrical energy to a continuous gas flow by means of a coaxial electrode discharge. In the usual coaxial geometry the cathode is the central electrode and the outer concentric electrode is the anode. After the first operation of a thermo-ionic thrustor with H_2 in the 3,000 to 10,000 second specific impulse range[1] there has been considerable interest in this device (and similar devices such as the MPD arc jet, Hall current accelerator, magnetic annular arc, and so forth) as a high thrust density, high specific impulse thrustor.

Since the early demonstrations of continuous, stable operation, emphasis has been placed on establishing the characteristics of this device as a thrustor, especially in the 3,000 to 6,000 second specific impulse range. The characteristics of principal interest are the electrical to thrust-power conversion efficiency and the length of time the device can produce thrust without significant degradation in performance. For this reason a large part of the development program pursued here has been directed toward this end. It has entailed extensive measurements of the efficiency of conversion of electrical to gas power and gas to thrust power as a function of such arc parameters as specific impulse, throat diameter, mass flow rate, applied magnetic field and propellant type. The endurance characteristics have been studied mainly by means of operating the thrustor continuously for 50-hour intervals. Efficiency measurements and careful observation of the degradation of thrustor components have then yielded much useful information.

The theoretical understanding of thermo-ionic thrustors is very imcomplete. This is partly due to the newness of the device and partly to the difficulty of treating analytically a reacting flow where electrostatic, Lorentz forces and pressure forces are important. There still seems to be considerable disagreement on such basic questions as the distribution of arc currents, whether the ions or electrons are the current carriers, the mechanism of electrical to gas energy transfer and the effect of an applied magnetic field on the current distribution and the plasma motion. In addition, there is no general agreement on the magnitude or "direction" of departure from energy equipartition of electrons and heavy particles, and on the degree of ionization in the plasma. In the present report we attempt to clarify certain aspects of these basic problems.

During the course of the thrustor development programs pursued here and at many other laboratories (e.g., AVCO, EOS, NASA Langley AFB), anomolously high efficiencies have been observed. In one case[2] the cause has been attributed to entrainment and acceleration of ambient gas. In our thrustors, the anomolies may be due to a combination of evaporation of electrode material and entrainment and perhaps electromagnetic interaction of the arc currents with the test tank. The resolution of the problem of the interaction of the arc with the testing environment has become, at least temporarily, an important part of arc jet technology. Some attempts to clarify this problem have been made here.

2.0 EXPERIMENTAL INVESTIGATION

Space missions are generally long in time. Weeks, months, and years are common periods today, but tens of years will become common in the near future. Operating times of the order of tens of thousands of hours must be considered as a conservative estimate of the requirements of space thrustors. Accordingly, the "life" of any space propulsion system is a characteristic that deserves a major effort in the development. In the following pages an experimental study to evaluate the life obtainable with current thermo-ionic thrustors is described, and the influences of the principal operating parameters on life are considered.

A second characteristic of major importance for a space propulsion system is the efficiency of the thrust producing mechanism. While future developments in the energy sources to be carried in space may somewhat reduce the importance of very high efficiencies in producing thrust, this characteristic is expected to have a primary role in any mission undertaken in the foreseeable future. An important part of the effort in this program has been devoted to the study of the efficiency in practical operation of thermo-ionic thrustors using the most common propellants and components. Other characteristics such as dimensions, weights, simplicity, costs, and so forth will need consideration in future comparisons of space propulsion systems, but their importance at least in this initial stage, is not so urgent.

During recent years some anomalies in the measurement of the performance of thermo-ionic thrustors have been suspected, and possible explanations have been suggested even though definite identification has not been successful to date. Specifically, it has been suggested by us and by others[1, 2] that certain measurements, especially in the highest ranges of specific impulses and at extremely low mass flows, are subject to errors due to reasons not yet identified. The errors, however, seem to be associated with the difficulty of accurately reproducing true space conditions in the laboratory. For these reasons the experimental results in certain ranges of testing conditions are subject to the above mentioned uncertainties. While the complete elimination of this uncertainty seems possible only through real space tests, suggestions for improved laboratory testing techniques have been tentatively formulated.

2.1 Life Behavior of the Thermo-Ionic Thrustor

2.1.1 General

In 1963 when the possibility of operating arc thrustors at specific impulses over 5000 seconds was confirmed, an urgency was felt to determine the life characteristics of this type of thrustor. The conduction of life tests of 50 hours at some specific impulse between 3000 and 10,000 seconds was the first prescribed goal of this program. This result was obtained without particular difficulties using hydrogen as the propellant for three successive life tests of 50 hours each conducted respectively at 3000, 6000, and 10,000 seconds (as reported in other sections).[3] The definition of the term "life" is subject to a certain amount of interpretation. Generally the definition of "life" is in terms of a period of operation during which the deterioration of selected engine characteristics do not exceed a certain percentage of the initial values. After the 50 hours of uninterrupted life test the principal characteristics of the thermo-ionic thrustors tested had deteriorated much less than the amount usually admitted. Through simple extrapolation a probable life of many hundreds of hours was estimated. Considering, as stated before, that operating life in space must exceed 10,000 hours to be useful and acceptable in the future, a test of a few hundred hours is, of course, of limited value. While it is easy to extrapolate successful life tests for much longer periods, it is evident that actual operation for extended periods is necessary as a final proof. To be really useful the life test must be done in environmental conditions simulating real space as nearly as possible. The difficulties of running extremely long

life tests of this kind are evident both from a technical and an economical point of view and for these reasons it seems advisable to study other solutions, at least until a final prototype is developed. In a thermo-ionic thrustor, life is determined mostly by the consumption of the electrodes and other components operating at high temperature. If a system can be developed with continuous feeding of consumable components, the life problem will be practically solved. To analyze the possibility of continuous feeding of electrodes, various experimental studies are necessary. These should consider the effect of changing the geometry of the thrustor, the type of electrodes, the polarity, and so forth. For this reason, during the experimental program the influences of various design parameters on the improvement of life were investigated. These included the influence of the geometry of the thrustor, the insulation, the type of propellant, the working pressure, the voltage, the current, the external magnetic field, and the external environment. Finally, because of the "emissive" nature of a space thrustor, it has been considered necessary to extend the criteria for determining "life" to components of nearby systems that can be deteriorated by the propellant exhaust (solar cells, insulators, structures, instruments, optical components, and so forth).

2.1.2 Effect of the Geometry on Thrustor Life

The coaxial geometry illustrated in Figure 1 was the primary configuration used in the life tests described elsewhere in this report. Small variations were made from time to time without departing too much from the original design. As illustrated, in this coaxial geometry the central electrode is the cathode and the outer electrode with a small conical termination is the anode. After many hundreds of hours of tests with this geometry it can be established that the life behavior of the cathode, especially if a substantial mass flow of propellant is used, is not critical. This is evidenced by the uniform distribution of the arc discharge along the surface of the cathode (see Figure 2) combined with the possibility of feeding the axially located cathode in a continuous manner to compensate for its consumption at whatever rate this occurs. The rate of consumption of the cathode in a thermo-ionic thrustor depends on the operating temperature and environmental conditions. During our life tests at low operating temperature a buildup of material was noted (Figure 3). The thermo-ionic emission of the cathode artificially increased with a certain percentage of thorium added to the pure tungsten base might diminish with long use, but this fact has never been investigated experimentally. A decrease in thermo-ionic emission might have a certain influence on the stability and starting qualities of a thrustor thereby reducing its useful life. For this reason a better knowledge of these effects will be desirable. If the mass flow is drastically reduced or even completely eliminated the uniformity of the discharge around the cathode continues to be satisfactory, but if the cathode temperature is

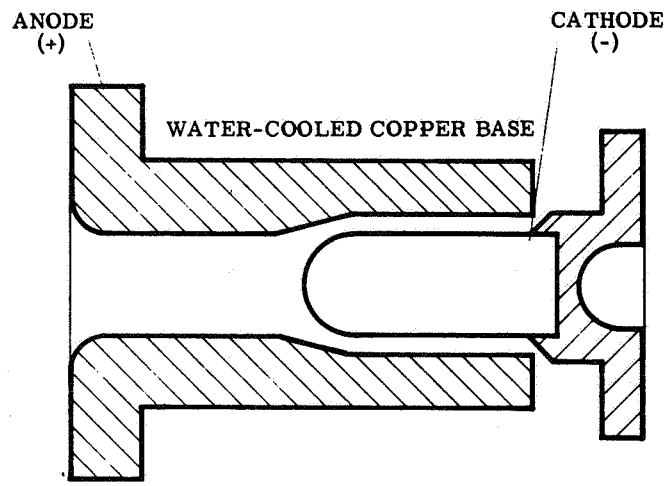

Figure 1. Typical Coaxial Electrode Configuration

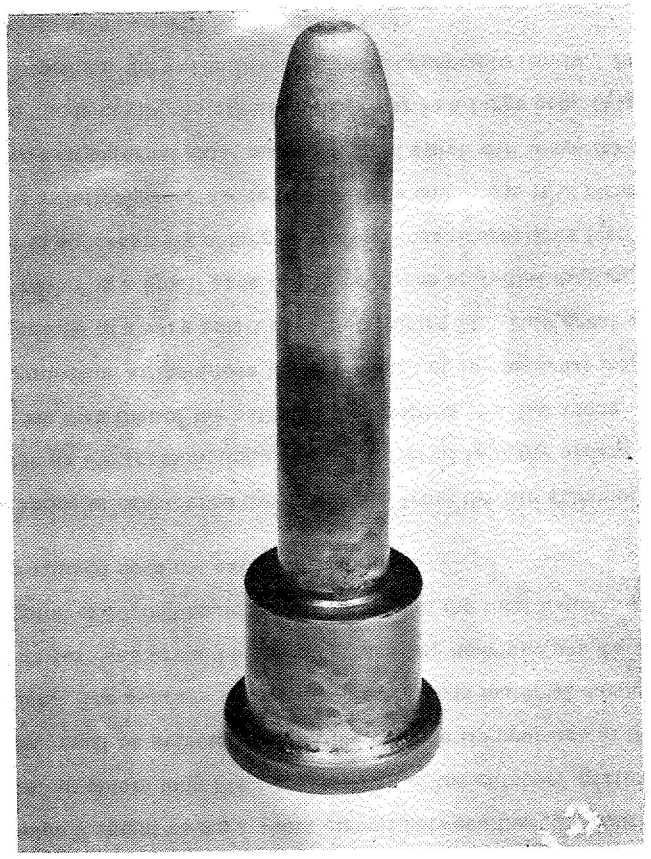

Figure 2. View of Cathode Tip Showing Even Distribution of the Arc Discharge

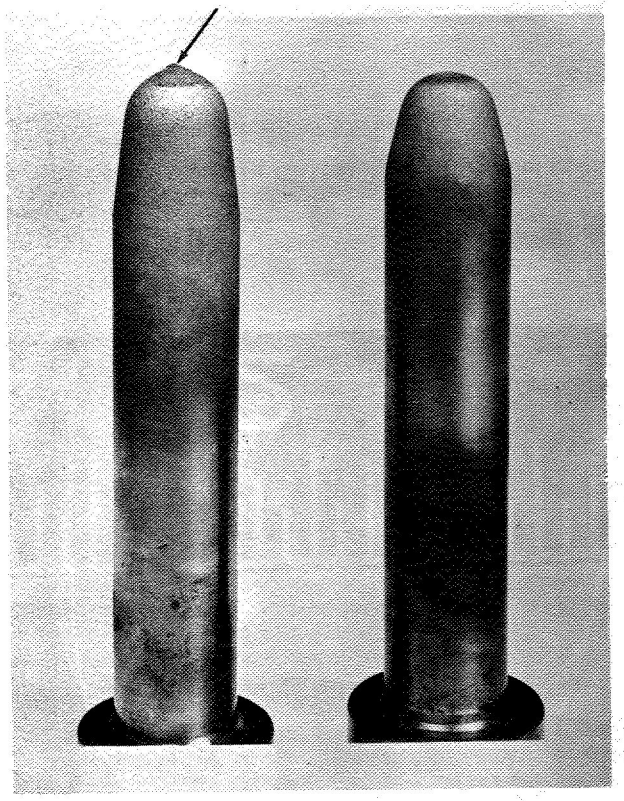

Figure 3. First Appearance of Cathode Build-up After 75 Hours of Operation

not high enough a deposit of small particles of tungsten builds up on the cathode tip (see Figure 4). This can be dangerous for long operation, especially since it might cause a short circuit between the electrodes. For this reason, to obtain long life the geometry of the cathode, particularly near its tip, must be selected so that the cathode tip operates at the right temperature. The average consumption of cathode material during the 50-hour life test was around 50 micrograms per hour and per kw input. For a mission of 10,000 hours and 100 kw input the total amount of cathode material required does not exceed 50 grams.

When the anode is considered the conditions from the life standpoint become much worse as the consumption of anode material is many orders of magnitude higher than that of the cathode. In addition, for the anode, the arc foot or termination at the anode in the absence of any external magnetic field is confined to a very small spot (see Figure 5). This great concentration of power in a small area easily produces an initial melting of the anode that is successively enlarged to dangerous proportions (see Figure 6). To obtain a relatively long anode life in these conditions it is necessary to superimpose an external axial magnetic field which will move the arc spot around the anode cavity distributing the power in a large area (Figure 7). With this expedient the anode life returns to acceptable limits. But other complications arise as will be discussed later.

When liquid or solid propellants (as alkali metals for example) are used, and especially when the working temperature of the thrustor body (not only of the electrodes) must be relatively high (to avoid condensation and for

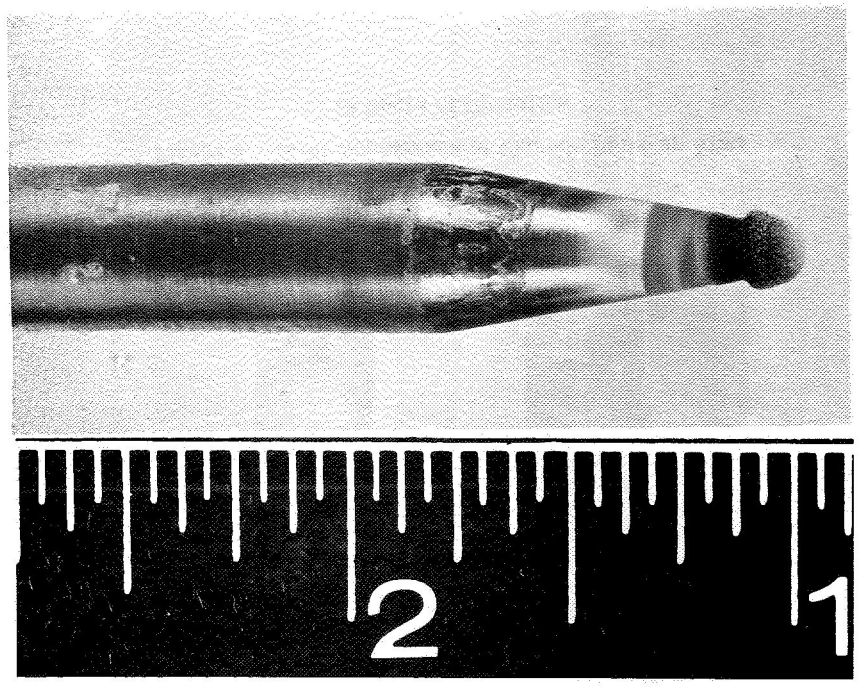

Figure 4. Build-up of Tungsten Cathode After 2 Hours of Operation Without Propellant Throughput

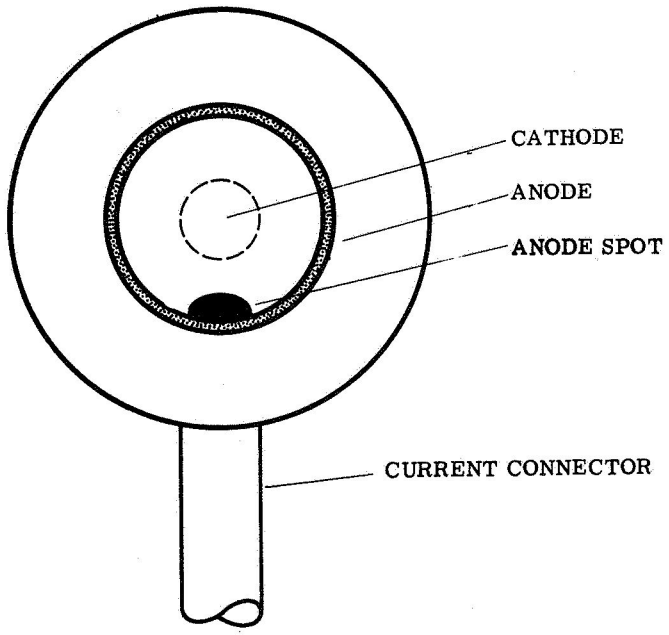

Figure 5. Anode Arc Termination Stabilized in a Single Spot at High Current Operation

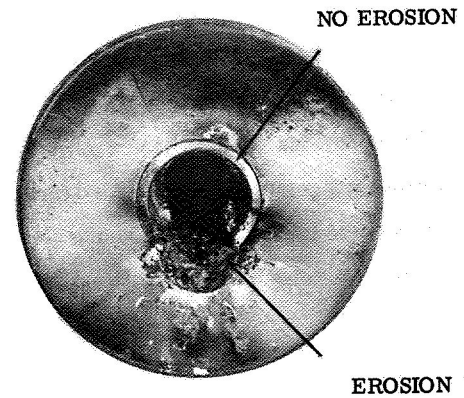

Figure 6. Anode Erosion During Life Test Due to Localized Arc Termination

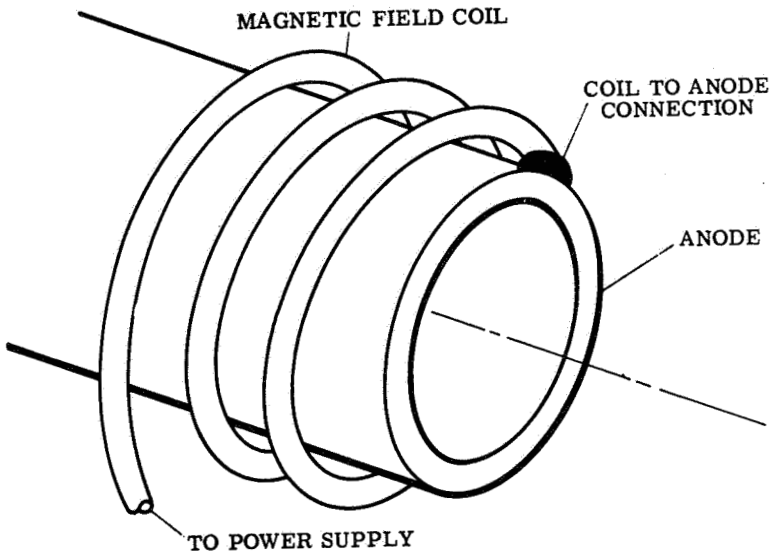

Figure 7. Magnetic Field Coil in Series With Anode Avoids Localized Arc Termination

radiation cooling), the influence of the design or geometry on the achievement of extremely long periods of life becomes critical. This is particularly true in free space where extremely low pressures result in significant amounts of evaporation at modest temperatures. Under the combined effect of temperature, low pressure and extremely active propellants; insulators, metals and components of any type interact reducing the desired lifetime. We have found in long high temperature life tests with thrustors protected in a pyrolytic graphite envelope that the carbon vapors reacted with tungsten forming tungsten carbide of very low melting point. Similar reactions have been found between carbon or metal vapors and the best existing refractory insulators with rapid deterioration of their electrical and mechanical qualities. In these cases the effect of the geometry on life becomes of primary importance.

In conclusion, from the results of many life tests on the thermo-ionic thrustors conducted during this program at various power levels and specific impulses and from experiments and studies conducted by others,[2, 4] it seems possible after a period of engineering development to design long life geometries if common gaseous propellants are used. If liquid and solid propellants and especially metal vapors are used, further efforts and slightly different geometries will be necessary

2.1.3 Effect of the Propellant on Thrustor Life

Due to the difficulty and high cost of life tests, an experimental comparison of the life obtainable with different propellants has not been made (to our knowledge) prior to the present program. From a purely theoretical viewpoint, the best propellant for long life is the one that can operate at the lowest temperature for any particular specific impulse and has the minimum chemical affinity with the thrustor components at that temperature. Table 1 tabulates the estimated working temperature ratios and the chemical reactivities of various propellants with electrodes and insulators. It is evident that hydrogen is by far the best propellant when long life is considered exclusively. Its working temperature is the lowest for any specific impulse, and its chemical affinity with metals is often, in practice, more beneficial than harmful. However, the effect of hot hydrogen on the insulators during extremely long periods of operation is not known. On long runs hot hydrogen, being a good reducing agent, should transform the best insulators of the oxide, nitride, or fluoride type to nearly perfect conductors. For this reason, in thrustors destined for long periods of operation the insulators have been located as far as possible from the hot zones to avoid contact with hydrogen. Some designs of electrode configurations, where the hot cathode tip is practically in contact with a concentric insulator, are not well adapted for long life operation (Figure 8). Using propellants other than hydrogen, a reduction of life can be expected both for conductors and insulators because of the higher operating temperature and of the increased chemical activity. When for storage or other reasons a propellant is required which is heavier than hydrogen (but has similar

TABLE 1

CHEMICAL ACTIVITY OF VARIOUS PROPELLANTS AND ELECTRODE MATERIALS AT HIGH TEMPERATURES

Propellant	T/T_{H_2}*	Chemical Activity				
		W	Mo	Cu	Al_2O_3	BN_3
H_2	1	None	None	None	Unknown	Unknown
D_2	2	None	None	None	Unknown	Unknown
He	4	None	None	None	None	None
Li	7	Strong	Strong	Strong	Strong	Strong
NH_3	18	Moderate	Moderate	Strong	Unknown	Unknown
K	39	Strong	Strong	Strong	Strong	Strong
A	40	None	None	None	None	None

*Temperature of various gases compared with temperature of H_2 assuming only first ionization.

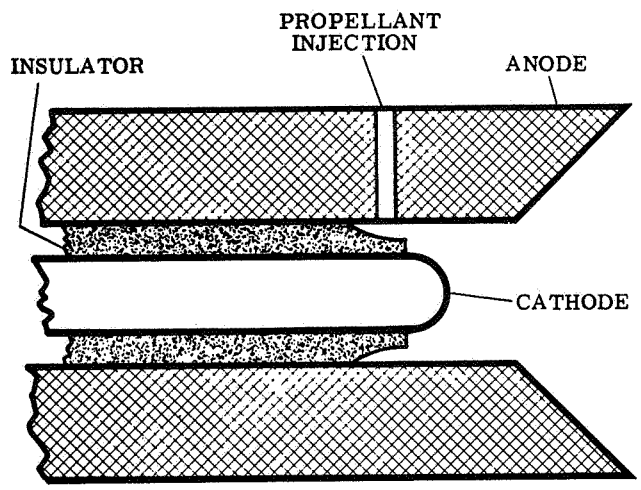

Figure 8. Hot Hydrogen or Metal Vapors Can Reduce Insulators to Metal Form

characteristics, at least as far as life is concerned) the choice may well be deuterium (D_2, molecular weight 4). This propellant has not been considered until now as a possible candidate for propulsion applications probably because of its cost, but it presents some interesting possibilities especially because of its thermodynamic properties. Extensive studies of this propellant have been made (see Section 2.2.3) but further investigations are necessary for determination of its effect on thrustor life. The higher operating temperature of deuterium limits somewhat the maximum specific impulse attainable with this propellant. From present test results it appears that for operation at the same temperature the same life can be obtained using either hydrogen or deuterium. Figure 9 is a photograph of electrodes (cathode and anode) operated for an extensive time with a relatively high current using deuterium as a propellant. The third lightest propellant available is helium (He, atomic weight 4). Although extensive tests have been made, its effect on the life of the thrustor for a very long run is not known. Comparison between deuterium and helium are suggested for future work. The fourth lightest propellant available is lithium (Li, atomic weight 6.9) which is solid at room temperature and presents various interesting properties for use in electric propulsion. While life tests exceeding 10 to 15 hours are not now available to the best of our knowledge, some 50-hour tests will be completed in the near future.[5] From our experiments which did not exceed 5 hours it appears that operation of a thermo-ionic thrustor with lithium produces very rapid deterioration of any hot insulating material, some deterioration of cathodic material (tungsten), and slight deterioration of anodic material (tungsten and molybdenum). Figure 10 shows a pair of electrodes after operation for a few hours with

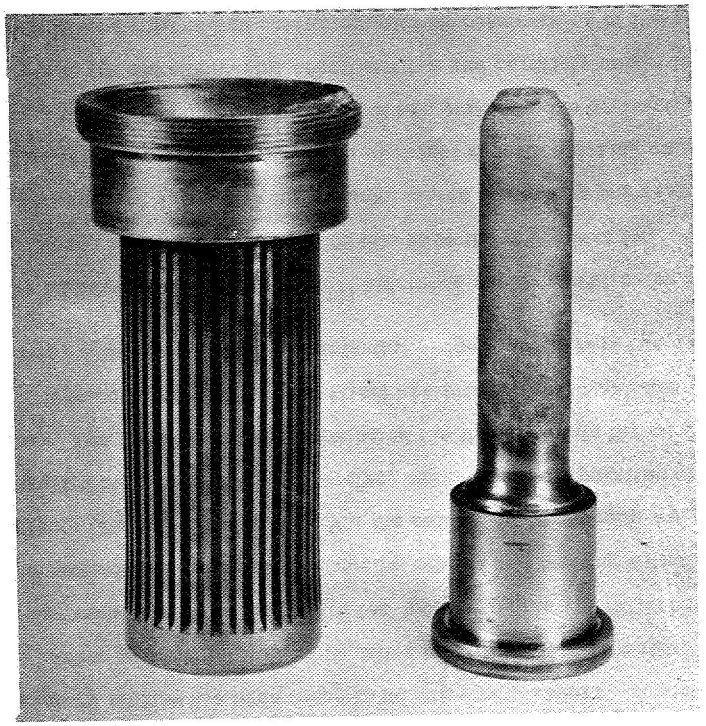

Figure 9. Electrodes After Long Operation With Deuterium at 5000 Seconds I_{sp} and 2000 Amperes Arc Current

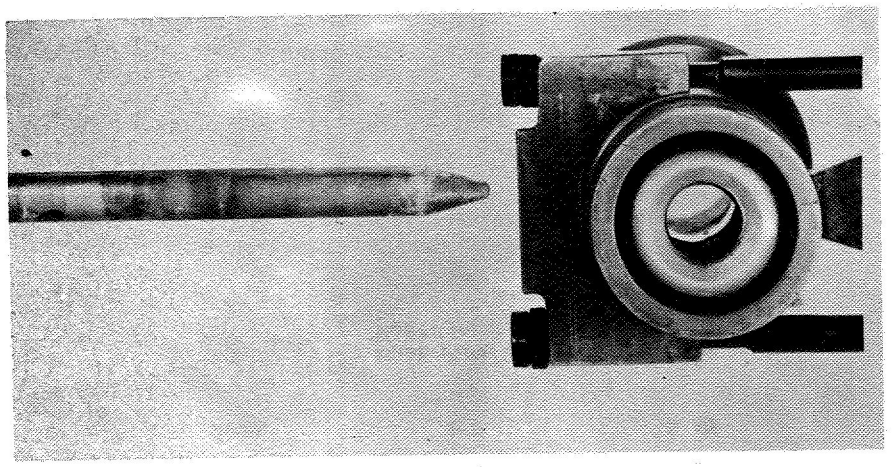

Figure 10. Electrodes After Two Hours of Operation With Lithium 3 Mg/Sec, 300 Amperes

lithium at a mass flow of 3 mg/sec. The weight loss for the anode was 1.3 gm/hour while the cathode gained 0.8 gm/hour. Lithium (as all the alkali metals at high and very high temperatures) has strong affinity for practically any substance (Table 2). Going up along the atomic weight scale we find beryllium (Be, atomic weight 9), and boron (B, atomic weight 12) has been indirectly studied for its effects on the electrodes in radiation-cooled thrustors and its activity with tungsten, molybdenum and other refractory metals has been found to be extremely severe. A small amount of carbon vapor is sufficient to cause localized transformation of most of these metals into carbides with low melting points and different expansion characteristics capable of producing cracks and melting with disastrous effects (Figures 11 and 12). But the relatively low atomic weight of carbon, its high refractory properties, the uniform evaporation at low pressure, and the possibility of operating the thermo-ionic thrustor with electrode vapors (as will be seen later) are interesting properties that can justify a better study of this potential propellant for long life operation.

We accidentally demonstrated[1] electrode vapor operation by reducing the hydrogen mass flow to zero. In this case the propellant (W, atomic weight 183) requires extremely high temperatures to develop any respectable specific impulse. The small values of thrust recorded during extended life tests using no propellant throughput are probably due primarily to anomalies in the environmental conditions but are certainly useful in studying long-life conditions and characteristics of consumption of the electrodes. Table 3 shows the loss of weight of various anodes at different operating temperatures. Table 4 shows the gain in weight of different cathodes in

TABLE 2

EROSION OF BORON NITRIDE INSULATION USING LITHIUM AND POTASSIUM PROPELLANTS

WEIGHT LOSS OF INSULATOR, GRAMS/HOUR

Cathode Temperature °K	Propellant Used Li	K
1500	0.1	0.24
1800	0.5	1.30
2000	1.5	2.40

Mass Flow = 0.5 - 3.0 mg/sec
Power Input = 3 - 8 kw

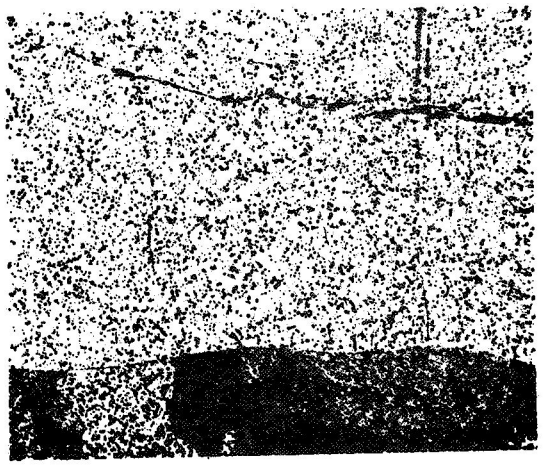

Figure 11. Micrograph Showing Deep Carburization of Tungsten Electrode Material

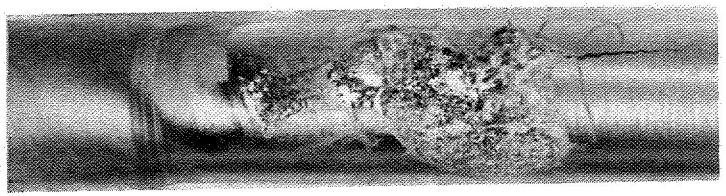

Figure 12. Erosion of Tungsten Anode Material Under Action of Carbon Vapor

TABLE 3

WEIGHT LOSS OF RADIATION-COOLED TUNGSTEN ANODES
AT DIFFERENT OPERATING TEMPERATURES
WITH NO PROPELLANT THROUGHPUT

Anode Temperature °K	Anode Weight Loss Gram/Hour Type A	Anode Weight Loss Gram/Hour Type B
1500	0.4	1.0
2000	1.3	3.0
2500	2.1	5.2

A: Power Input = 2 - 10 kw

B: Power Input = 10 - 30 kw

TABLE 4

WEIGHT INCREASE OF RADIATION-COOLED TUNGSTEN
CATHODE AT DIFFERENT OPERATING TEMPERATURES
WITH NO PROPELLANT THROUGHPUT

Cathode Temperature °K	Cathode Weight Increase Gram/Hour
1500	1.4
1800	0.8
2000	0.1

Power Input = 2 - 8 kw

the same conditions. Figure 13 shows the thrust values obtained at various conditions of operation. Tungsten deposits have been found at almost any position in the vacuum system demonstrating not only the presence of tungsten vapor, confirmed also by spectrographic analysis,[6] but also of a new characteristic of metal vapor operation capable of indirectly affecting the life conditions. This initial test demonstrated for the first time that solid propellants, and especially metals, might present some difficulties in connection with their condensation on vital parts of the spacecraft producing mechanical, optical, or electrical disturbances. In the analysis of long life operation this possibility must be considered. In successive tests using alkali metals (particularly lithium and potassium) the condensed metals built up substantial conducting layers in the vacuum tank (see Figures 14 and 15). If similar deposits are produced on the vital parts of the spacecraft (as windows, antennas, and so forth) especially during long missions, the use of condensable metals as propellants may be untenable (see Figures 16 through 19). In conclusion, it seems advisable, in the choice of a propellant for space operation, to consider its direct and indirect effect on the life and on the performance of the various components of the spacecraft.

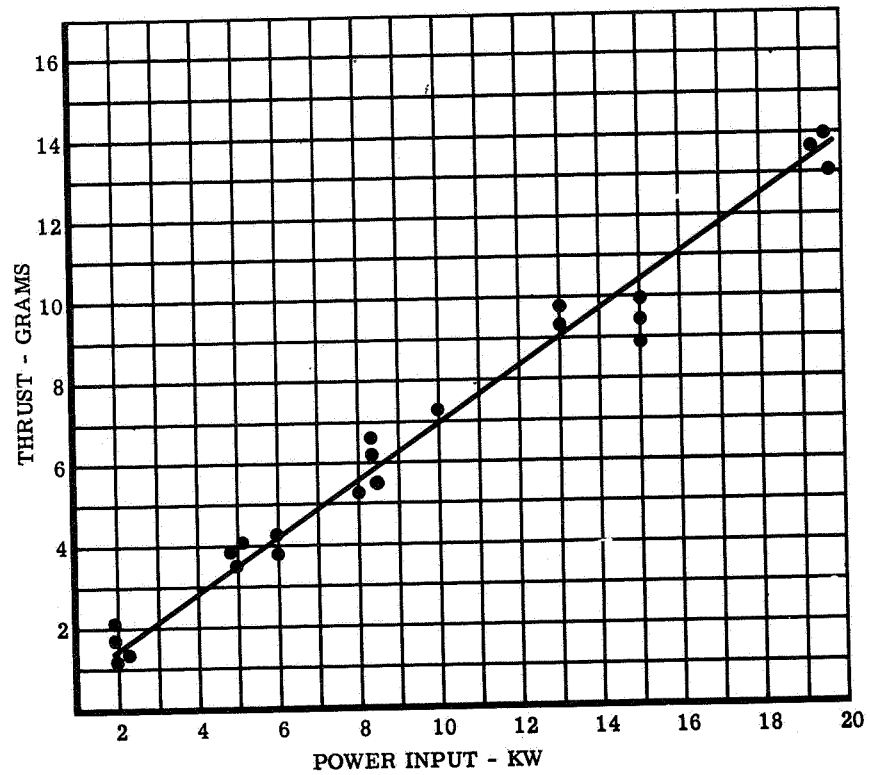

Figure 13. Thrust Versus Input Power for Radiation- Cooled Thermo-Ionic Thrustors Without Propellant Throughput

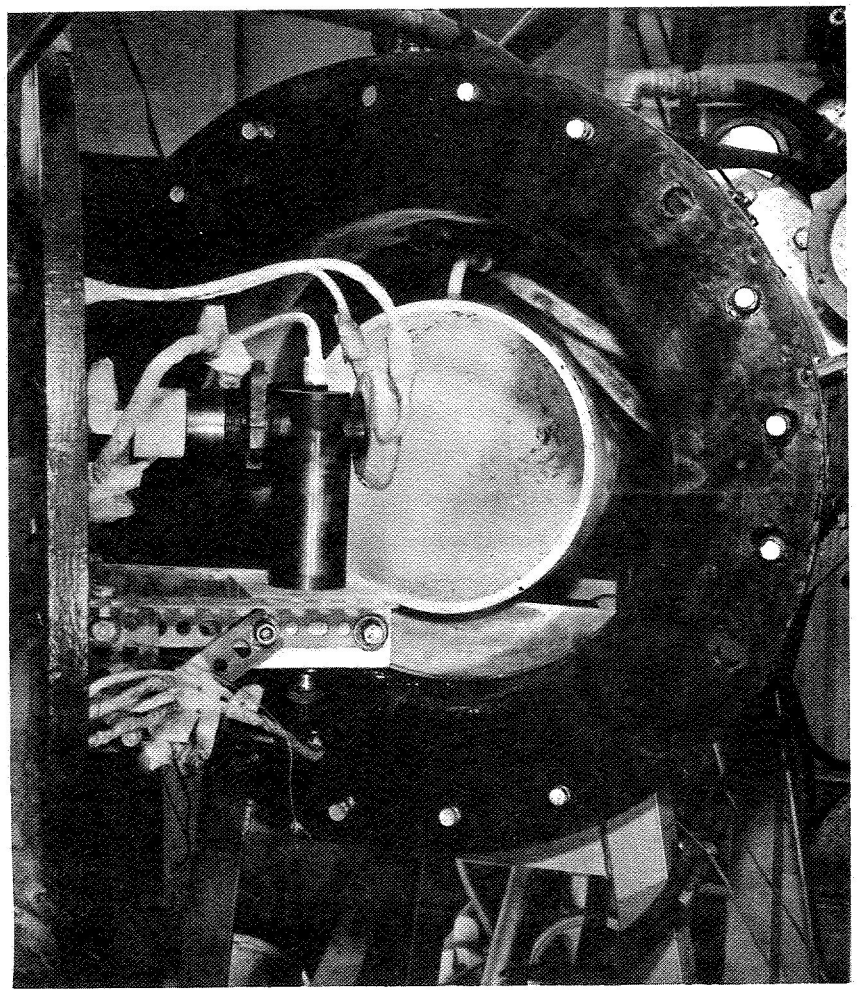

Figure 14. Condensation of Lithium Vapor on Engine Components and Vacuum Chamber

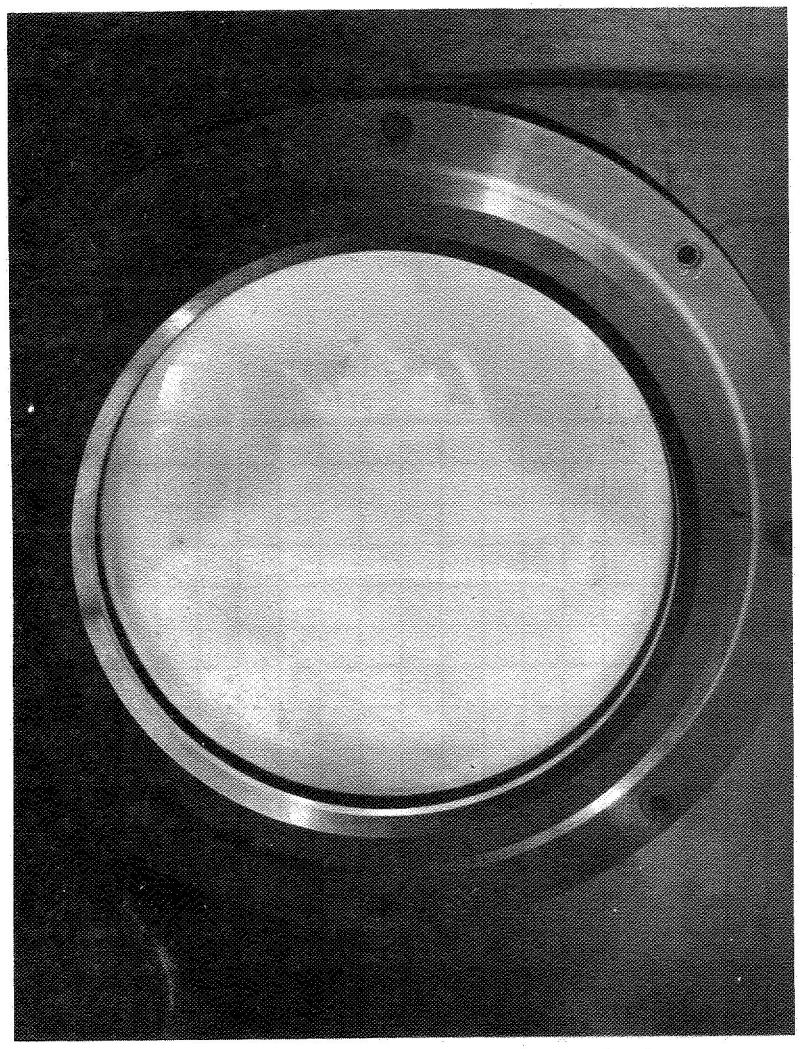

Figure 15. Deposit of Lithium on Tank Window (Opacity in one hour at 1 mg/sec mass flow)

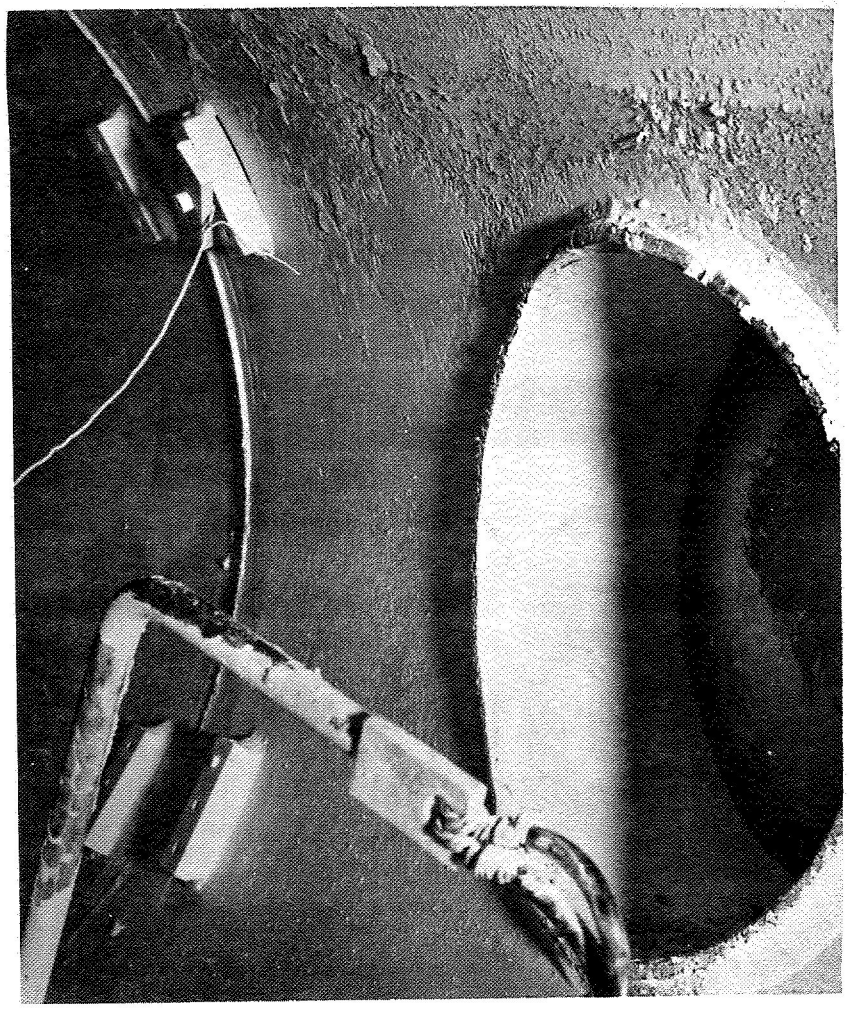

Figure 16. Lithium Condensed From Vapor in Vacuum Tank

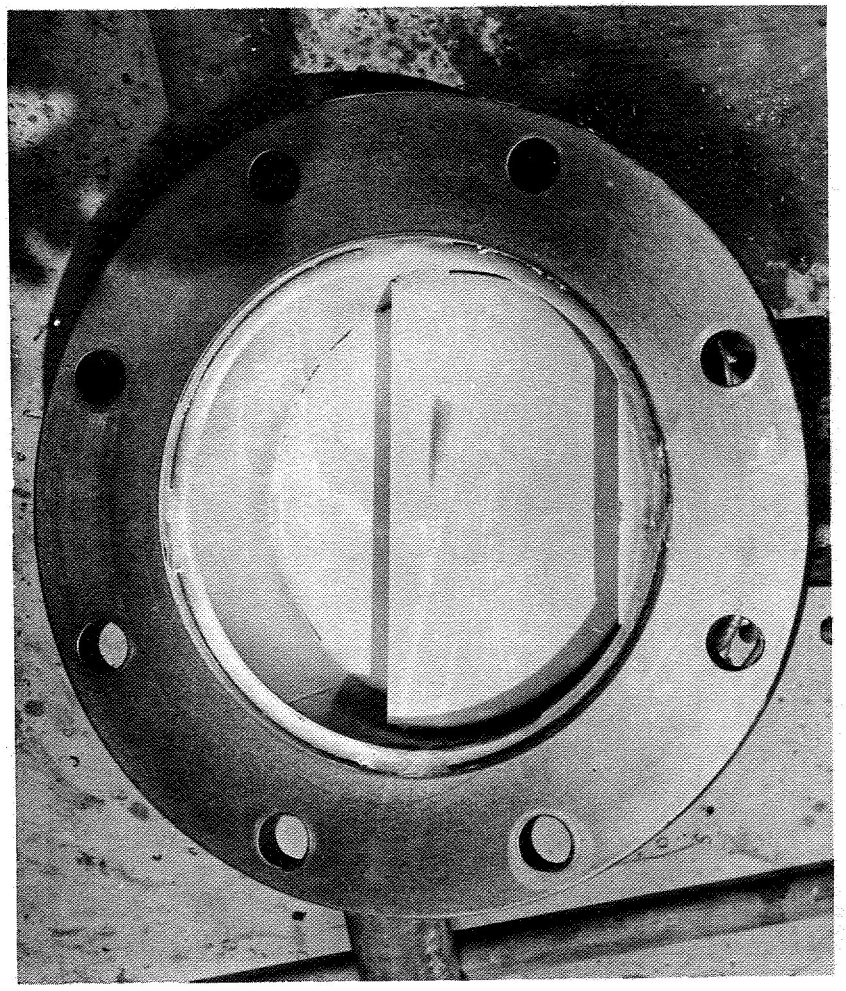

Figure 17. Lithium Condensed in Vacuum Pump Baffle (20 Feet From Vapor Jet)

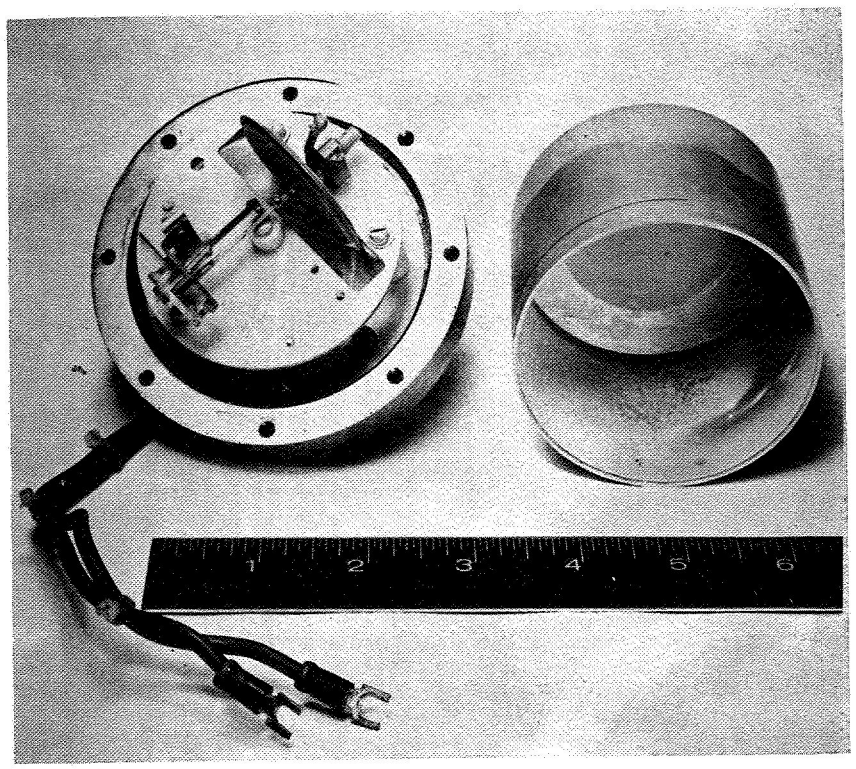

Figure 18. Lithium Deposit in Vacuum Switch Connected to Tank Through -/2-Inch Pipe 20 Feet Long

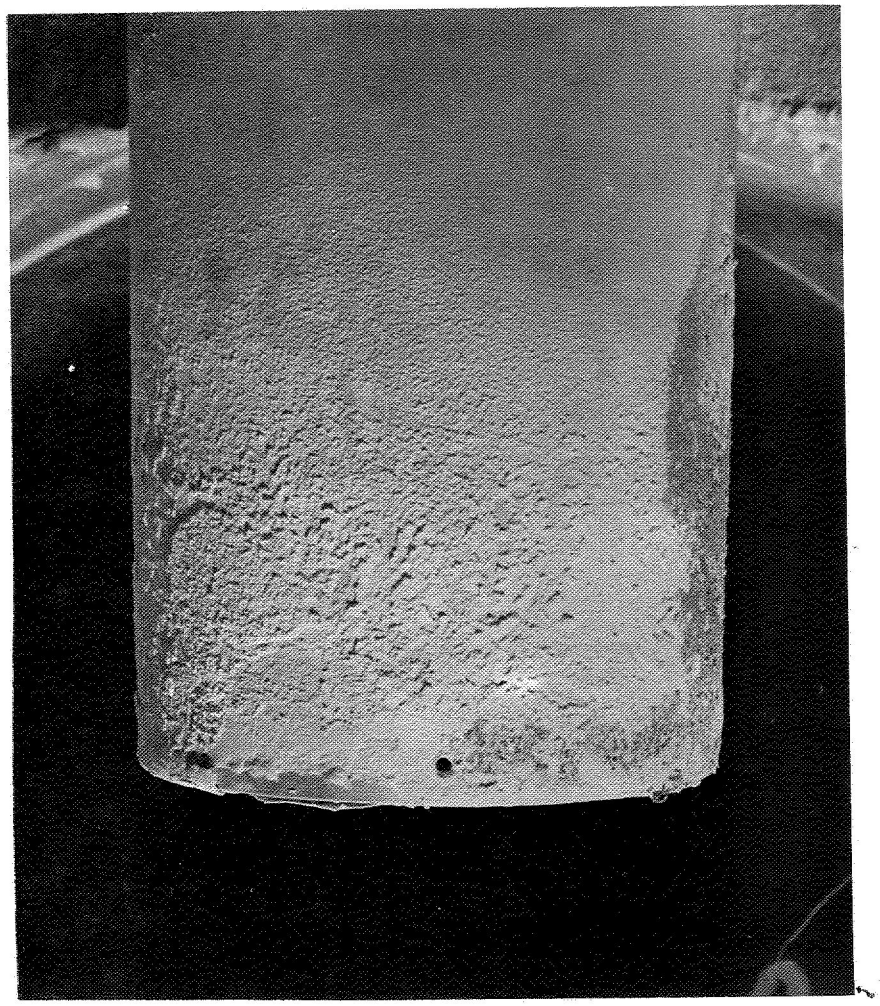

Figure 19. Potassium Deposited in Vacuum Tank, One Hour Operation at 30 Mg/Sec Propellant Flow Rate

2.1.4 Effect of the Arc Chamber Pressure on Thrustor Life

One of the principal effects of changing pressure in the arc chamber is the variation of the spreading of the arc foot on the cathode surface. When the pressure is increased, the arc concentrates in a smaller and smaller area. The increase in power density produces a melted spot at the tip of the cathode (see Figure 20). Further increase in pressure increases the power density and produces a bigger and bigger crater at the cathode tip (Figure 21) until cathode destruction occurs (Figure 22). When the pressure is decreased the arc foot spreads on the surface of the cathode and the melted spot disappears. The reduction of the pressure in the arc chamber has been one of the principal factors in the development of the thermo-ionic thrustor. Early in the development (1963) it was found possible to operate a cathode of 6.3 mm diameter at over 3000 amps for long periods of time (Figure 23). The improvement of electrode life results from a more uniform distribution of current. At very low pressure (a few Torr) the discharge covers all the cathode surface often extending back several inches from the tip (Figures 24 and 25). In this case artifices to reduce the cathode foot spreading may be required. Cann[4] shows that a certain pressure around the cathode is beneficial for increasing the stability of the arc. During our life tests we have found that both cathode and anode can benefit if an optimum operating pressure is adopted. However, this optimum pressure is generally different for the two electrodes. For the cathode, when the pressure is low, the spreading of the arc foot is too wide. The best condition of operation is obtained by creating around the cathode an ambient pressure slightly higher than the pressure to which the anode is exposed.

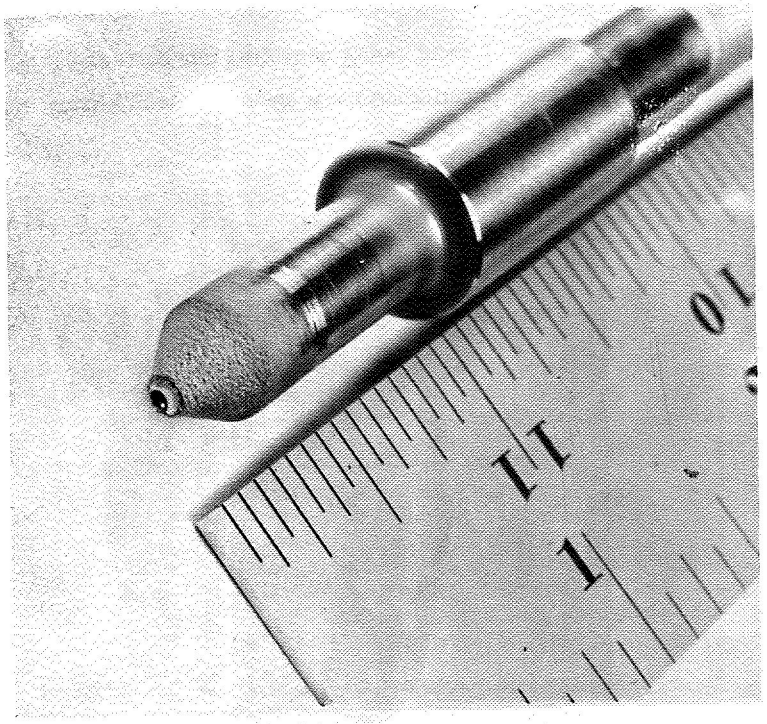

Figure 20. Melted Cathode Spot Operating at High Pressure and Low Power

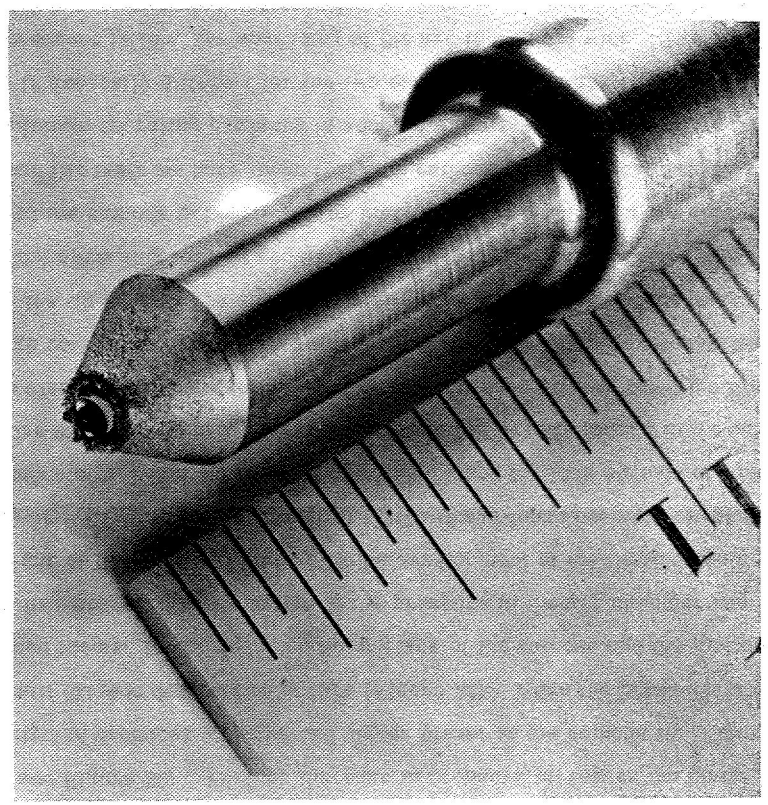

Figure 21. Increased Cathode Crater Operating at High Pressure and High Power

Figure 22. Destruction of Cathode When Operating at Very High Pressure and Very High Power Input

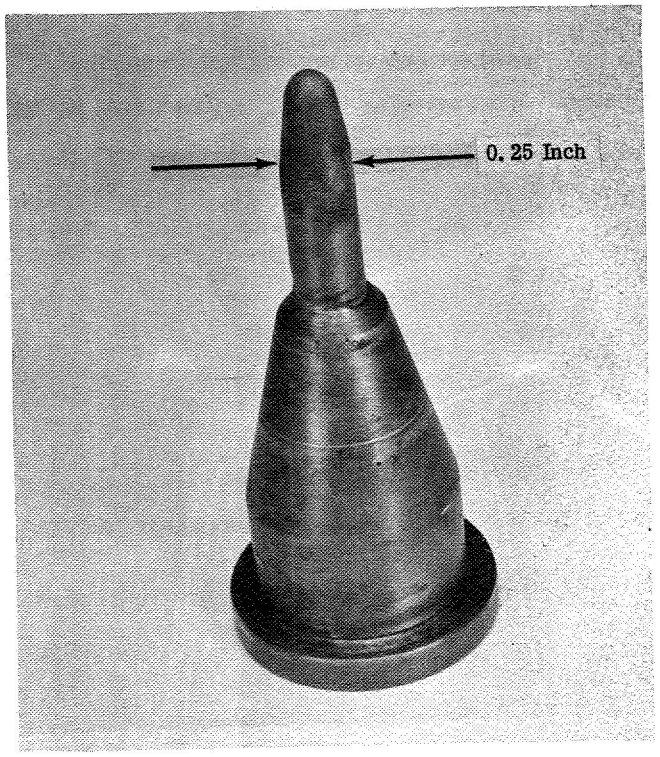

Figure 23. First Thermo-Ionic Cathode After Operation at Low Arc Chamber Pressure and 3500 Amperes

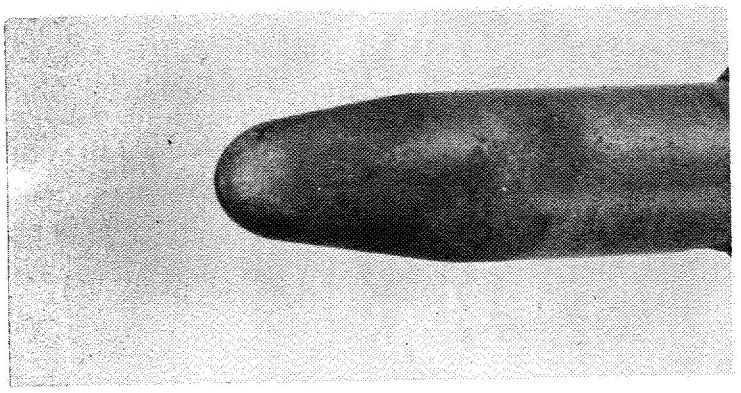

Figure 24. At Low Pressure Operation the Arc Attachment is Spreading on the Cathode Surface

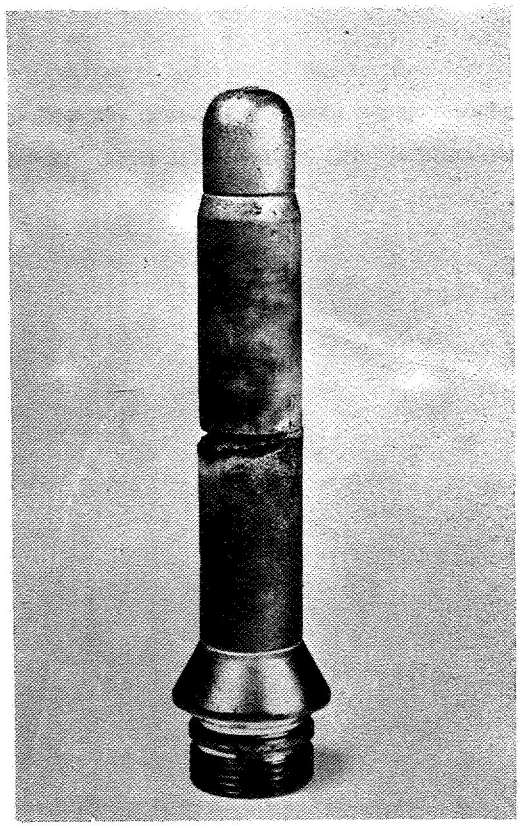

Figure 25. At Very Low Arc Chamber Pressure the Spreading of the Arc Attachment Reaches the Cathode Base

The choice of working pressure for the anode and cathode has an appreciable influence on both the rate and uniformity of the electrode consumption, especially for the anode because of electron bombardment. As is well known, variations in the chamber pressure are also obtained by changing the power density, the mass flow, the magnetic field, and so forth, so in the design and in the experimentation all these effects must be considered. When the outside pressure is very low (as in good simulated space conditions) other influences appear and require consideration if long life is to be obtained. The effects of environmental conditions will be considered further in Section 2.1.7.

2.1.5 Effect of Power, Current, and Voltage on Thrustor Life

While the power density is a determining factor in the thrustor life, different proportions of current and voltage for the same power density can produce appreciable differences in the life behavior of the electrodes. Figure 26 shows the cathode power density during our three life test periods at 3000, 6000, and 10,000 seconds. The consumption of the cathode electrode was only 50 micrograms per hour and per kw. These results indicate that higher power densities can be tolerated. During the first life tests the arc was operated without external magnetic field, and the anode current was concentrated in a spot on the surface of the anode. This resulted in an excessive consumption of the anode in the particular spot where the arc foot was standing (maximum power density 17 kw/cm^2), but at the same time permitted us to determine the maximum anode power density which is acceptable in a long life test without an external magnetic field (Figure 27). The total erosion of the anode (mostly in the arc spot) was about 5 mg/hour per kw. This is about 100 times more than the cathode. Figure 28 shows the anode power density for three different specific impulses with an external magnetic field applied. The power density was calculated considering all the anode internal surface participating as the arc foot was continuously rotated around it by the action of the external magnetic field. The power density of the anode now appears comparable to that of the cathode. Its low value explains the very small consumption of the anode during the 50-hour life test.

It is interesting to study the influence on life of changes in the proportions of current and voltage. These can be produced by changing the intensity

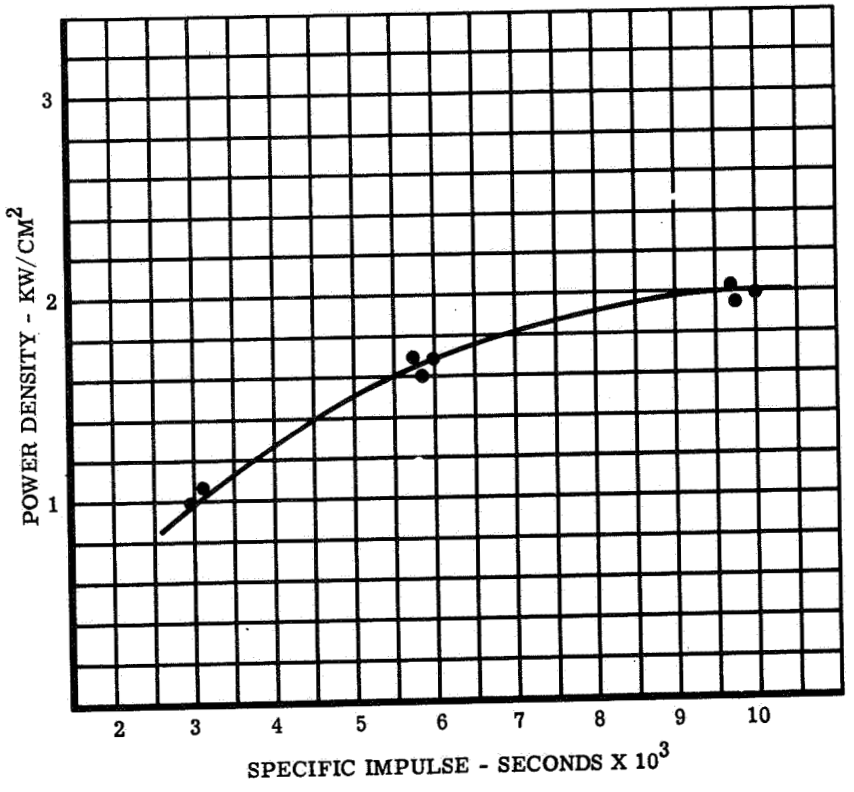

Figure 26. Power Density for Effective Cathode Surface Area Used During 50-Hour Life Tests at 3000, 6000, and 10,000 Seconds Isp

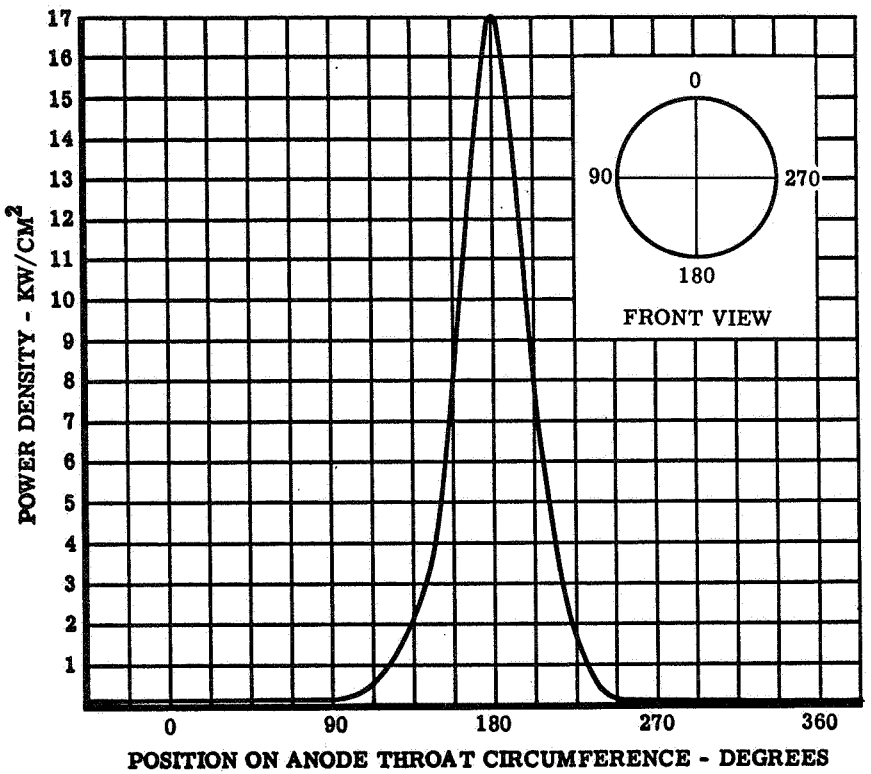

Figure 27. Variation of Power Density in Effective Anode Surface Area at 3000 Seconds Isp Without External Magnetic Field

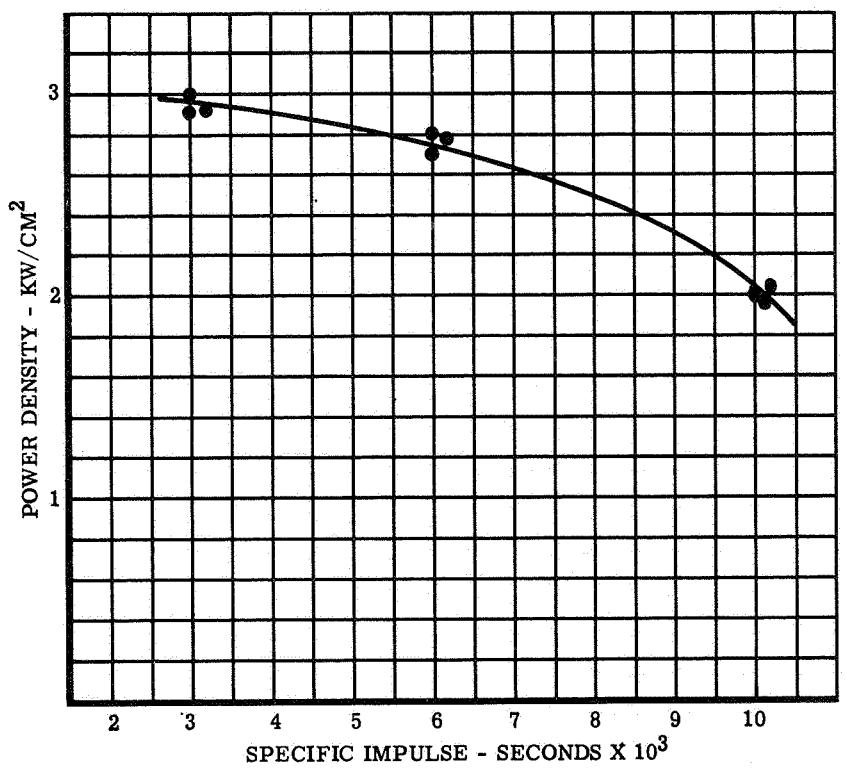

Figure 28. Power Density for Effective Anode Surface Area With Applied External Magnetic Field at 3000, 6000, and 10,000 Seconds Isp

of the field at constant power density (Figure 29), and represent a separate effect from the direct influence of an external magnetic field on life as discussed in Section 2.1.6. The behavior of the electrodes from the life standpoint at constant power input and with various proportions of current and voltage is not clearly known. From our test results it appears that the cathode and anode react differently to excesses of current and voltage. If the distribution of the current on the anode is uniform, very high currents do not seem to produce excessive damage until the voltage is relatively low. On the other hand, increasing the voltage also at moderate currents appears to result in damage because this condition causes localized spots of very high current density resulting in melting of the anode material even when the most elaborate cooling system is used.

During our life tests the operating voltage has always been kept under certain limits empirically determined and known as "dangerous" values. If the operating voltage exceeds these values, sudden anode damage results even when the operation seems normal. A "dangerous" voltage zone may be detected by gradually increasing the external magnetic field or the power while the front part of the anode is visually observed. Figure 30 is a photograph of the jet before this dangerous condition is reached. No localized luminous spots are visible. When the voltage is increased, some of these spots appear (Figure 31) and they increase in number and intensity as the voltage is further increased (Figure 32). The safe operating voltage is below the value at which the luminous spots appear. A good margin of safety must be allowed because immediately before the appearance of the luminous spots, the destructive mechanism is already in action, and

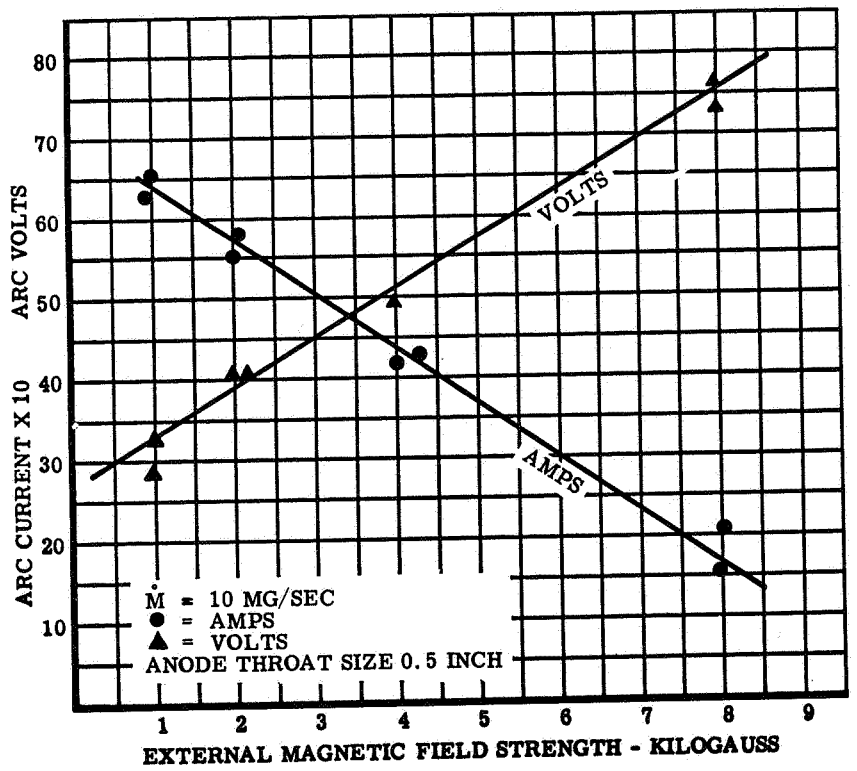

Figure 29. Variation of Current and Voltage With the Intensity of External Magnetic Field

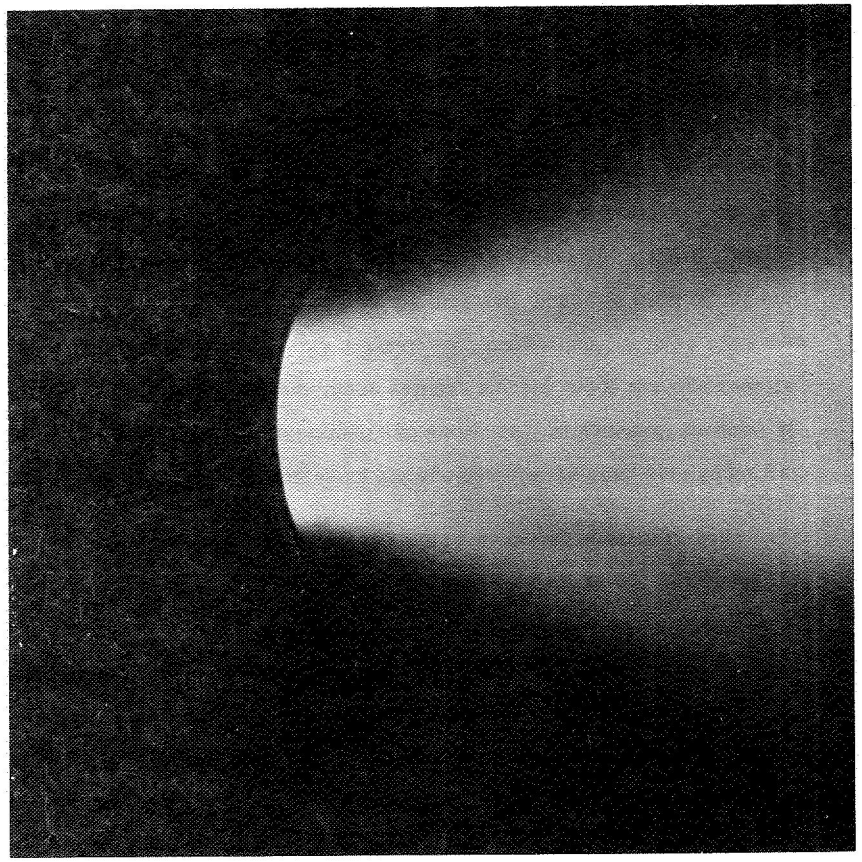

Figure 30. Jet Operating Normally Without Anode Luminous Spots

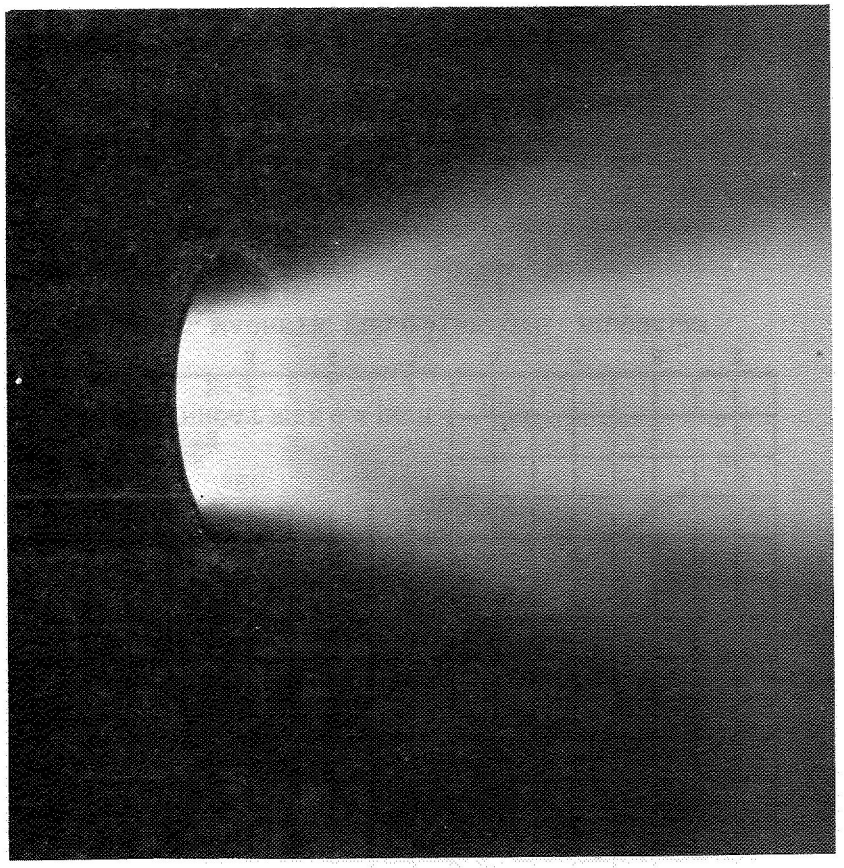

Figure 31. First Appearance of Luminous Anode Spots at Increasing Voltage

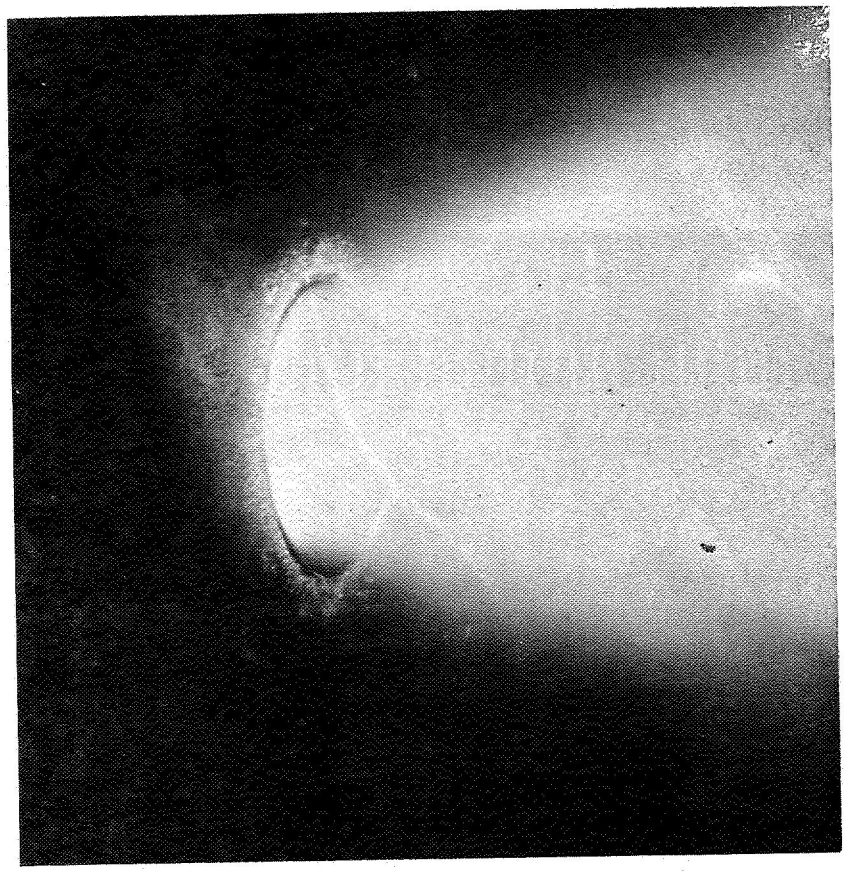

Figure 32. Anode Spots Increase Both in Number and Intensity as Voltage is Further Increased

its effects can be felt after long hours of testing. An example of the effects of localized high current density is illustrated in Figure 33 which shows a water-cooled anode that was life tested for a long time under stable operating conditions with reproducible results. After 13 hours of testing, the value of the pressure in the vacuum chamber increased by a small percentage for no apparent reason. The test was interrupted, and a careful examination revealed a water leak on the anode surface. The electrode surface appeared to be undamaged, but a microscopic hole was found connecting the surface to the inside of the water cooling circuit. This phenomenon, which we have tentatively attributed to electrons returning to the anode from downstream zones of the jet without producing luminous spots, is further discussed in Sections 2.1.6 and 2.1.7. If the conditions of dangerous voltage (as in Figures 31 and 32) are reached and the power input is increased more and more, a complete destruction of the anode is obtained even though the most elaborate cooling systems are used (Figure 34). From the preceding experimental data it can be concluded that the life of the anode in thermo-ionic thrustors depends on obtaining a uniform distribution of the electrons carrying the arc current. If the current is high and the voltage low, the uniformity seems to improve, whereas the opposite seems to happen at low current and high voltage. Using a single hollow anode, improved uniformity is obtained by rotating the arc with an external magnetic field. Future tests are necessary to extend our understanding of the influences of power, current, and voltage on anode life.

There is a similar need for experimental work to improve our understanding of the effect of these variables on cathode life. The cathode is ion dominated

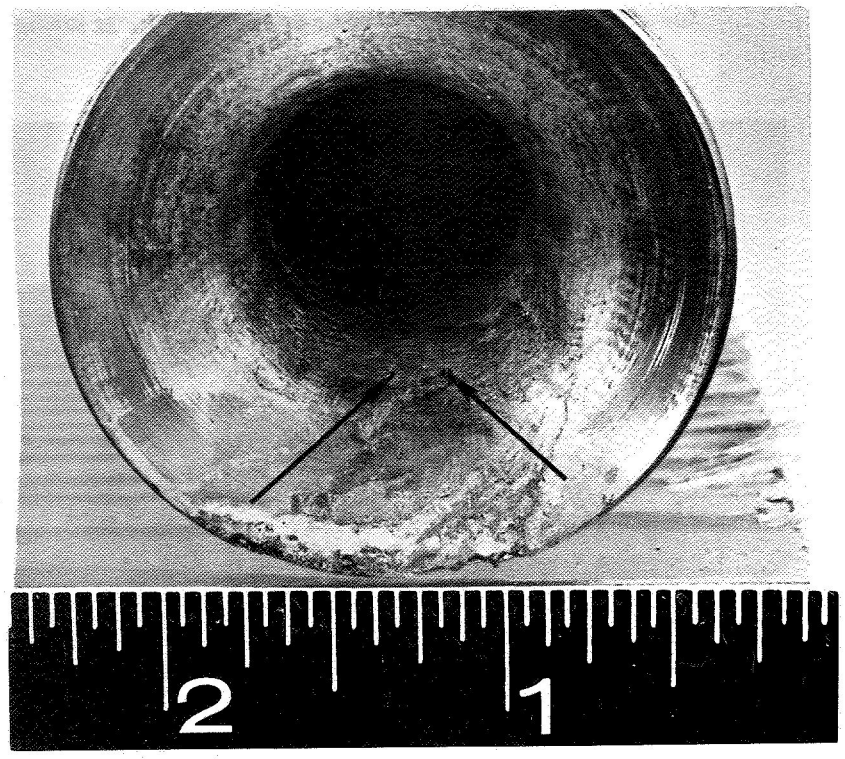

Figure 33. Unexpected Pinhole Erosion After a Long Period of Operation

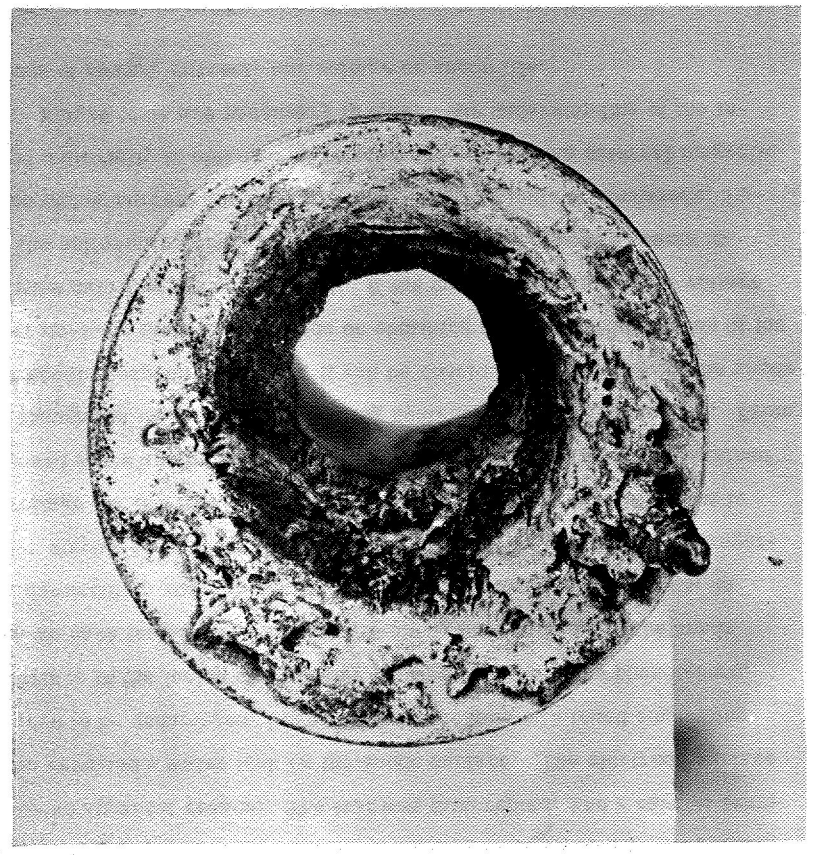

Figure 34. Destructive Effects With Complete Anode Melting. Power Input is Increased After Reaching Dangerous Voltage Level

and emits electrons. This constitutes the basic difference affecting the life characteristic of the cathode. Reduction of thermo-ionic emission can be a limiting factor in extremely long life operation of the cathode because of its effect on starting and stability. Experiments have been conducted during this program to find the limits in current capacity of the cathode. As illustrated in Section 2.1.4, Figure 23, cathodes have been operated successfully with very high currents without external magnetic fields by using relatively low arc chamber pressures. An examination of the cathodes reveals an unusually uniform but small consumption for the level of arc current used (Figure 35).

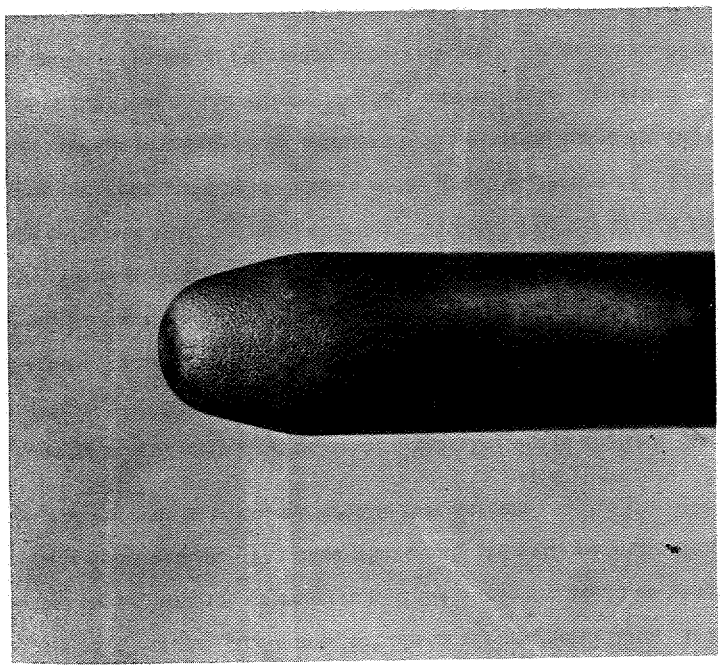

Figure 35. Cathode of Thermo-Ionic Thrustor After Operation at 4000 Amperes Arc Current Without Externally Applied Magnetic Field

2.1.6 Effect of the External Magnetic Field on Thrustor Life

The first life test of a thermo-ionic thrustor was made at a specific impulse of about 3000 seconds using a coaxial geometry without an external magnetic field. A tungsten anode and cathode were used. An examination of the electrodes after 50 hours of testing revealed (Section 2.1.2, Figure 6) that the anode consumption was mostly due to the stabilization of the arc foot in a single spot on the surface with a local increase in power density sufficient to produce melting of that sector of the electrode while other sections were not working at all. To avoid this, a small coil was connected in series with the arc and centered between the anode and cathode (Section 2.1.2, Figure 7). The axial magnetic field so produced was about 800 gauss for every 1000 amps of current in the arc. It was sufficient to produce a rotation of the arc foot on the anode surface thereby reducing electrode erosion. The use of an axial magnetic field has since proved to be very useful for improving the life of the anode by continuously changing the position of the rotating arc foot. Fields of gradually increased intensities, to 10,000 gauss and over, have been used with significant improvements in the life characteristics of the arc, and in the stability of operation.

The tests show that aside from improving life and stability of operation, the use of external magnetic fields in thermo-ionic thrustors bring few important advantages and disadvantages. In the following section we will report on both positive and negative experience obtained with the use of an external magnetic field. To conduct our experiments we adopted initially the simple solution of putting a coil of a few turns around the anode. Copper tubing was used carrying high pressure cooling water and relatively

high currents. Figure 36 shows a series of coils used during the tests. With separately fed external coils, field intensities continuously variable from zero to over 16,000 gauss have been obtained. The power necessary to obtain various field intensities with a few of the different coils used is given in Figure 37. This power is expressed in kw per cubic centimeter of coil core volume and can naturally be reduced with more elaborate construction of the arc chamber and of the coil. The use of permanent magnets, cryogenic magnets, and improvements in the general design can reduce the cost, weight, and complications of the magnetic field. It is evident that its elimination or reduction to the minimum would be beneficial for space applications. The case where only the self-magnetic field due to the arc current is not considered in this section.

As soon as a relatively light external magnetic field is applied, the anode spot begins to rotate and a beneficial effect on the thrustor life is obtained. The minimum intensity necessary to obtain a stable rotation is variable and depends on the thrustor geometry, the arc current, the propellant, and so forth. We have run all our life tests using only a few turns of water-cooled tubing in series with the main current. The effect on life of this relatively modest magnetic field is condensed in the graph of Figure 38. Figure 39 shows how the arc exhaust is modified by an external magnetic field. The effect of the field on the efficiencies is reported in Section 2.2.6. It is evident that if a change in efficiency occurred due to the presence of the external magnetic field this might influence the life behavior of the thrustor. If this influence exists it is certainly modest and cannot be distinguished in life tests of short duration, and with low field intensities. To study the

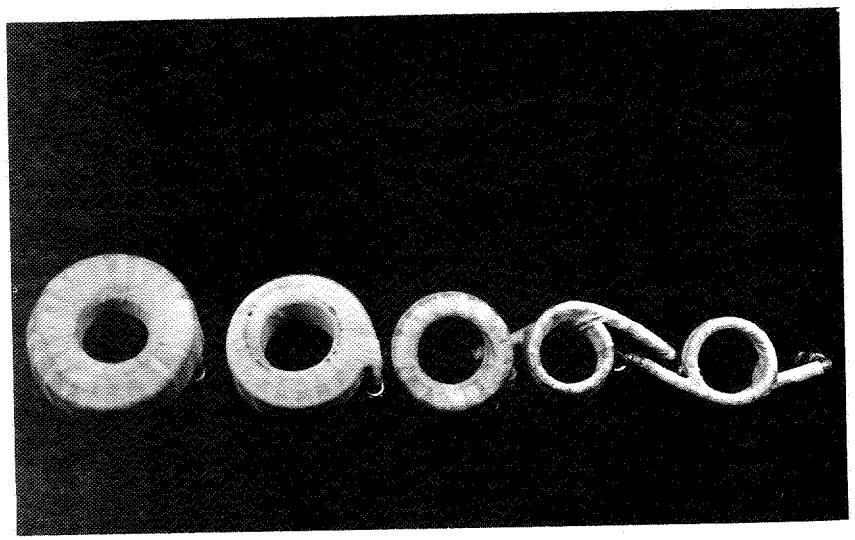

Figure 36. Photograph of Various Water-Cooled Magnetic Field Coils Used During Experimental Investigation

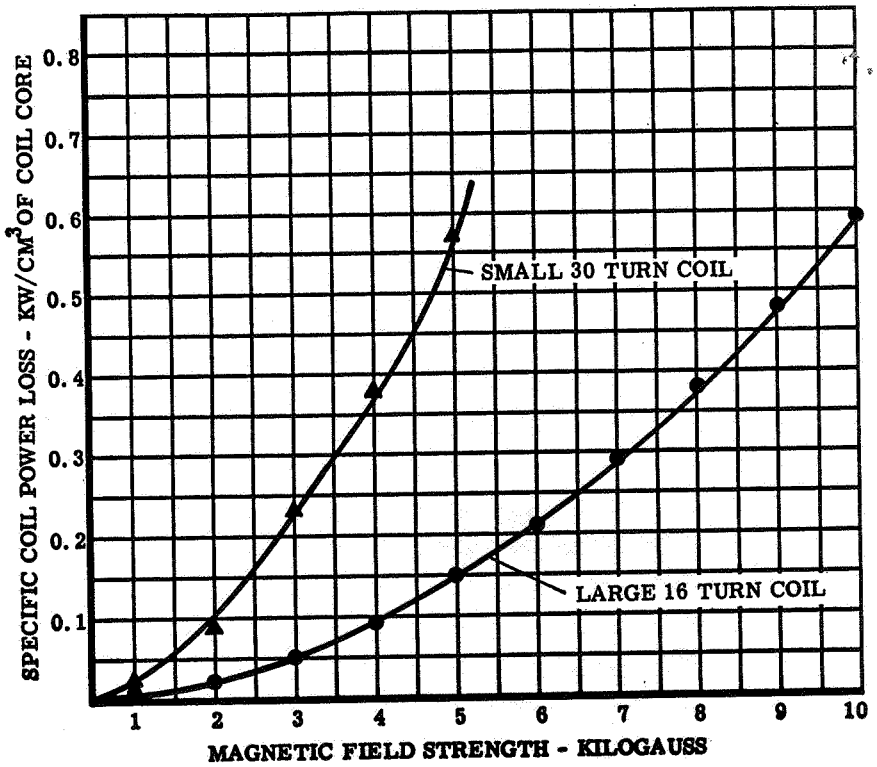

Figure 37. Specific Coil Power Loss Versus Magnetic Field Strength

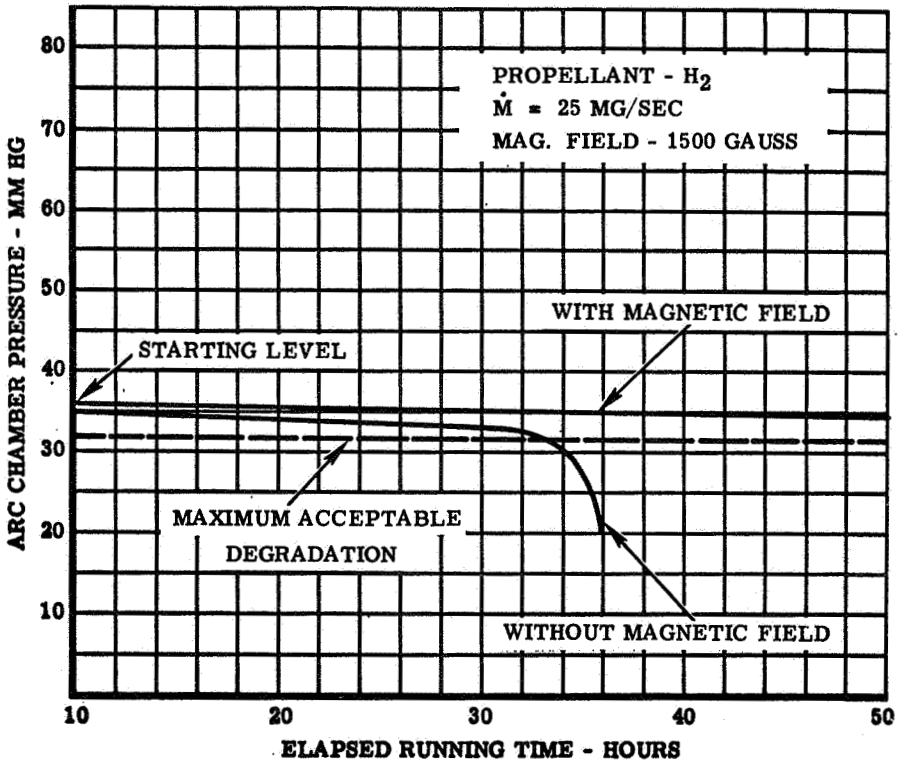

Figure 38. Degradation of Arc Chamber Pressure Due to Anode Throat Erosion With and Without Externally Applied Magnetic Field at 3000 Seconds Isp

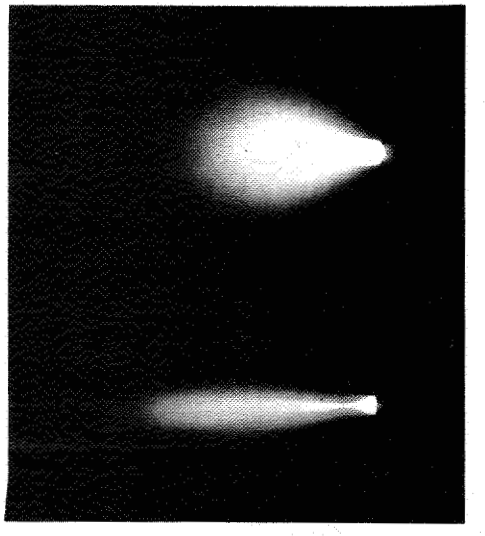

Figure 39. Arc Exhaust of Thermo-Ionic Thrustor Without (Top) and With (Bottom) Externally Applied Magnetic Field

effect on life of magnetic fields of gradually increased intensities a series of tests were conducted in the range from 1 to 16 kilogauss and the effects on cathode, anode, and other components of the thrustor accurately analyzed. While in the presence of a very weak or no magnetic field the thermoionic cathode can operate safely at extremely high currents (see Figure 23), this is not the case when a relatively strong magnetic field is present. In this condition and with a relatively high current we consistently obtained a crack on the top of the cathode (see Figures 40 and 41). This crack was probably due to strong thermal shock during the starting operation with the simultaneous application of magnetic forces along the current paths near the cathode tip. However, it appeared to have no influence in subsequent operation. It is also suspected that a strong external magnetic field can interact with the current flow in the cathode exerting strong mechanical forces near the electrode surface which are capable of producing permanent deformations. To test this effect on a hotter surface an artificially heated cathode was used (Figure 42). The heater was arranged so that the electrode surface could be brought to a plastic consistency. When the intensity of the arc current and of the field was high enough, the surface of the cathode assumed a strange form that may eventually reveal the nature of the forces acting on its surface (see Figure 43). By operating at different currents and field intensities the effect was gradually increased as shown in Figure 44. The effect was finally reproduced in regular cathodes without separate artificial heating by suddenly applying a strong over-current in the presence of a very strong external magnetic field (Figures 45 and 46). These results seem to indicate that a strong external magnetic field has a negative effect on cathode life due to the twisting forces induced in the high

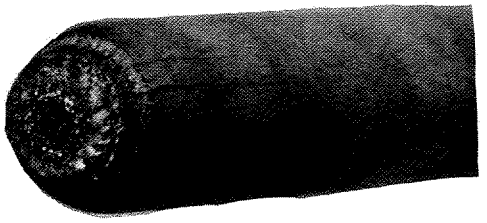

Figure 40. Cathode Tip After Operation at 3000 Amperes Arc Current and Moderate External Applied Magnetic Field

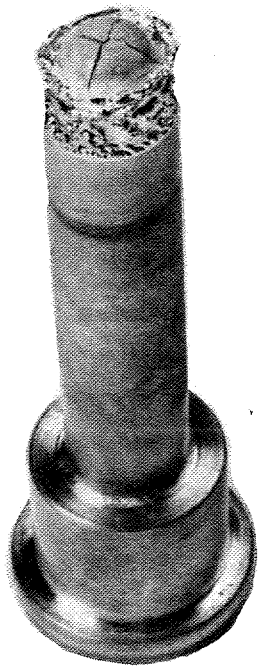

Figure 41. Deep Cross-Like Crack on Cathode Tip After Operation at 2500 Amperes Arc Current and Strong External Applied Magnetic Field

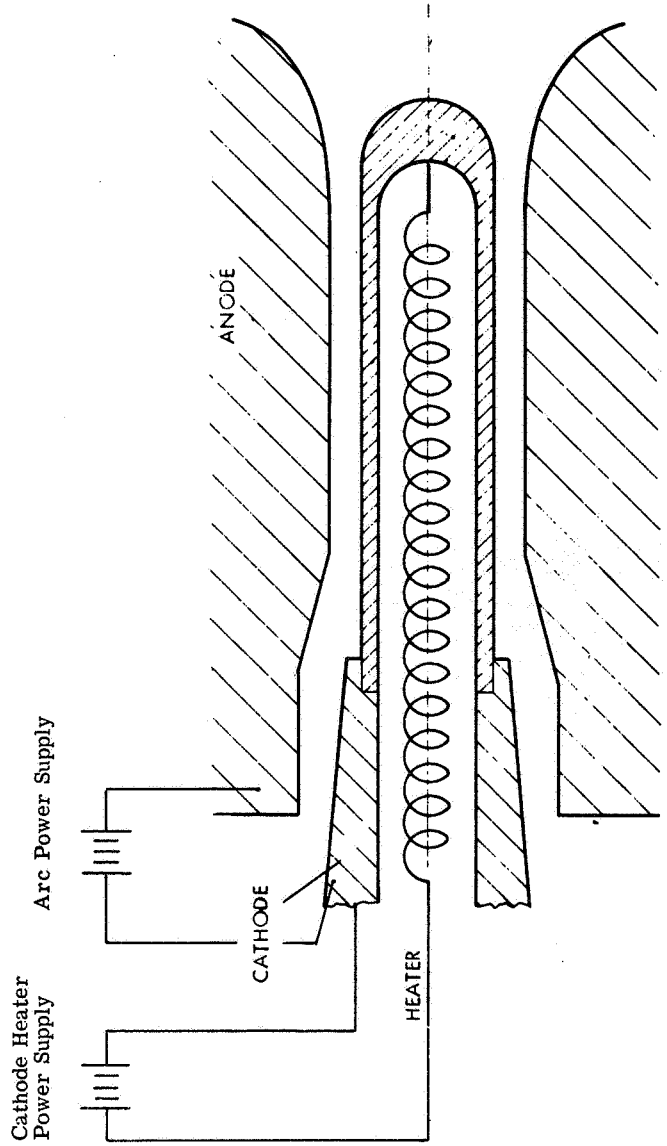

Figure 42. Schematic of Artificially Heated Cathode for Studies of Magneto-Mechanical Forces on Its Surface

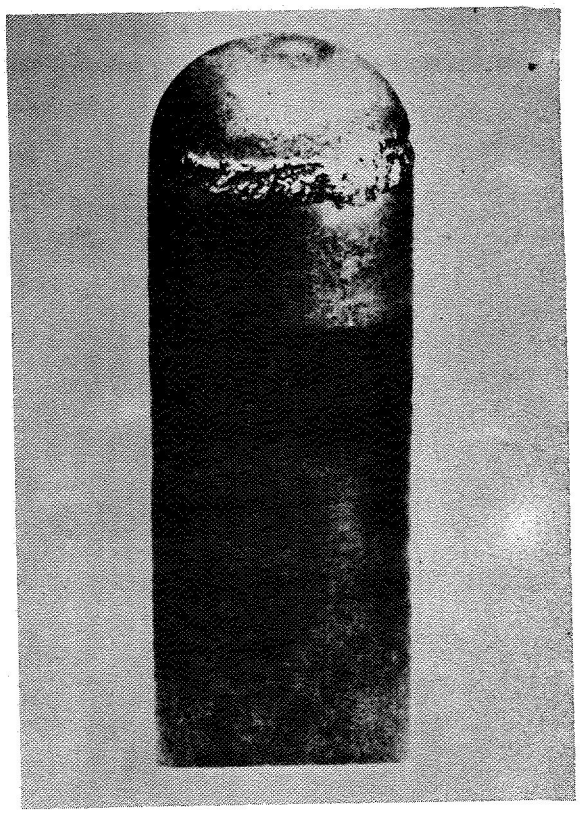

Figure 43. Photograph of Swirl Effect of Molten Cathode Material Caused by the Externally Applied Magnetic Field

Figure 44. Photograph of Cathode Showing Increased Swirl Effect of Molten Cathode Material at Moderate Externally Applied Magnetic Field Strength

Figure 45. Cathode Showing Strong Swirl Effect on Molten Cathode Material at Increased Externally Applied Magnetic Field Strength

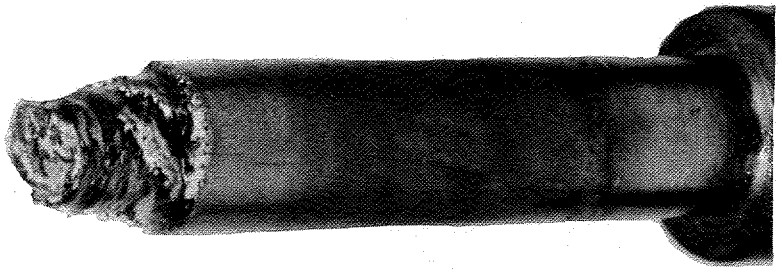

Figure 46. Cathode Showing Heavy Swirl Type Erosion at Very Strong Externally Applied Magnetic Field Strength and Increased Cathode Temperature

temperature metal surface (see Figure 47). While this effect has not been studied with similar detail in the case of the anode, there are reasons to anticipate that if the anode temperature and magnetic field intensity were sufficiently high, similar results would be observed. Figure 48 shows clearly a melted portion of metal extending in a large swirl around the internal surface of a water-cooled anode. Similar conditions have been verified at other times using copper anodes but not to date using hot tungsten electrodes. Further experiments are necessary, but from the first series of tests it is clear that very strong external magnetic fields can be detrimental to the life of electrodes if their temperature is high.

The external magnetic field (and in a certain sense the self-magnetic field also) produced another important secondary effect on the anode which can influence its life. This effect (already pointed out in Section 2.1.5, Figure 30) depends on the anode geometry as well as the field strength. If the diameter of the throat is too large or the length too short the arc extends into the space outside the thrustor as illustrated in Figure 49. In this case, part of the electrons arrive at the anode by a path of relatively low density and are accelerated by relatively high voltages. Their effect on the anode is similar to the well-known effect obtained on the target by electron-beam welding and their destructive power can exceed that illustrated in Figures 31 and 32 to the point of causing total melting of the anode (Figure 34). This serious limitation on the anode life can usually be avoided by increasing the length to diameter ratio of the anode or by reducing the magnetic field strength depending on which of these alternatives give the minimum of undesirable side effects (see Figure 50).

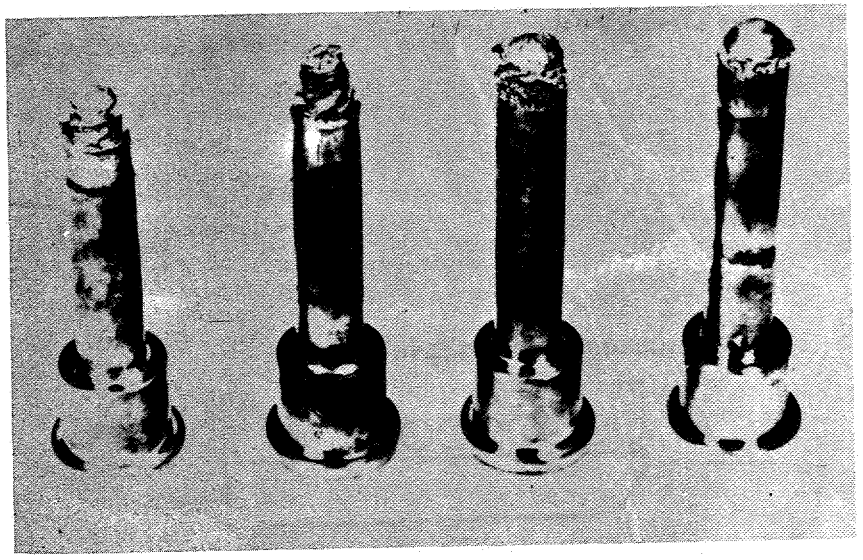

Figure 47. Series of Cathodes Showing Swirl Type Erosion at Gradually Increased Arc Current and Externally Applied Magnetic Field Strength

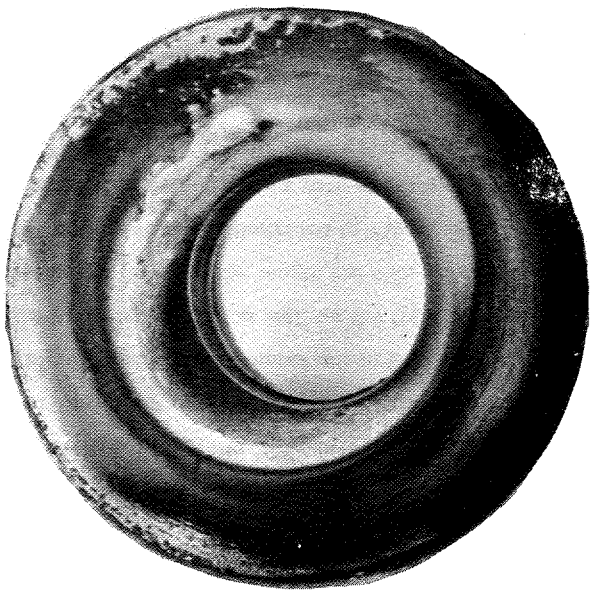

Figure 48. Face of Water-Cooled Copper Anode Showing Swirl of Molten Material Due to Influence of the External Magnetic Field

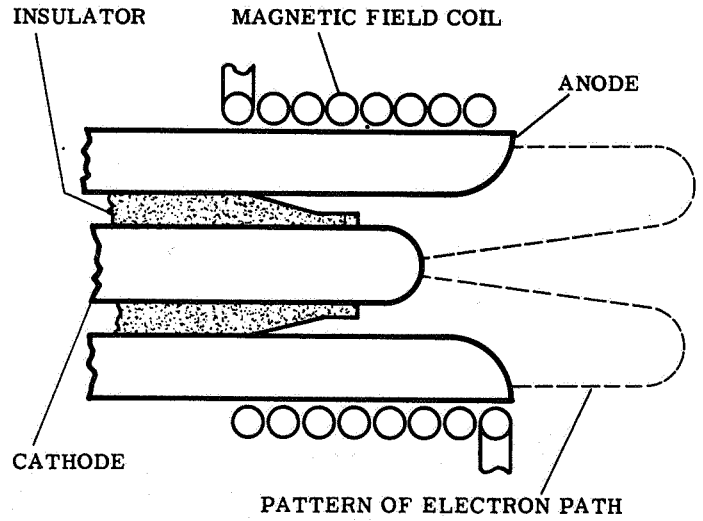

Figure 49. Excessive External Magnetic Fields and Large Anode Throat Diameters Result in Destructive Electron Bombardment on the Anode

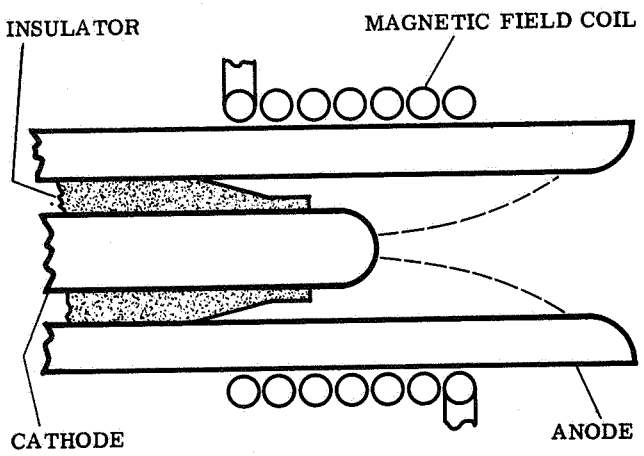

Figure 50. Increased Anode Throat Length or Decreased Anode Throat Diameter or Decreased Magnetic Field Help to Eliminate Anode Erosion Due to Electron Bombardment

The conclusions reached regarding the effects of an external magnetic field on thrustor life are that an external magnetic field is necessary to assure long life for current thermo-ionic thrustors by rotation of the arc foot along the internal surface of the anode. However, the intensity of the field should be the minimum necessary to achieve stable rotation. Higher intensities may result in more severe erosion of the electrodes unless methods can be found to reduce the detrimental effects. It may be possible to eliminate the axial magnetic field entirely without paying a penalty in life by using multiple electrodes with a suitable division of the total current between them.

2.1.7 Effect of External Environment on Thrustor Life

All the life tests conducted to date on the thermo-ionic thrustors have been done in metal vacuum tanks of relatively small dimensions and under a pressure ranging from 0.2 to 10^{-4} Torr. This environment is completely different from the environment that will be encountered in real space. For this reason a considerable amount of effort has been devoted to studying the effects of the external environment on thrustor life. The study was concerned with the effects of conditions in space as well as "simulated" space conditions in the laboratory (which are naturally very far from the real ones) on the life obtainable. While the effects of the laboratory environment are based mostly on real measurements, the effects of true space conditions must be based mostly on hypothesis and calculations. Terrestrial laboratory conditions can reduce some damaging effects while real space conditions can reduce others. Figure 51 shows the density of "space" at relatively low altitudes over the earth. It is evident that our best above mentioned simulation of space (0.1 to 1.0 millitorr) does not bring us higher than 60 to 80 miles. Few laboratories on earth can go higher if a mass flow of a few milligrams of propellant per second must be exhausted in the testing tank.

Let us consider how this laboratory environment can influence the life test results in comparison with the real space environment. One of the most important influences of high vacuum on hot materials is evaporation. Figure 52 shows the vapor pressure versus temperature for various materials. For very high vacuum levels and relatively high temperatures the evaporation

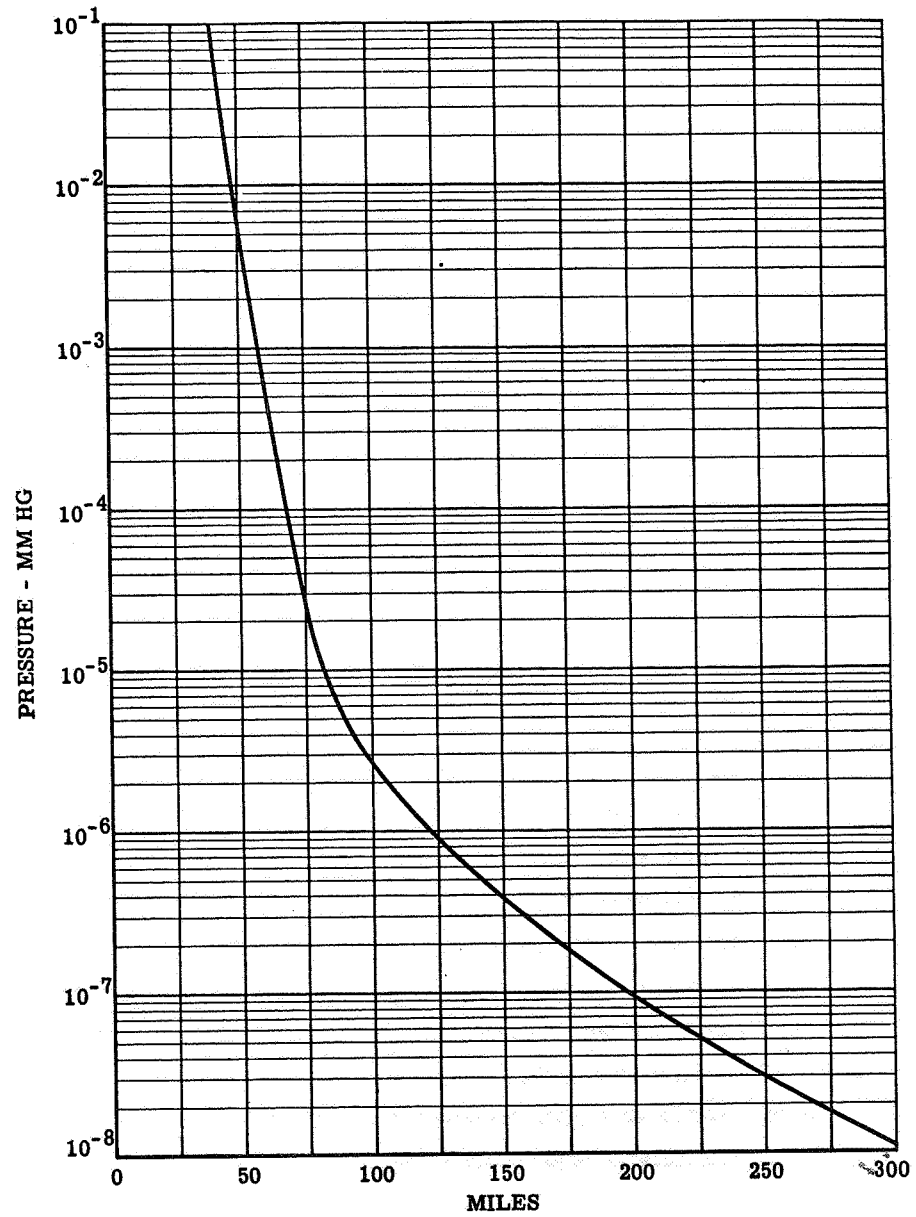

Figure 51. Pressure at Various Altitudes From Earth's Surface

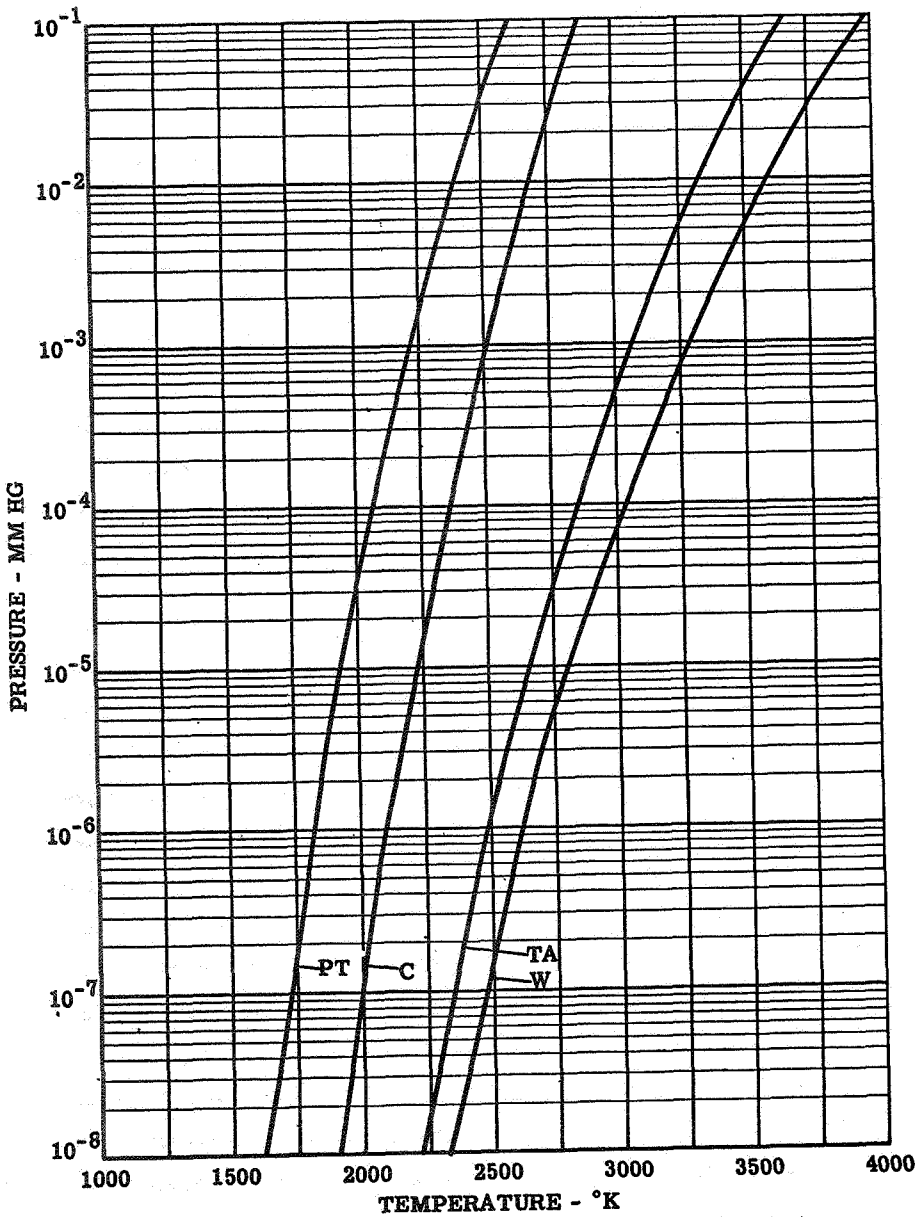

Figure 52. Variation of Vapor Pressure With Temperature for Various Materials (From R. E. Honig, "Vapor Pressure Data for the Solid and Liquid Elements," RCA Review, XXIII, No. 4 (1962), pp. 567-586)

becomes a very important factor in determining life. Sublimation under low pressure and high temperature follows the same trend. While data extended to space vacuum is unavailable at present, a real space life test can show rates of evaporation and sublimation higher than a laboratory test conducted in the best vacuum possible today. When very long life periods are necessary it is evident that our testing conditions on earth are not capable of simulating the real conditions in space and that the result obtained in the laboratory will tend to be optimistic. For example, the well-known system of radiation cooling of the electrodes, if used in deep space missions, must operate at low working temperatures if long life is desired.

If the influence of evaporation and sublimation on life is more severe in space than in the laboratory, another phenomenon also connected with the life test is not so severe in space as on earth. This is the effect of interactions between the atmosphere surrounding the thrustor and the thrustor parts. A residual amount of oxygen of a few parts per million is capable of appreciable erosion of exposed parts by oxidation in long life tests. Carbon, fluorine, and even nitrogen can produce similar effects in the laboratory environment, while in real space reactions of this type are improbable. As considered in Section 2.1, the presence of traces of contaminating elements (like carbon) can have secondary effects on life, making compounds with the electrodes and other parts of the thrustor. These compounds normally have different characteristics (like a lower melting point) which can have a strong detrimental effect on the life of the engine.

Another important phenomenon connected with evaporation and sublimation may have important indirect effects on the useful life in space. This is the

possibility that the evaporated vapors condense forming deposits on important secondary components of the space vehicle. A metal film of a thickness of 10^{-5} mm can destroy any insulation in an area of 100 square feet using only 0.1 cc of material (see Figure 53). It is evident that even if the depositing efficiency is very low, during a long period this process can have serious effects on the life of the entire mission. Deposited film can also have undesirable effects in coating windows, optical systems, and so forth (Figure 54). Considering side effects on life testing it is well-known that during long tests with metal vapors (alkali metals, electrode materials, and so forth) strong deposits are normally seen and tolerated on any imaginable cold surface of the laboratory vacuum system (see Section 2.1.3, Figures 18 through 23). It follows that if similar deposits are obtained during real space operation the deposit may reach an excessive thickness after a long operating period even if the rate of deposition is low.

Another important difference between life testing in a laboratory and in real space is the influence of the high vacuum environment on the shape and dimensions of the jet. As damage might occur on other parts of the space vehicle besides the anode zone because of return paths through numerous unexpected connections, the outside path of the jet (Figure 55) must be considered if space vacuum conditions are present. Figures 56 through 59 show the expansion of the jet plume with a modest decrease of pressure. The difficulty of examining the influence of this particular condition on life in a laboratory is so great that it is probably advisable to investigate the possibility of its elimination by substantial modifications in the thrustor design.

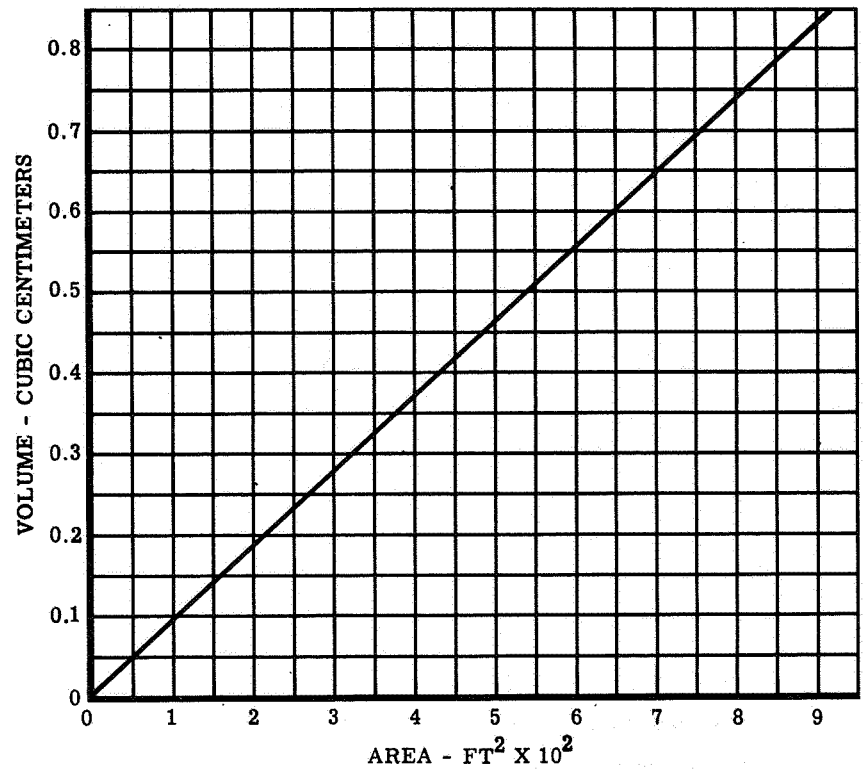

Figure 53. Volume of Evaporated Solids Versus Deposition Area for a Skin Depth of 10^{-5} MM

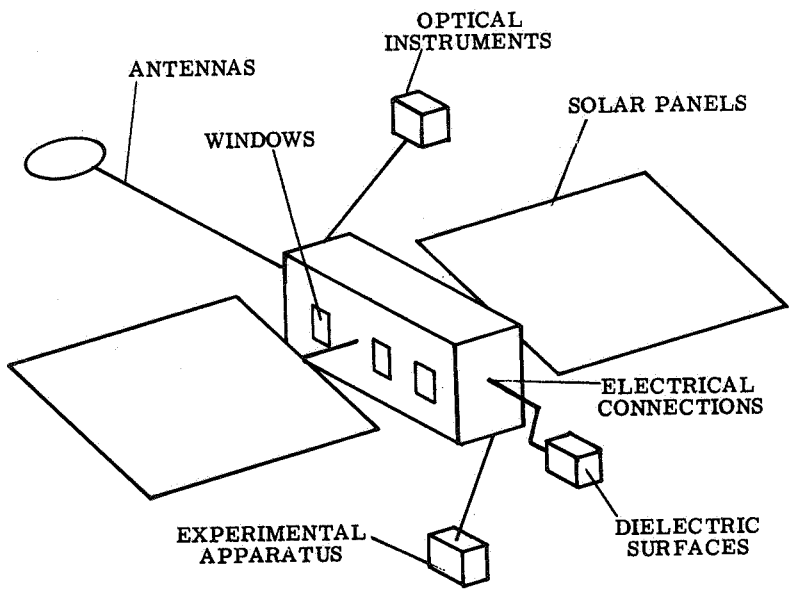

Figure 54. Spacecraft Components Whose Functions can be Degraded by Deposition of Metal Films From Thrustor Exhaust

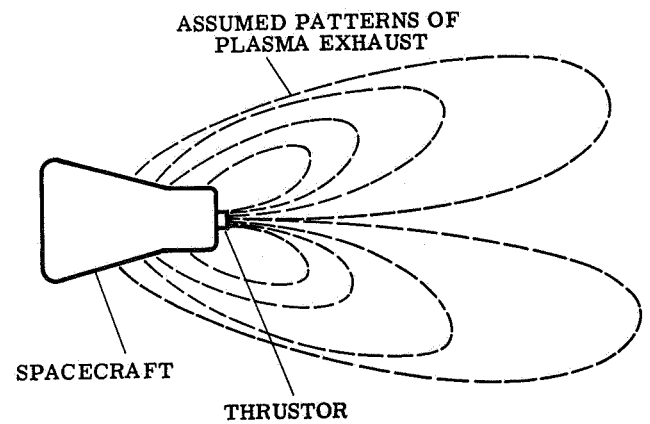

Figure 55. Possible Envelope of Plasma Exhaust From Thermo-Ionic Electric Thrustor During Space Operation

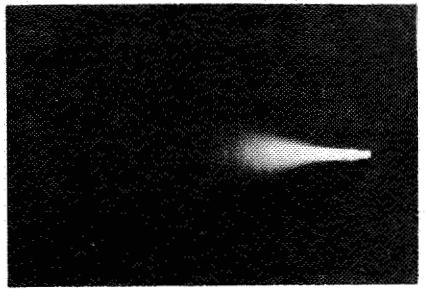

Figure 56. Thermo-Ionic Jet at Environmental Pressure of 10^{-1} Torr.

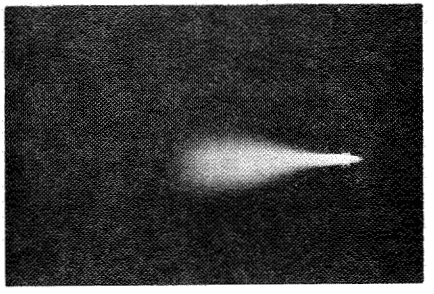

Figure 57. Thermo-Ionic Jet at Environmental Pressure of 5×10^{-2} Torr

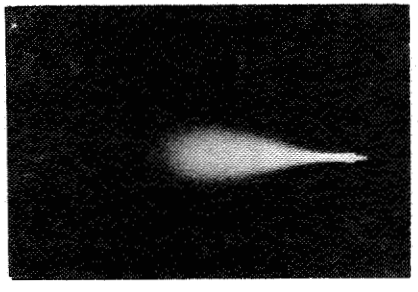

Figure 58. Thermo-Ionic Jet of Figure 57 at Decreased Environmental Pressure

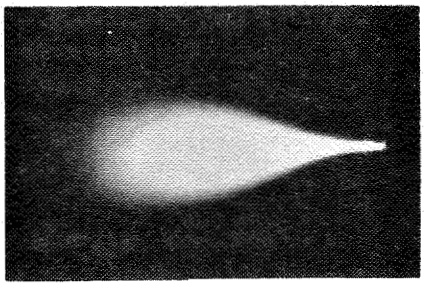

Figure 59. Thermo-Ionic Jet of Figure 58 at Further Decreased Environmental Pressure

Another important secondary effect connected with these phenomena is the influence that the extended ionized zones of plasma exhaust might have on radio communications as soon as operation starts or after a certain length of time. If, through gradual deterioration of nearby components of the spacecraft disturbances or interferences can appear after a certain period of operation, the life of the entire mission might be endangered. While the exact reproduction of space environment conditions will be impossible for some time, it is evident that in evaluating any life test the actual space conditions must be taken into account. For this reason it seems advisable to consider in the design the elimination of any condition capable of producing damaging effects in real space.

2.2 Efficiency of the Thermo-Ionic Thrustor

2.2.1 General

The efficiencies of arc and plasma thrustors have been well defined throughout the literature since 1961. For purposes of clarity the definitions will be restated for correlation with our terminology and notation.

The most elementary definition of efficiency is the ratio between power in the jet and total electric input power. This type of efficiency does not express propulsion efficiency but gives a measure of the efficiency of transfer between input electric power and total power in the propellant (dissociation, ionization, random and directed energy). This type of efficiency, often called "thermal efficiency" is expressed in our tables by $\eta^{eg}\%$. Because of these various forms of energy in the propellant a great part of the power in the jet cannot be used for propulsion or for production of thrust. For this reason, a second type of efficiency can be defined as the ratio of the directed (or propelling or thrusting) power in the jet and the total electric input power. Our tables express this type of efficiency with the notation $\eta^{ek}\%$. To discriminate between the various losses it sometimes appeared useful to use a third type of efficiency, i.e., to express the ratio between the already defined thrusting or kinetic power in the propellant and the total power in it. This efficiency discriminates between the energy destined for propulsion and the energy stored in the gas in the form of dissociation, thermal and kinetic energy. In our tables this type of efficiency is expressed with the notation $\eta^{gk}\%$. The anomalies pointed out on page 1, which will be described in more detail in Section 2.3, can have different effects on

the various types of efficiencies already described. The increase of the thermal efficiency represents, in our opinion, the most important and positive part of any program of electrothermal propulsion. The medium value of thermal efficiency of thermo-ionic thrustors at the present state of the art is around 50 percent. It is evident that any improvement in the thermal efficiency can be of considerable benefit to the propulsion efficiency. For this reason it is our opinion that a great part of the initial effort for improvement of thermo-ionic propulsion must be devoted to increasing thermal efficiency.

2.2.2 Effect of Geometry on Efficiency

In Section 2.1.2 we tried using experimental test results to determine the influence of geometry on thrustor life. The purpose of this section is to find out how the thrustor geometry can affect efficiency. It is natural that geometries capable of long life are used whenever possible, especially for future designs as more experimental data are available. The effect of the geometry on measurements of performance and on anomalies in the values obtained will be discussed in Section 2.3.2. Our experience during this program indicates that geometry can have a primary role in determining the efficiency of thermo-ionic thrustors. This fact, together with the observation that geometry has an important affect on life and on the precision obtainable in performance measurements, makes the development of the best geometry one of the most important subjects for any future work in this field. The coaxial geometry of Figure 1 has been used as a basis for tests to determine the influence of variation of its dimensions on the various efficiencies. For each series of tests the mass flow has been kept constant while dimensions and specific impulses have been varied in predetermined steps. When an external magnetic field was used its intensity was also varied in fixed steps changing the coil turns or the current, depending on whether a series or parallel circuit was used. The proportion of the various geometries was normally kept constant, i.e., when diameter was changed, a corresponding change in length was made. Toward the end of the program it was found that to have complete coverage of the region of interest (especially in the presence of external magnetic fields), various

ratios of throat length/diameter (L/D) were necessary rather than the single one initially used. The final series (which unfortunately has not been completely tested) includes 6 diameters and 4 lengths for each diameter. The L/D ratios have been fixed at 1.0, 1.5, 2.0 and 4.0. Figure 60 shows the outline of different L/D proportions. Figure 61 shows a photograph of the various interchangeable testing heads. Figures 62 through 67 give the dimensions of the series of throats which were fabricated. For testing with hydrogen, deuterium, and similar propellants, all the cathodes were thoriated tungsten and the anodes were copper. Water cooling was used throughout. For testing with alkali metals a similar series was prepared using radiation-cooled electrodes assembled on a water-cooled base. Figure 68 shows a photograph of the interchangeable radiation-cooled head used in alkali metal testing and Figures 69 through 71 show the relative dimensions. Only two ratios of throat diameter/throat length have been used in the initial tests. A third series of testing heads was prepared for analyzing the operation without propellant throughput, i.e., with electrode vapors and gas entrainment operation. Figure 72 is a radiation-cooled head with electrodes dimensioned to reach the best temperature for operation without external propellant and Figures 73 and 74 show the principal dimensions of the series prepared for the test. Because of priority in testing other propellants this investigation was conducted with a limited series of dimensions. For testing the effect of reversing the polarity a special prototype was built (Figure 75). Numerous other prototypes were also constructed to test different working conditions, different propellants, very low power operation, and so forth. Photographs of thrustors and

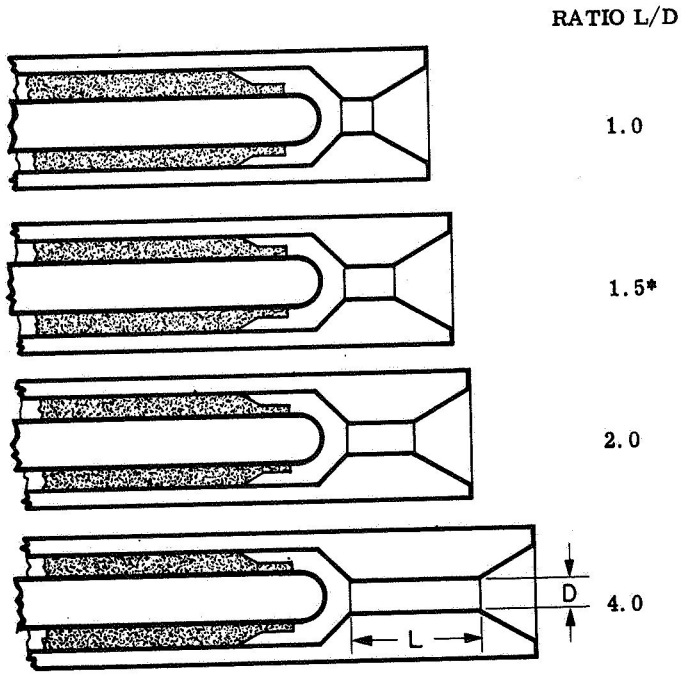

*Most used configuration

Figure 60. Ratios of Throat Length to Throat Diameter for Electrode Configurations Used During Testing

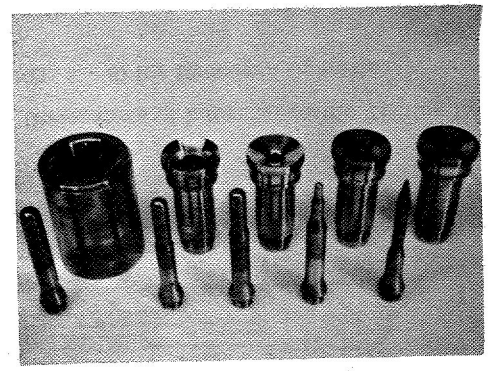

Figure 61. Photograph of the Various Interchangeable Testing Heads Used During the Experimental Investigation

Head No.	Throat Dia.		Throat Length (L)	
	mm	inch	mm	inch
1	3.18	0.125	3.18	0.125
2*	3.18	0.125	4.77	0.187
3	3.18	0.125	6.36	0.250
4	3.18	0.125	12.72	0.500

*L/D = 1.5

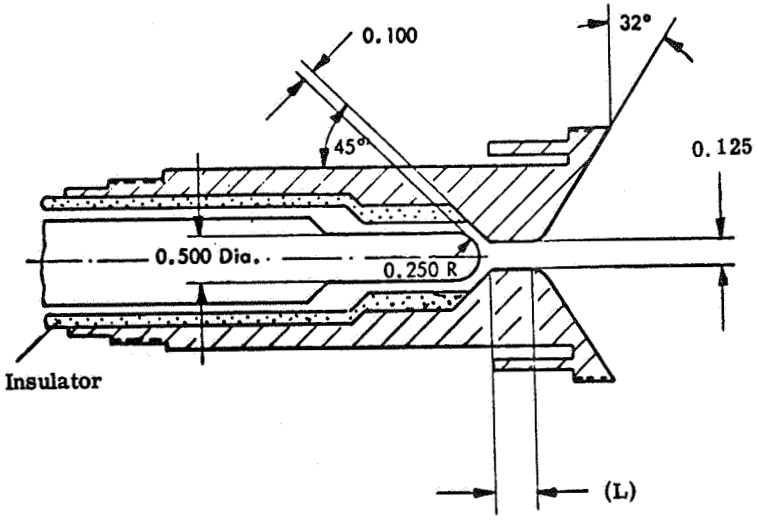

Figure 62. Dimensions of Interchangeable Testing Head (No. 1 - 4) for Hydrogen Operation

Head No.	Throat Dia.		Throat Length (L)	
	mm	inch	mm	inch
5	6.35	0.250	6.35	0.250
6*	6.35	0.250	9.53	0.375
7	6.35	0.250	12.70	0.350
8	6.35	0.250	25.40	1.000

*L/D = 1.5

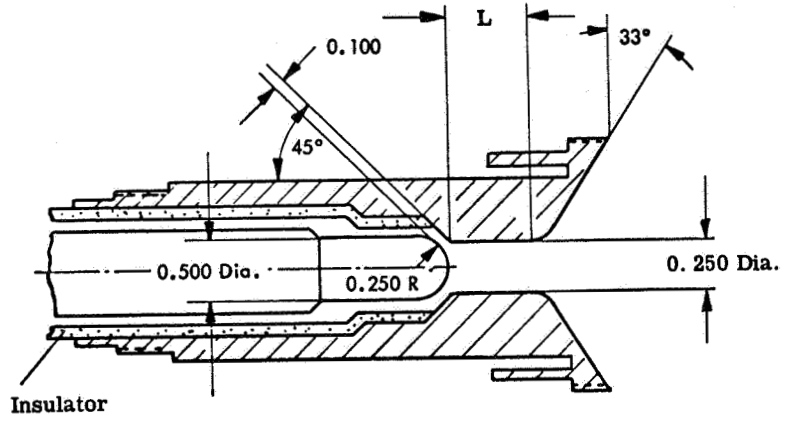

Figure 63. Dimensions of Interchangeable Testing Head (NO. 5 - 8) for Hydrogen Operation

Head No.	Throat Dia.		Throat Length (L)	
	mm	inch	mm	inch
9	12.70	0.500	12.70	0.500
10*	12.70	0.500	19.05	0.750
11	12.70	0.500	25.40	1.000
12	12.70	0.500	50.80	2.000

*L/D = 1.5

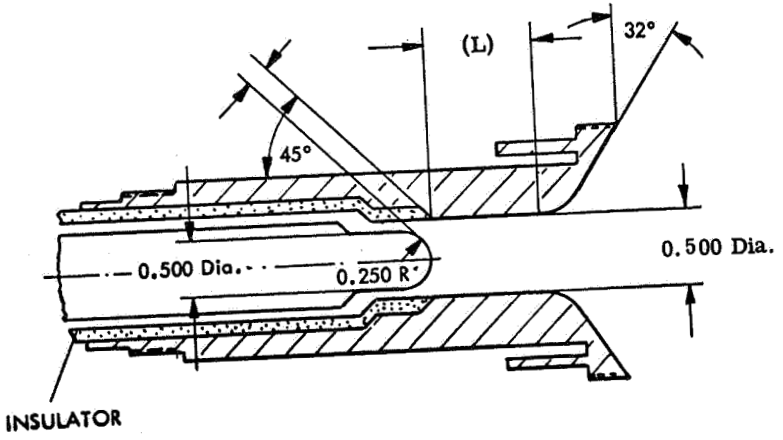

Figure 64. Dimensions of Interchangeable Testing Head (No. 9 - 12) for Hydrogen Operation

Head No.	Throat Dia.		Throat Length (L)	
	mm	inch	mm	inch
13	20	0.800	20	0.800
14*	20	0.800	30	1.200
15	20	0.800	40	1.600
16	20	0.800	80	3.200

*L/D = 1.5

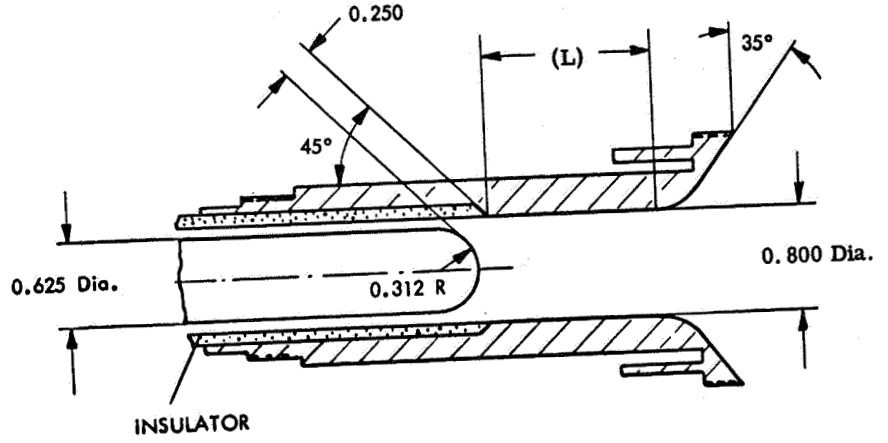

Figure 65. Dimensions of Interchangeable Testing Head (NO. 13 - 16) for Hydrogen Operation

Head No.	Throat Dia.		Throat Length (L)	
	mm	inch	mm	inch
17	25	1.000	25.0	1.000
18*	25	1.000	37.5	1.500
19	25	1.000	50.0	2.000
20	25	1.000	100.0	4.000

*L/D = 1.5

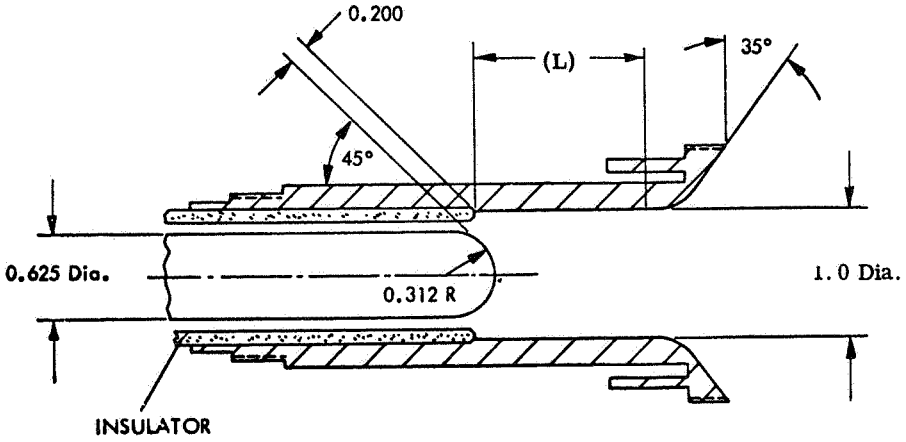

Figure 66. Dimensions of Interchangeable Testing Head (No. 17 - 20) for Hydrogen Operation

Head No.	Throat Dia.		Throat Length (L)	
	mm	inch	mm	inch
21	50	2.00	50	2.00
22*	50	2.00	75	3.00
23	50	2.00	100	4.00
24	50	2.00	200	8.00

*L/D = 1.5

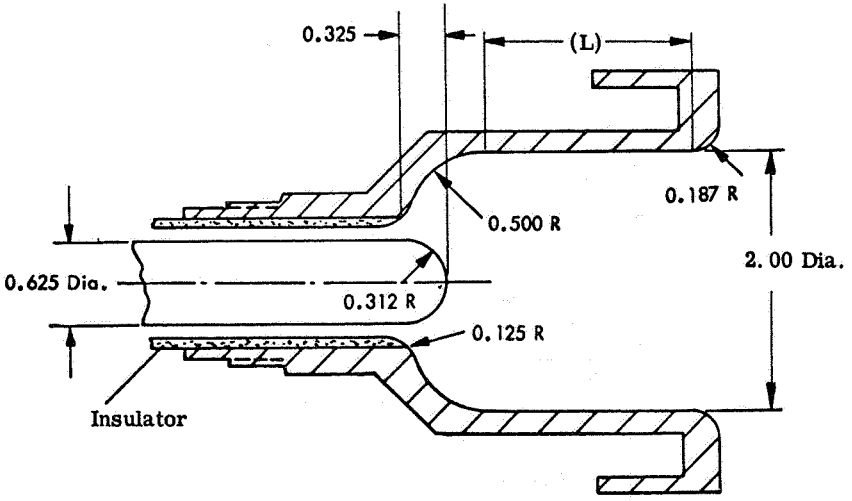

Figure 67. Dimensions of Interchangeable Testing Head (No. 21 - 24) for Hydrogen Operation

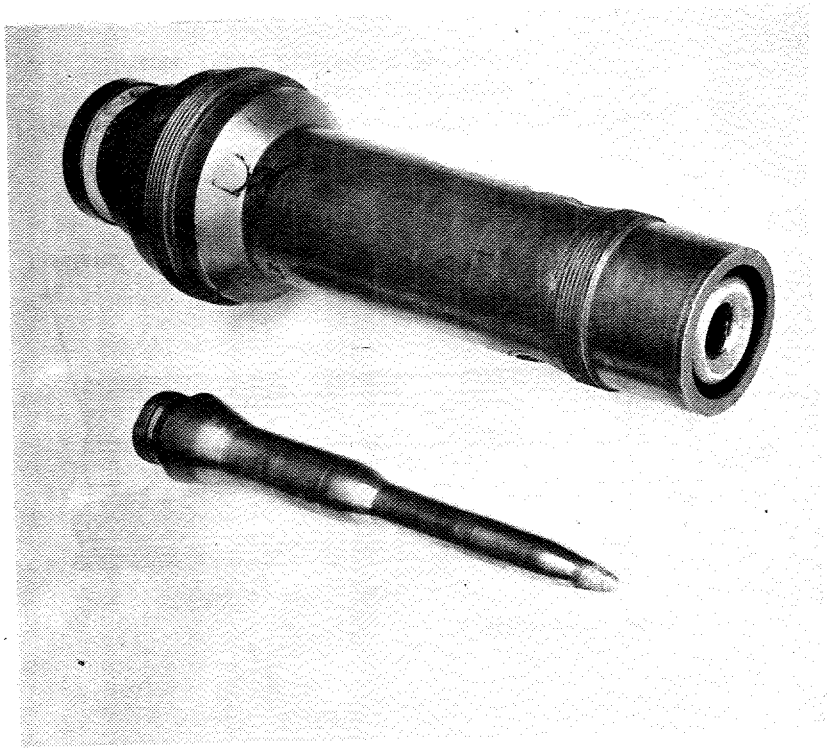

Figure 68. Photograph of Typical Interchangeable Radiation-Cooled Testing Head for Operation With Lithium and Potassium

Head No.	Throat Dia.		Throat Length (L)	
	mm	inch	mm	inch
1*	6.3	0.250	6.3	0.250
2	6.3	0.250	9.5	0.375

*L/D = 1.5

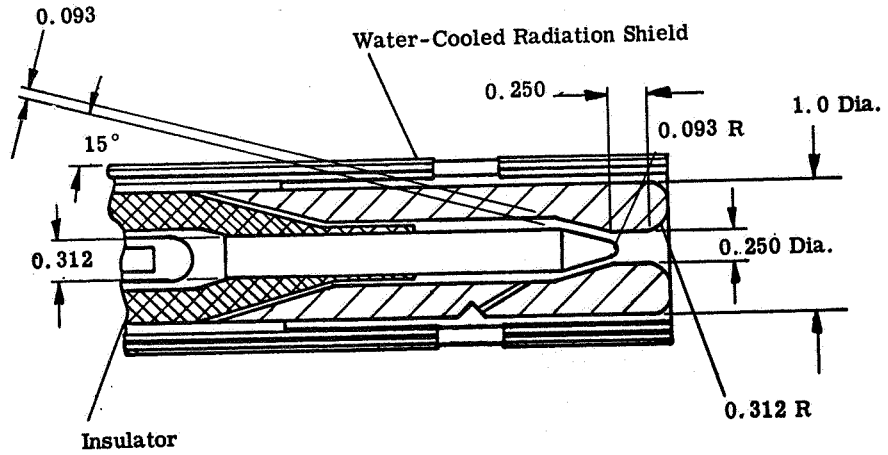

Figure 69. Dimensions of Interchangeable Testing Head for Lithium - Potassium Operation (Anode Throat Diameter 0.250 Inches)

Head No.	Throat Dia.		Throat Length (L)	
	mm	inch	mm	inch
3*	8.9	0.350	8.9	0.350
4	8.9	0.350	13.3	0.525

*L/D = 1.5

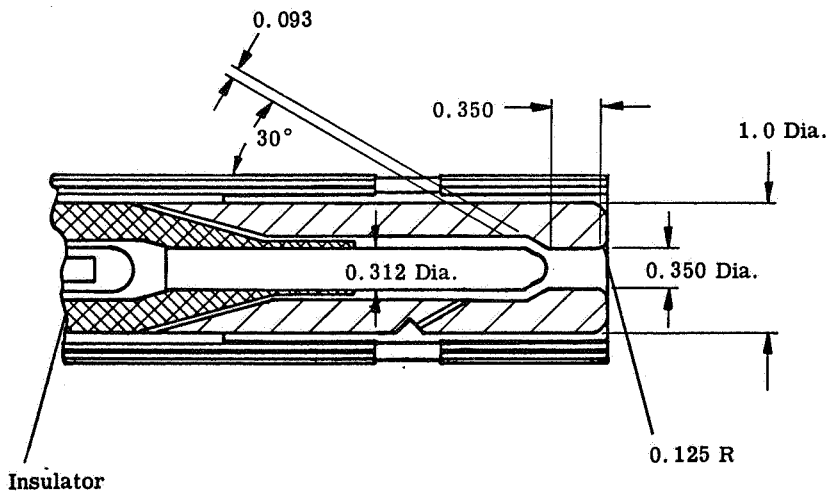

Figure 70. Dimensions of Interchangeable Testing Head for Lithium - Potassium Operation (Anode Throat Diameter 0.350 Inches)

Head No.	Throat Dia.		Throat Length (L)	
	mm	inch	mm	inch
5*	11.1	0.440	11.1	0.440
6	11.1	0.440	16.7	0.660

*L/D = 1.5

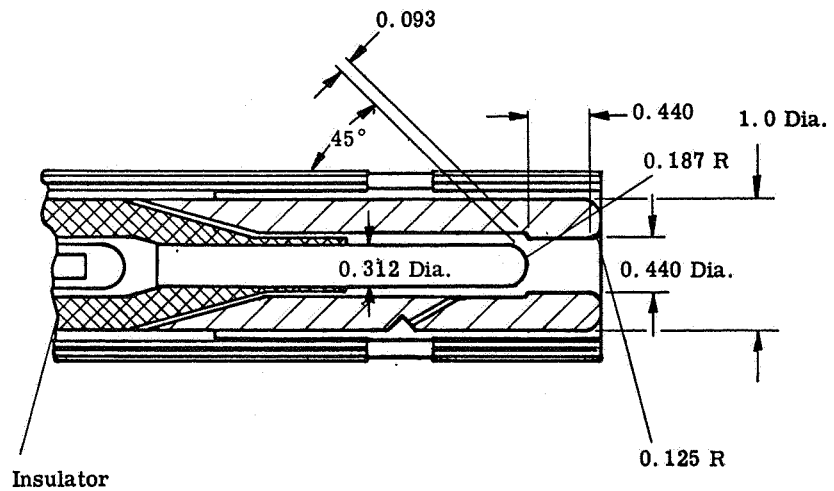

Figure 71. Dimensions of Interchangeable Testing Head for Lithium - Potassium Operation (Anode Throat Diameter 0.440 Inches)

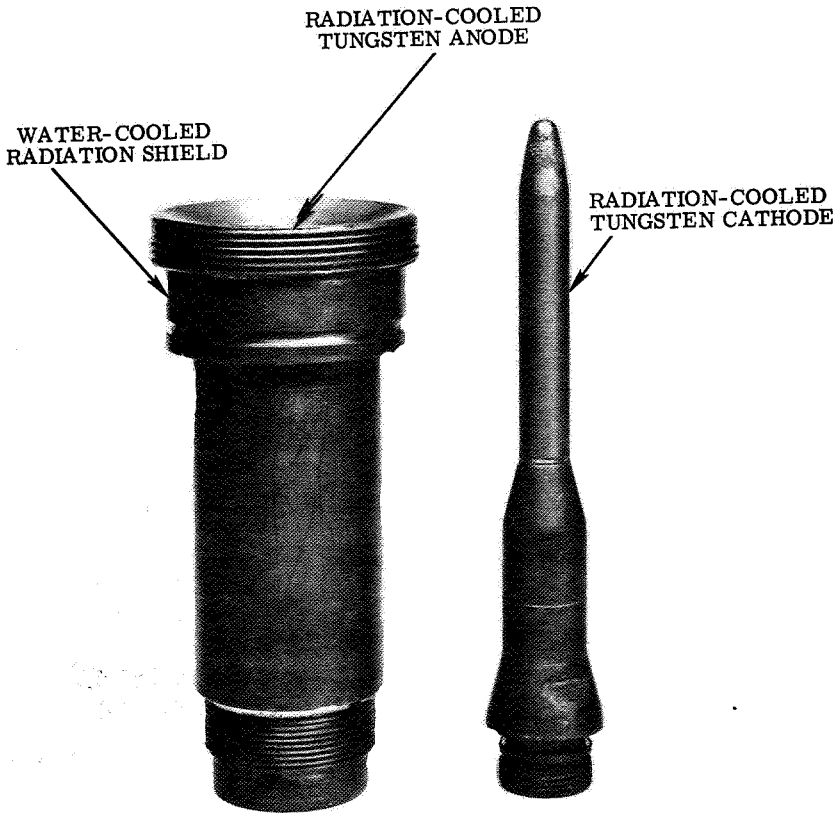

Figure 72. Photograph of Interchangeable Radiation-Cooled Testing Head for Operation Without Propellant Throughput

Head No.	Throat Dia.		Throat Length (L)	
	mm	inch	mm	inch
1*	6.3	0.250	6.3	0.250
2	6.3	0.250	9.3	0.375

*L/D = 1.5

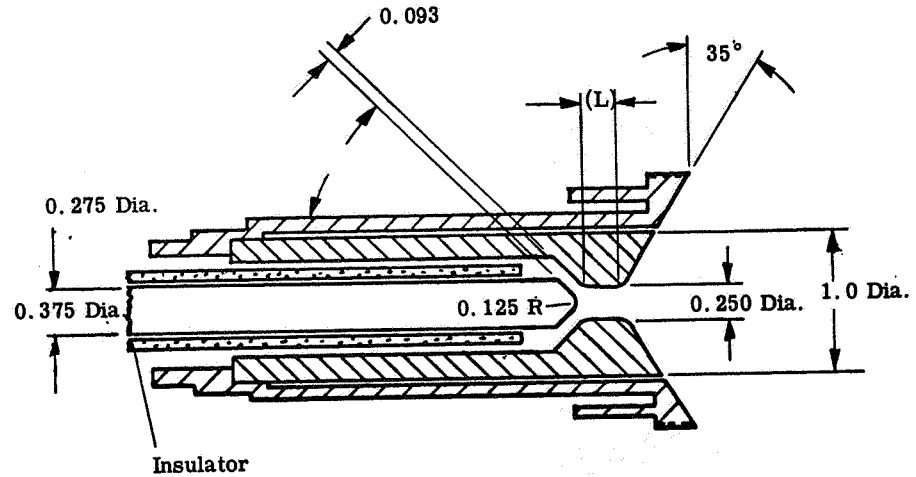

Figure 73. Dimensions of Interchangeable Radiation-Cooled Testing Head for Operation Without Propellant Throughput (Anode Throat Diameter 0.250 Inches)

Head No.	Throat Dia.		Throat Length (L)	
	mm	inch	mm	inch
3*	9.3	0.375	9.3	0.375
4	9.3	0.375	14.0	0.560

*L/D = 1.5

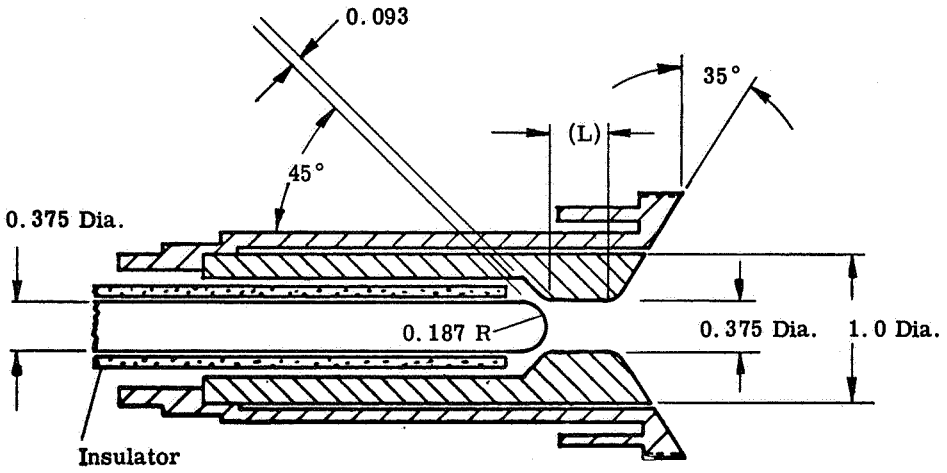

Figure 74. Dimensions of Interchangeable Radiation-Cooled Testing Head for Operation Without Propellant Throughput (Anode Throat Diameter 0.375 Inches)

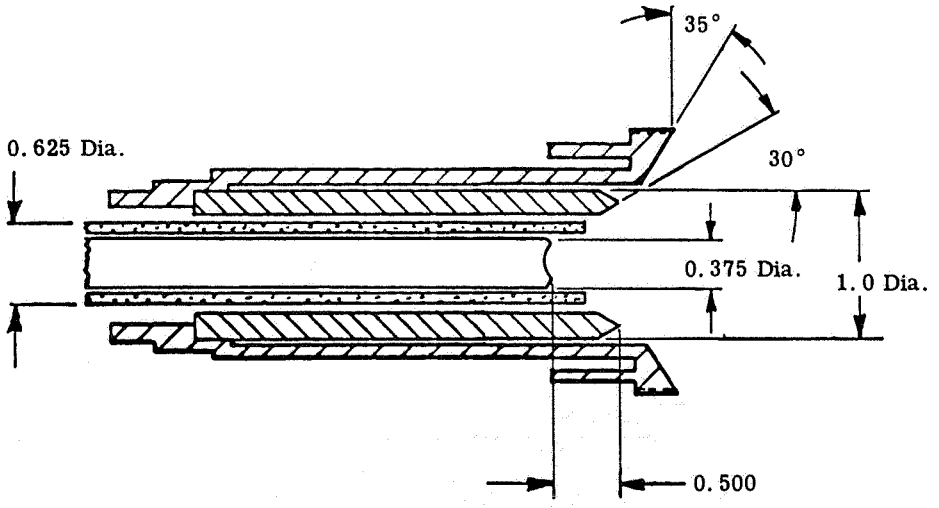

Figure 75. Dimensions of Interchangeable Prototype Testing Head With Reversed Polarity Electrode Configuration for Operation Without Propellant Throughput

electrodes constructed to analyze special working conditions are shown in Figures 76 through 79. The test points have been grouped to provide convenient comparison of performance as geometry is changed. Sometimes the subdivision is difficult because various influences overlap and cannot be separated. When this is the case the results under one principal influence have been grouped together with cross references to the others. Some results where testing anomalies are suspected are described in detail in Section 2.3.

Because of the large number of variables involved, the tests are not as complete as would be desired, and in some cases it is not possible to draw conclusions. The vastness of this work and the limited time did not permit covering all the program as planned, but the long series of tests conducted may be considered as a preparation or orientation toward a more sophisticated program. The tests described next were conducted to determine the effect of changing geometry while keeping the propellant, the mass flow, and the specific impulse constant for each series of measurements. The simplest change in geometry is the variation of throat diameter. As said in the preceding pages, the diameter was varied with a simultaneous change in length to maintain a constant ratio between these two parameters. During most of the test work this ratio was held at 1.5. These points are marked with asterisks in Figures 61 through 67. Results have also been obtained using other ratios, but the analysis has not been completed due to the termination of this work. Some typical examples are given for a different ratio in Section 2.3.2. The variation of diameter has been studied separately for gaseous propellants, alkali metals and electrode vapor operation.

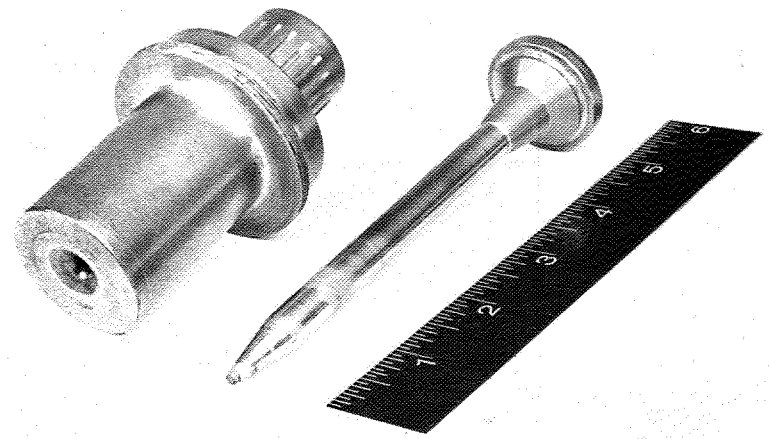

Figure 76. 5 KW Interchangeable Water-Cooled Head With Anode and Cathode

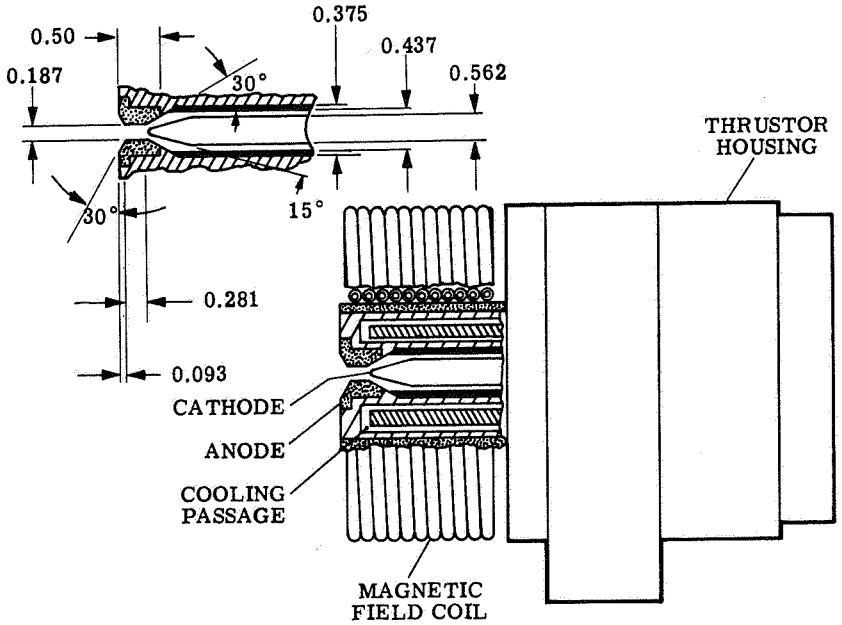

Figure 77. Design of a 5 KW Water-Cooled Thermo-Ionic Thrustor for High Specific Impulse Operation

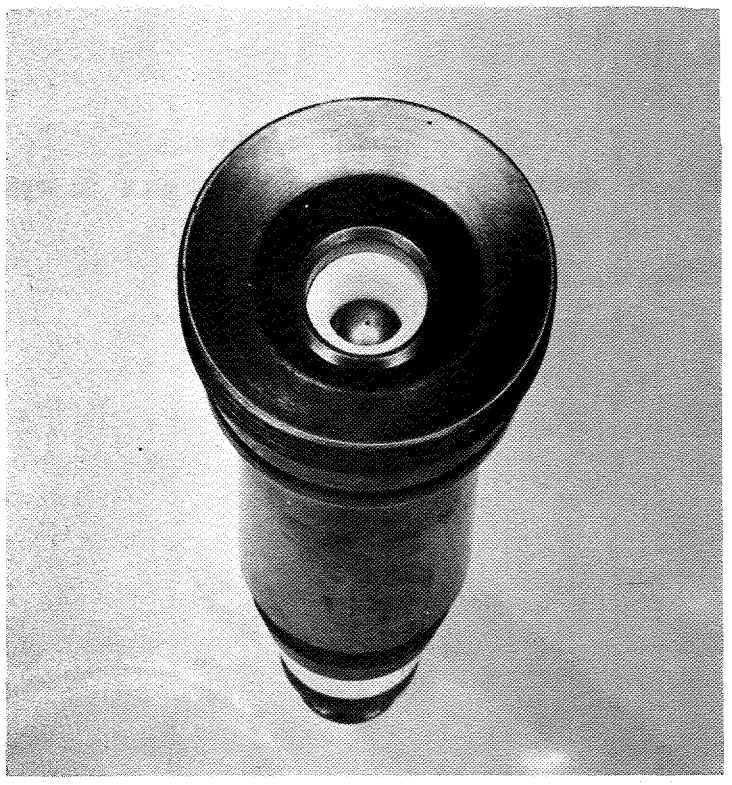

Figure 78. Photograph of Interchangeable Prototype Testing Head With Reversed Polarity Electrode Configuration for Operation Without Propellant Throughput

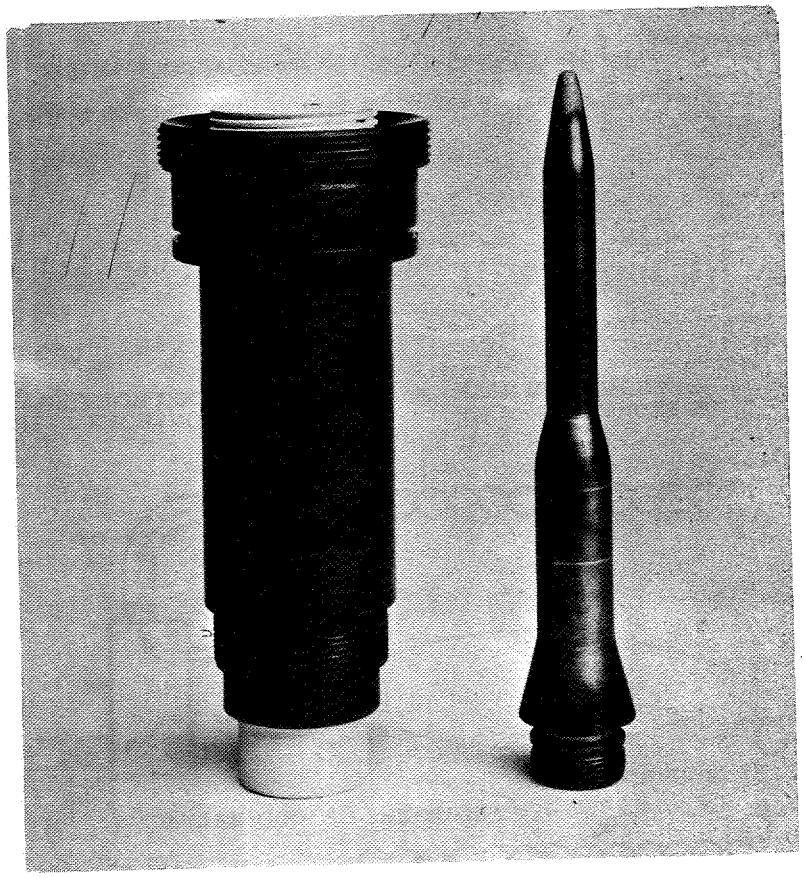

Figure 79. Photograph of Interchangeable Testing Head With Pressure Regulated Cathode for Stability Study

The most interesting effects are on the thermal efficiency (eg). Figure 80 shows schematically the two systems used to simultaneously measure the thermal efficiency and to cross-check the results. A well calibrated flow of water is established across the thrustor and the stagnator. The power lost in the thrustor, the power recovered in the stagnator and the total power are given by the temperature differential $(T_2 - T_1)$, $(T_3 - T_2)$, and $(T_3 - T_1)$ which are recorded and compared with the total input power. The system is very simple and gives good reproducible results (see Section 2.3.2 for more detailed analysis and recommendations for avoiding secondary influences). A large number of measurements have been averaged in Figures 81 and 82 to show the effect of changing the throat diameter at a constant length to diameter ratio (L/D = 1.5) and for two different mass flows (10 and 25 mg/sec) of H_2. The graphs show that the thermal efficiency decreases when the throat diameter is increased keeping all other parameters constant. This effect is especially strong at low values of specific impulse as illustrated in Figure 83 (see also Section 2.3.2).

The measurement of the thermal efficiency becomes more difficult with radiation-cooled thrustors but good results can be obtained with the system illustrated in Figure 84 which substitutes a thrustor radiation recovery section for the thrustor water cooler. The three temperature differentials $(T_2 - T_1)$, $(T_3 - T_2)$, and $(T_3 - T_1)$ give the power radiated by the thrustor, the power recovered from the jet, and the total power. Figure 85 is a picture of a typical radiation-cooled thrustor with an external water-cooled section which recovers the radiation. Figure 86 shows that (in this

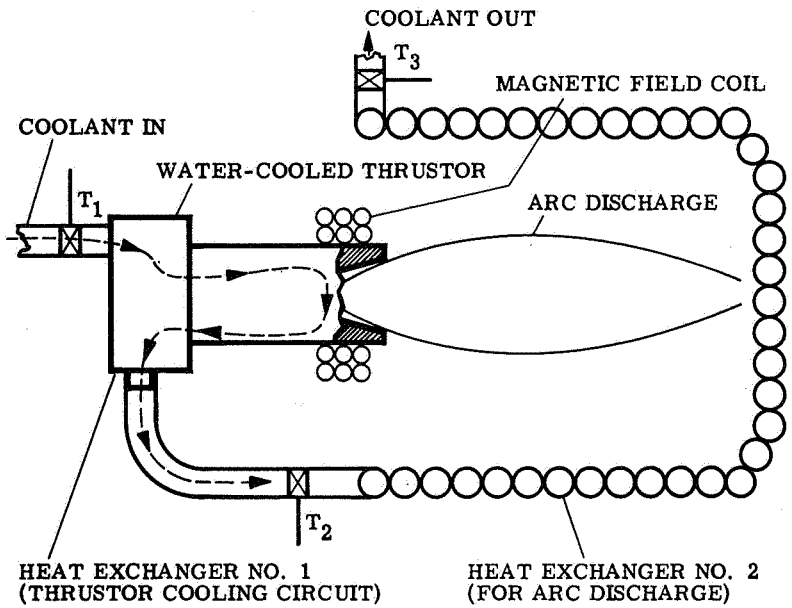

Figure 80. Schematic of Heat Exchanger System for Measuring Thermal Efficiency and Jet Power of a Water-Cooled Thermo-Ionic Thrustor

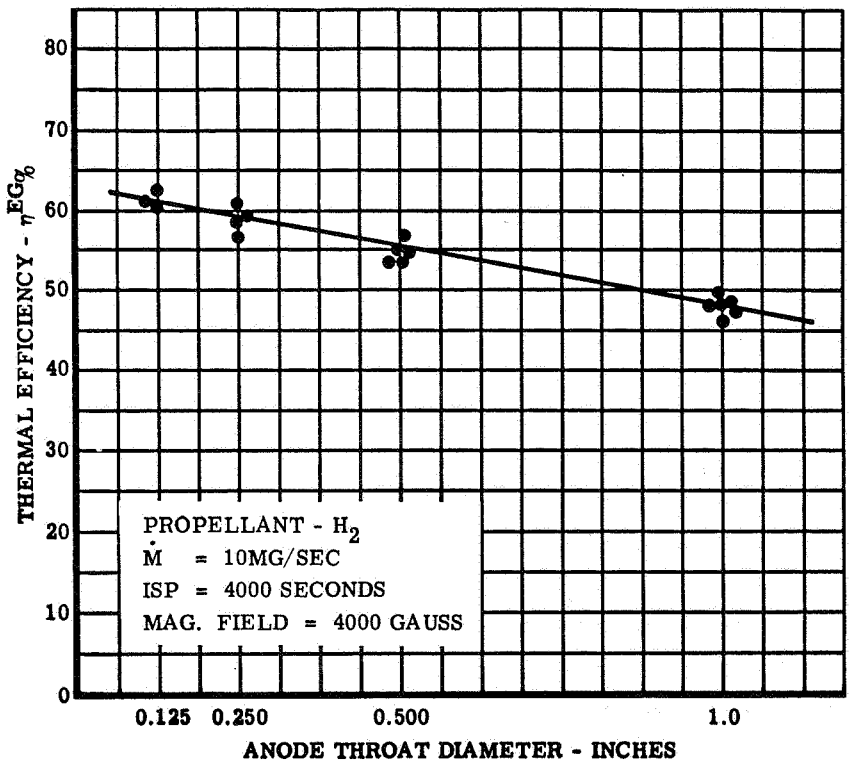

Figure 81. Thermal Efficiency Versus Anode Throat Diameter (Throat Length/Throat Diameter = 1.5)

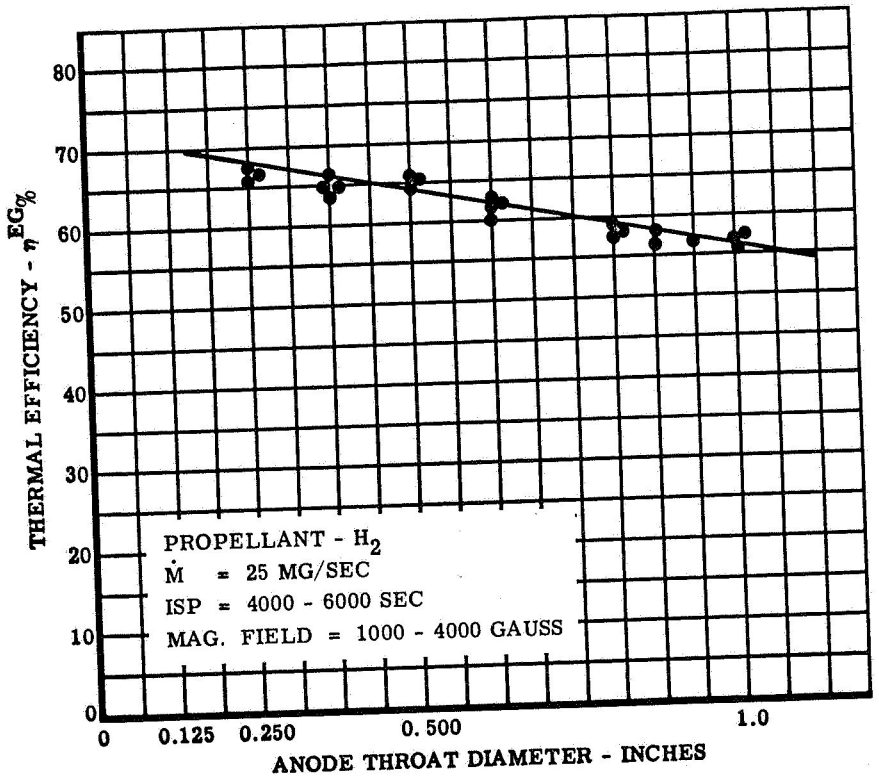

Figure 82. Thermal Efficiency Versus Anode Throat Diameter (Throat Length/Throat Diameter = 1.5)

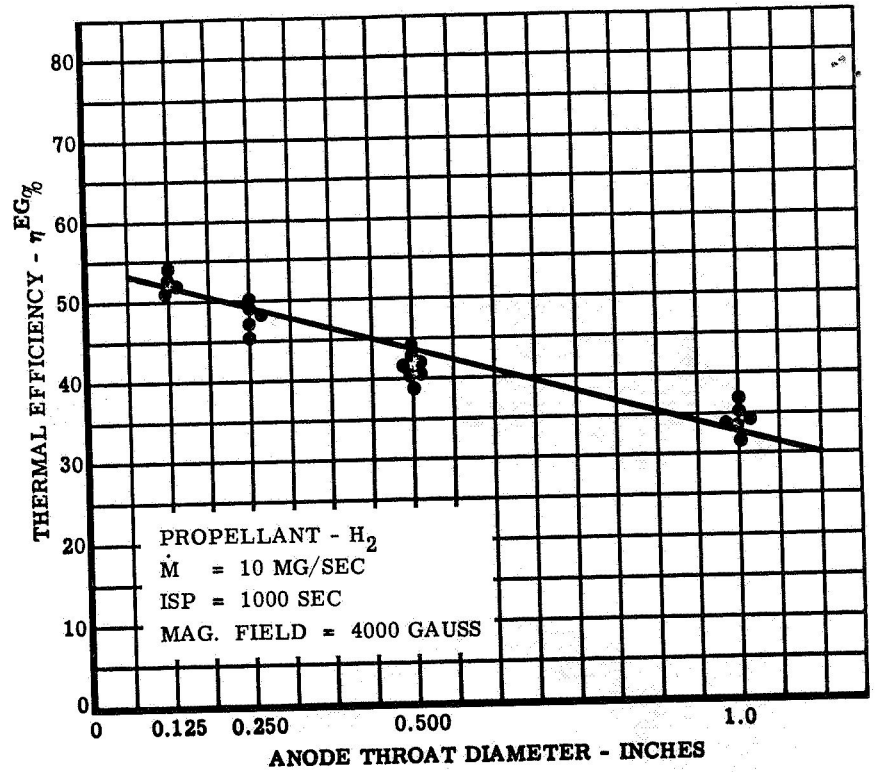

Figure 83. Thermal Efficiency Versus Anode Throat Diameter (Throat Length/Throat Diameter = 1.5)

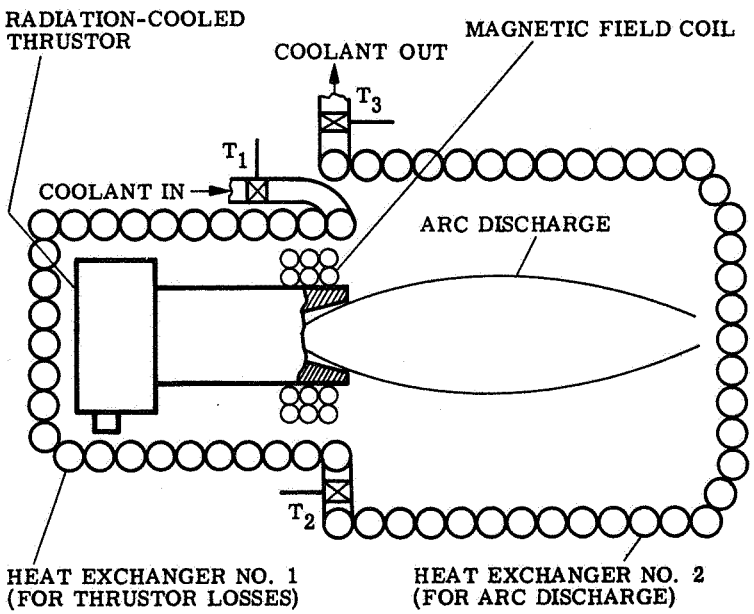

Figure 84. Schematic of Heat Exchanger System for Measuring Thermal Efficiency and Jet Power of a Radiation-Cooled Thermo-Ionic Thrustor

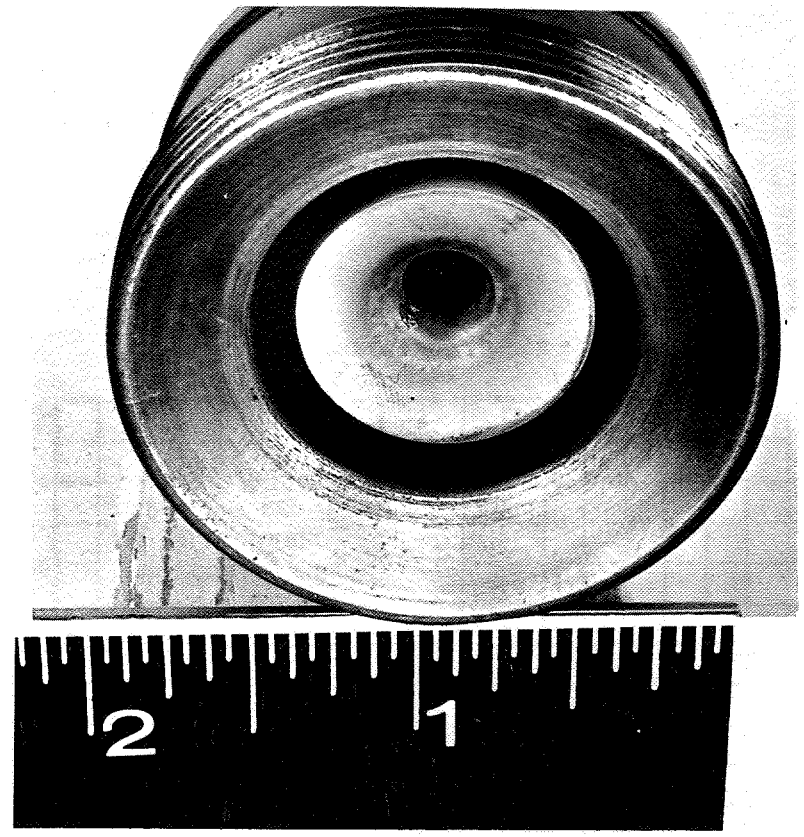

Figure 85. Typical Radiation-Cooled Testing Head With Water-Cooled Radiation Shield

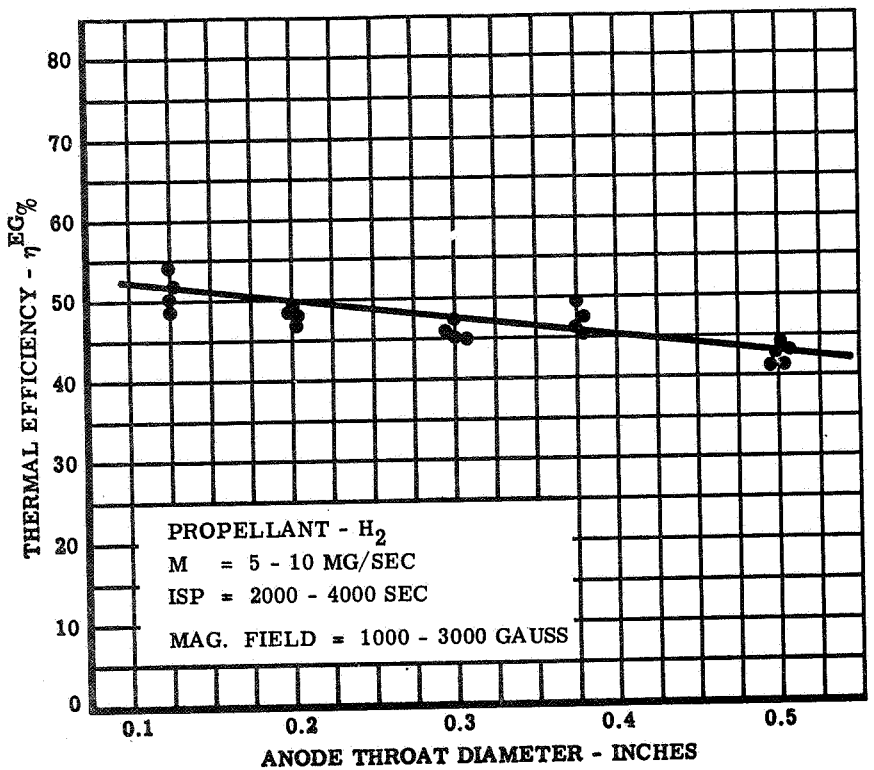

Figure 86. Thermal Efficiency Versus Anode Throat Diameter for Radiation-Cooled Thermo-Ionic Thrustor (Throat Length/Throat Diameter = 1.5)

case also) the thermal efficiency decreases with increasing throat diameter while Figure 87 demonstrates the same trend when lithium propellant is used. This trend has been obtained with a L/D ratio of 1.5. In order to study the influence of the throat diameter on the gas kinetic efficiency (gk), the measurement of thrust is necessary. As previously illustrated the kinetic efficiency is easily obtained as soon as thrust power transferred to the propellant and mass flow are known. While more detailed information on the thrust measurement are given in other sections, it is interesting to note that the gas kinetic efficiency follows a variation similar to that of the thermal efficiency with changing throat diameter. This is illustrated in Figures 88 and 89 using H_2 for two different mass flows. (The thrust efficiency measurements, especially at very low mass flows and high specific impulses, are subject to environmental effects that are examined in Section 2.3.2.) Since the influence of varying the throat diameter is similar for the thermal and for the thrust efficiency, the total efficiency follows the same trend. This is illustrated in Figures 103 and 104. After the termination of the investigation at other L/D ratios, a much better picture of the effect of the throat size on the various efficiencies will be obtained. The throat diameter is only one of the geometrical parameters to be considered in the study of the influence of geometry on efficiency. Although a large number of tests have been conducted to analyze various influences, complete studies have not yet been accomplished. The influence of the cathode geometry should be investigated much more systematically than has been done to date.

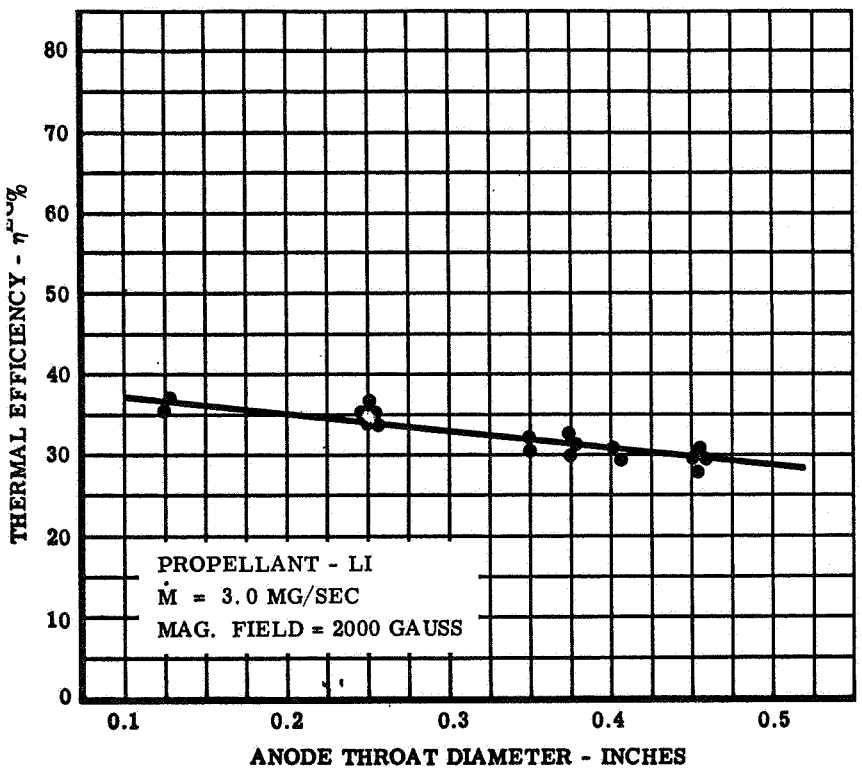

Figure 87. Thermal Efficiency Versus Anode Throat Diameter (Throat Length/Throat Diameter = 1.5)

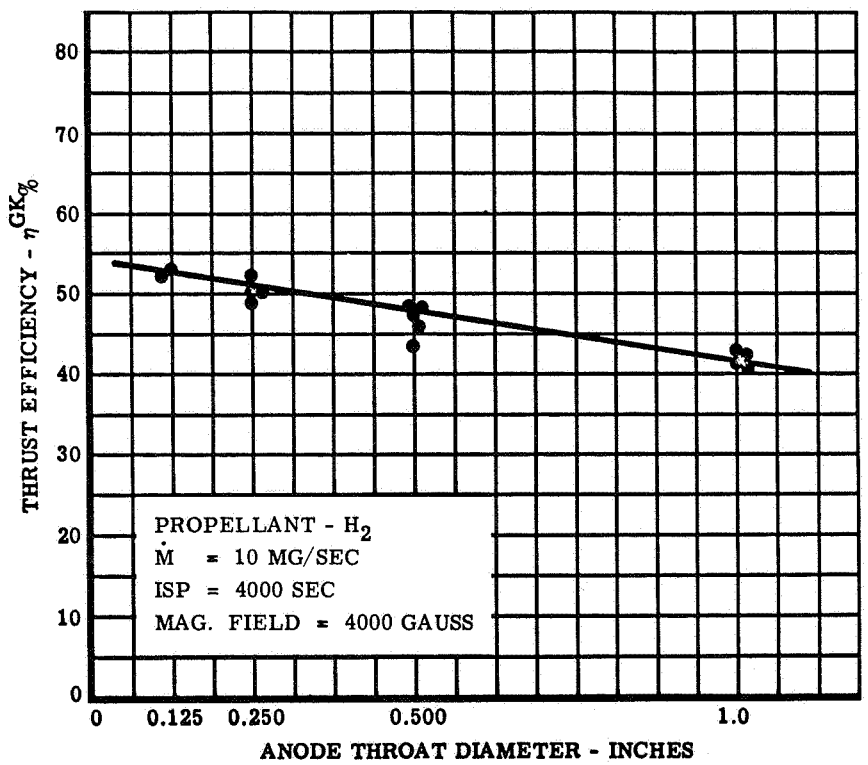

Figure 88. Thrust Efficiency Versus Anode Throat Diameter (Throat Length/Throat Diameter = 1.5)

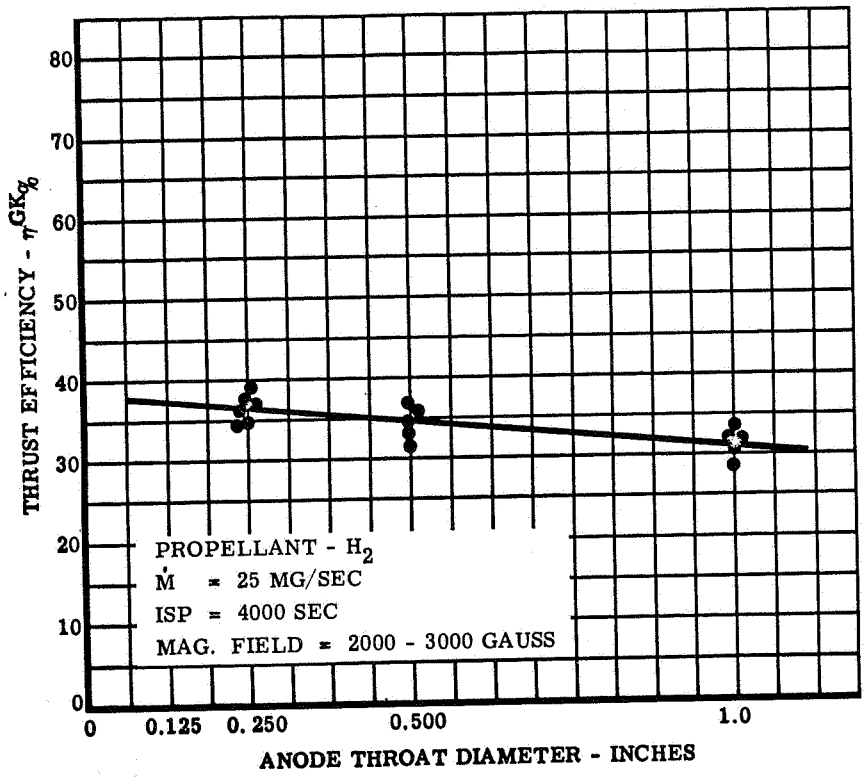

Figure 89.. Thrust Efficiency Versus Anode Throat Diameter

(Throat Length/Throat Diameter = 1.5)

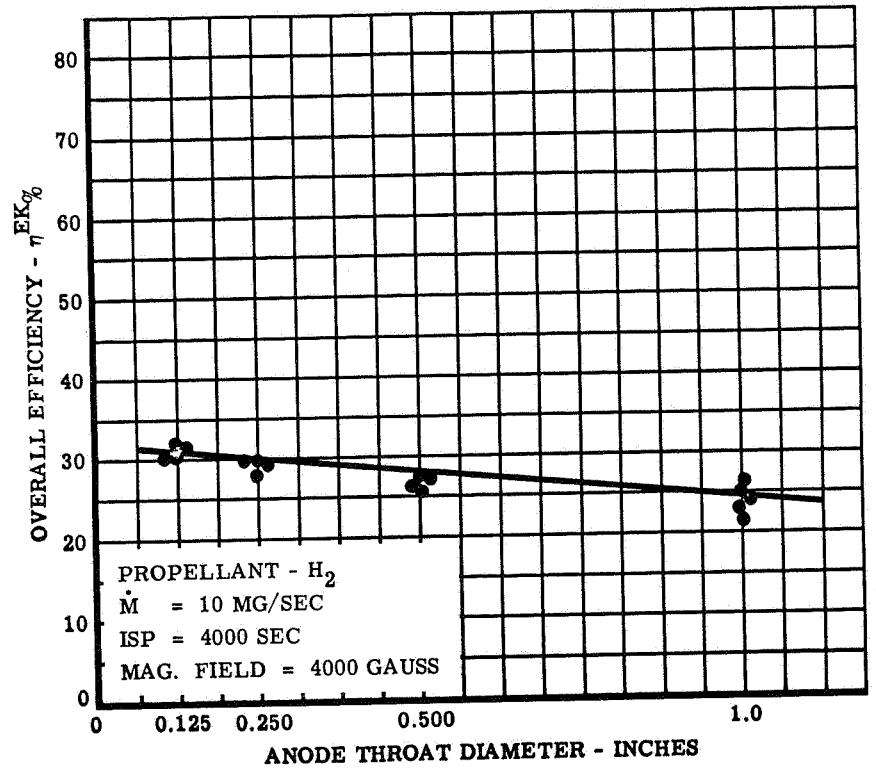

Figure 90.. Overall Efficiency Versus Anode Throat Diameter

(Throat Length/Throat Diameter = 1.5)

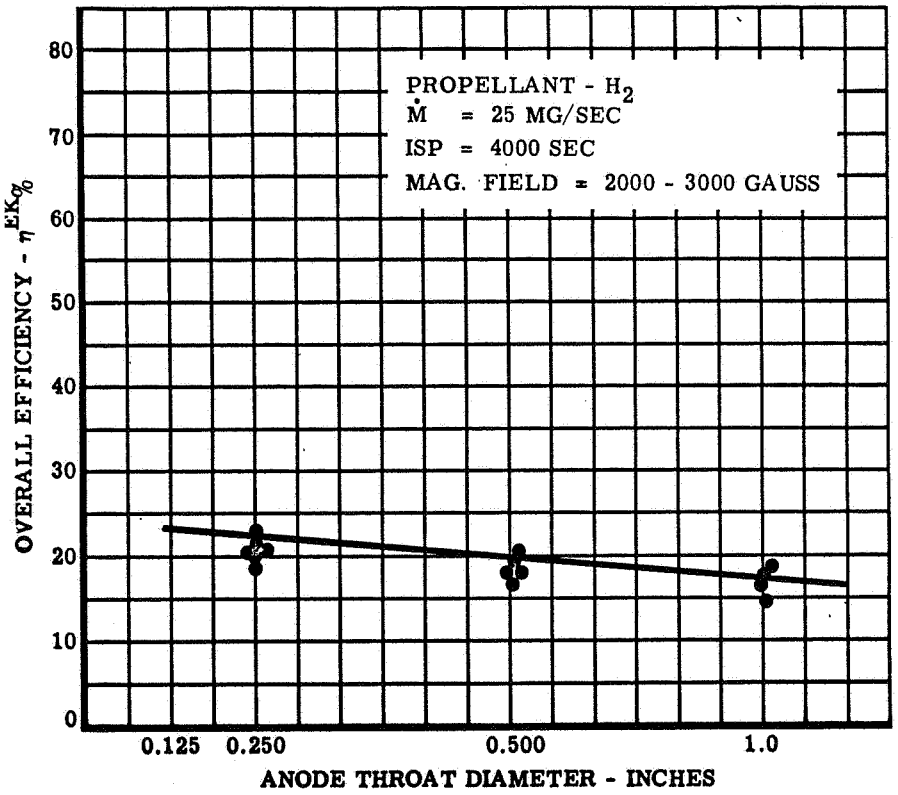

Figure 91. Overall Efficiency Versus Anode Throat Diameter (Throat Length/Throat Diameter = 1.5)

This is also the case for variations of polarities, special geometries for radiation, regeneration, transpiration cooling, systems for the use of multiple electrodes and so forth. In other sections partial results along these lines are given.

2.2.3 Effect of Propellant on Efficiency

While it is believed that the nature of the propellant used has a strong affect on the efficiencies measured, we are not yet able to classify various propellants as more or less efficient at this stage of the investigation. As we have seen in the preceding section, a number of effects add to or subtract from the overall efficiency so that before defining a "best" all the influences must be considered and compared. For this reason it seems to us that because of the complexities of the study and of the costly and time consuming program required, the analysis must be limited to a minimum number of propellants until completely reliable results are obtained. It seems advisable in the future to concentrate the research effort on one propellant before extending the analysis to others. Hydrogen seems the most suitable propellant to use as a standard with deuterium as a substitute when higher molecular weight is desired. The two propellants are simple in molecular and atomic structure, are gases at room temperature, and have been used successfully in enough past tests and analyses to qualify in practical applications. The storage problem of these propellants that has to some extent limited their use is, in our opinion, strongly offset by a number of important advantages. For this reason the data accumulated by us during this program on the influence of the propellant characteristics and on the efficiency are mostly related to the use of hydrogen and deuterium. The data obtained on other propellants such as ammonia and the alkali metals are not extensive enough to supply practical conclusions. In Section 2.3.3 the influence of different propellants on possible experimental anomalies in the measurements are exposed.

In the thermo-ionic acceleration should the dominating action be thermal, the principal influence of any propellant on the efficiency would be the temperature to which it must be heated to provide the desired jet velocity. A low operating temperature is beneficial because convective and radiative losses are reduced. For any desired velocity (or specific impulse) the minimum working temperature is obtained by reducing the molecular weight of the propellant. From this point of view, hydrogen being the lightest element (molecular weight 2) is the best propellant. (At higher temperatures atomic hydrogen is naturally better.) The weight of atomic hydrogen being one, all the other substances follow in the order of their molecular weight as illustrated in Table 5 which also gives the theoretical temperature necessary to reach a certain specific impulse. The increase in temperature also produces the well-known investment of energy in dissociation and ionization. It is customary to consider this as a loss because where very high velocities are involved, insufficient time is available for recombination. It is not known if future advances in technology will permit the recovery, at least in part, of this energy (Table 6). This might be the only approach possible to further increase the efficiency for certain propellants. Our experimental work in studying the influence of propellants on the thermal and kinetic efficiency has been based mostly on the use of hydrogen and deuterium. Of the alkali metals, lithium and potassium have been evaluated only with regard to their influence on the thermal efficiency. The kinetic results have not attained sufficient reproducibility to be published at the end of this program for the reasons illustrated in Section 2.3. For analogous reasons the operation without propellant throughput has been

TABLE 5

APPROXIMATE TEMPERATURES VERSUS SPECIFIC IMPULSE FOR PROPELLANTS OF VARIOUS ATOMIC WEIGHTS*

Propellant	Atomic Weight	Specific Impulse (Seconds) 1000	2000	3000	4000	5000
H_2	1	2800°K	8,400	I 11,000	I 19,000	I 30,000
D_2	2	4,800	12,000	I 22,000	I 38,000	I 60,000
He	4	9,600	22,000	I 43,000	I 76,000	I 120,000
Li	7	I 8,500	I 34,000	I 77,000	I 133,000	I + II 150,000
K	39	I 47,000	I + II 125,000	--	--	--
A	40	I 48,000	I + II 128,000	--	--	--

* I and II mean calculated using complete first and second ionization.

TABLE 6.

RATIO OF USEFUL ENERGY TO TOTAL ENERGY IN VARIOUS PROPELLANTS AT SEVERAL ISP*

Propellant	Atomic Weight	Specific Impulse (Seconds) 1000	2000	4000	8000
H_2	1	0.460	0.43	I 0.34	I 0.670
D_2	2	--	0.32	I 0.51	I 0.810
He	4	1.000	1.40	I 0.57	I 0.843
Li	7	0.350	I 0.61	I 0.86	--
K	39	I 0.824	I + II 0.69	--	--
A	40	I 0.570	I + II 0.66	--	--

* I and II mean calculated using complete first and second ionization.

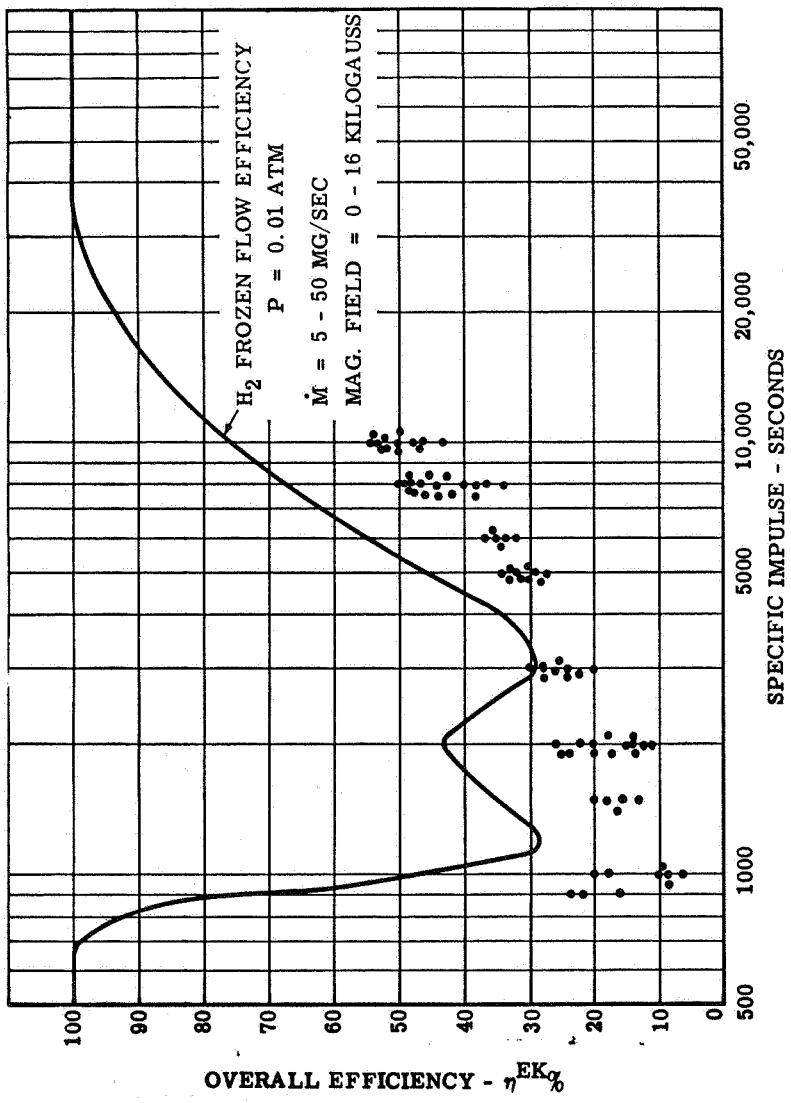

Figure 93. Average Reported Overall Efficiency Versus Specific Impulse for Thermo-Ionic Thrustors Operating With Hydrogen Propellant

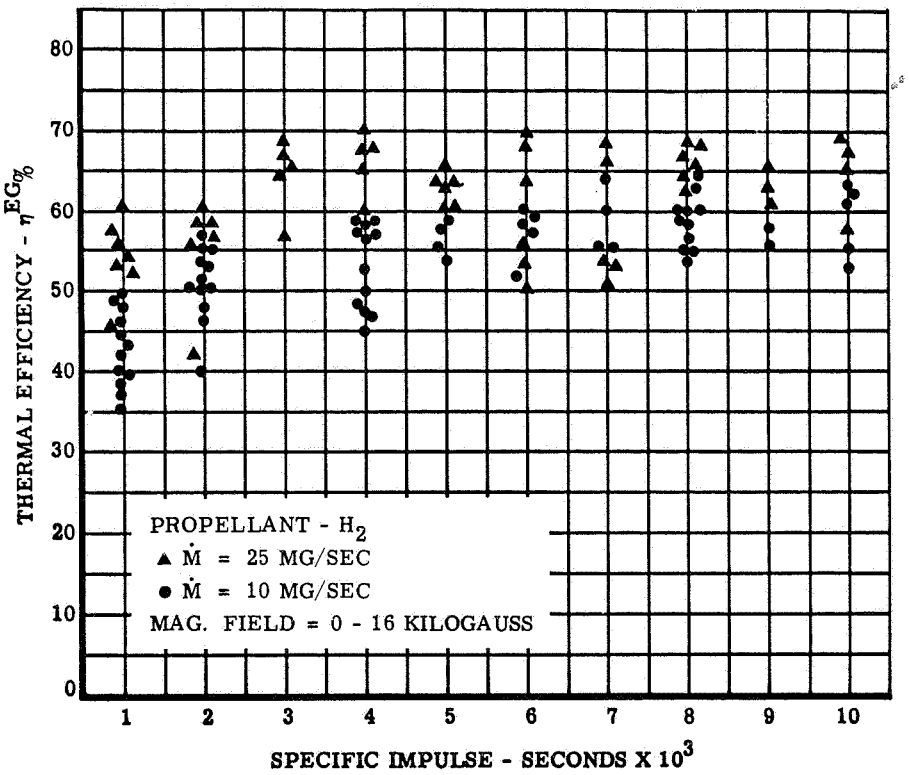

Figure 94. Thermal Efficiency Versus Specific Impulse for Various Thrustors Using H_2 Propellant

analyzed primarily with regard to its effect on thermal efficiency. As said in Section 2. 2. 2, the complete separation of the effects of propellants on the efficiencies from the numerous other variable parameters is not a simple operation. We have tried to keep as constant as possible any condition and vary only the propellant during the test. But some variations cannot be eliminated, especially if they are affected by the different characteristics of the propellants. More sophisticated programs of comparison will probably be necessary in the future. The time necessary to reach a highly refined level for each propellant is so long that a single laboratory can hardly afford it. In our case, hydrogen has been used as the standard and other propellants have been compared to it holding other parameters as constant as possible. The geometry of the thrustor was identical for all propellants and is illustrated schematically in Figure 92. As we have seen in the preceding section, the efficiency with any propellant is influenced by many factors simultaneously so that quantitative theoretical interpretations are usually very difficult. Figure 93 shows average measured values of total efficiency (ek) at various specific impulse levels for hydrogen as compared to frozen flow conditions. It is evident that much remains to be done to bring the total efficiency (at least for some operating conditions) up to the 50 percent limit that is desirable for most space missions. As said before, we have always tried to separate the thermal efficiency (eg) and the thrust efficiency (gk) with the intention of obtaining a better understanding of the distribution of the input power. Average values for the thermal efficiency obtained using hydrogen by ourselves and other laboratories are illustrated in Figure 94. The average

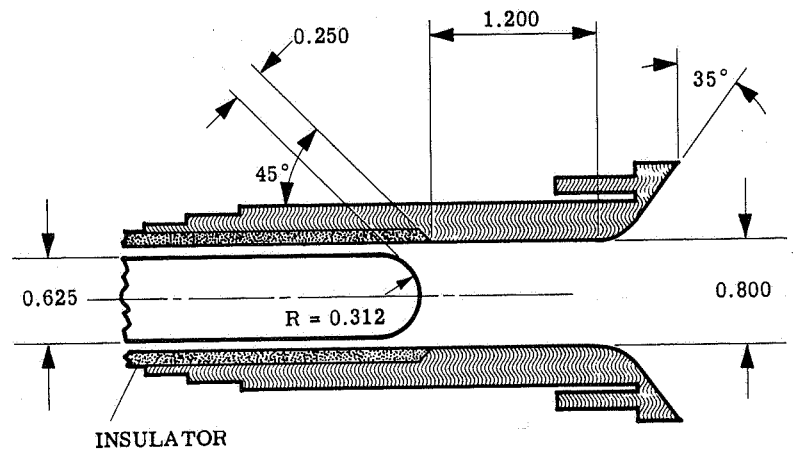

Figure 92. Dimensions of Electrode Geometry Used for Comparative Test With H_2 and D_2 Propellants

includes variations in geometry, magnetic field, pressure, and so forth, and include all the values obtainable to the best of our knowledge. It is interesting to note that (while there are a few exceptions) the majority of the data available falls around 50 percent. The thrust efficiency (gk) of hydrogen, averaged from many different results, increases with specific impulse following the same general trend as the frozen flow efficiency (Figure 95). At very high specific impulses the measured efficiency is unrealistically high. The cause of this anomaly remains to be determined (see Section 2.3). Data on the thermal and kinetic efficiencies using deuterium have been averaged from many measurements made during this program and are shown in Figures 96 and 97. The average thermal efficiency obtained using deuterium is about 5 percent lower than the average thermal efficiency obtained using hydrogen (more data are necessary to determine if this difference can be eliminated with technological improvements). The average thrust efficiency obtained with deuterium seems higher than the average thrust efficiency obtained with hydrogen by about 10 percent. If this result is confirmed, total efficiency of deuterium might be higher than the equivalent efficiency of hydrogen. Because of the relatively small differences more tests are required (more data on the efficiencies of hydrogen and deuterium can be found in other sections in singular not averaged results). As said before, it is of interest to compare monatomic helium with diatomic deuterium because of their identical weight. Unfortunately the data on helium are quite limited. Figure 98 shows the thermal efficiency obtained with helium in a few tests conducted by us, and Figure 99 shows a relatively high thrust efficiency obtained with the same

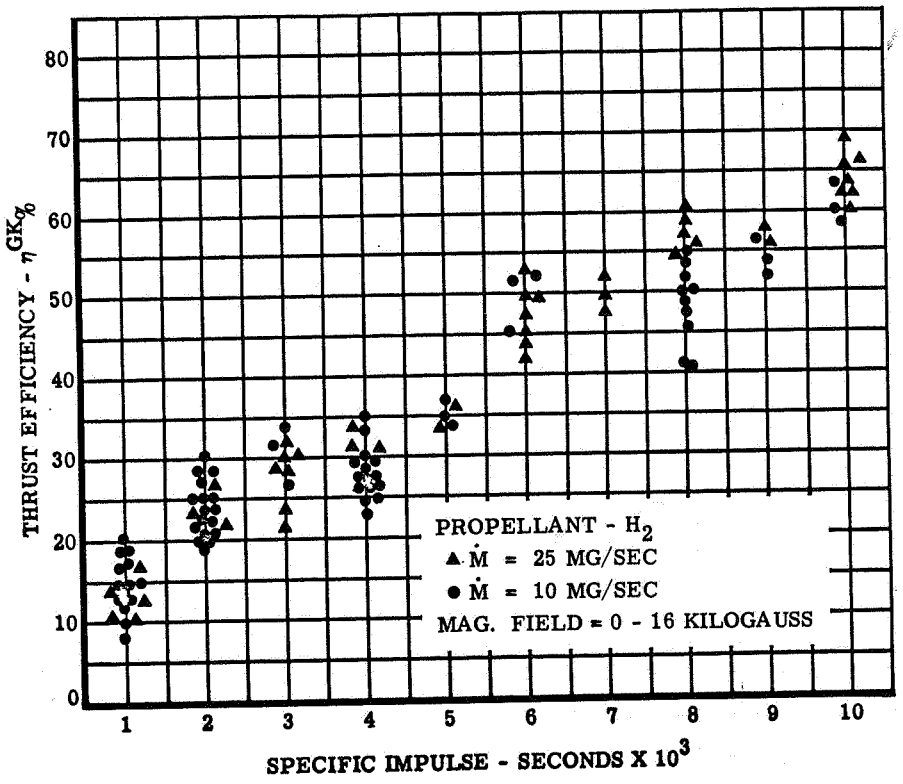

Figure 95. Thrust Efficiency Versus Specific Impulse for Various Thrustors Using H_2 Propellant

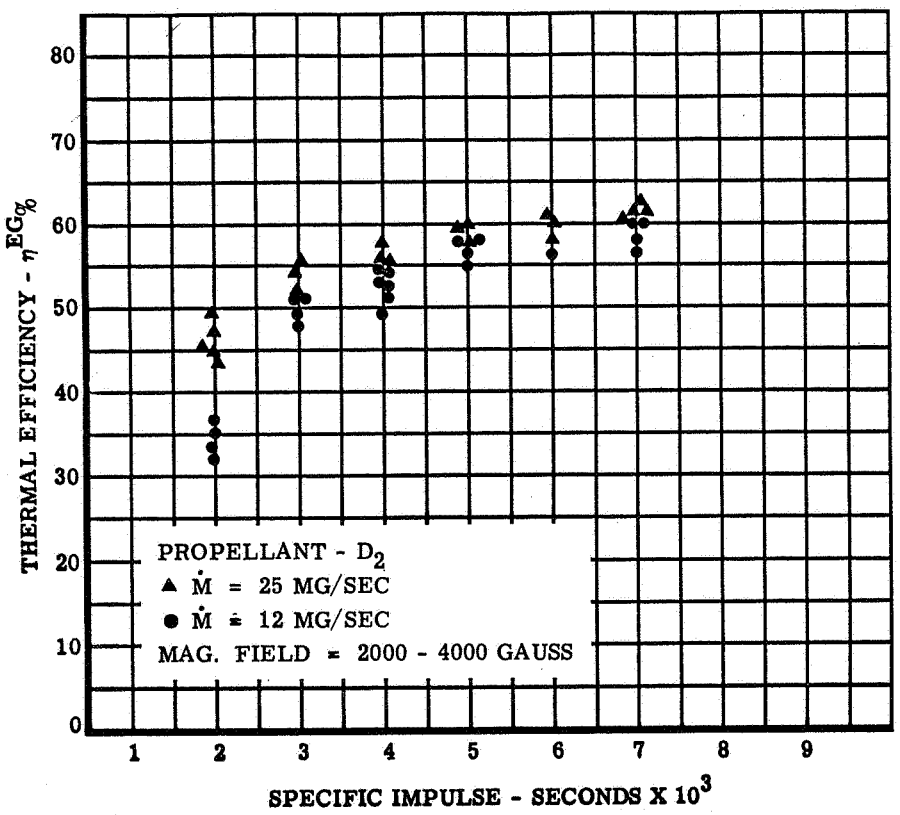

Figure 96. Thermal Efficiency Versus Specific Impulse for Thermo-Ionic Thrustor Using D_2 Propellant

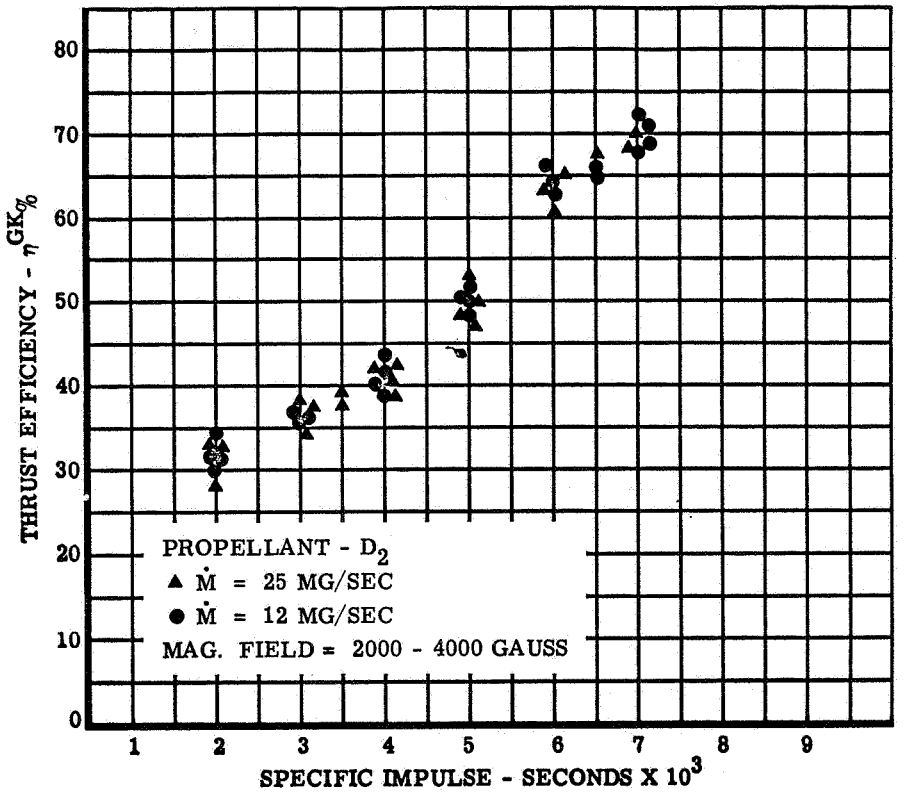

Figure 97. Thrust Efficiency Versus Specific Impulse for Thermo-Ionic Thrustor Using D_2 Propellant

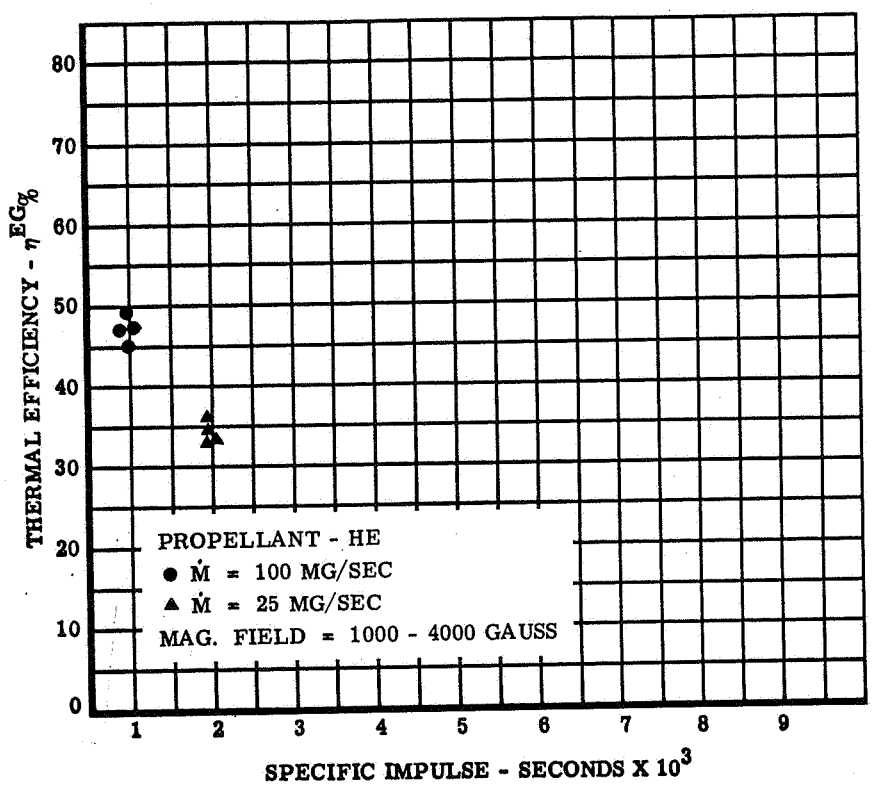

Figure 98.. Thermal Efficiency Versus Specific Impulse for Thermo-Ionic Thrustor Using He Propellant

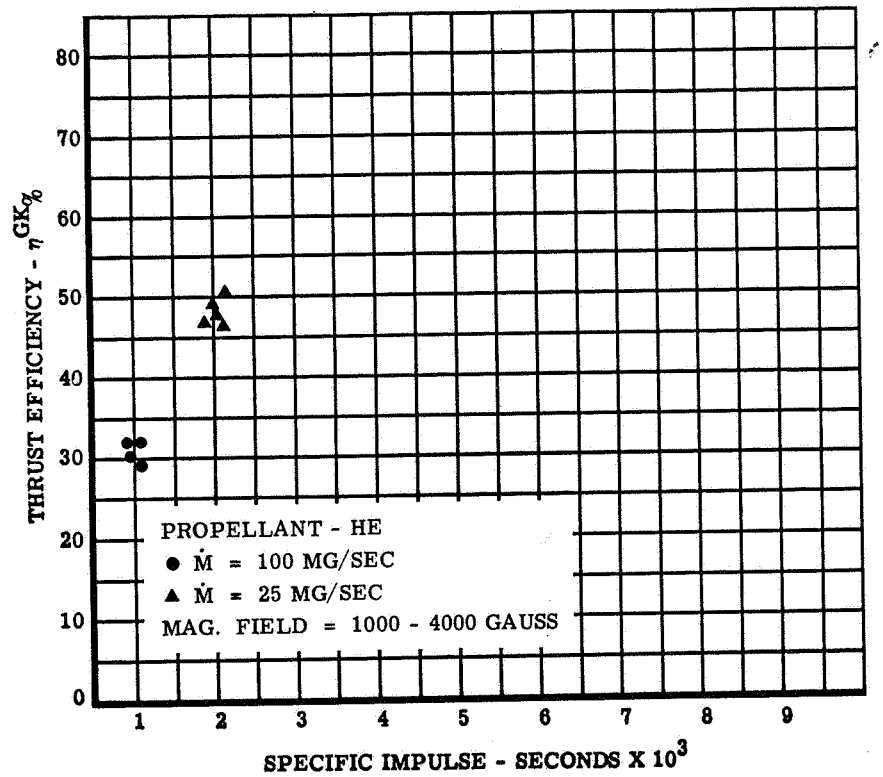

Figure 99.. Thrust Efficiency Versus Specific Impulse for Thermo-Ionic Thrustor Using D_2 Propellant

propellant. Ammonia is a promising propellant that deserves more effort than was devoted to it during this program. Averages from available data are illustrated in Figures 100 and 101. A long time has been spent during the program to obtain reproducible results using alkali metals as propellants. As said before, only the thermal efficiency of lithium and potassium has been studied extensively. The thrust efficiency obtained did not show sufficient reproducibility for publication (see Section 2.3.3). The average thermal efficiency of lithium is shown in Figure 102. The triangular points at a high level of efficiency refers to very recent data obtained in other laboratories.[5] Figure 103 shows the average of equivalent data on potassium from our tests and from others. Other data on the efficiencies obtained using alkali metals can be found in other parts of this section and in Section 2.3). In our long series of tests without propellant throughput (using electrode vapors or other residual gases as propellants) we constantly noted a strong decrease in the thermal efficiency as illustrated in Figure 104 (average values are shown). Unfortunately, to the best of our knowledge, no other data are available for this type of operation (see also Section 2.3). Figure 105 shows the improvement in thermal efficiency obtainable in electrode vapor operation as soon as a small amount of hydrogen is injected between the electrodes. This bi-propellant operation (which requires further investigation) seems promising from the results obtained by us and by others, especially with regard to the possible use of mixtures containing condensable propellants (as consumable electrodes, insulators, arc chamber, and so forth). It is our opinion that only traces of other materials can sometimes improve the overall qualities of many propellants. This type of operation often known as "seeding" deserves further investigation.

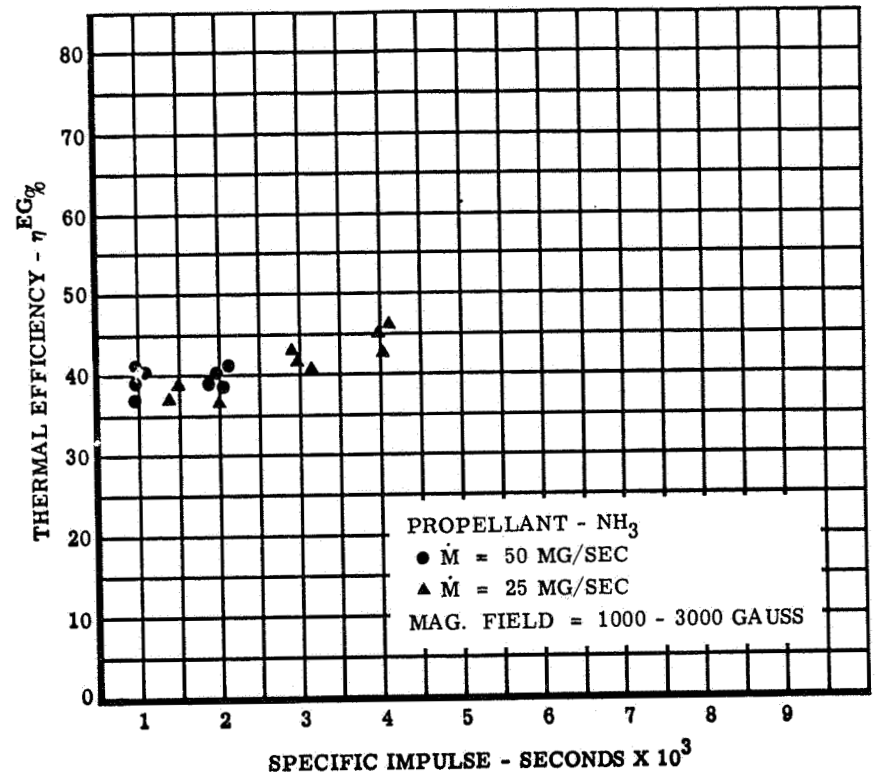

Figure 100. Thermal Efficiency Versus Specific Impulse for Thermo-Ionic Thrustor Using NH_3 Propellant

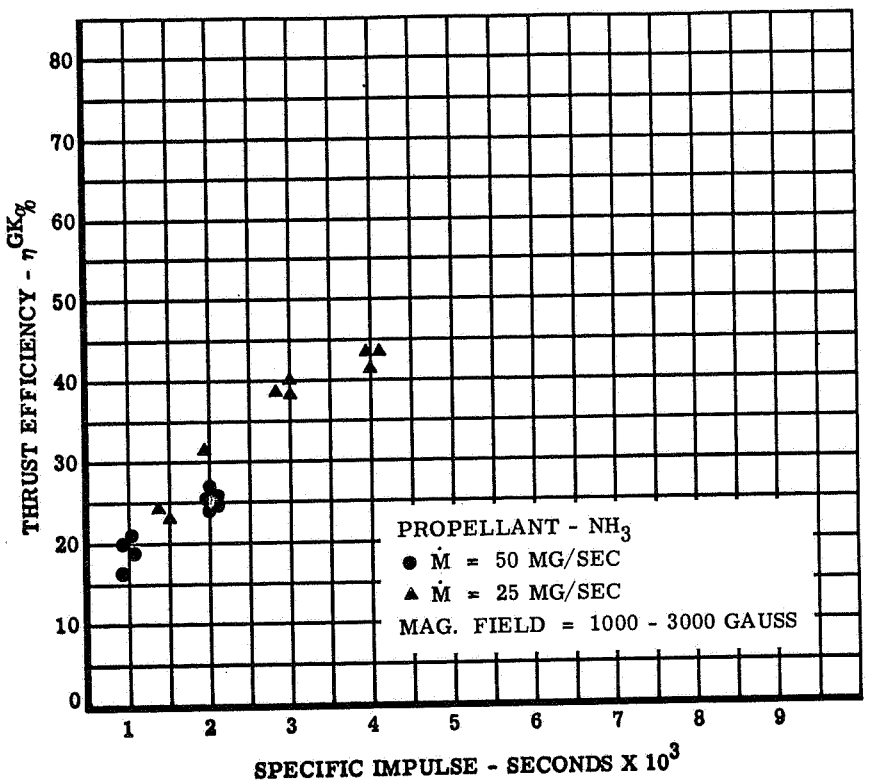

Figure 101. Thrust Efficiency Versus Specific Impulse for Thermo-Ionic Thrustor Using NH_3 Propellant

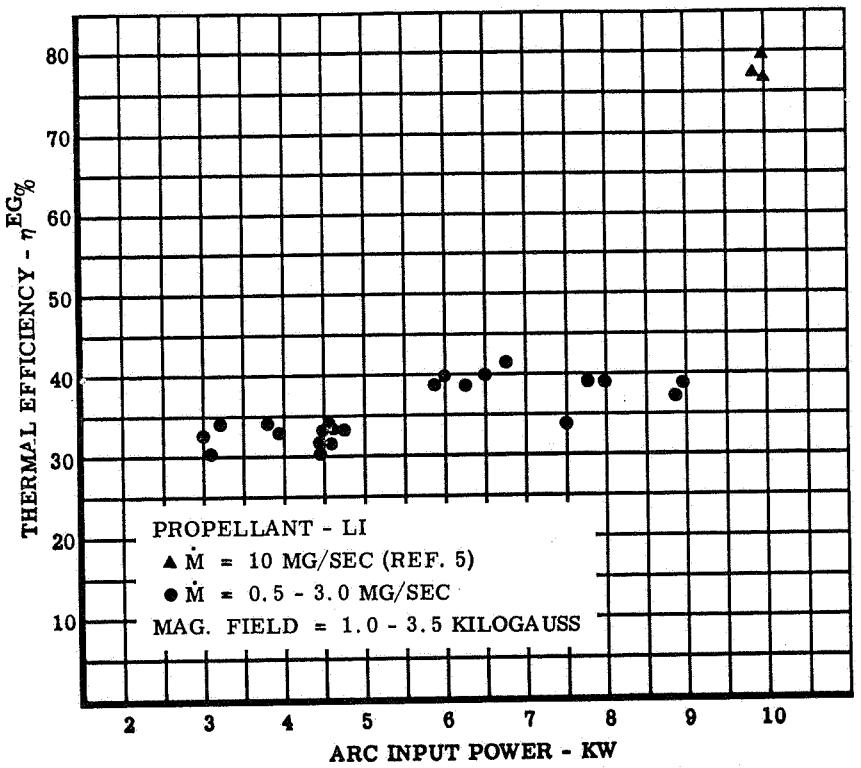

Figure 102. Thermal Efficiency Versus Arc Input Power for Thermo-Ionic Thrustor Using Lithium Propellant

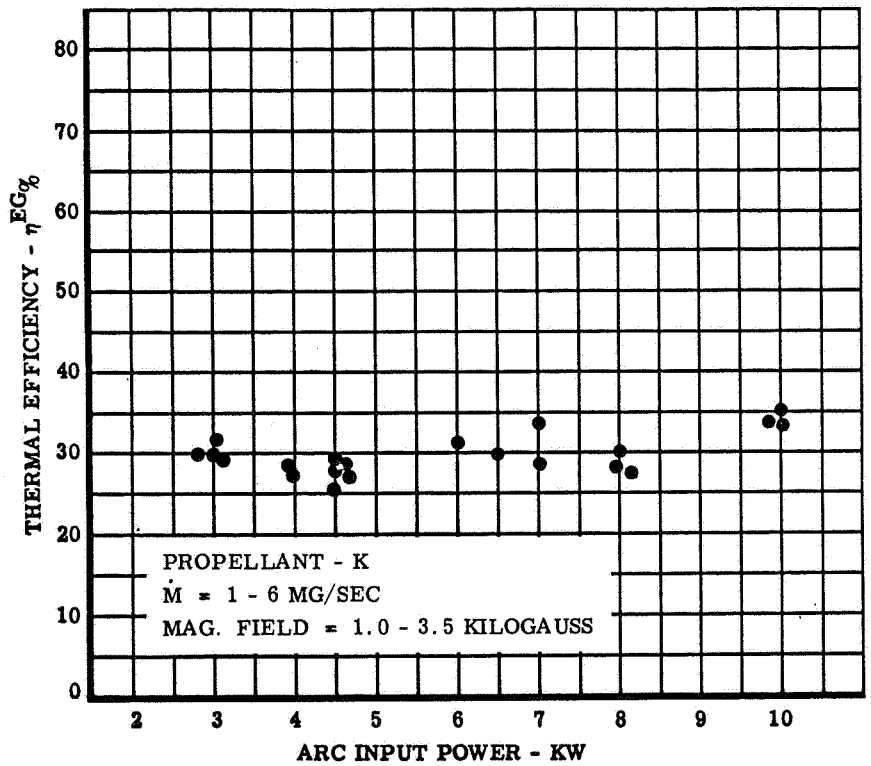

Figure 103. Thermal Efficiency Versus Arc Input Power for Thermo-Ionic Thrustor Using Potassium Propellant

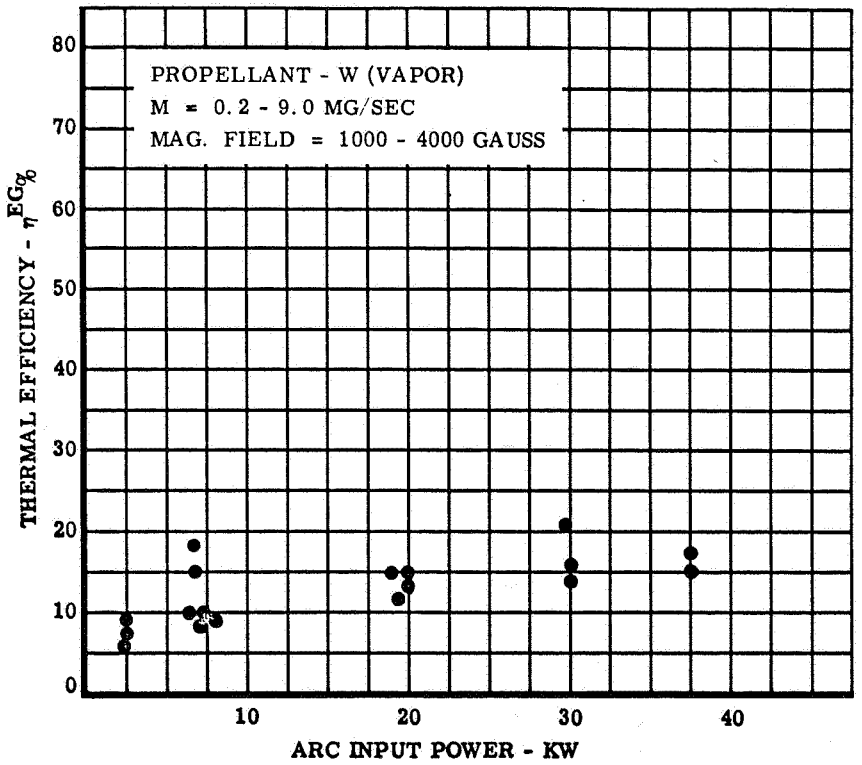

Figure 104. Thermal Efficiency Versus Arc Input Power for Thermo-Ionic Thrustor Without Propellant Throughput

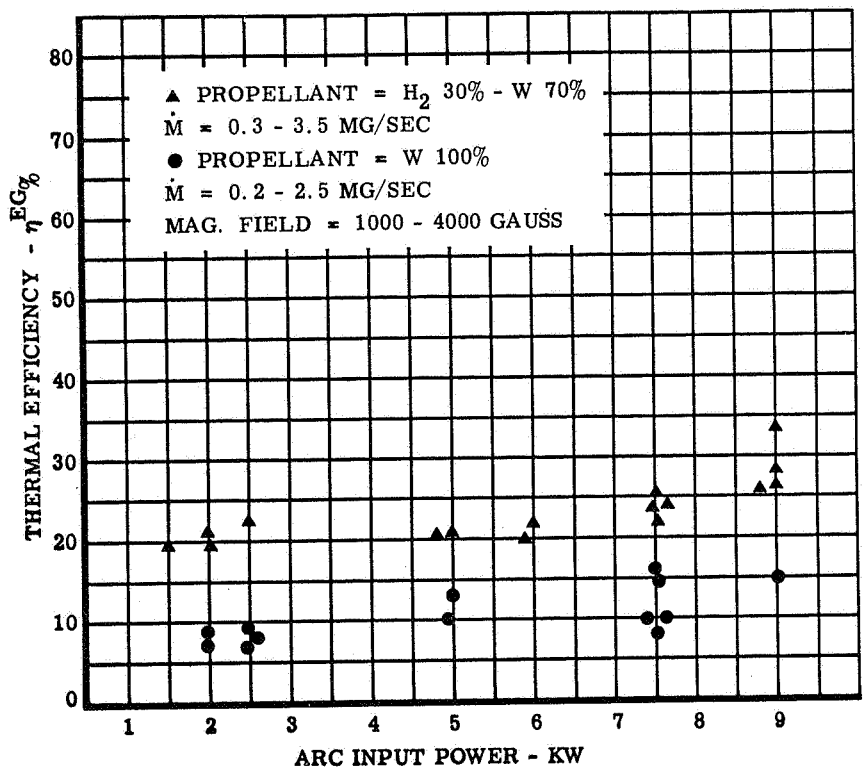

Figure 105. Thermal Efficiency Versus Arc Input Power for Thermo-Ionic Thrustor Operating With Electrode Vapor and H_2 Seeded Propellant

2.2.4 Effect of Pressure on Efficiency

The arc chamber pressure depends on the mass flow, the geometry of the arc chamber and the operating specific impulse. To understand the influence of arc chamber pressure on the efficiency it would be desirable to operate at different pressures while keeping as many other parameters constant as possible. A simple method for changing the arc chamber pressure is to change the mass flow while leaving all the other variables unchanged. To hold the specific impulse constant while varying the mass flow it is necessary to vary the power input approximately in proportion to the variation of mass flow. Another way of varying the pressure is to change the throat diameter. Small variations of pressure can be obtained by varying the intensity of the magnetic field, which at the same time changes the arc voltage and current and can produce secondary effects. Variation of pressure between wide limits can be obtained using propellants of different molecular weight, but secondary influences are to be expected in this case also. In studying the effect of changing the pressure, all these methods have been used, but we have tended to adopt the method of changing the throat diameter. The effect due to varying the throat diameter can be derived from the data shown in Section 2.2.2. When the throat diameter is changed, the heat transfer to the wall is also changed. This makes it difficult to discriminate between the effects of the change in pressure and the effect of the change in geometry. For these reasons we have averaged the efficiencies obtained at constant pressure without considering how the pressure was obtained.

During the initial part of the program very high values of specific impulse could only be obtained by reducing the arc chamber pressure. As demonstrated in Section 2.1.2, the reduction in the working pressure of the arc improved the distribution of the arc discharge both on the cathode and on the anode permitting higher enthalpies to be reached without destruction of the electrodes. Another important result of the decreased operating pressure was the increased uniformity of the jet with the elimination or at least a reduction of the high temperature center core, which results in a better kinetic efficiency of the jet. Another advantage of the reduced operating pressure is the reduction of radiation losses. A negative effect of the lower operating pressure can be the increased current necessary to compensate for the reduction in voltage (if special precautions in the application of an external magnetic field are not taken). This increase of the arc current can introduce conspicuous losses in the electrodes and in their immediate proximity. For these reasons and for others not listed, the study of the effect of the operating pressure on the efficiencies of a thermoionic arc is still very far from completion. The decrease of the chamber pressure, while permitting a more uniform operation, introduces some effects which are contrary to the obtainment of maximum efficiencies. However, in many cases (especially at the highest specific impulses), technical difficulties oppose the use of higher pressures (reduction of throat diameter) because power density limits are reached. If the problem of magnetic containment could be solved, higher pressures could be used resulting in a probable improvement in the thermal and kinetic efficiencies. Initial tests at extremely high magnetic fields and with different geometries

indicate that higher efficiencies can be obtained by employing higher arc chamber pressures. When an external magnetic field is not used, the pressure measured at the tip of the cathode increases with increasing arc current, while the pressure at the walls of the anode chamber increases up to a certain value of current, then decreases with a further increase in current (Figure 106). When a magnetic field is applied, a different trend results so that an increase in magnetic field strength causes a decrease in pressure. In Figure 107 we have averaged all the results available for thermal efficiency versus arc pressure at an Isp of 1000 seconds. The efficiency increases appreciably at higher pressures. The same trend in more modest proportions is shown in Figure 108 for an Isp of 4000 seconds. The thermal efficiencies of hydrogen and deuterium follow the same pattern. Figure 109 shows the thermal efficiency of H_2 and D_2 at various arc chamber pressures using the same throats for both gases. If the diameter of throats are adjusted to obtain equal pressures, the thermal efficiencies of H_2 and D_2 coincide. Figures 110, 111 and 112 show the variation of thermal efficiencies with arc chamber pressures for other propellants. The H_2 thrust efficiency also depends on chamber pressure as shown in Figure 113. It is known that the pressure on the cathode tip is different from the pressure on the anode in the arc chamber. It is also known that an improvement of operation can be obtained by increasing the pressure around the cathode as described in Section 2.1.2. The combined effect of pressure and external magnetic field are reported in Section 2.2.6.

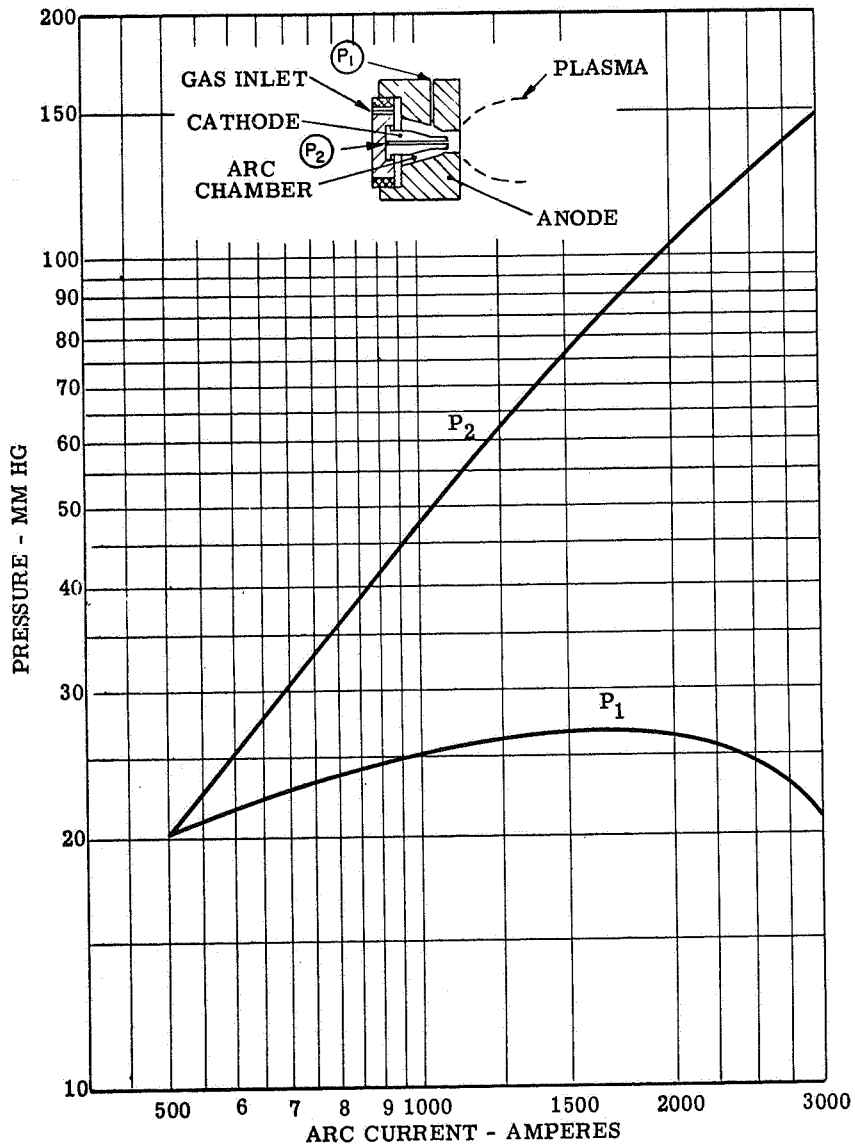

Figure 106. Variation of Arc Chamber Pressure With Arc Current at Different Locations

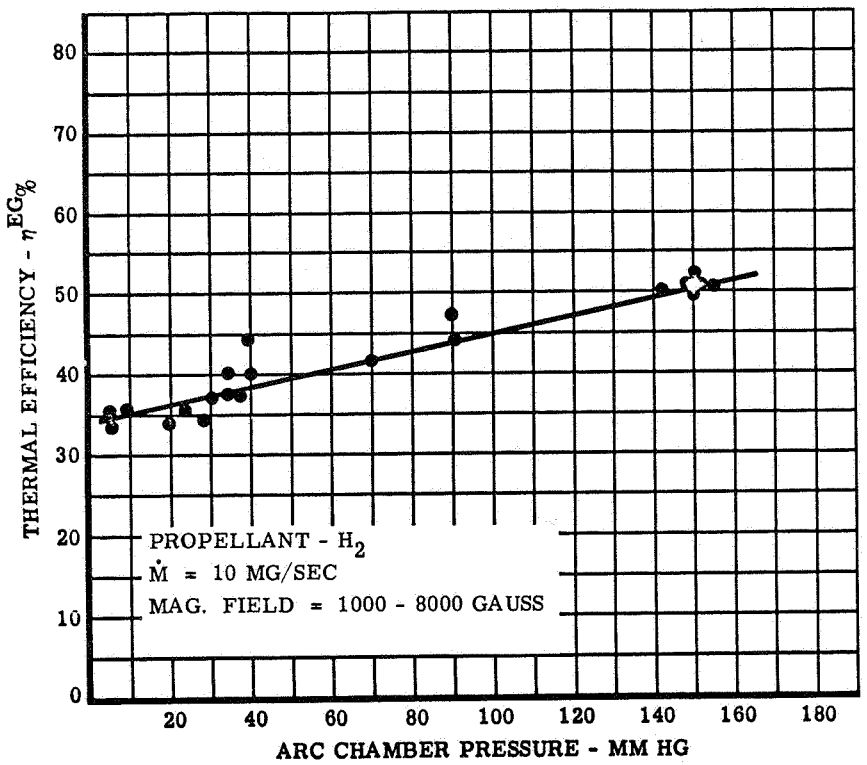

Figure 107. Thermal Efficiency Versus Arc Chamber Pressure for Thermo-Ionic Thrustor Using H_2 at 1000 Seconds Isp

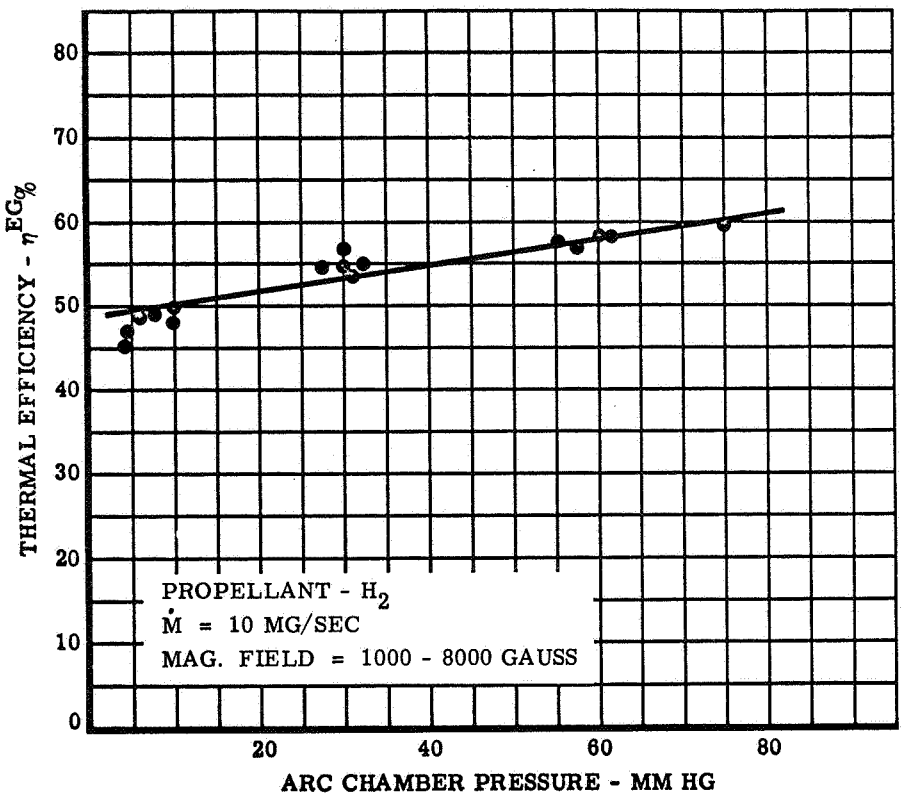

Figure 108. Thermal Efficiency Versus Arc Chamber Pressure for Thermo-Ionic Thrustor Using H_2 at 4000 Seconds Isp

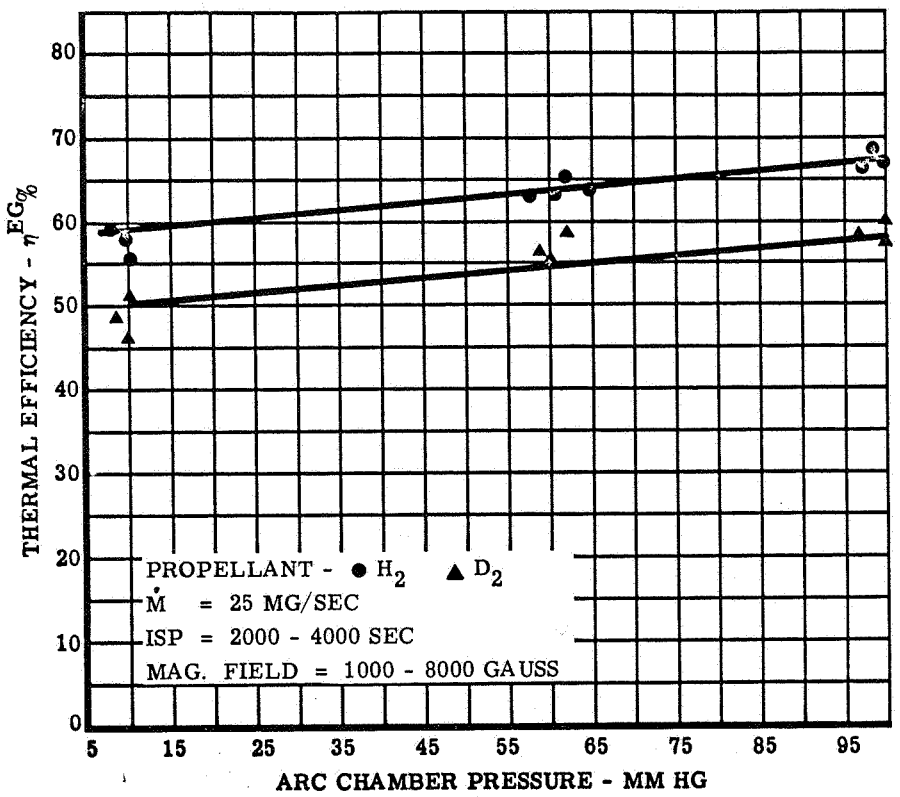

Figure 109. Thermal Efficiency Versus Arc Chamber Pressure for Thermo-Ionic Thrustor Using H_2 and D_2 Propellants

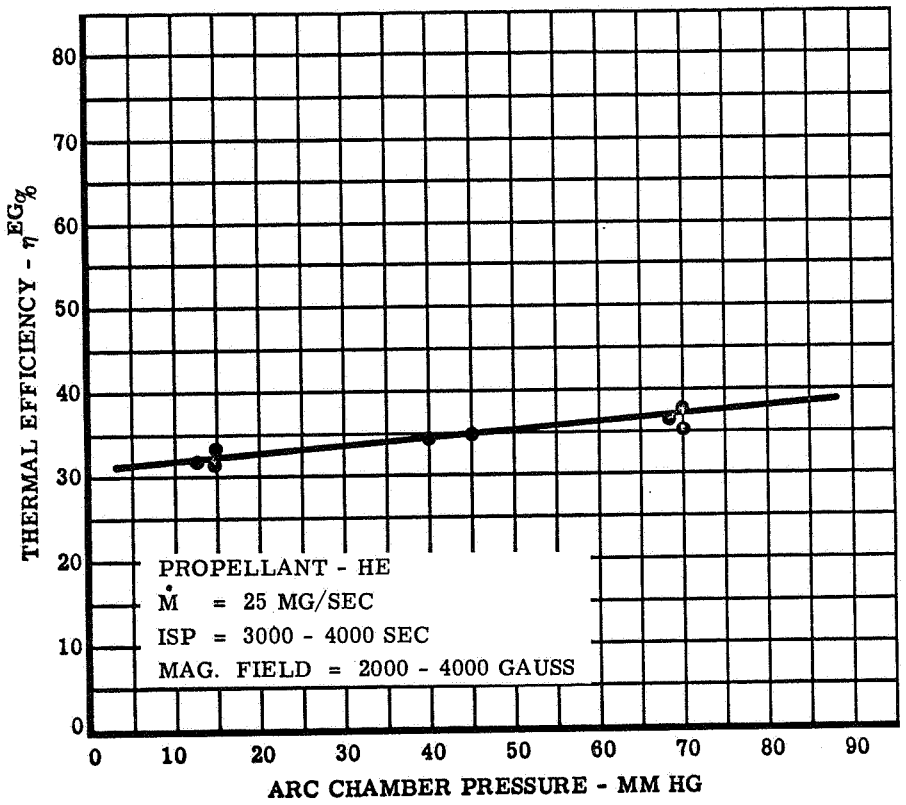

Figure 110. Thermal Efficiency Versus Arc Chamber Pressure for Thermo-Ionic Thrustor Using He Propellant

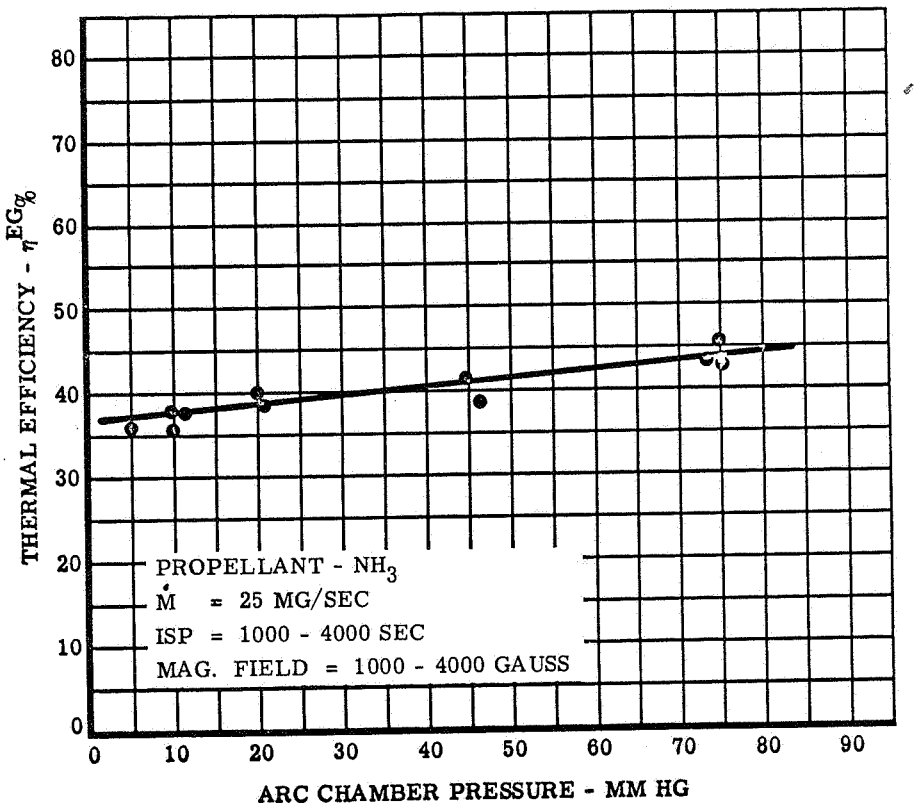

Figure 111. Thermal Efficiency Versus Arc Chamber Pressure for Thermo-Ionic Thrustor Using NH_3 Propellant

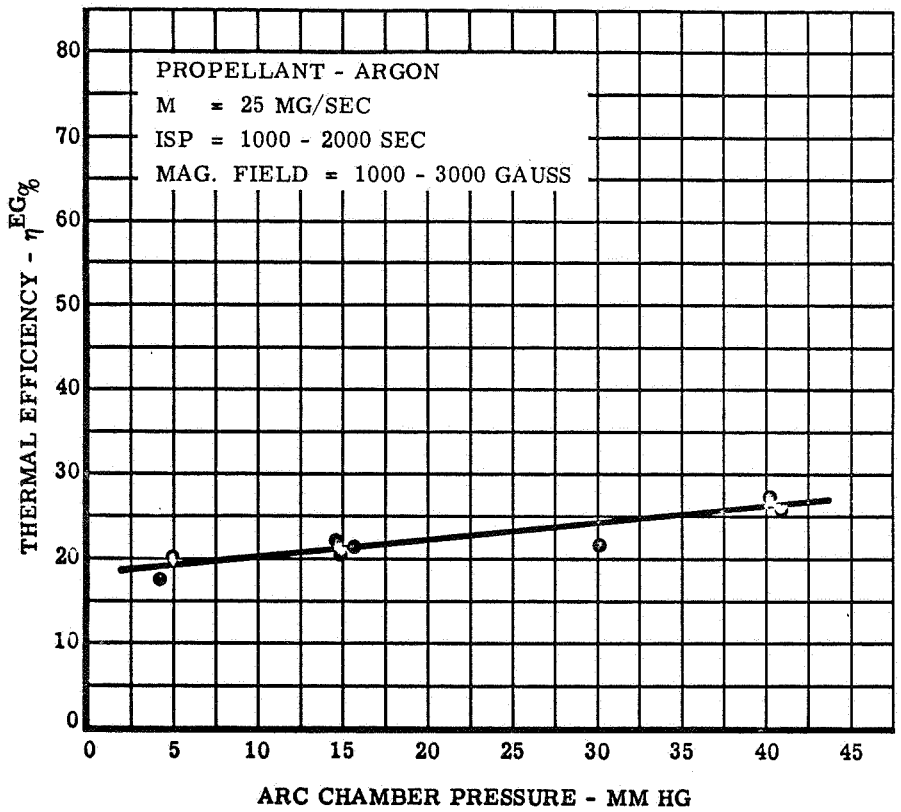

Figure 112. Thermal Efficiency Versus Arc Chamber Pressure for Thermo-Ionic Thrustor Using Argon Propellant

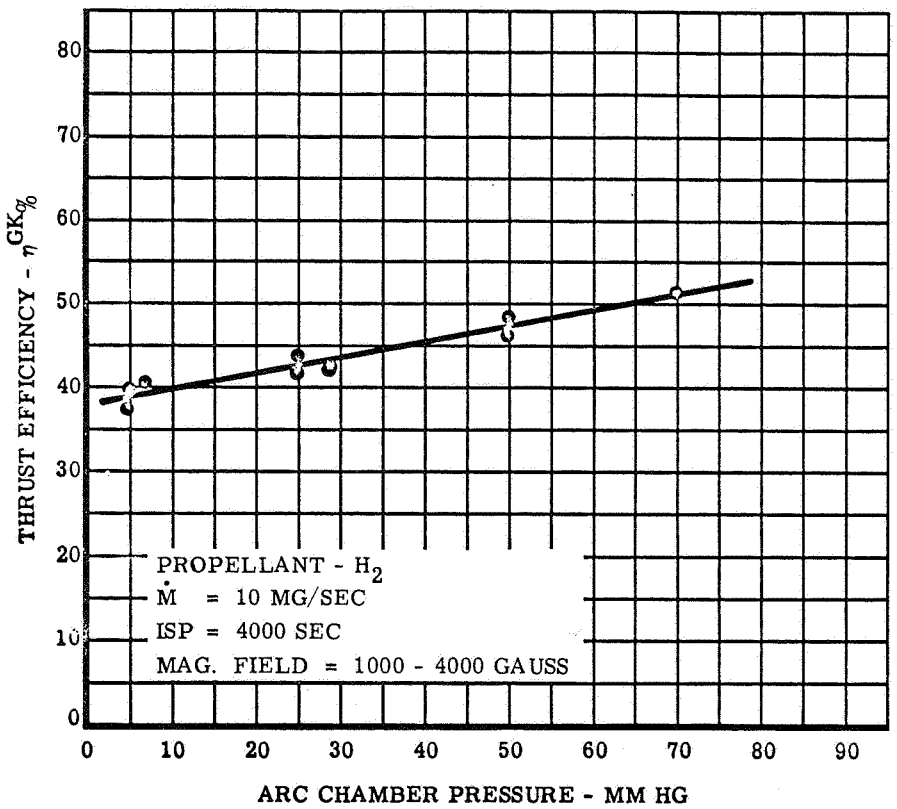

Figure 113. Thrust Efficiency Versus Arc Chamber Pressure for Thermo-Ionic Thrustor Using H_2 Propellant

2.2.5 Effect of Power, Current and Voltage on Efficiency

If the thermo-ionic thrustor is considered as a thermal energy exchanger the various efficiencies might well remain unchanged if currents and voltages are changed while their product the power remains constant. Many tests which we carried out show this to be approximately the case. A variation of current and voltage at constant power may be obtained by changing certain arc parameters. For example, it is possible to vary the voltage by changing the geometry, mass flow, propellant types and by changing the strength of the external magnetic field.

Figure 114 shows an average dependence of the thermal efficiency in power input without consideration of the variation of other parameters. It is seen that a slight improvement in efficiency is obtained with the increase of the power input. Coming to a more selective average, Figure 115 shows the variation of the thermal efficiency with variation of the anode energy flux density in the throat plotted without considering the variation of other parameters. The plot shows that the thermal efficiency increases slightly with the increase of power input and with the energy flux density (reducing still further the limits of the average). Figure 116 shows the variation of the thermal efficiency as a function of the power input when the specific impulse is kept fairly constant in all the tests. Figure 117 shows the variation of the efficiency with the total power in the gas at various specific impulses using hydrogen as a propellant. It is evident that the thermal efficiency increases slightly with the power with a more pronounced increase at higher specific impulses.

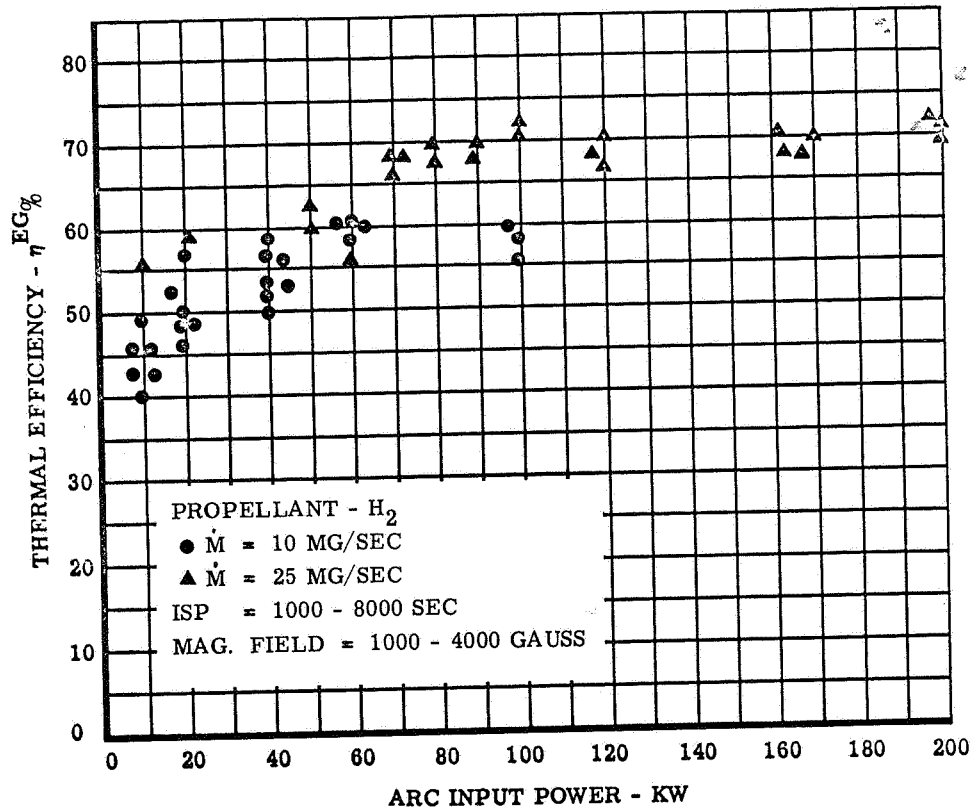

Figure 114. Thermal Efficiency Versus Arc Input Power for Thermo-Ionic Thrustor Using H_2 Propellant

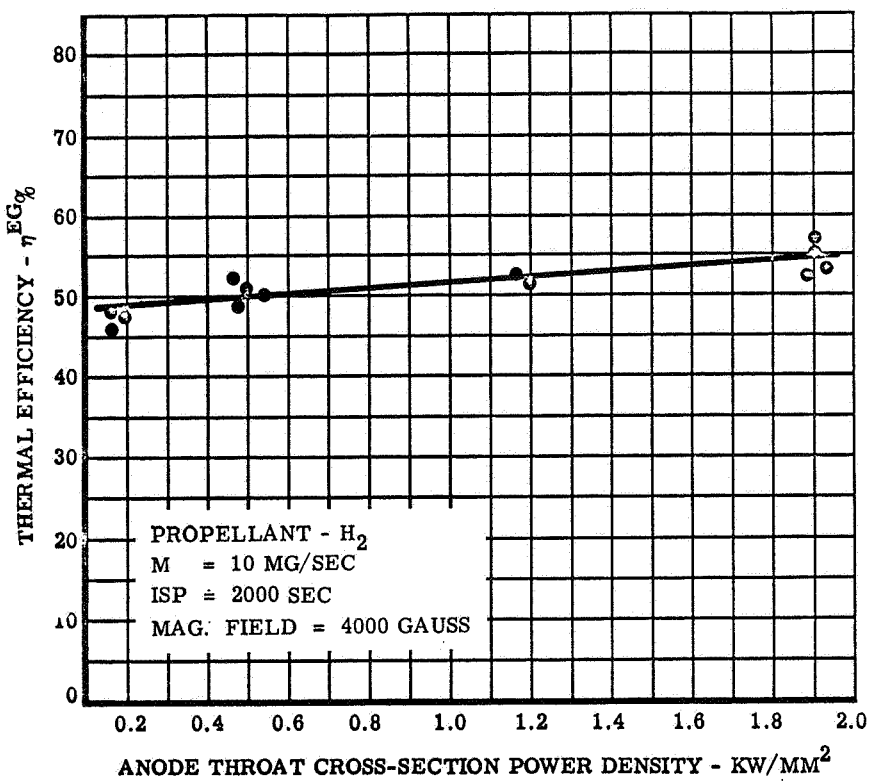

Figure 115. Thermal Efficiency Versus Power Density in Throat Cross-Section for Thermo-Ionic Thrustor Using H_2 Propellant

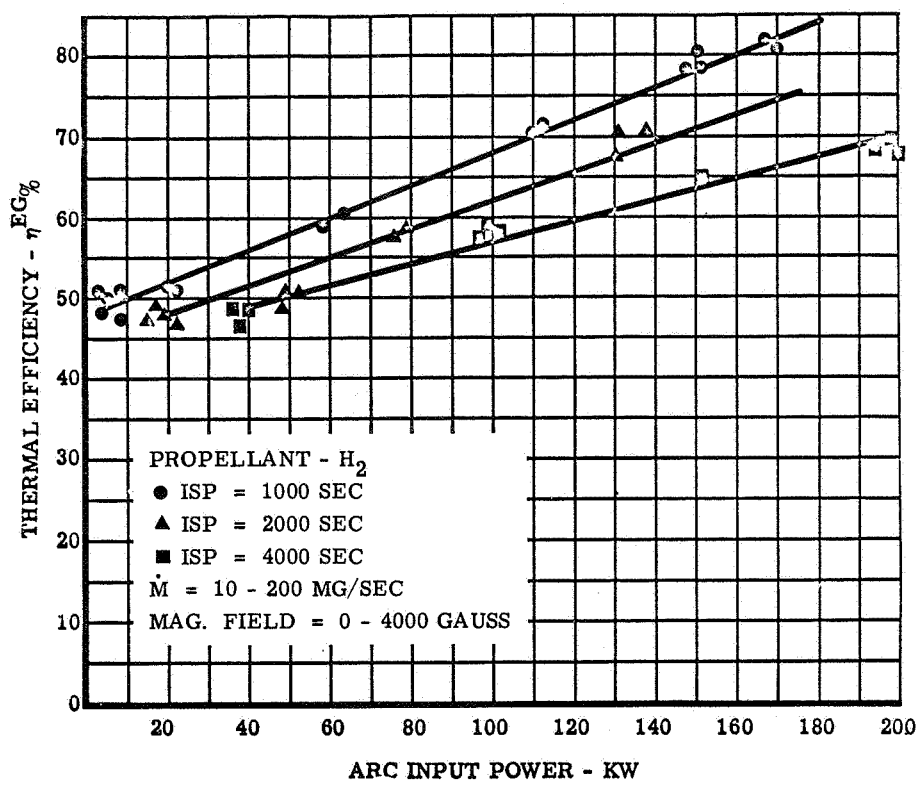

Figure 116. Thermal Efficiency Versus Arc Input Power at Constant Isp for Thermo-Ionic Thrustors Using H_2 Propellant

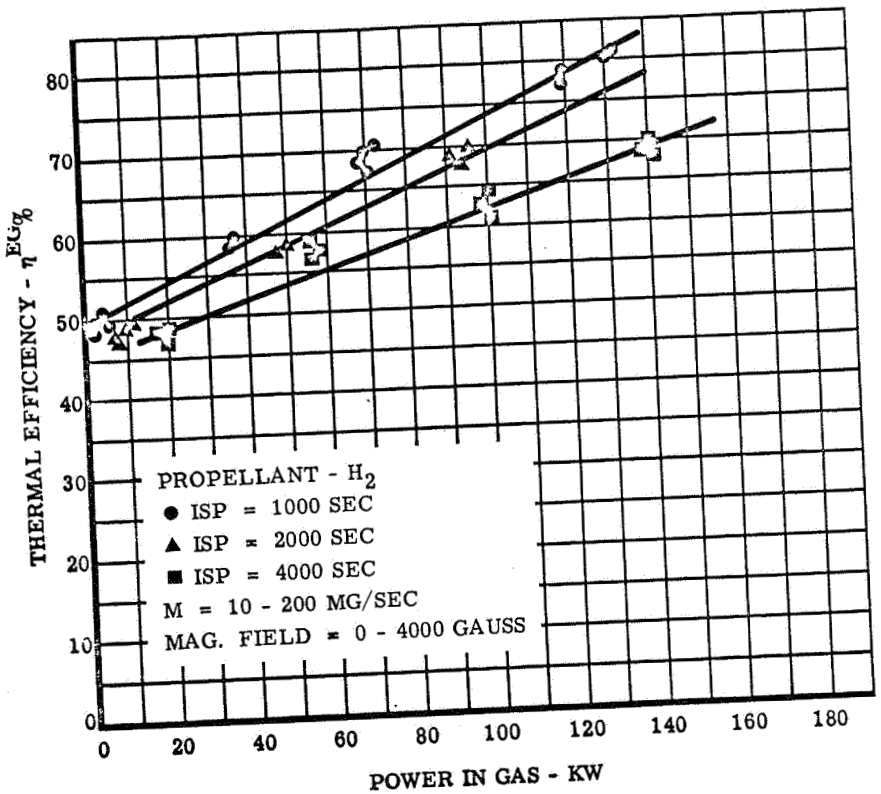

Figure 117. Thermal Efficiency Versus Power in Gas at Constant Isp for Thermo-Ionic Thrustor Using H_2 Propellant

Another average along the same lines is presented in Figure 118 which shows the thermal efficiency versus power input. It is interesting to note that the thermal efficiency displays the usual slight increase with power, in this case the increase is slightly more pronounced at higher specific impulses. Figure 119 shows the same dependence of thermal efficiency on power for deuterium as was seen for hydrogen. Figure 120 presents data for lithium, showing the variation of efficiency as a function of the total input power. Figure 121 shows the same variation for potassium and it is evident that a slight increase in efficiency is obtained as the power increases and that the rate of improvement increases toward the higher powers. Thus our measurements show that the thermal efficiency depends on power in about the same way for hydrogen, deuterium and the two alkali metals tested. Figures 122 through 125 show the variation of current and voltage over wide ranges at constant power obtained by changing such things as geometry, mass flow, pressure, and magnetic field strength. Figure 122 shows a variation of voltage obtained by changing the throat diameter at various external magnetic fields. It is interesting to note the larger change in voltage with throat diameter at higher magnetic field strengths (see also Sections 2.2.6 and 2.3.6). The arc current follows an opposite pattern, decreasing with the increase of the throat diameter (see Figure 123). Figure 124 shows an average of thermal efficiency measurements as a function of current. Note that the thermal efficiency slightly increases with increasing current. Figure 125 shows that the reverse is true for an increase in voltage. Figure 126 shows the variation of the thrust (η^{gk}) efficiency obtained by changing the operating current at constant mass flow,

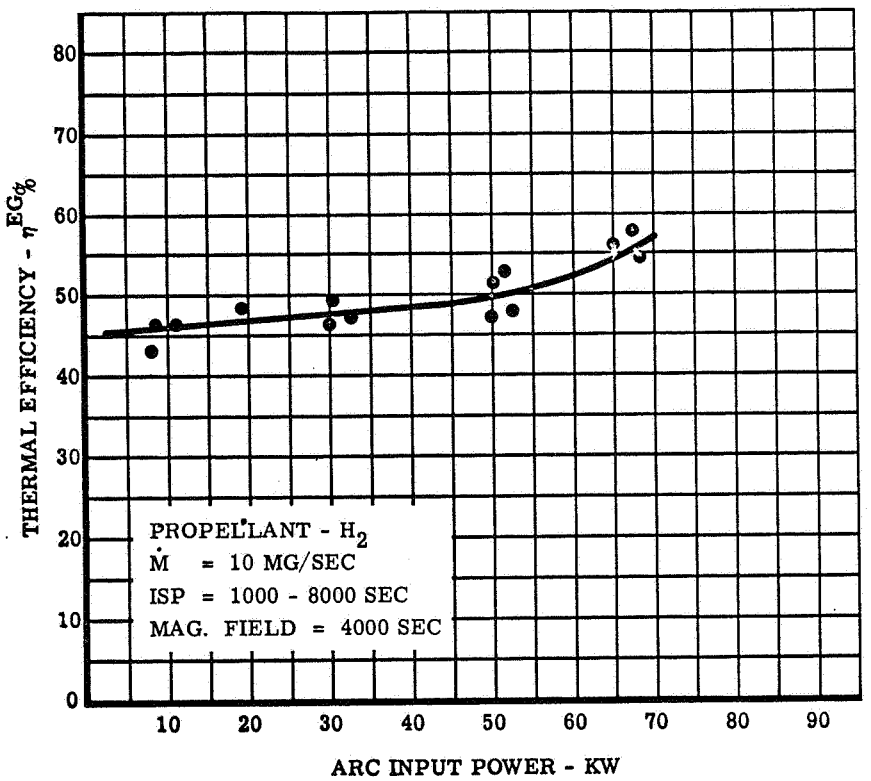

Figure 118. Increased Rate of Change in Thermal Efficiency With Increased Arc Input Power at Constant Propellant Mass Flow Using Hydrogen

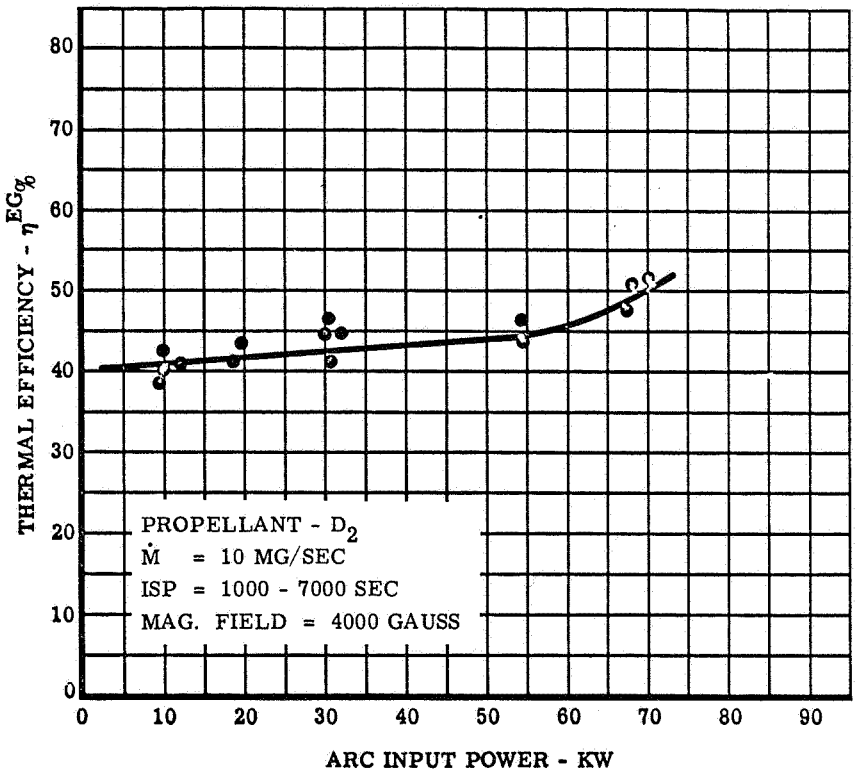

Figure 119. Increased Rate of Change in Thermal Efficiency With Increased Arc Input Power at Constant Propellant Mass Flow Using Deuterium

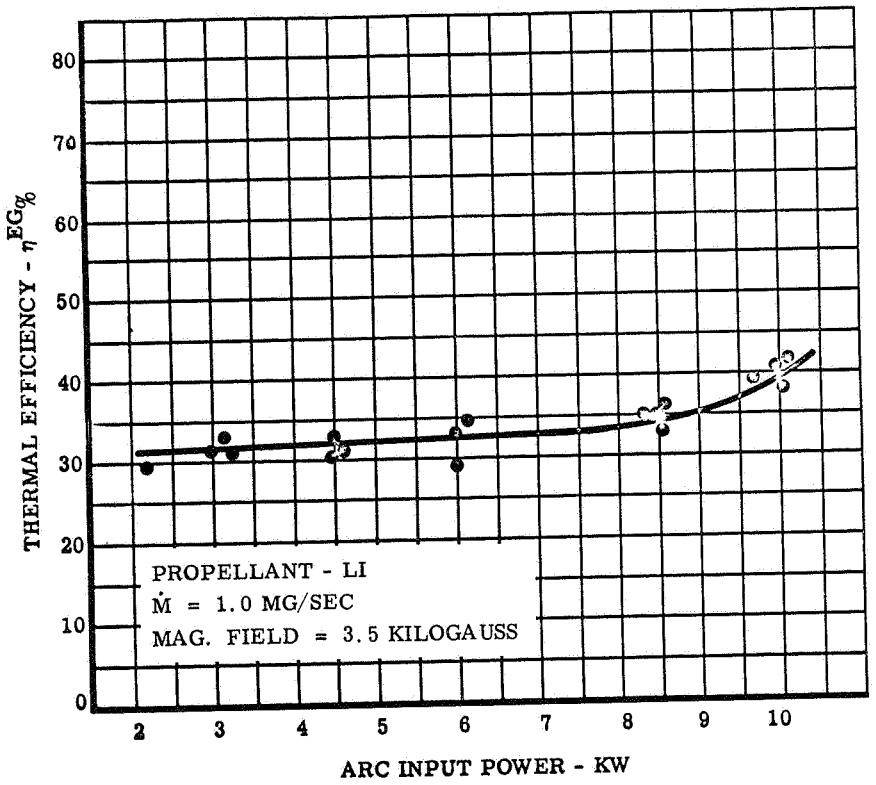

Figure 120. Increased Rate of Change in Thermal Efficiency With Increased Arc Input Power at Constant Propellant Mass Flow Using Lithium

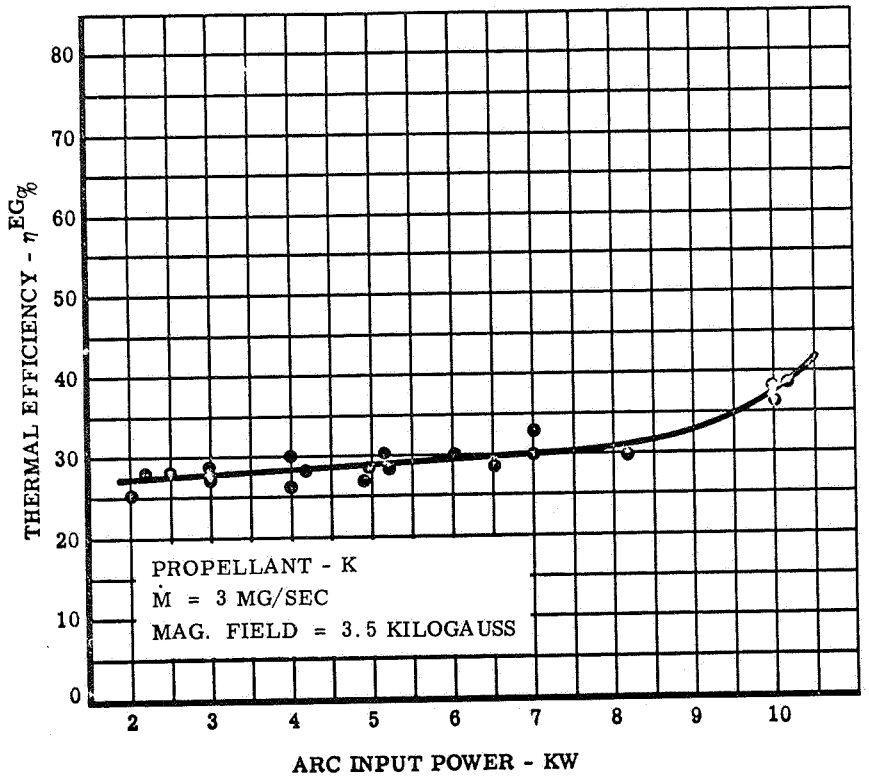

Figure 121. Increased Rate of Change in Thermal Efficiency With Increased Arc Input Power at Constant Propellant Mass Flow Using Potassium

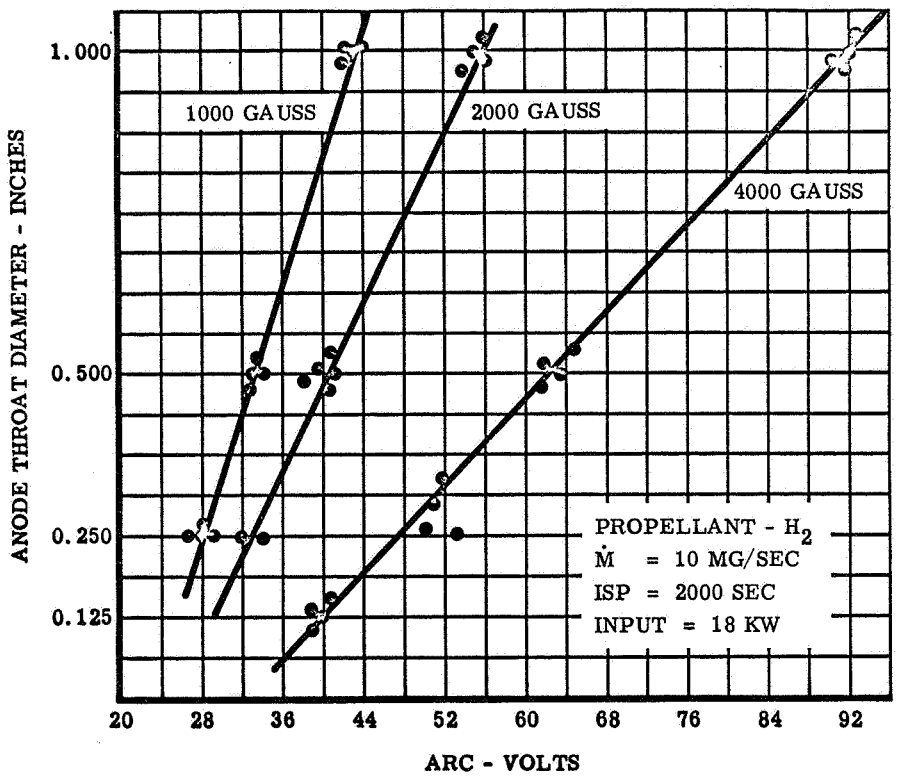

Figure 122. Variation of Arc Voltage at Different Throat Diameters and Magnetic Fields and Constant Input Power

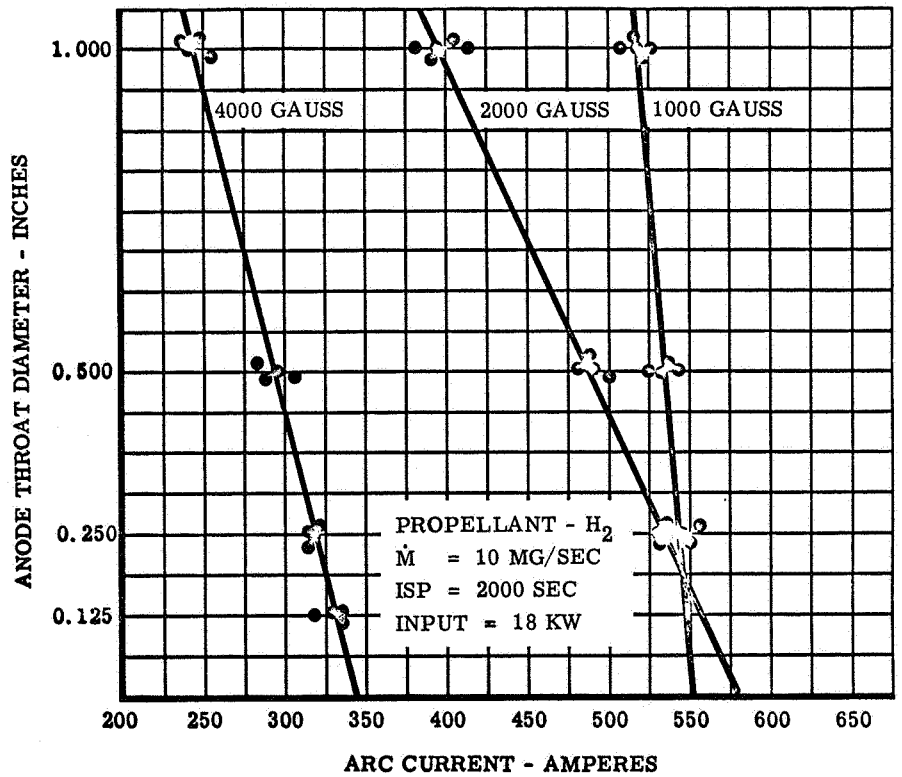

Figure 123. Variation of Arc Current at Different Throat Diameters and Magnetic Fields and Constant Input Power

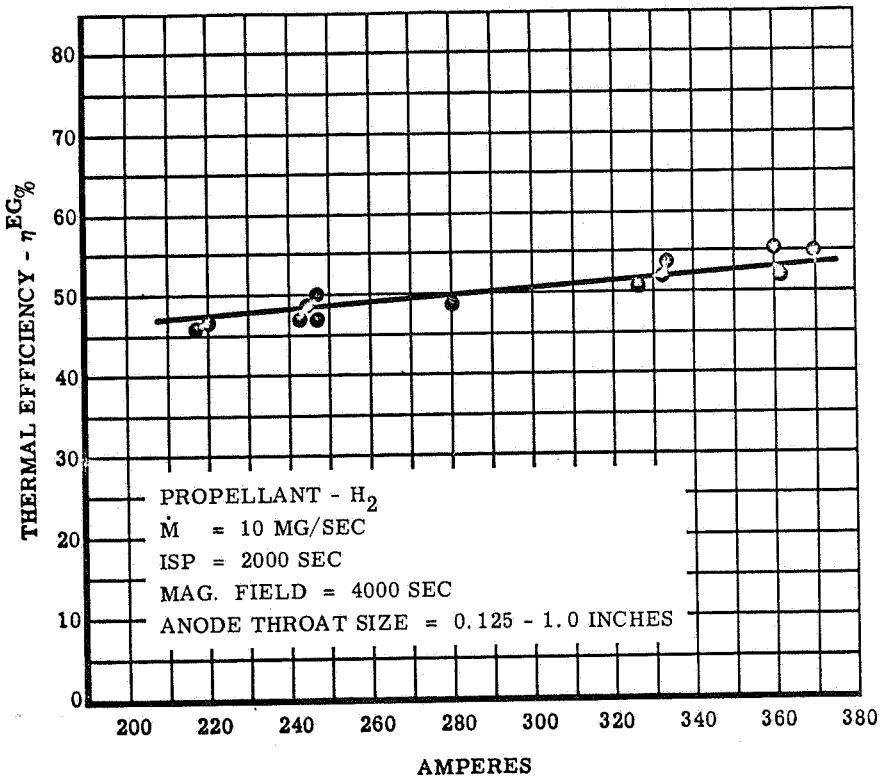

Figure 124. Thermal Efficiency Versus Arc Current Using H_2 at Constant Specific Impulse, Mass Flow Rate and External Magnetic Field

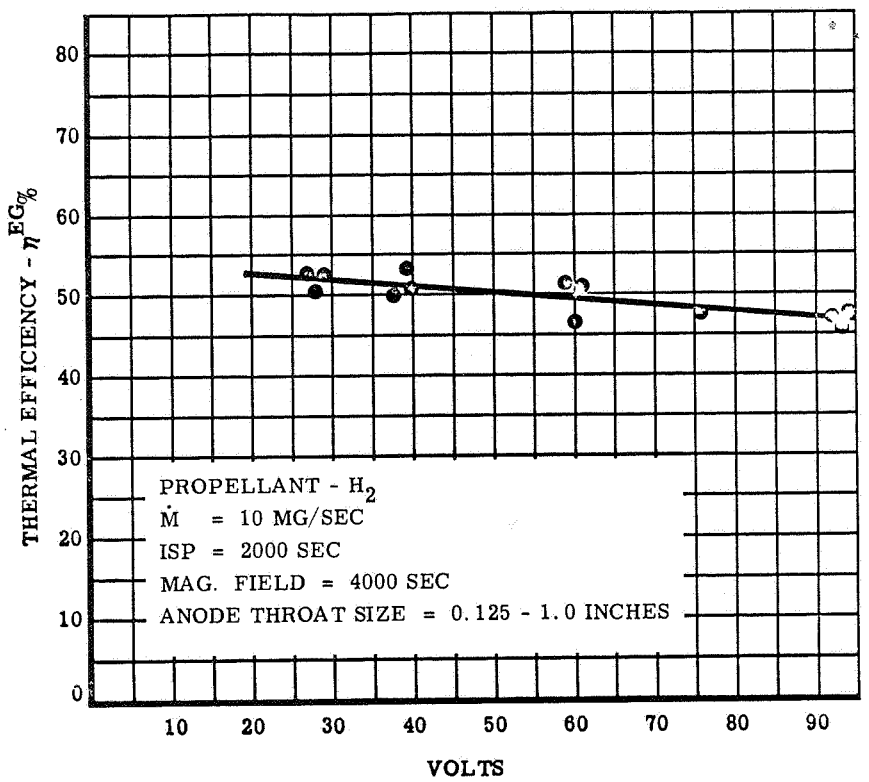

Figure 125. Thermal Efficiency Versus Arc Voltage Using H_2 at Constant Specific Impulse, Mass Flow Rate and External Magnetic Field

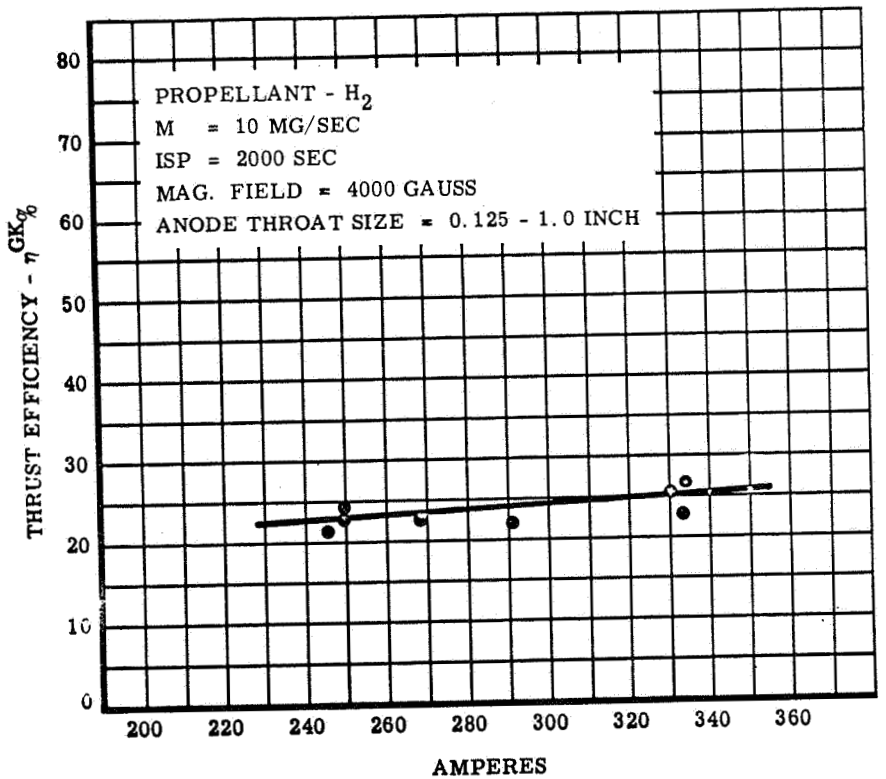

Figure 126. Thrust Efficiency Versus Arc Current for H_2 at Constant Power, Mass Flow Rate and Magnetic Field

specific impulse and magnetic field. Again a very slight increase of the efficiency with increasing current is noted. Figure 127 shows a similar but opposite effect, i.e., a light reduction in thrust efficiency with the increase of voltage. Figures 128 and 129 show the effect in the overall efficiency (η^{ek}) when current and voltage are changed.

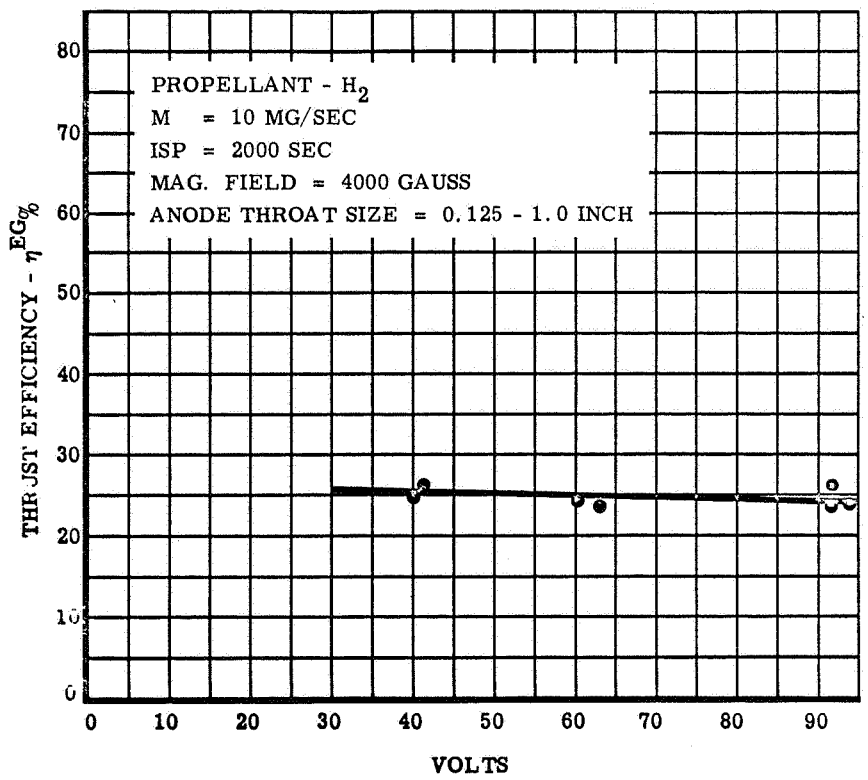

Figure 127. Thrust Efficiency Versus Arc Voltage for Hydrogen at Constant Power, Mass Flow Rate and Magnetic Field

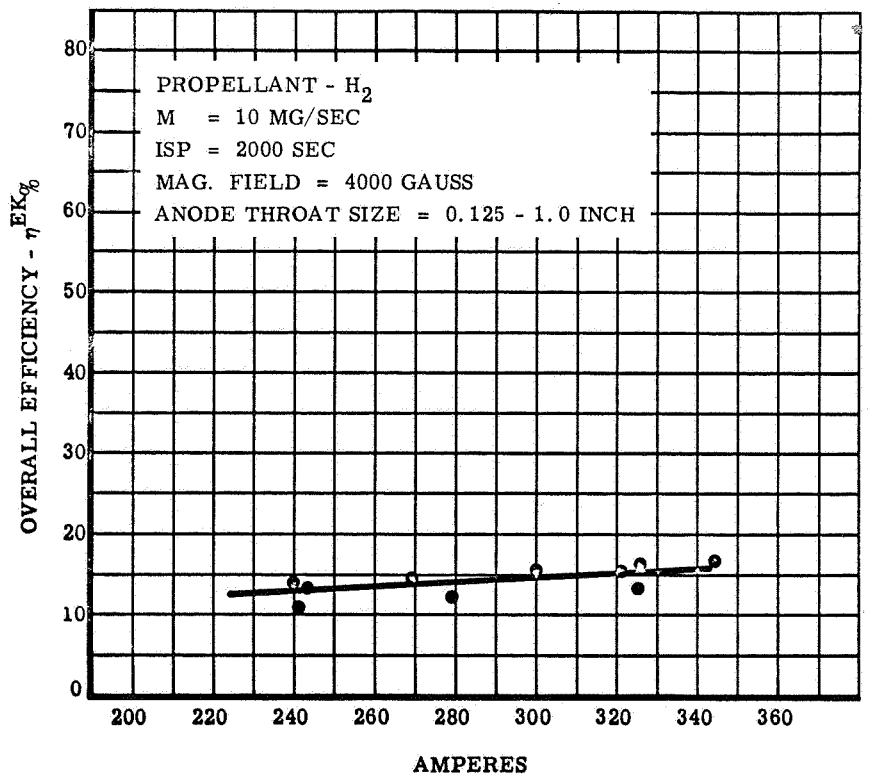

Figure 128. Overall Efficiency Versus Arc Current for Hydrogen at Constant Power, Mass Flow Rate and Magnetic Field

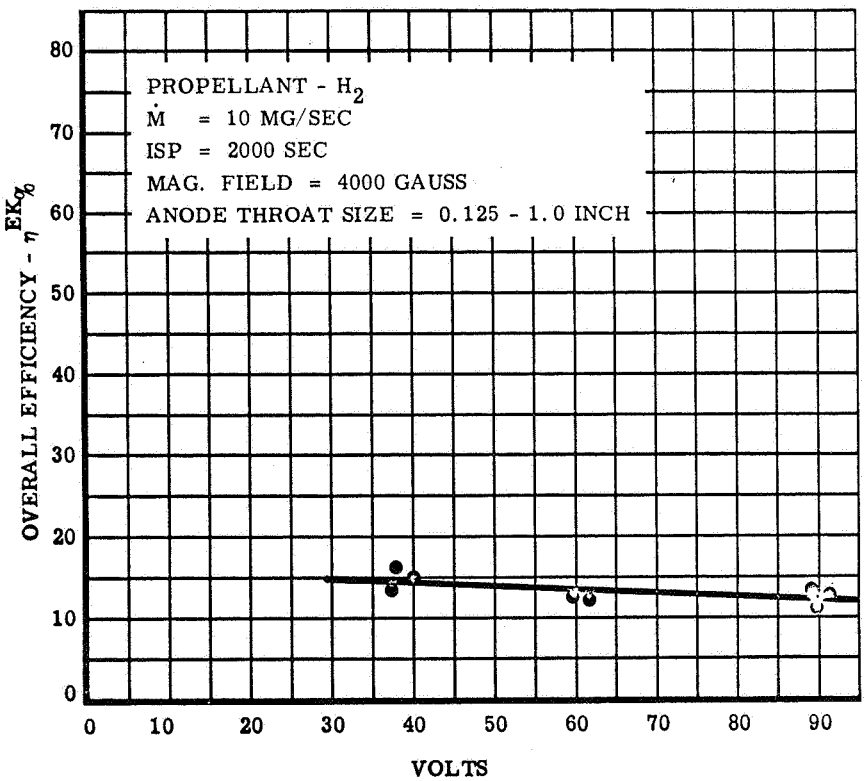

Figure 129. Overall Efficiency Versus Arc Voltage for Hydrogen at Constant Power, Mass Flow Rate and Magnetic Field

2.2.6 Effect of External Magnetic Field on Efficiency

As described in Section 2.1.6, the initial results for thermo-ionic systems were obtained with very high arc currents and without the use of any external magnetic field. During the life tests it was found that most of the electrode damage was due to the stabilization of the anode arc foot at a single small spot, with resulting excessive power density. The use of a small external magnetic field, resulting in a rotation of the anode spot, cured the malfunction. During successive tests higher fields were used to study their affect on the life and efficiency of the thrustors. Recently field strengths of over 10,000 gauss were applied. The effects on life have been described in Section 2.1.6. In this section we will report only on the effect of field strength on the efficiencies. It has been found that the most conspicuous effect of changing the intensity of the external magnetic field is a change in the voltage to current ratio at constant input power. The ratio increases with increasing throat diameter (lower arc chamber pressure) and can be varied at will over a relatively wide range by a proper choice of throat diameter and magnetic field strength. With present thrustor designs there seems to be no significant variation in efficiency (thermal or kinetic) obtained by changing the field intensity from 1000 to 10,000 gauss. This apparent insensitivity to the field strength may, of course, result from offsetting effects caused by changes in the current or other important parameters with the increase of the field. Future tests are planned where the current and power will remain unchanged as the magnetic field is varied, in order to detect changes in the various efficiencies.

However, the requirements in cost and power of a strong external magnetic field do not seem justified from the results obtained to date.

During this program a variety of external coils were built to produce a magnetic field of gradually increasing intensity. These are described in the quarterly reports.[7, 8] The last coil used is made of thick copper tubing with 32 turns and reaches 16 kilogauss at 3500 amperes. Figure 130 is a photograph of this coil as assembled on the thermo-ionic thrustor while Figure 131 is a graph of field to current relationship. Normally the field intensity is fixed during a full series of tests, but sometimes the field is varied during the measurements, the desired strength being set with the aid of a direct reading gaussmeter. Any force on the thrust stand due to this magnetic field is detected and eliminated leaving only an extremely small residual force which is magnetically compensated. A description of other details of the measurements (including the external magnetic field) can be found in Section 2.3.6. The most conspicuous effect of varying the magnetic field intensity is a change in the voltage current ratio at constant input power as illustrated in Section 2.2.5. To analyze the effect of the pure external magnetic field without this attendant change in the voltage, other parameters (as the geometry) must be changed at the same time. This has not been done during the present program but deserves further attention. Figure 132 shows the variation of the thermal efficiency as a function of the magnetic field intensity for various throat sizes and a single specific impulse. Figure 133 shows the same variation for various specific impulses and a single throat size. The measurement of the influence

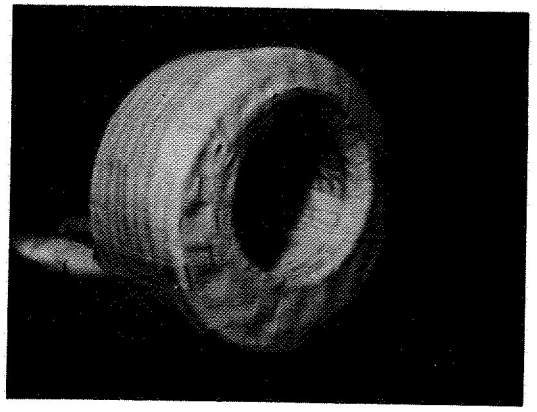

Figure 130. Photograph of Water-Cooled 32 Turn External Magnetic Field Coil Used During Testing

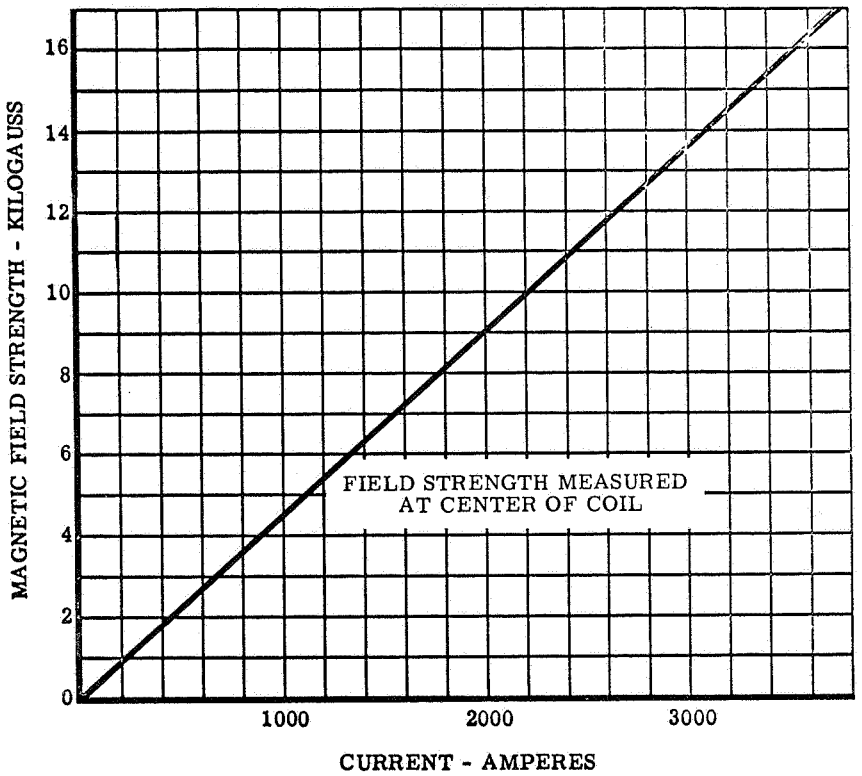

Figure 131. Magnetic Field Strength Versus Coil Current for External Field Coil Used During Testing

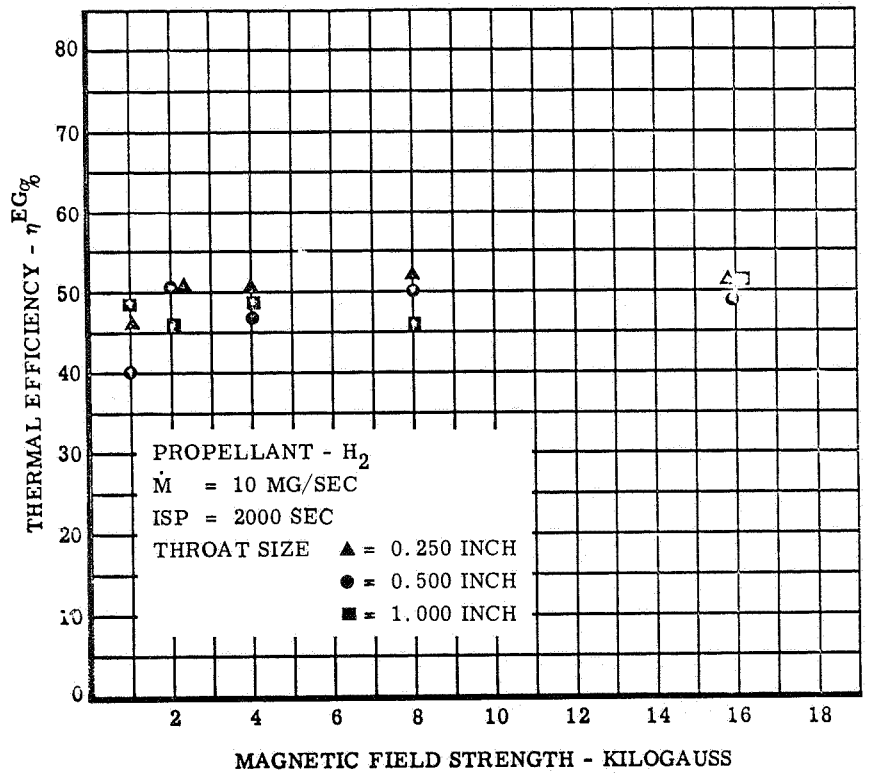

Figure 132. Thermal Efficiency Versus External Magnetic Field Strength for H_2 at Various Anode Throat Diameters and Constant Isp

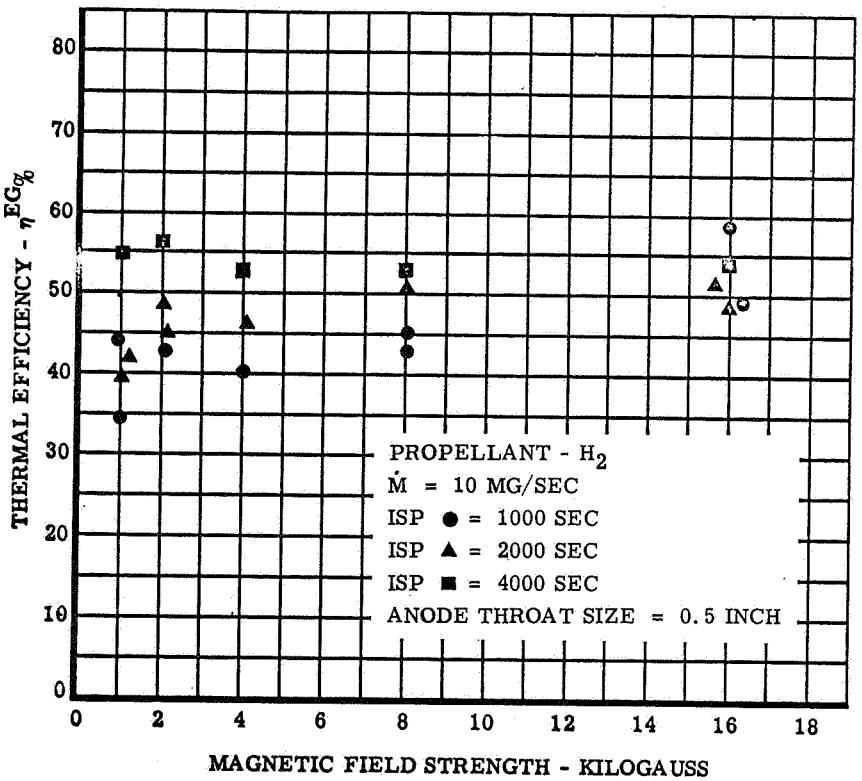

Figure 133. Thermal Efficiency Versus External Magnetic Field Strength for H_2 at Various Specific Impulse Levels and Constant Anode Throat Diameter

of the external magnetic field on the thrusting efficiency is more difficult because any parasitic influence must be eliminated (see Section 2.3.6). Figure 134 shows the results of a series of measurements where the specific impulse was kept constant while the magnetic field strength was varied. The field strength covers a range from 1 to 16 gauss. Figure 135 is very similar except that the throat diameter was kept constant for two specific impulses. From this series of tests and from the results of many others, it appears that the influence of the external magnetic field on both the thermal and the thrust efficiency is slightly beneficial but extremely small (as reported in Section 2.1.6, the effect of the magnetic field is very important for improving the life characteristics). Figures 136 and 137 show the effect of the external magnetic field on thermal and thrust efficiency using deuterium as a propellant.

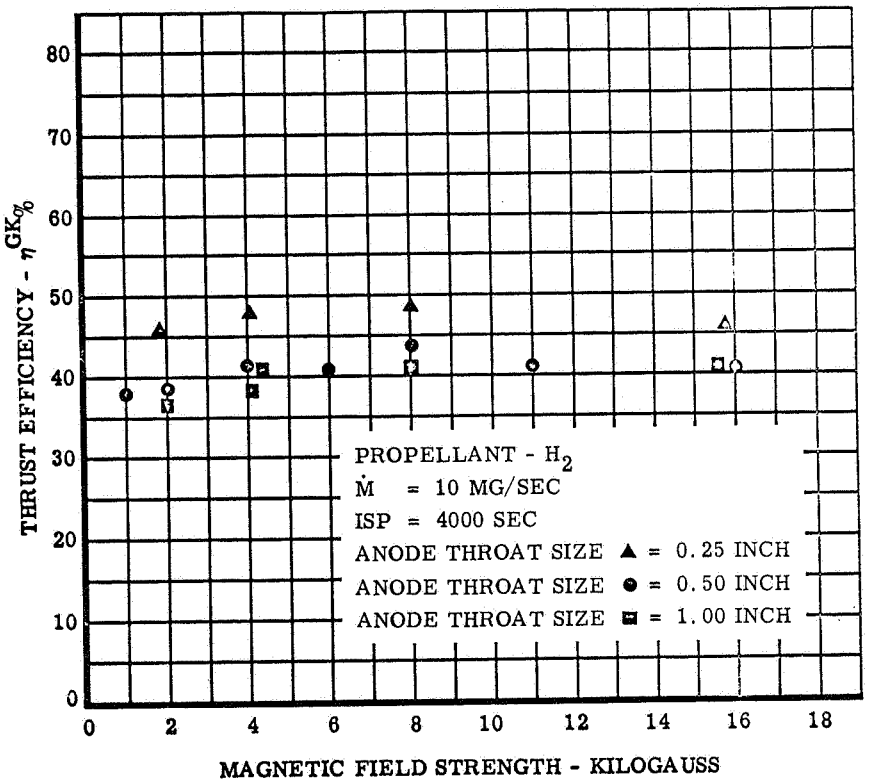

Figure 134. Thrust Efficiency Versus External Magnetic Field Strength for H_2 at Various Anode Throat Diameters and Constant Isp

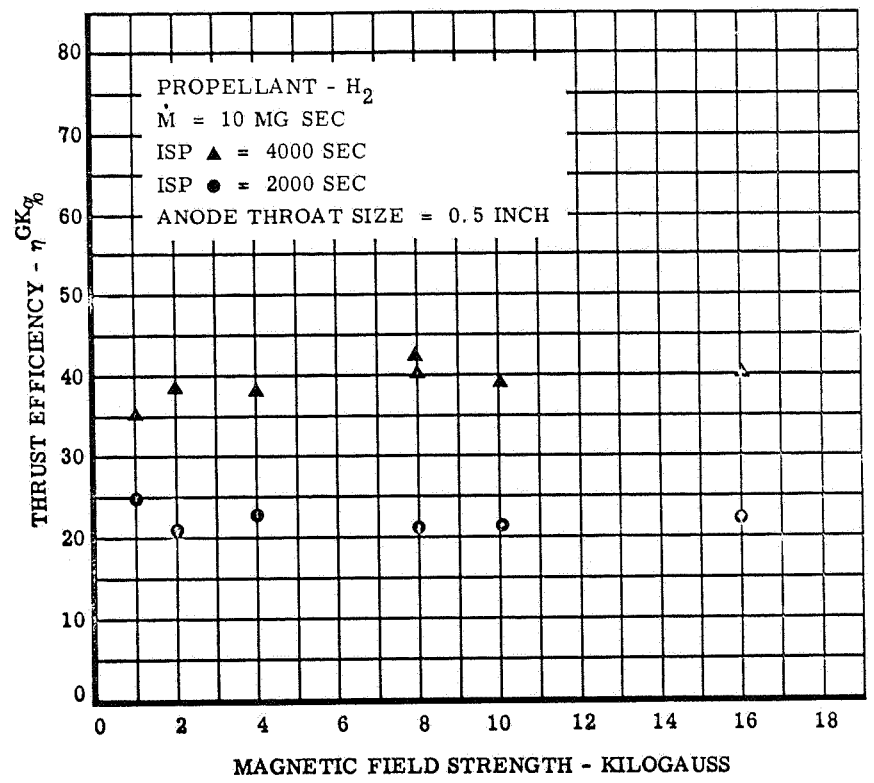

Figure 135. Thrust Efficiency Versus External Magnetic Field Strength for H_2 at Two Specific Impulse Levels and Constant Anode Throat Diameter

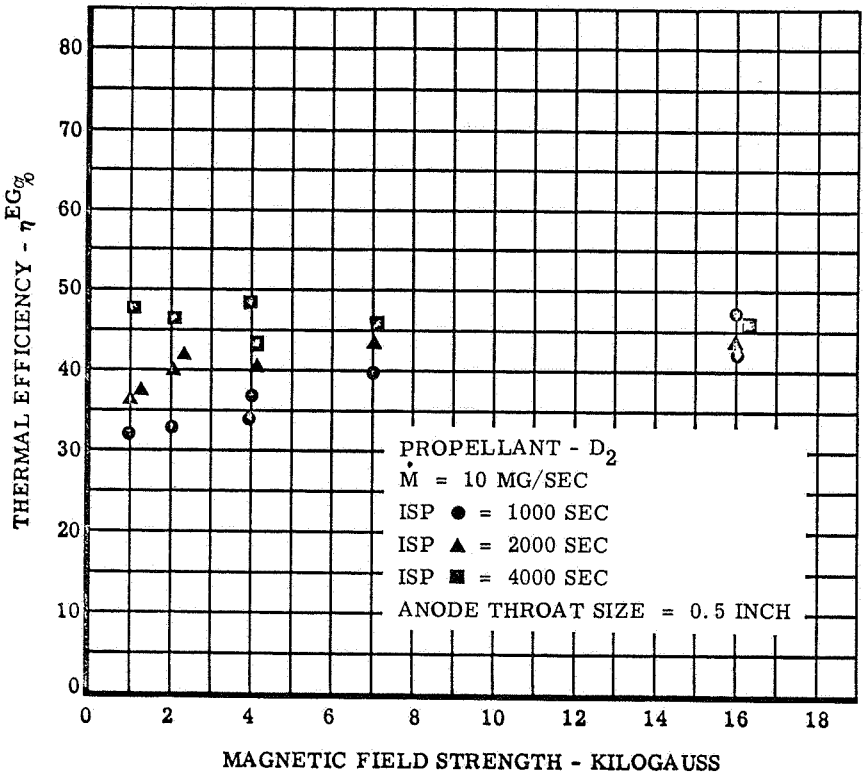

Figure 136. Thermal Efficiency Versus External Magnetic Field Strength for D_2 at Various Specific Impulse Levels and Constant Anode Throat Diameter

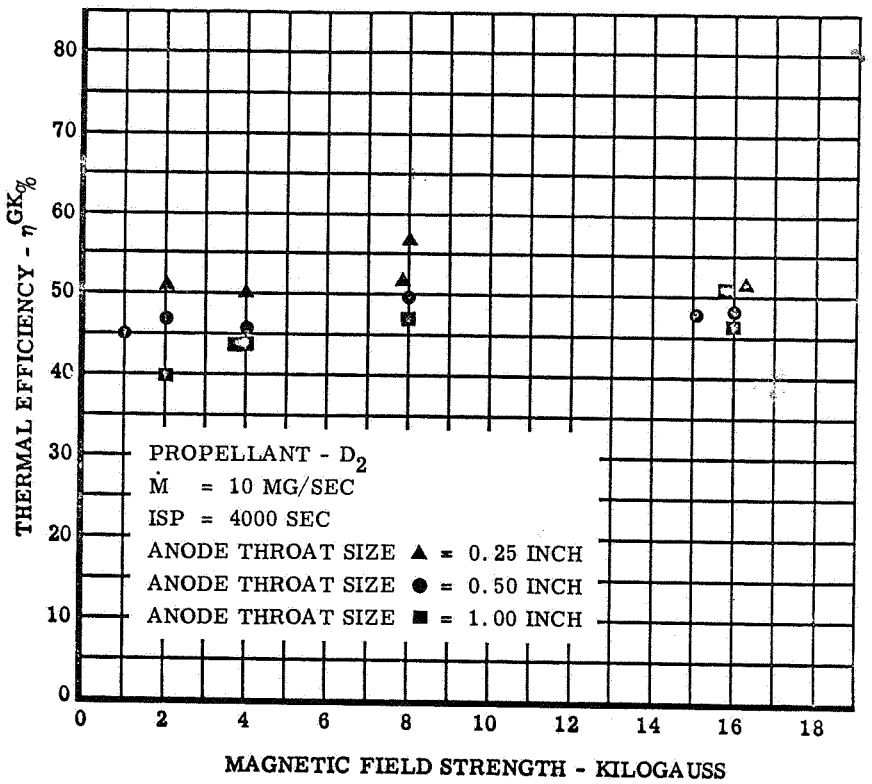

Figure 137. Thrust Efficiency Versus External Magnetic Field Strength for D_2 at Various Anode Throat Diameters and Constant Isp

2.2.7 Effect of External Environment on Efficiency

The external environment, i.e., the ambient conditions surrounding the thrustor, has a significant effect on performance characteristics. We have already discussed the effect of the environment on life in Section 2.1.7. The study of the effects of the external environment on the efficiency is still more important, and is concerned with the elimination of anomalies in the measurements as well as the improvement of performance characteristics (see Section 2.3.7). As in the case of life, we must consider two environmental regimes, each having its own affect on performance characteristics. The first is the simulated condition available in our laboratories which as said in 2.1.7 is very far from a perfect simulation of space. The second is the real space condition that (at least for the moment) is not available and can be evaluated only through calculations. The first condition is given the most consideration here while a limited number of references are discussed for the second condition. The propelling functions of the thermo-ionic thrustor extend outside the thrustor proper and along the plasma jet that emanates from it. This is the main reason for the importance of the space surrounding the jet. Until space tests become possible, the simulated space environment on earth must be used and improved to obtain the best results. This is not a simple task, especially in consideration of the primitive facilities available for these tests. A few facilities with better capabilities are already in existence but are rarely available for these experiments, and then only for a very limited time. Figure 138 shows the vacuum chamber used for the very first tests with thermo-ionic thrustors. Its dimensions (as illustrated) are relatively small. The

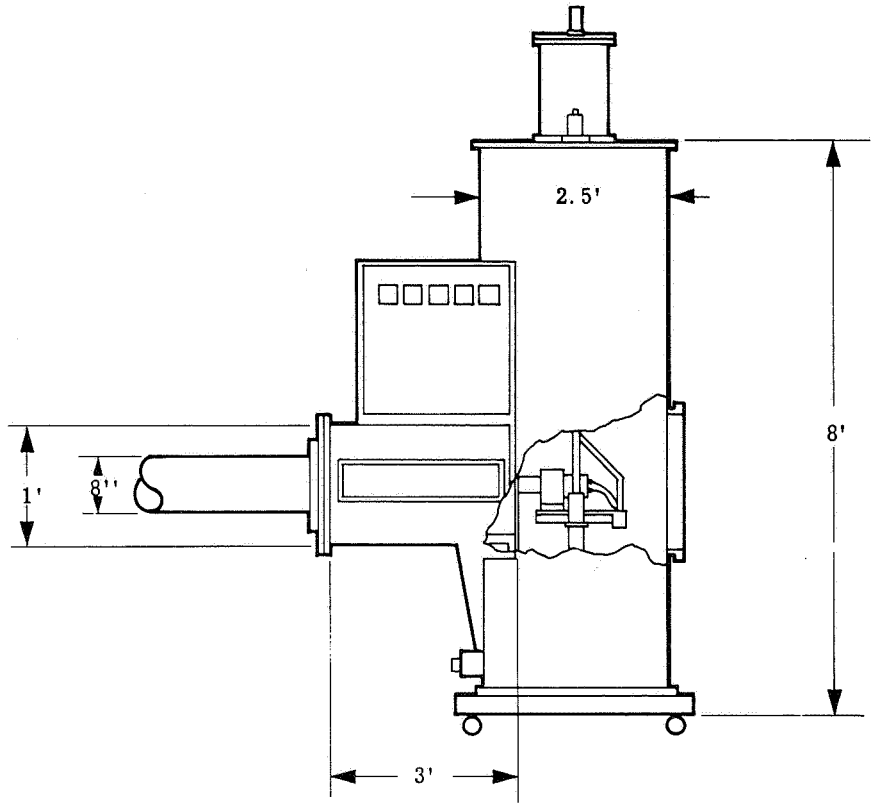

Figure 138. Dimensions of Vacuum Chamber With Thrust Stand Used During Early Experiments With Thermo-Ionic Thrustor

material is carbon steel and complete water cooling is used throughout. The operating pressure in this chamber was between 0.1 and 0.3 Torr with a pumping capacity of about 4000 liters per second. No electrical insulation was provided for the internal walls. A second environmental tank, which was used for the continuation of the tests, is illustrated in Figure 139. The inside diameter is increased, but much of the tank is still made of carbon steel without insulation. The internal walls are thoroughly water-cooled. The access flange (shaded in the picture) is made of aluminum to reduce interaction effects with the magnetic field coil. The operating pressure in this chamber is between 0.01 and 0.05 Torr with a pumping capacity of about 4500 liters per second. The improvement in the reduction of the operating pressure has been obtained with elimination of most of the leakage, increase of the diameter and reduction of the length of the connecting lines. The environmental facilities used by other laboratories for conducting similar studies are illustrated in Figures 140 and 141. Both are made of metal without insulation for the internal walls. Pumping capacities range from 4000 to 400,000 liters per second resulting in testing pressures from 0.05 to 0.0001 Torr at very low mass flows. During the program the need for a tank with sufficient dimensions to largely eliminate the influence of the walls on the thrustor was strongly felt, and was the need for a layer of insulation to avoid possible discharges to the walls. A tank of this type has been designed (Figure 142) but not constructed for economic reasons. Another tank constructed exclusively of insulating material has been designed and is in the process of being constructed for the conduction of further tests in the near future (Figure 143). Figure 144 shows the dimensions of the first vacuum tank made exclusively of insulating materials

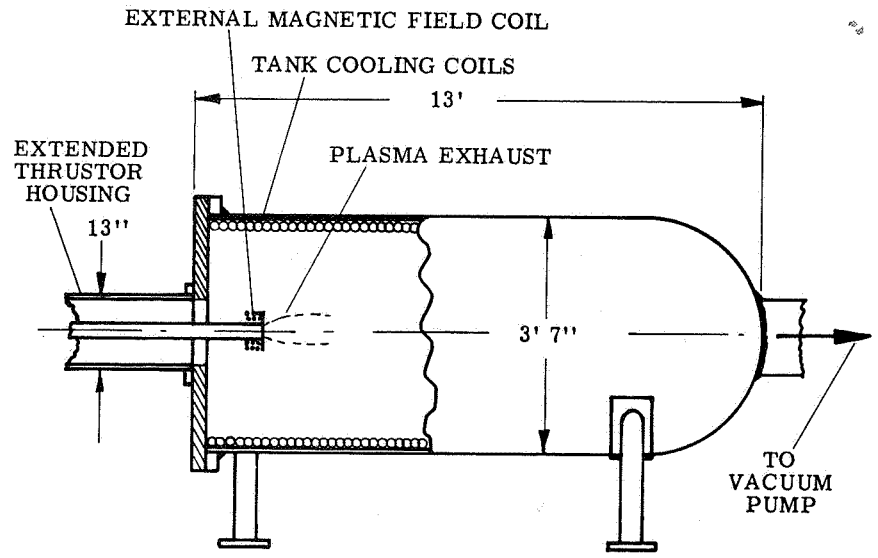

Figure 139. Enlarged Vacuum Tank Used During Most of the Experimental Investigation

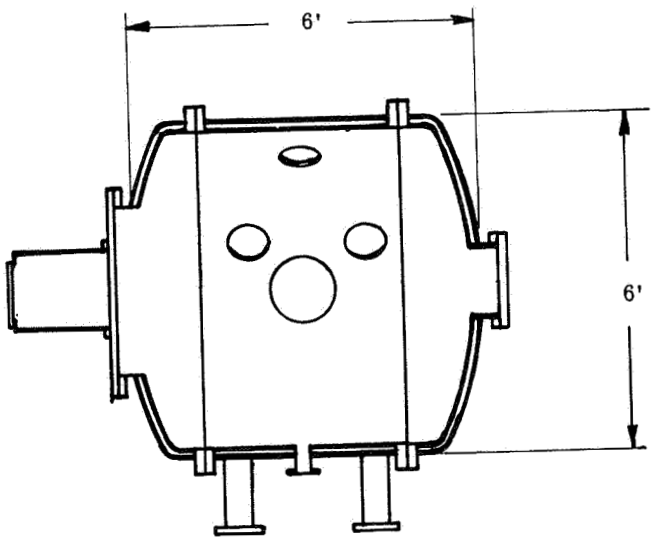

Figure 140. Vacuum Chamber Used at the Electro-Optical Systems Inc. Laboratory[4]

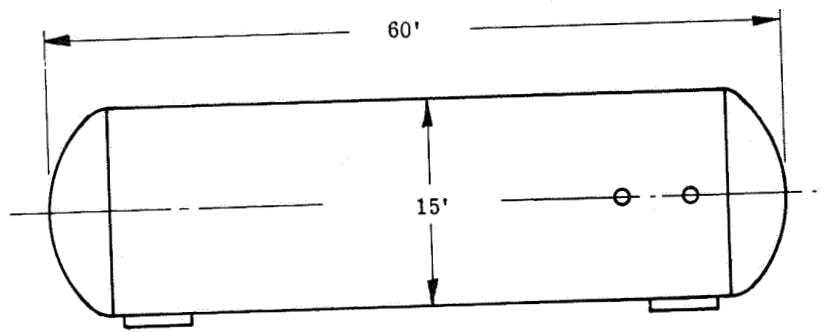

Figure 141. Large Vacuum Test Tank Used at NASA Lewis Laboratories

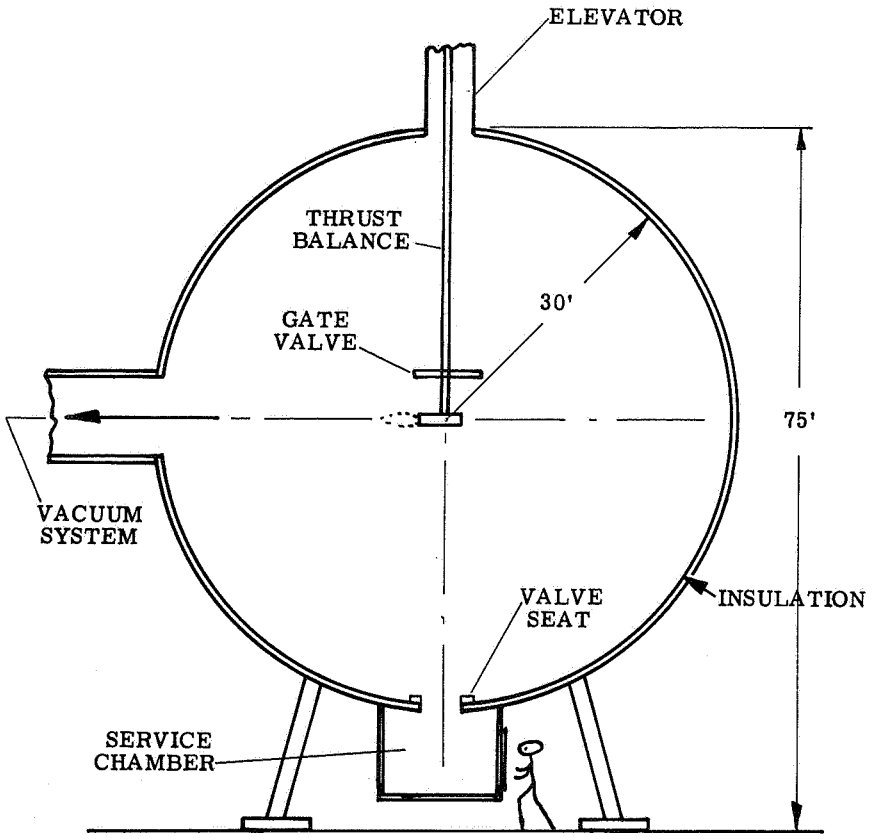

Figure 142. Design of Very Large Metal Vacuum Tank Lined With Insulation for Future Experiments

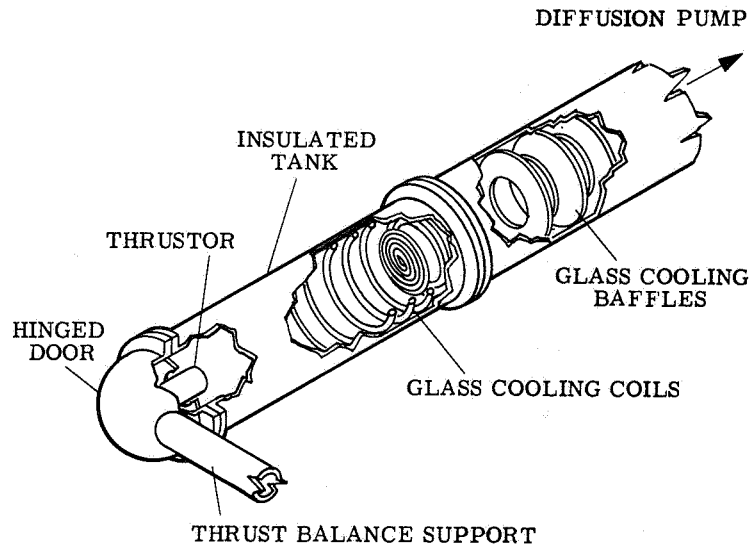

Figure 143. Design of High Vacuum Test Facility Constructed Entirely of Insulating Materials

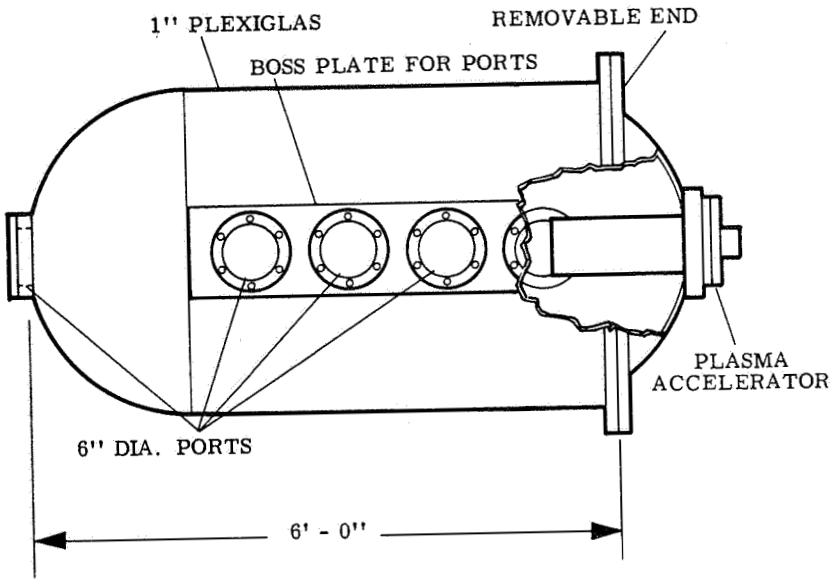

Figure 144. Dimension of High Vacuum Chamber Constructed of Plexiglas at Princeton University[9]

constructed and tested at Princeton University.[9] For preliminary experiments on the behavior of the plasmajet interaction with the walls a refractory insulating lining has been inserted in the regular metal tank of Figure 139 (see Figure 145).

Ideally, the study of the effect of environmental conditions on the thermal and thrust efficiency would compare performance obtained in the laboratory environmental conditions with those of real space. Until this is possible, the effects of minor variations can be compared to detect symptoms and tendencies capable of providing some information. Some simple tests that can be attempted include effects of the following: change of the dimensions of the testing chamber, change of the pressure, change of the residual gas, and change of the material (metal or insulator) of the chamber. We have done some extensive work with the first two variations and some with the third. No attempt has been made to date to test the effect of a chamber made totally of insulating material (except preliminary experiments with the lining of Figure 145). Figure 146 shows that the variation of the thermal efficiency with the dimensions of the testing chamber cannot be discerned from the spread of the data. Figure 147 shows a similar trend for the overall efficiency. However, a decrease in overall efficiency with the increase of the testing chamber dimensions, especially at very low pressures, has been observed by other laboratories. Specifically, a test conducted in the tank of NASA Lewis Research Center of Figure 141 with a diameter of 15 feet and length of 60 feet showed a reduction in thrust of about 40 percent compared with tests at another laboratory.[10] The

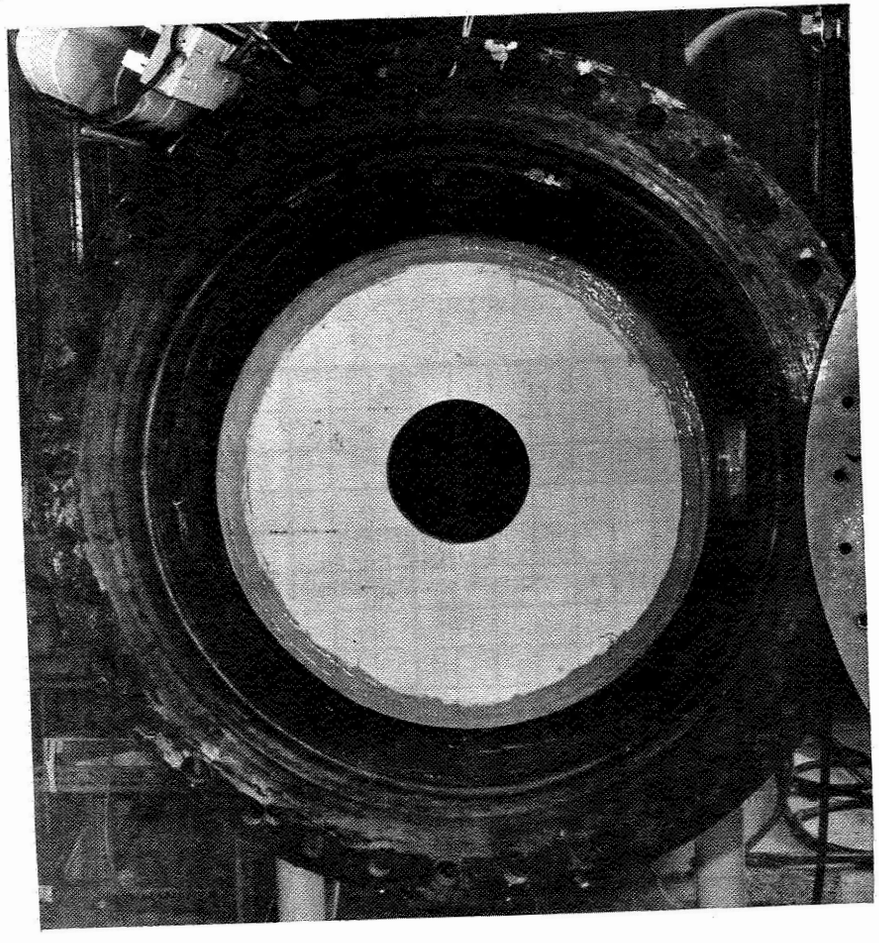

Figure 145. Photograph of Metal Vacuum Tank With Insulating Refractory Lining for Preliminary Experiments

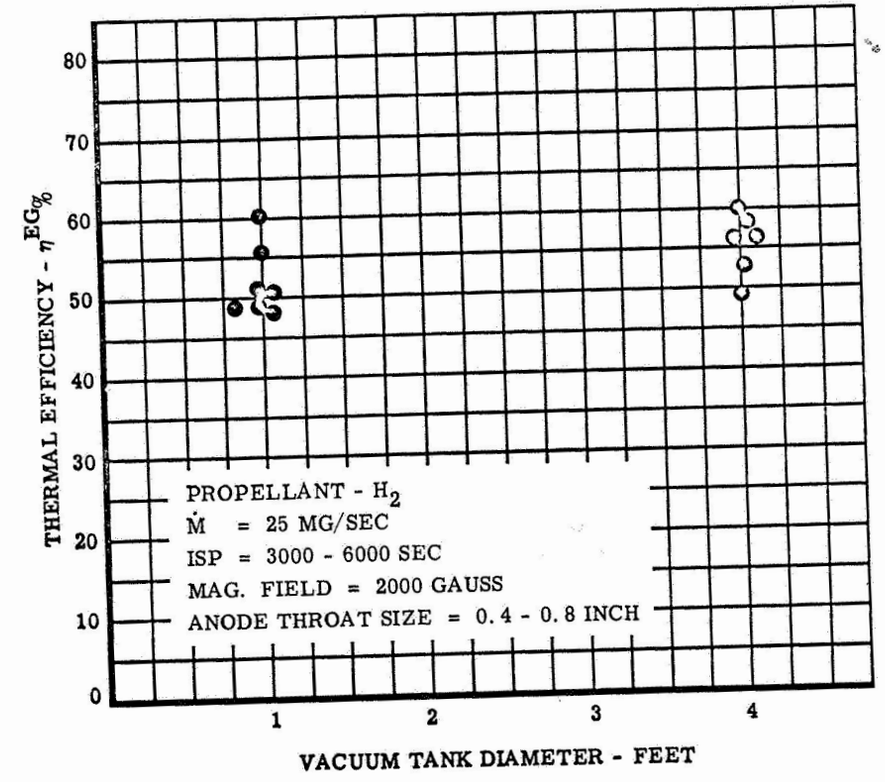

Figure 146. Thermal Efficiency Versus Vacuum Tank Diameter for Hydrogen at Various Test Conditions

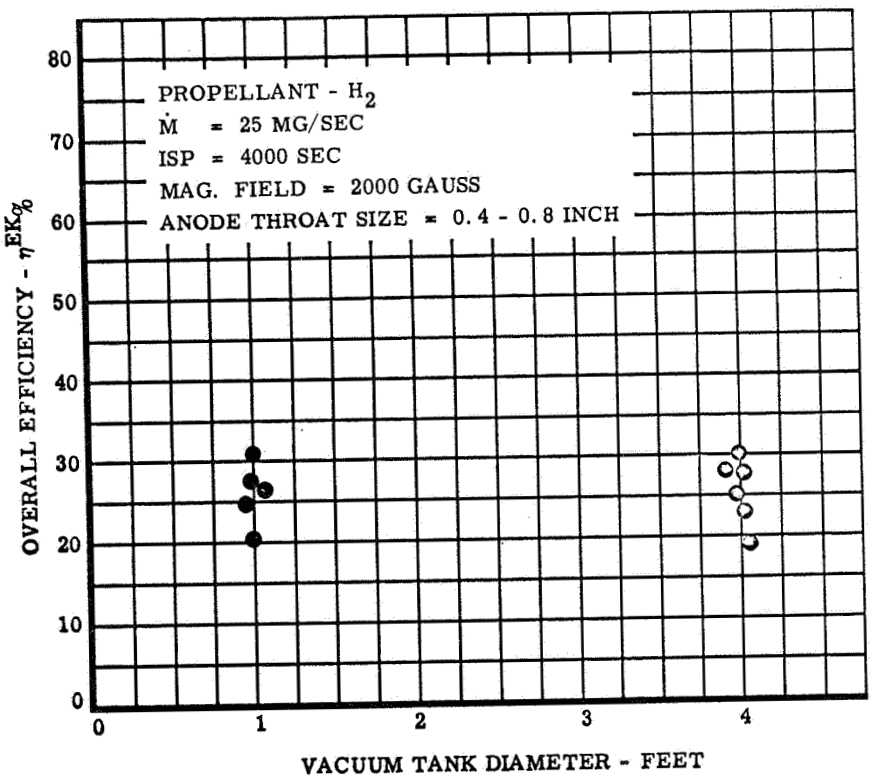

Figure 147. Overall Efficiency Versus Vacuum Tank Diameter for Hydrogen at Various Test Conditions

"proximity" effect of the testing chamber walls has been one of the principal reasons for our design of the giant chamber of Figure 142 and of the insulating one of Figure 143. To study the effect of changing the environmental pressure on the efficiency of operation, a stable condition of operation was found at the minimum chamber pressure. The exhaust valve of the vacuum system was then gradually closed to increase the ambient pressure. Practically no variation was noted when the pressure was increased from 0.05 to 0.3 Torr in the tank of Figure 138. Using the tank of Figure 139 the reverse process was applied. The pressure was maintained relatively high when the arc was started and was allowed to decrease very slowly under the action of the pumping facility. A slight increase in the thrust efficiency was noted. Tests conducted in other laboratories showed that improvements in the efficiency were obtained when the ambient pressure was reduced to extremely low values.(11) Visual observations have consistently shown that when the vacuum level is increased, a proportional increase in the dimensions of the arc jet (or plume) is to be expected (Figure 148). Figure 149 shows the average of our preliminary measurements on the variation of the thrust with ambient pressure. An interesting environmental test suggested recently(2) would involve the artificial creation of an atmosphere of different gases surrounding the thrustor and its jet. We have conducted a certain number of tests of this type, but our data are not yet comprehensive enough to permit conclusions to be reached. As is reported in Section 2.3.7, the development of new methods for studying the effect of different environmental conditions on the thrustor efficiency is to be strongly recommended.

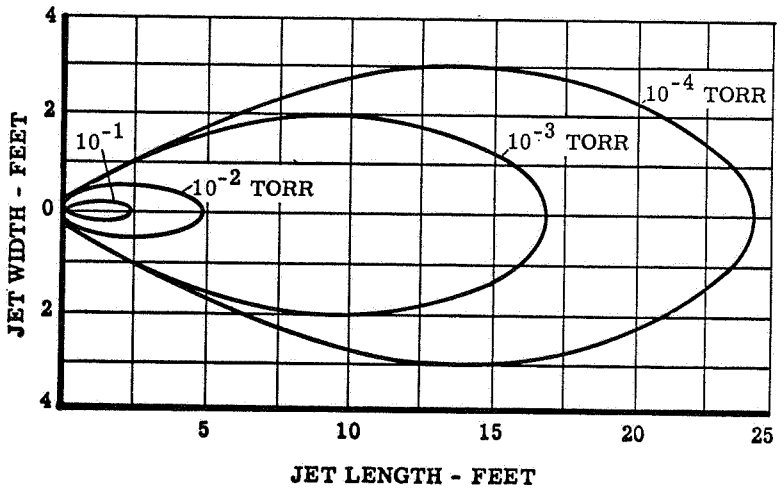

Figure 148. Visual Expansion of Thrustor Exhaust Plume at Gradually Decreased Test Chamber Pressure

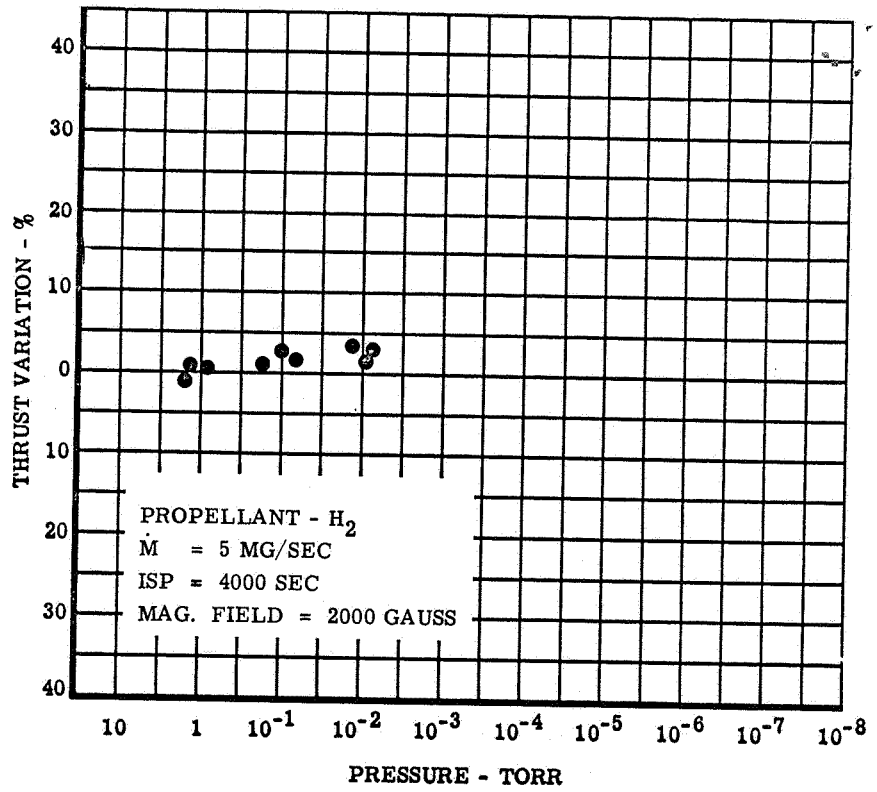

Figure 149. Preliminary Test Results of Thrust Variation Versus Vacuum Tank Pressure

2.3 Testing Anomalies With Thermo-Ionic Thrustor

2.3.1 General

During the experimental work conducted with thermo-ionic acceleration by us and by others, some anomalies in the measurements have been detected and various hypotheses have been advanced to explain them. The impossibility of reproducing the exact environmental conditions of real space in the laboratory has been the principal obstacle to the solution of the problem. While better reproduction of space conditions are in preparation, various attempts have been made to gradually eliminate all the experimental errors capable of altering the final measurement values. The task has proved to be extremely difficult and after two years of tentative efforts the results are still questionable.

The most obvious single anomaly detected in the measurements of thermo-ionic thrustors is an excess of thrust at very low values of mass flow. The error can be imputed to an extraneous influence in the thrust measurement that introduced a parasitic thrust superimposed on the regular thrust, or to an extraneous mass flow superimposed on the regular mass flow, or to both of these influences. In the following paragraphs we will analyze, on the basis of past experimental results, the effect of various operative conditions on the probable errors in the measurements of thrust and mass flow.

2.3.2 Effect of Geometry on Anomalies

The influence of the geometry on life and efficiency examined in Sections 2.1.2 and 2.2.2 was relative only to the thrustor (arc chamber, electrodes, insulators, and so forth). In this section we consider the influence of the geometry on probable errors in the measurement of thrust and mass flow that are suspected of causing anomalies in the operation. The geometry to be considered will not be limited to the thrustor only, but will include the thrust stand used to support and measure it and any other mechanical attachment to the thrustor proper. Our purpose is to detect some parasitic thrust or some parasitic mass flow which is dependent on the geometry of the above mentioned system. Our knowledge of these effects is still sketchy. It is postulated that the basic difficulty in the detection of these parasitic parameters is that they may appear only during the operation and in that case cannot be balanced away before or after the testing period. In any normal thrust measurement a zero reading is always taken before and after the test. If the instrumentation is well-designed the zero reading remains unvaried and no correction is applied to the recorded results. But if a variation of the zero reading due to a parasitic force appears, an error in the thrust measurement is indicated. During our experiments it has been found that effects of this kind are numerous. In this section we attempt to evaluate effects capable of producing anomalous results in measurements that can be imputed to the geometry of the thrustor thrust stand and similar supporting hardware. When water cooling is used, thermal effects are washed out rapidly after the test. Thermal designs are recommended and

a simple rule is to avoid high temperature differentials. In our tests temperature differentials of more than a few °C are considered detrimental. It is necessary to avoid a multiplication effect through the action of differential expansions as illustrated in Figure 150. This effect can originate not only from cooling lines at different temperatures, but also from electrical conductors with different current intensities (in this case magnetomotive interactions between conductors can also cause disturbing effects, see Section 2.3.5 and 2.3.6). Figure 151 shows a balanced system to take care of the expansion of a water-cooled magnetic coil feeding circuit. The complete elimination of all the effects of this kind is sometimes difficult or even impossible. For this reason we have designed a so-called "thrust killer" illustrated schematically in Figure 152. This accessory deflects the jet at right angles eliminating the thrust and permitting a zero reading to be taken during operation. Figure 153 is a picture of one of the first thrust killers constructed during this program. This system has been used successfully for a long time and has given good results when the thrustors tested did not use strong external magnetic fields. The measurement of thrust was made by recording the difference in the reading with and without insertion of the thrust killer. However, we found that with relatively strong magnetic fields the insertion of the thrust killer had an effect on the thrustor operation because of the path of the current outside the arc chamber. This effect persisted after the dimensions of the thrust killer were increased (Figures 154 and 155) demonstrating the necessity of still greater dimensions and of the use of insulating material in place of metals. It is felt now that greater dimensions and complete insulation will permit

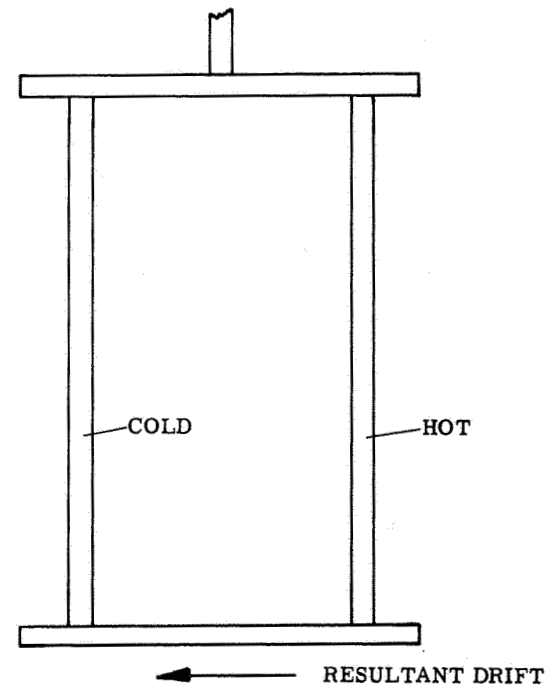

Figure 150. Parasitic Zero Shift Produced by Nonuniform Heat Load on Thrust Balance Components

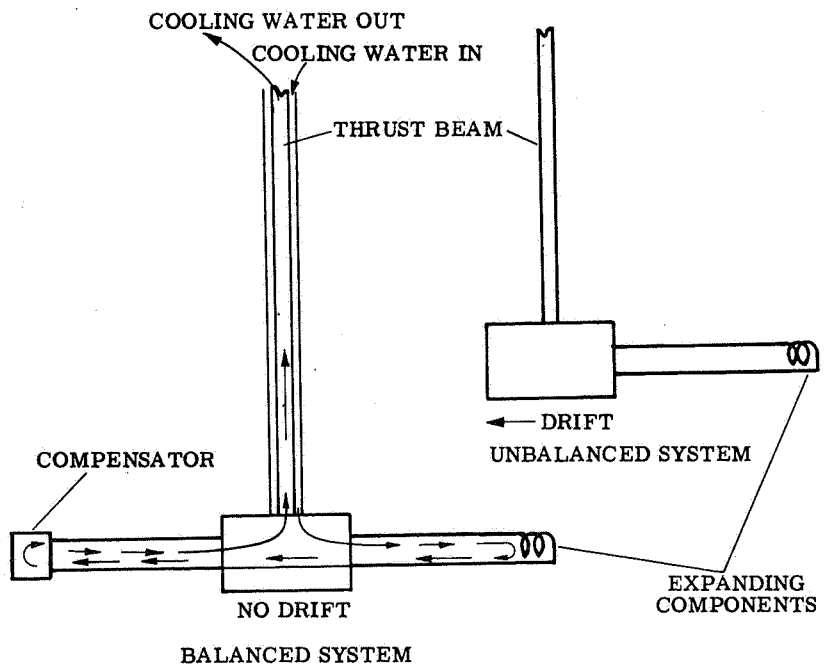

Figure 151. Schematic of Thrust Balance With and Without Compensation of Thermal Expansion

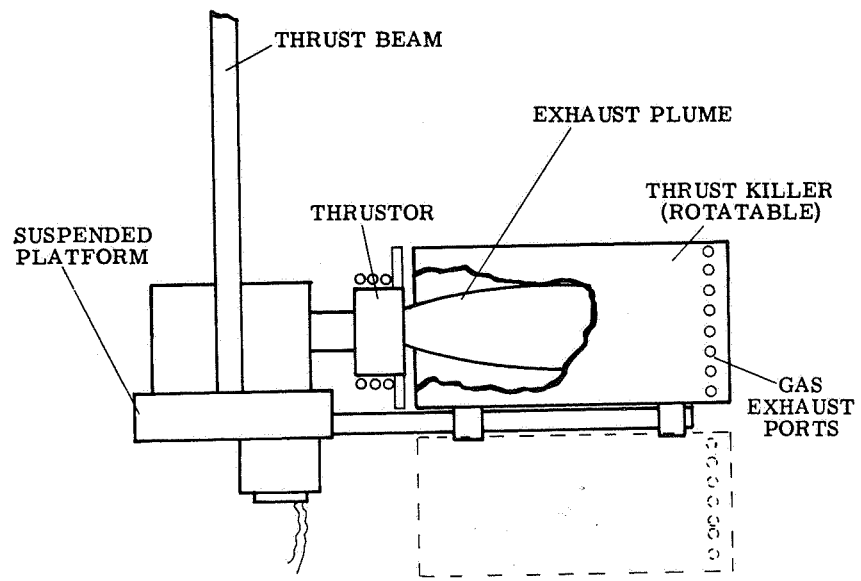

Figure 152. Schematic of Thrust Killer Attached to Suspended Platform on Thrust Beam

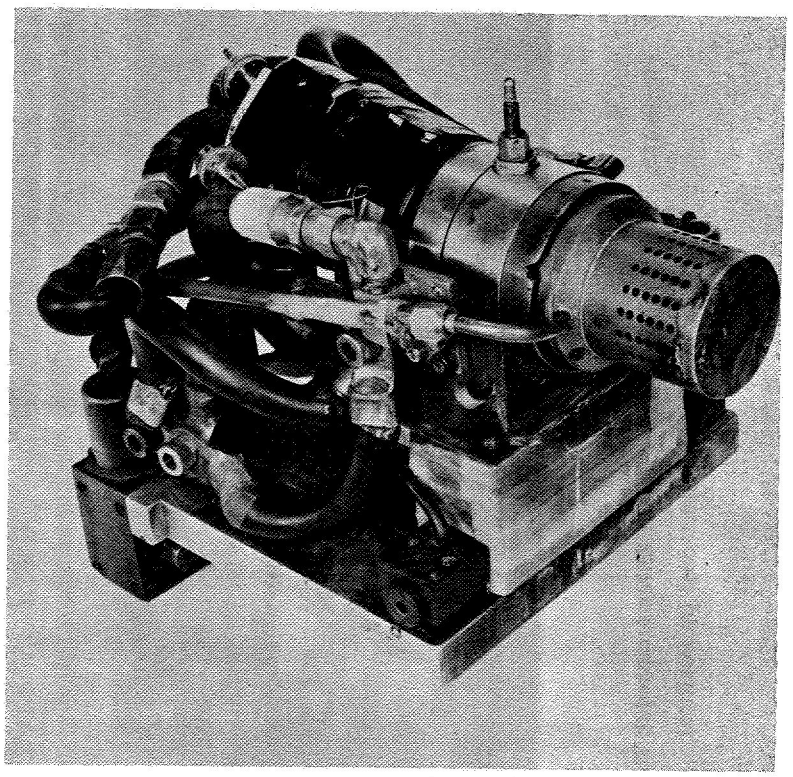

Figure 153. Photograph of Prototype Thrust Killer Attached to Thermo-Ionic Thrustor

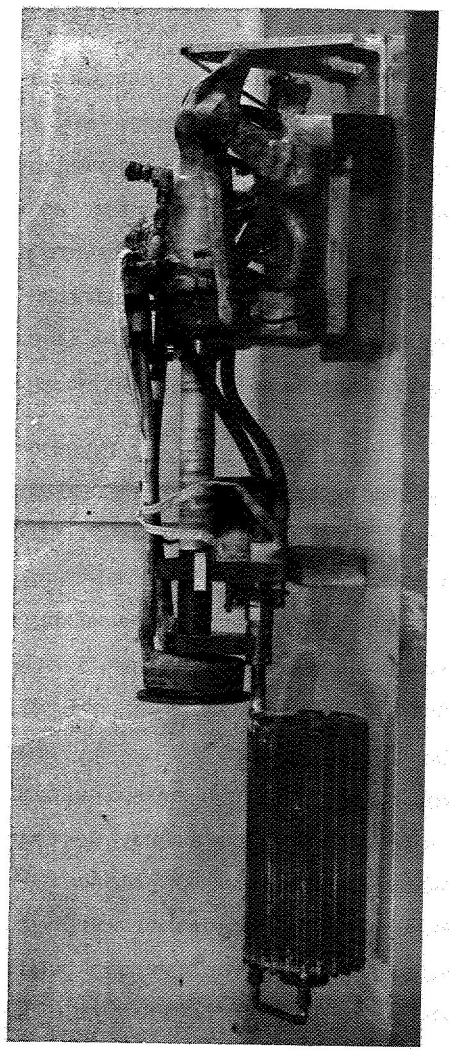

Figure 154. Photograph of Enlarged Thrust Killer Attached to Thermo-Ionic Thrustor With Extended Electrodes (Out Position)

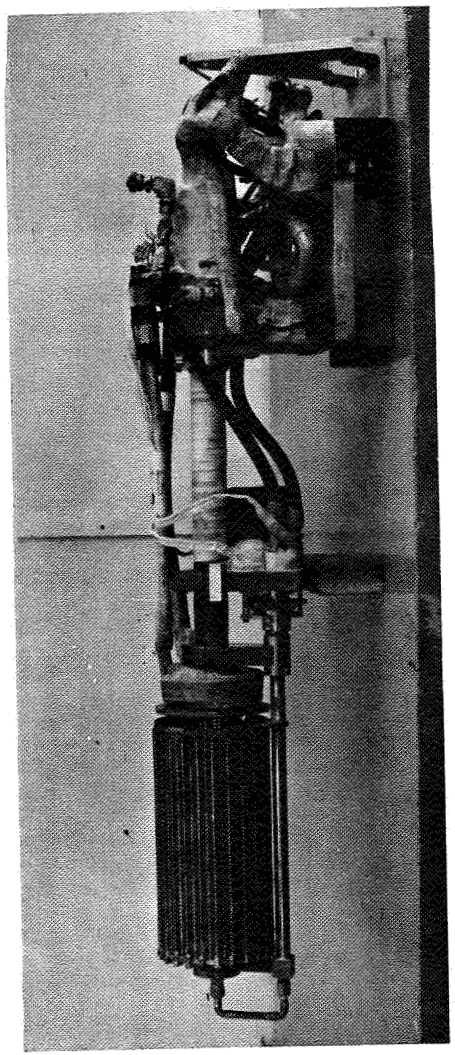

Figure 155. Photograph of Enlarged Thrust Killer Attached to Thermo-Ionic Thrustor With Extended Electrodes (In Position)

extending the use of this important accessory to cases involving strong magnetic fields (Figure 156). Figure 157 illustrates another system where the thrust is eliminated, changing the jet direction without interrupting the operation. Continuing to consider the effects based on pure geometry we have found that when an external magnetic field is used it is necessary to avoid any mechanical movement of the magnetic coil relative to the thrustor (Figure 158). Without this precaution, shifts in the center of gravity are produced introducing apparent thrust variations. When the anode throat diameter, the external magnetic field, and the arc current are large enough, it is well established that some part of the arc current flows through the jet region producing magnetodynamic effects that can alter the thrust reading. The geometry of the thermo-ionic thrustor can also have an effect in producing a parasitic mass flow or "mass entrainment" superimposed on the regular mass flow supplied to the thrustor. Apparently a decrease in the tank pressure of many orders of magnitude is required to eliminate this possibility.

Because of the possibility of reaching these vacuum levels, we have tried to obtain a better understanding of the entrainment phenomenon by seeing if an increase in the thrust reading would be obtained by increasing the throat diameter while keeping other parameters as constant as possible. While the results obtained have tended to oppose the hypotheses that larger throat diameters result in greater entrainment, it seems justified to insist on this type of test because if a conspicuous entrainment does exist, the thrustor geometry probably will influence the importance of the effect.

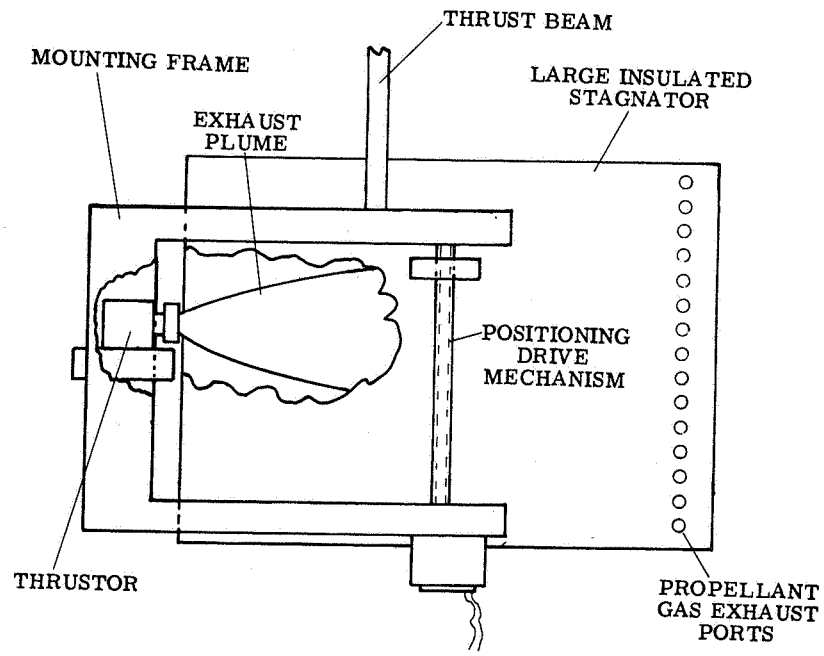

Figure 156. Schematic of Enlarged Fully Insulated Thrust Stagnator

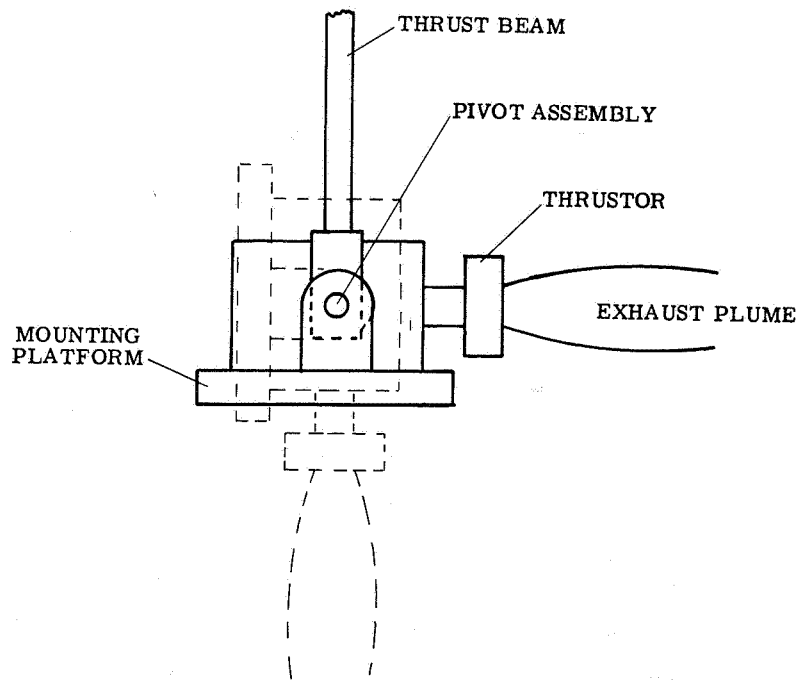

Figure 157. Schematic of Mechanism for Thrust Cancellation by Changing the Thrust Axis

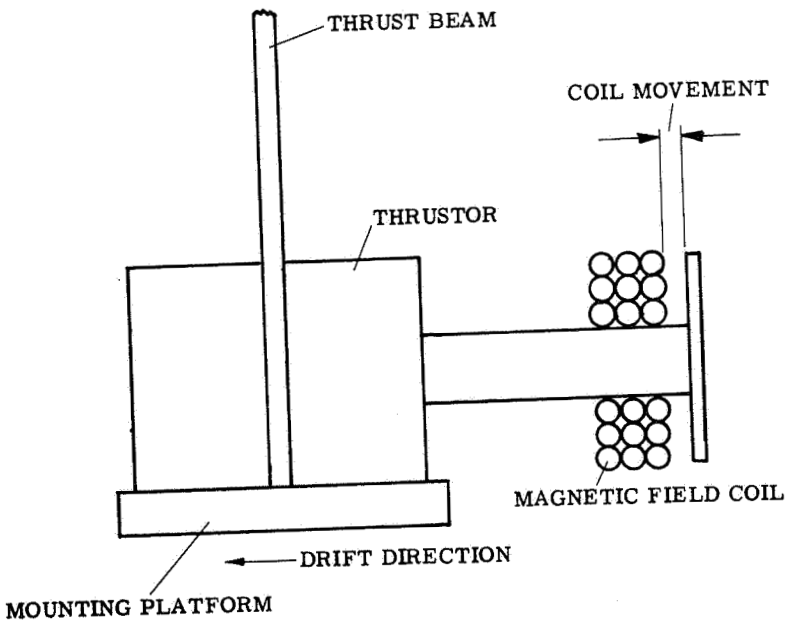

Figure 158. Illustration of Coil Movement on Thrustor Producing Center of Gravity Shift

If the second solution indicated in 2.3.1 is to be followed (design of thermoionic thrustors not sensitive to the environmental conditions) the study of the effect of their geometry will be of primary importance. For particular operating conditions (throat size, magnetic field, voltage and current, vacuum level) part of the arc current is outside the arc chamber and returns to the thrustor by different paths. One of these is through glow discharges appearing often on the connections to anode and cathode or on simple metal structural parts. For these reasons the use of insulating materials or insulating protection on metals has been adopted to reduce this erratic operation that could possibly cause anomalous results. Figure 159 is a schematic indicating the use of insulation in the thrustor and its supporting hardware and Figures 160 and 161 are actual pictures of how this has been economically obtained using commercial silicone protective paint. It is not known if the above mentioned glow (whether uniformly distributed along conductors or concentrated in one or more spots) is capable of producing a parasitic thrust either directly or indirectly. However, its characteristic of acting only during operation makes it similar to the other mentioned effects (thermal, magnetic, and so forth) in that it is difficult to pinpoint because it cannot be detected before starting the arc or after shut-off.

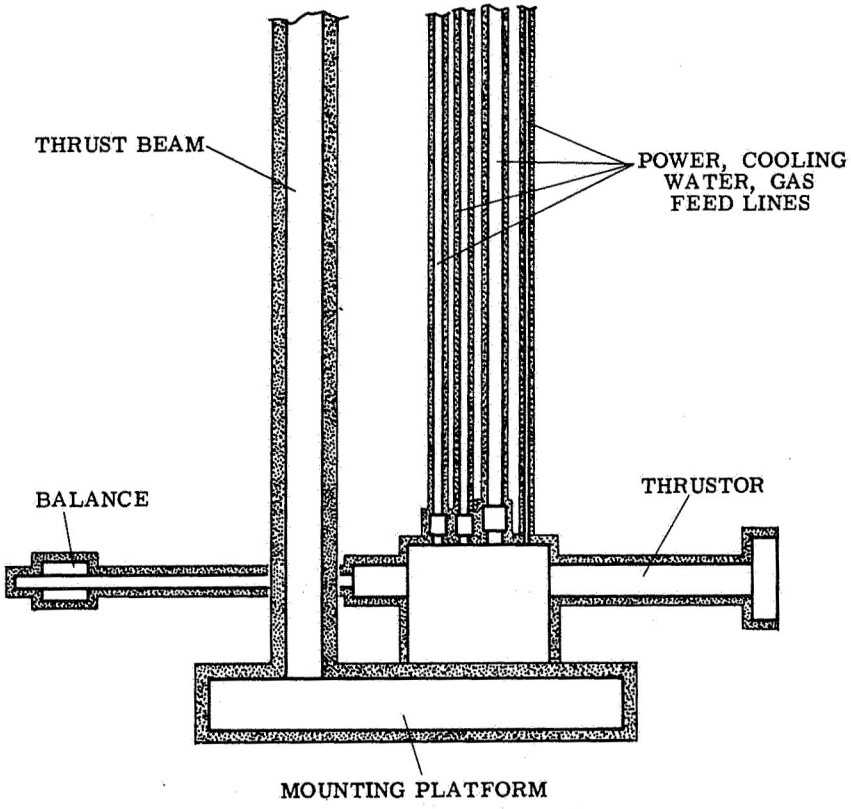

Figure 159. Schematic of Completely Insulated Thrustor Suspension System

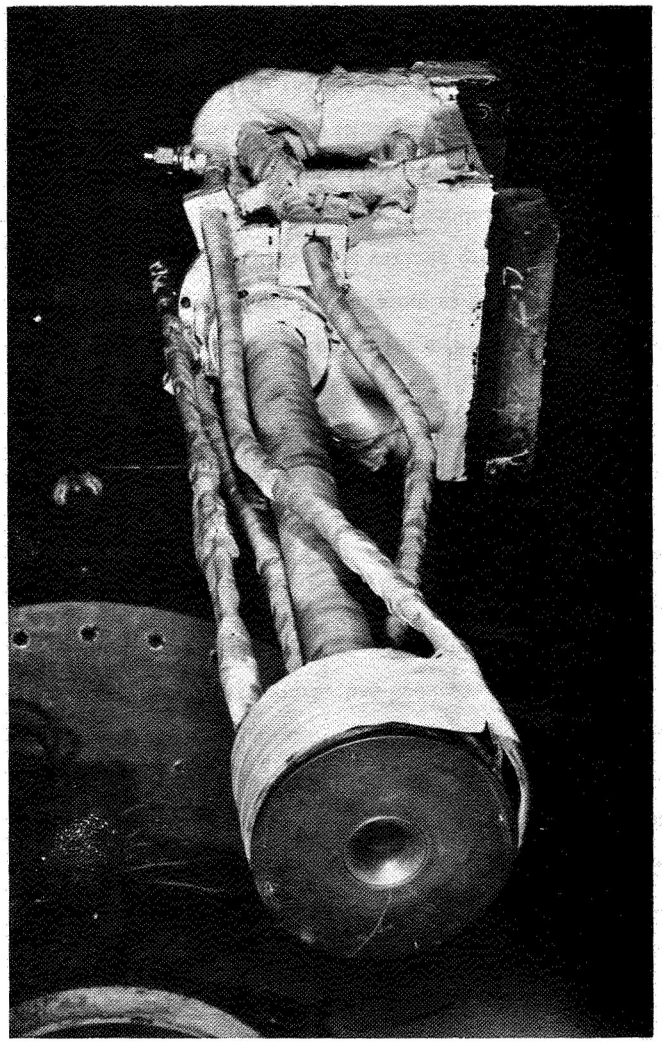

Figure 160. Photograph of Thermo-Ionic Thrustor Totally Insulated With a Thick Layer of Silicone Rubber

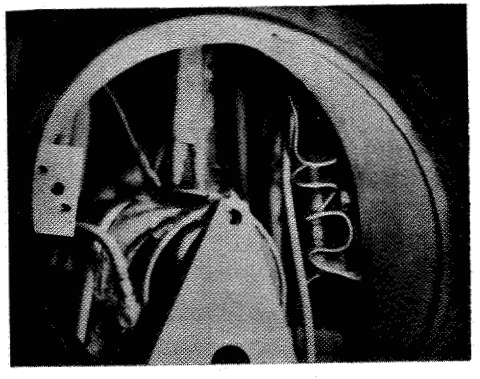

Figure 161. Photograph of Complete Thrustor Suspension System Insulated With a Thick Layer of Silicone Rubber

2.3.3 Effect of Propellant on Anomalies

The analysis of the effect of the propellants on anomalies in thrust and mass measurement is very important. During this work the effort has been concentrated mostly on hydrogen. Deuterium was found very useful for evaluating performance because it is similar to hydrogen while having twice the molecular weight. Also helium, with the identical weight of diatomic deuterium but with atomic structure, has been considered useful. Further studies of the effects of these three propellants on the various measurements are necessary. Other propellants such as lithium and potassium have been studied on a limited scale. Electrode vapors (tungsten in particular) have also supplied some useful information. Some results from other laboratories have also been very useful in this study. These have been obtained by verbal communication or through regular reports and have included information on the use of sodium, cesium, ammonia, and so forth. Table 7 shows the ionization potential for a few of the propellants that have been used in our work. Table 8 shows the range of voltages reported in the literature for a plasma jet using various propellants. A series of measurements have been made for various propellants for a range of mass flows. It has been found that a general trend exists which is practically valid for any propellant. This is illustrated in Figures 162 and 163. When the mass flow is decreased, the thermal efficiency decreases and the thrust efficiency increases. At extremely low mass flows a low value of the thermal efficiency has been found in most of the tests (as would be expected). At these extremely low values of mass flow an increase of the thrust

TABLE 7

IONIZATION POTENTIALS FOR COMMON PROPELLANTS

Propellant	Atomic Weight	Ionization Potentials ev. I	II
H	1.0	13.6	
D	2.0	13.6	
He	4.0	24.6	54.14
Li	6.9	5.3	75.2
NA	22.9	5.12	47.06
A	39.9	15.68	27.76
K	39.0	4.31	31.66
Cs	132.9	3.87	23.4
W	184.0	8.1	

TABLE 8

AVERAGE WORKING VOLTAGE RANGES FOR VARIOUS PROPELLANTS

Propellant	Voltage Range	Reference
H_2	35 - 300	*
D_2	40 - 120	*
He	40 - 200	*
Li	20 - 110	(4)
NH_3	25 - 60	*
NA	30 - 100	(10)
A	15 - 50	*
K	10 - 50	(10)
Cs	10 - 120	(12)
W	10 - 35	(13)

* Giannini Scientific Corporation test points.

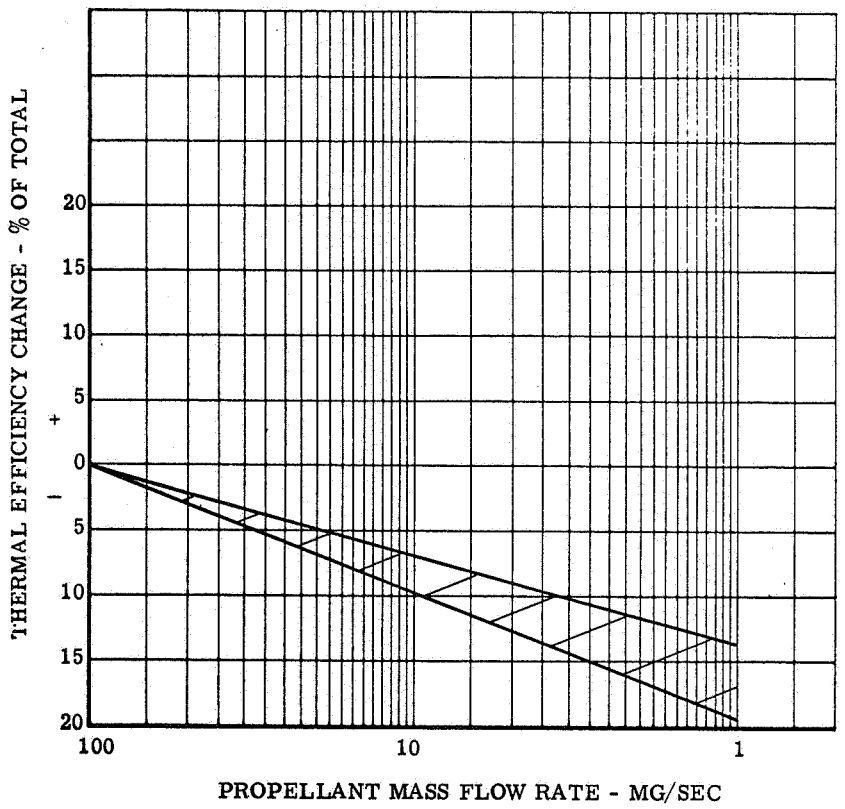

Figure 162. General Trend of Decrease in Thermal Efficiency Versus Decrease of Propellant Mass Flow Rate at Constant Isp

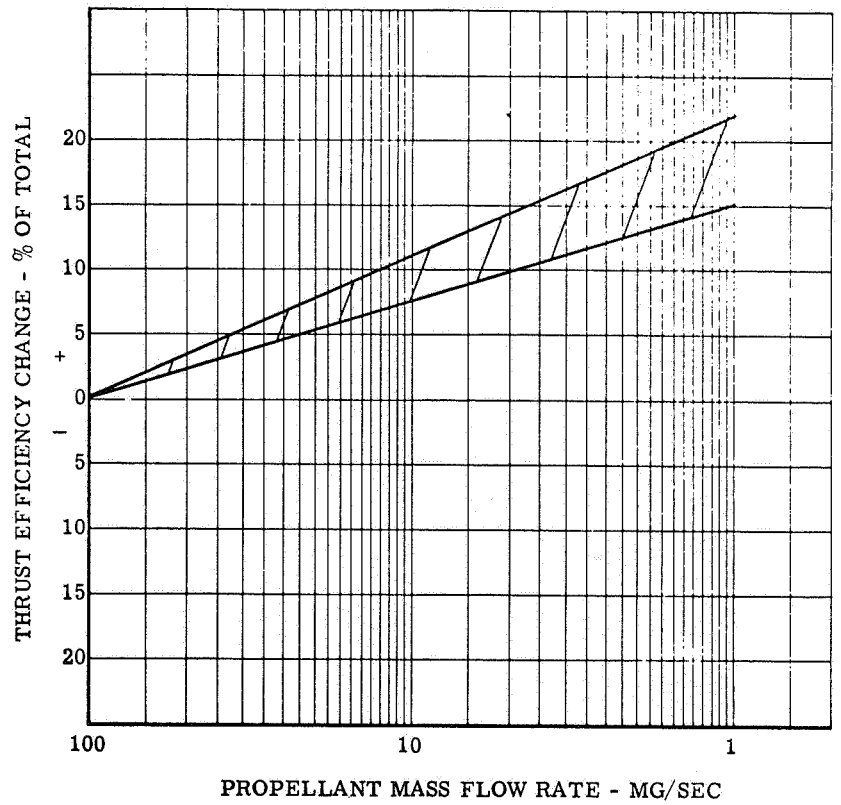

Figure 163. General Trend of Increase in Thrust Efficiency Versus Decrease of Propellant Mass Flow Rate at Constant Isp

efficiency might also be expected if the general trend continues consistently. Sometimes unreasonable values have been measured, and this must be considered an anomalous result as will be discussed later. The influence of the propellant characteristics on other parameters can have some indirect effects on this behavior. For this reason it appears useful to analyze different propellants of similar characteristics but with some basic differences (as for example hydrogen and deuterium). At this stage of our investigation no one propellant seems to present exceptional differences from the others. However, this conclusion is open to some question because of the far from perfect environmental facilities available today for testing. It seems that testing anomalies are more apt to occur and are more difficult to trace when the propellant used has a low ionization potential. For example, the glow observed on the metal parts of the thrustor is extremely visible when helium is used while it is difficult to detect with other propellants which have a lower ionization potential. The simultaneous use of different propellants is promising as an aid for diagnostic work (such as tracing) as is reported elsewhere.

2.3.4 Effect of Pressure on Anomalies

A fairly comprehensive series of tests have been conducted to investigate the effects of changing the arc chamber pressure while keeping other parameters as constant as possible. At constant Isp there is a tendency for both the thermal and thrust efficiency to decrease as the arc chamber pressure is decreased. This is illustrated in Figures 90 through 99 of Section 2.2.2. This well established experimental result can be used to trace anomalous or suspected behavior whenever the trend of the variation of the thermal or thrust efficiency changes. During the tests it has been noted that changes in other operating conditions sometimes result in very small variations in pressure. To detect these, high precision in the measurement of pressure is necessary. Another important point derived from these tests is the need for reducing to a minimum the time constant of the pressure gauge. For this reason all the connections must be very short and of ample diameter. Pressure transducers located very near the arc chamber are preferred (Figure 164). The range of pressure used in the tests ranged from 1 to 200 Torr as illustrated in Table 9. For a constant mass flow and for each propellant there is a well-defined relationship which gives the increase in pressure associated with an increase in specific impulse. The presence of an external magnetic field sometimes complicates this picture as illustrated in Section 2.3.6. The precise measurement of the arc chamber pressure is somewhat complicated when condensable propellants are used, as for example alkali metals. We have not yet found a practical solution to this problem; however, a system has been devised and is illustrated in Figure 165. A sensitive flowmeter (F) detects the

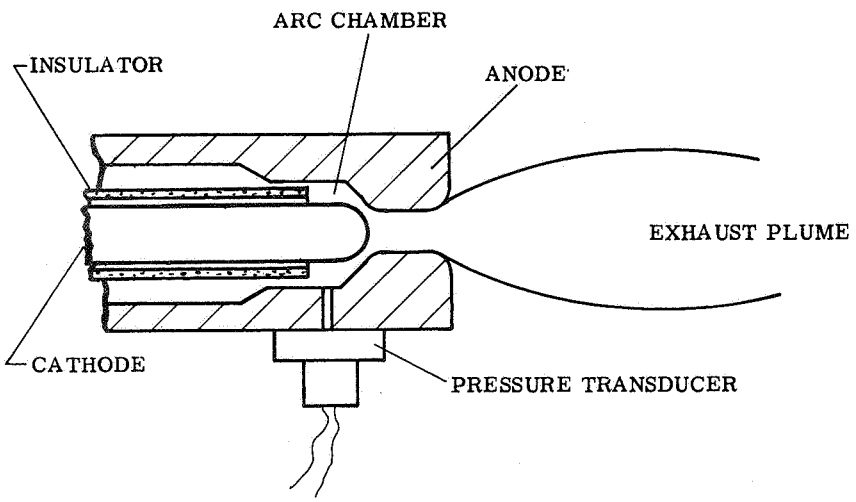

Figure 164. Schematic of Location of Pressure Sensors in Close Proximity of Arc Chamber

TABLE 9

COLD FLOW ARC CHAMBER PRESSURES AT VARIOUS ANODE THROAT DIAMETERS AND PROPELLANT MASS FLOW RATES FOR H_2 AND D_2

Propellant	Anode Throat Diameter Inches	Arc Chamber Pressure mm Hg Mass Flow Rate mg/sec 5	10	25
H_2	0.125	160.0		
	0.250	40.0	80.0	200.0
	0.500	10.0	20.0	50.0
	1.000	2.5	5.0	12.5
D_2	0.125	113.0		
	0.250	31.0	57.0	141.0
	0.500	7.0	14.0	35.0
	1.000	1.8	3.5	9.0

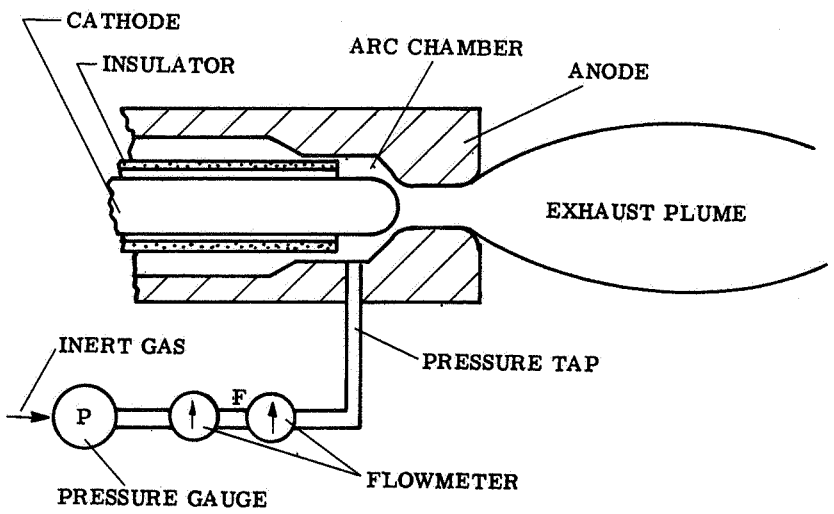

Figure 165. Schematic of Arc Chamber Pressure Sensing Apparatus for Alkali Metal Propellants

flow of a testing gas into the arc chamber. A gauge (P) detects the relative pressure which is reduced until conditions of no flow are reached.

When gaseous propellants are used, the measurement of the pressure in various positions in the arc chamber is very useful for the detection of flow patterns which might lead to anomalies. However, these measurements have always proved very difficult to make. The pressure at the tip of the cathode sometimes has a variation in opposition to the variation of the average pressure in the arc chamber (as power or field strength is changed (see Figure 166). This behavior is related to the increase of the outside portion of the jet under the interaction of self-magnetic or external magnetic forces. A pressure map can be very useful if the results are accurate and repeatable.

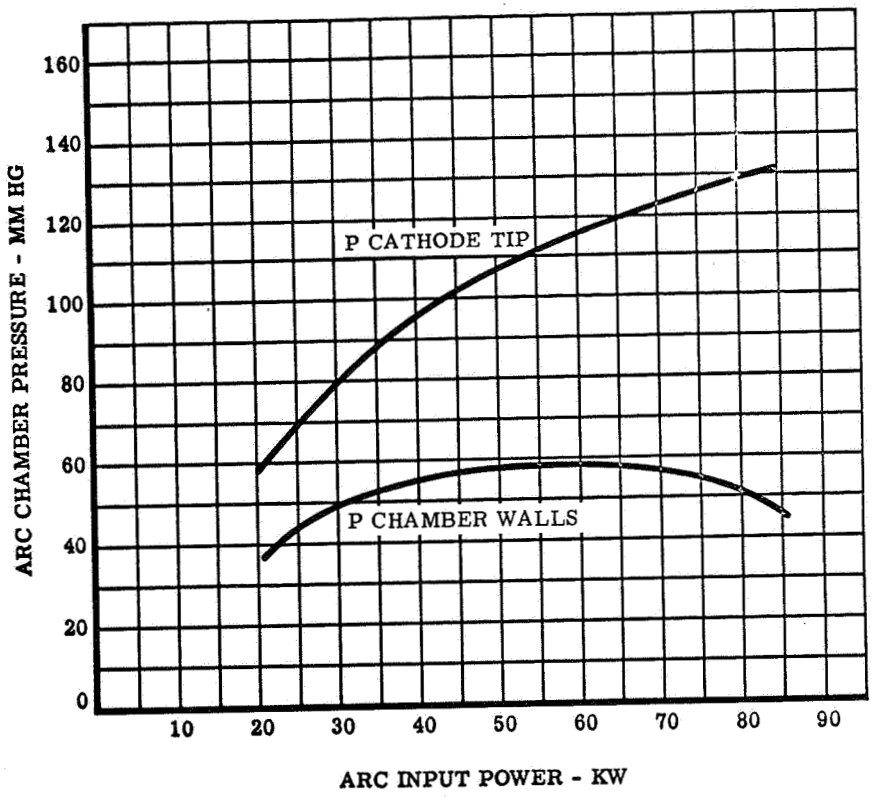

Figure 166. Comparison of Arc Chamber Pressure Variation at Two Locations With Increased Arc Input Power and Constant Mass Flow Rate

2.3.5 Effect of Power, Current and Voltage on Anomalies

One of the most singular experimental results of this program is that the specific impulse increases nearly linearly with increasing power (Figure 167). This relationship has been confirmed under similar circumstances by other laboratories. It can be explained for part of the range of power densities in terms of a reduction in the proportion of power stored in the propellant as dissociation and ionization. If very high ionization levels are reached, the explanation becomes more difficult and other factors or anomalies must be introduced to explain the measured values of thrust and mass flow. Considering the total power input versus the thrust power as illustrated in Figure 168, anomalies are not easily detected because the total power input is reasonable. But when the thermal power and the thrust power are separated, the anomalous behavior is easily pinpointed as illustrated in Figures 169 and 170. In this last figure the gas power is nearly equal to the thrust power at very high specific impulse. This operation at nearly theoretical efficiency was the first confirmation of the presence of some anomalies in the measurements. For this reason the precise separation of the thermal power or power in the propellant from the total input power is very important in this study. Two methods have been used during the tests to separate the gas power. The first, illustrated in the left part of Figure 80 (or Figure 92 if the thrustor is radiation-cooled), is based on the thermal measurement of the power lost in the thrustor cooling. This power subtracted from the total input power gives the power in the propellant. The second method illustrated in the right part of Figure 80

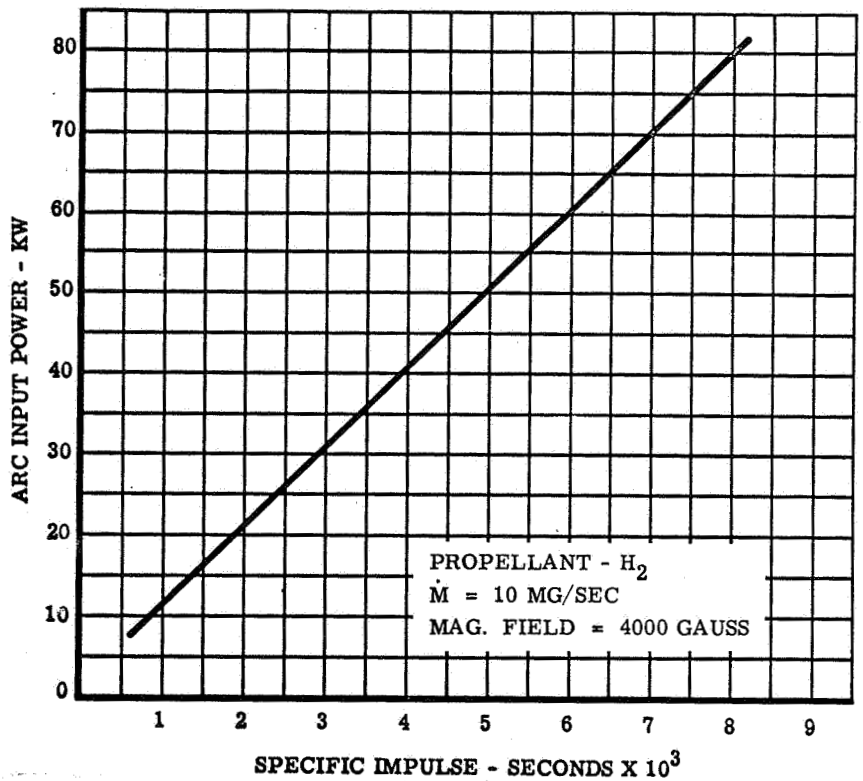

Figure 167. Average Total Input Power Versus Specific Impulse at Constant Propellant Mass Flow Rate

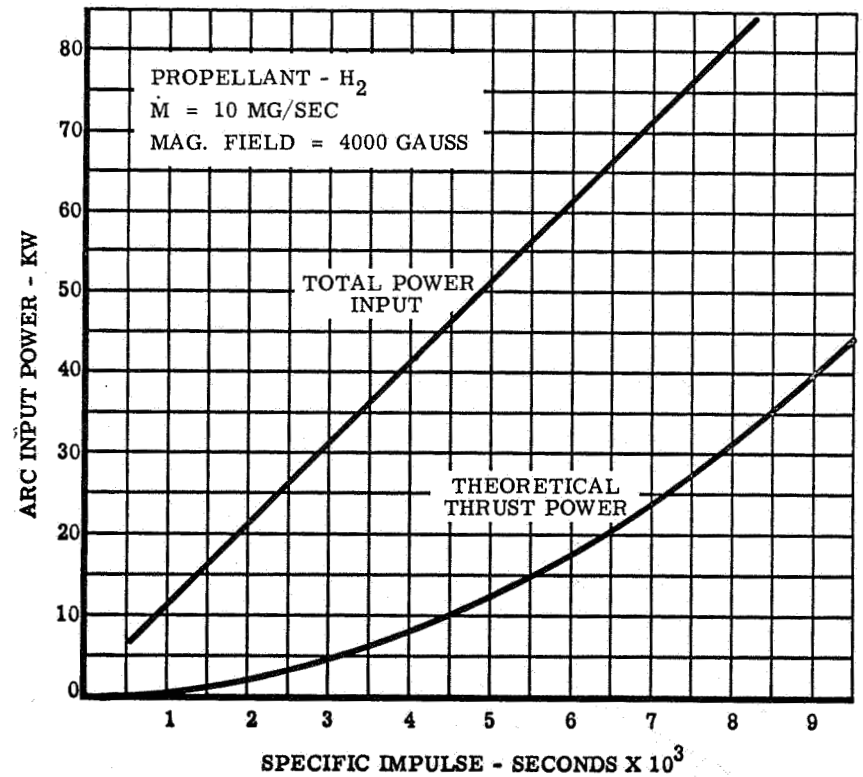

Figure 168. Average Total Input Power and Theoretical Thrust Power Versus Specific Impulse at Constant Propellant Mass Flow Rate

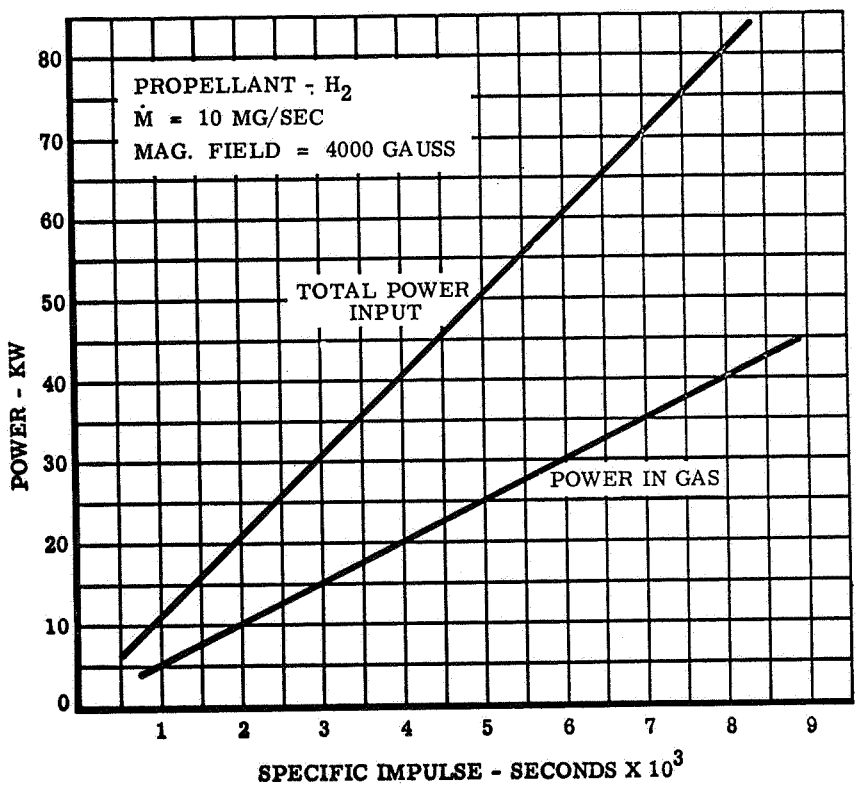

Figure 169. Average Total Input Power and Power in Gas Versus Specific Impulse at Constant Propellant Mass Flow Rate

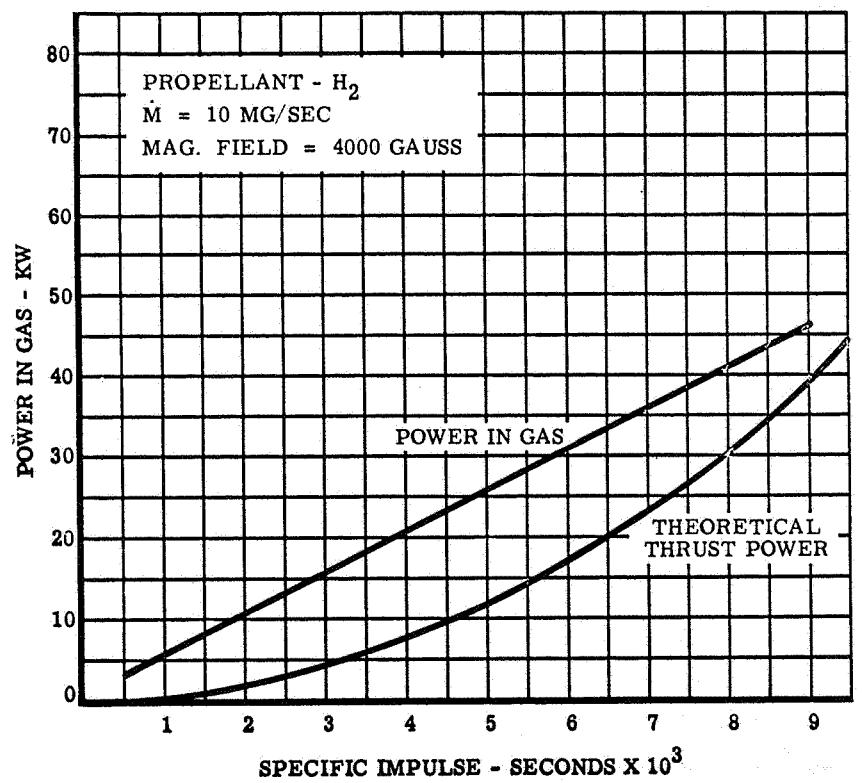

Figure 170. Average Power in Gas and Theoretical Thrust Power Versus Specific Impulse at Constant Propellant Mass Flow Rate

(or Figure 84) is based on the direct thermal measurement of the power in the propellant using a special stagnation system. In practice both systems are used simultaneously to provide a check of the results. This method has been used in our laboratory for many years with good results and has been recently improved for more accurate discrimination between the thermal and thrust power. It has been thought for a long time that while the measurement of the thrust at very high specific impulse and low mass flow might be affected by some anomalies, the determination of the power in the propellant is relatively immune to extraneous influences. We have recently discovered conditions in which errors in the measurement of thermal power can also occur. If the losses from cooling the thrustor are subtracted from the input power to obtain the power in the propellant (without cross-checking with the stagnation system), this calculated power is sometimes more than the real value. Apparently some of the supposed propellant power is transferred directly to the testing tank and from there dissipated by radiation or water cooling. To avoid this it is necessary to use a system similar to the one illustrated in Figure 171. The thrustor cooling system is extended and includes part of the testing tank while the stagnator is restricted and is a smaller completely independent cooler made possibly of insulating material. The result of this modification is that the measured thermal efficiency drops and more power will be found as thermal losses. Consequently the available gas power will also drop and the detection of any anomalous measurement will be improved. It is important to note that with increasing specific impulse or specific enthalpy the thermal efficiency generally drops. If an opposite trend is measured, this could be a sign of

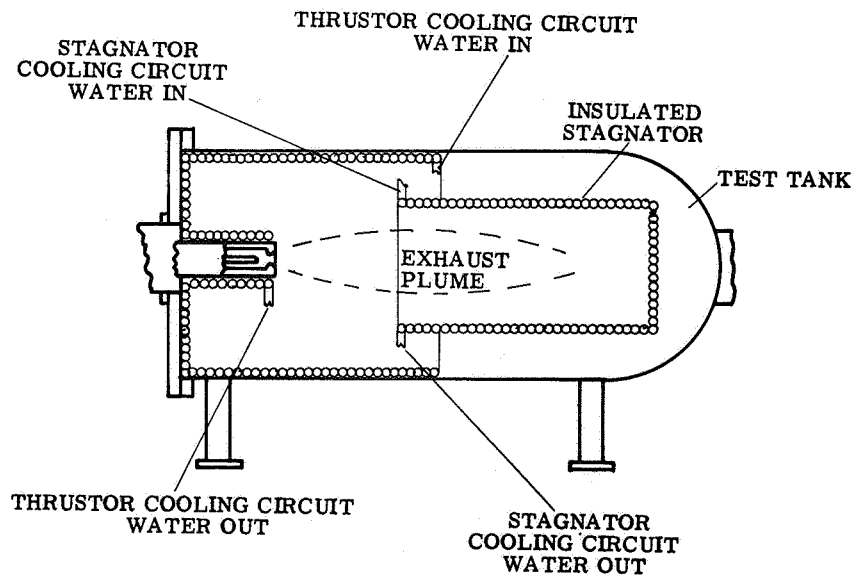

Figure 171. Schematic of Improved Heat Exchanger System for Precise Determination of the Thermal Efficiency of Thermo-Ionic Thrustors

anomalous operation in the thermal cooling system. For the study of anomalous results to be traced in particular operating conditions of power, current and voltage, an important section can be the observation of the effects produced by changing the polarity of the electrodes. For given conditions of throat geometry, magnetic field and power density and using the conventional polarity (i.e., central cathode rod and coaxial anode) luminous spots are observed on the anode surface due to concentrated electron beams. Figure 172 is a photograph of the anode front plate after a relatively short operation for these conditions. Differences in color ranging from very dark to very bright zones suggest the possibility to use this system to record the behavior of the arc discharge from the external part of the jet. For this reason a uniform and clean anode front surface should be used. Figure 173 shows interesting marks of current paths on the front plate obtained with reversed polarity (i.e., front plate negative). Experiments on the effect of changing the polarity of the arc on eventual anomalies have only been initiated at the termination of this work. From the first experiments it appears that the geometry of the inverse polarity thrustor requires careful design studies to find the proper position of cathode and insulating materials for the most stable operating conditions. Figure 174 shows a tentative geometry for this kind of thrustor.

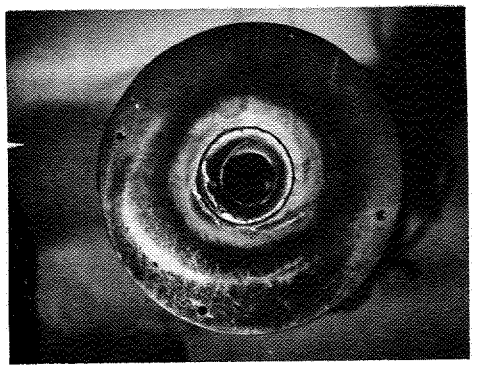

Figure 172. Photograph of Anode Front Surface (Conventional Polarity) After Short Operation Showing Distinct Zones of Arc Discharge Pattern

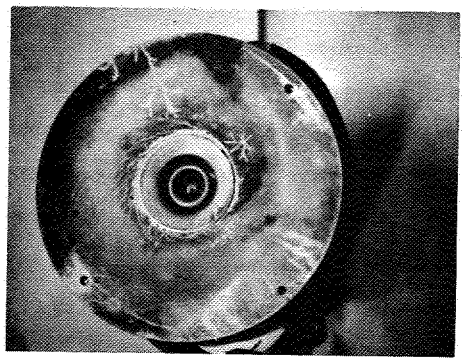

Figure 173. Photograph of Cathode Front Plate (Reversed Polarity) After Short Operation Showing Distinct Marks of Current Discharge Path

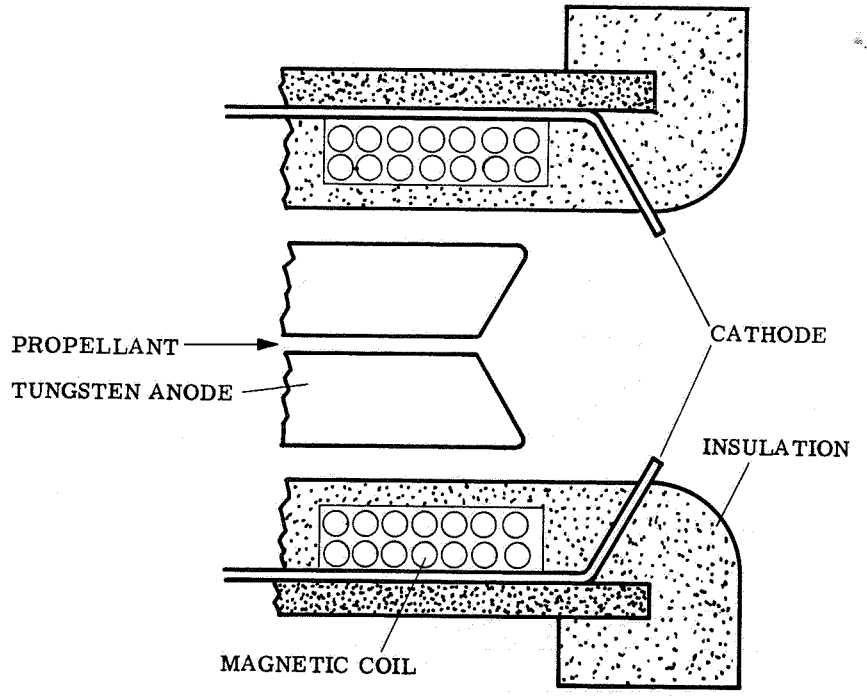

Figure 174. Schematic of Experimental Reversed Polarity Arc Chamber for Short Tests

2.3.6 Effect of External Magnetic Field on Anomalies

The first test results on thermo-ionic acceleration were obtained without an external magnetic field and with relatively high mass flow. It is our intention to repeat those early experiments with a lower mass flow (but without an external magnetic field) to compare with the early ones. During this period we did a substantial amount of testing at medium and low mass flow (between 1 and 10 mg/sec) using external magnetic fields of various intensities (from 100 to over 16,000 gauss). While striking differences in the visual appearance of the exhaust jet have been observed and recorded, only small variations have been detected in the overall efficiency (as a result of changes in the mass flow and magnetic field strength). Figures 175 to 179 are typical representations of the effect of varying the external magnetic field intensity on a number of performance parameters. Similar data can be found in Sections 2.1.6 and 2.2.6. An increase in the intensity of the external magnetic field produces a decrease of the pressure in the arc chamber. This effect can be duplicated by increasing the diameter of the throat. The opposite trend is found for the arc voltage which increases with increasing magnetic field. This effect also can be duplicated by increasing the diameter of the throat. Figure 180 shows lines of constant voltage obtained by changing the relationship between field intensity and throat diameter. The hypothesis suggested by this behavior is that the anodic foot of the arc can be pushed farther away by increasing the magnetic field or the throat diameter as illustrated in Figure 181. Using a strong continuously variable magnetic field we have run a comprehensive

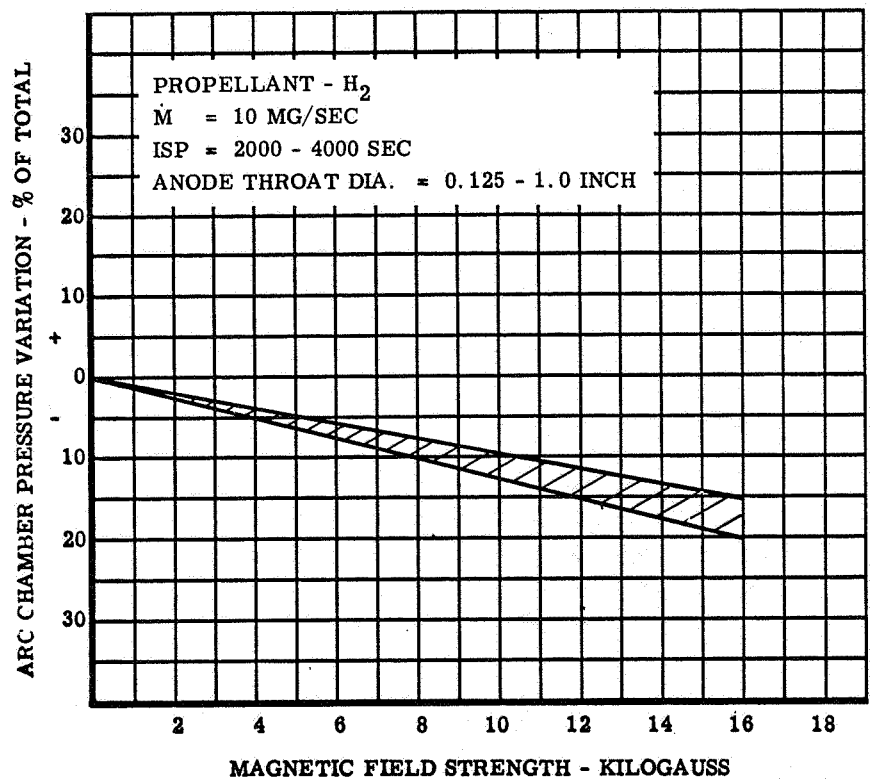

Figure 175. Variation of Arc Chamber Pressure Versus External Magnetic Field Strength at Various Anode Throat Diameters and Constant Propellant Mass Flow Rate

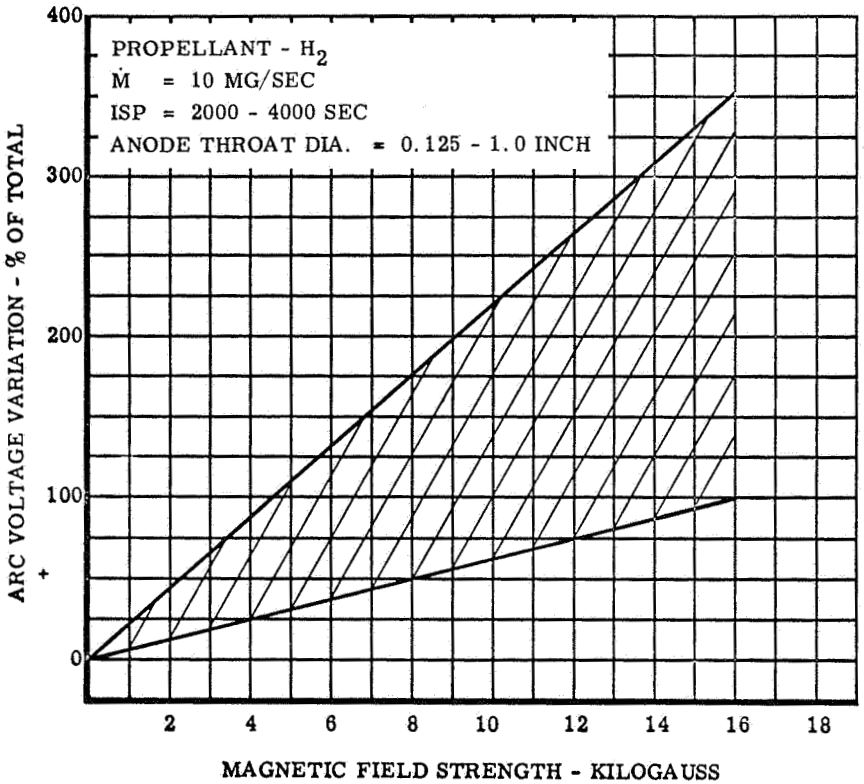

Figure 176. Variation of Arc Voltage Versus External Magnetic Field Strength at Various Anode Throat Diameters and Constant Propellant Mass Flow Rate

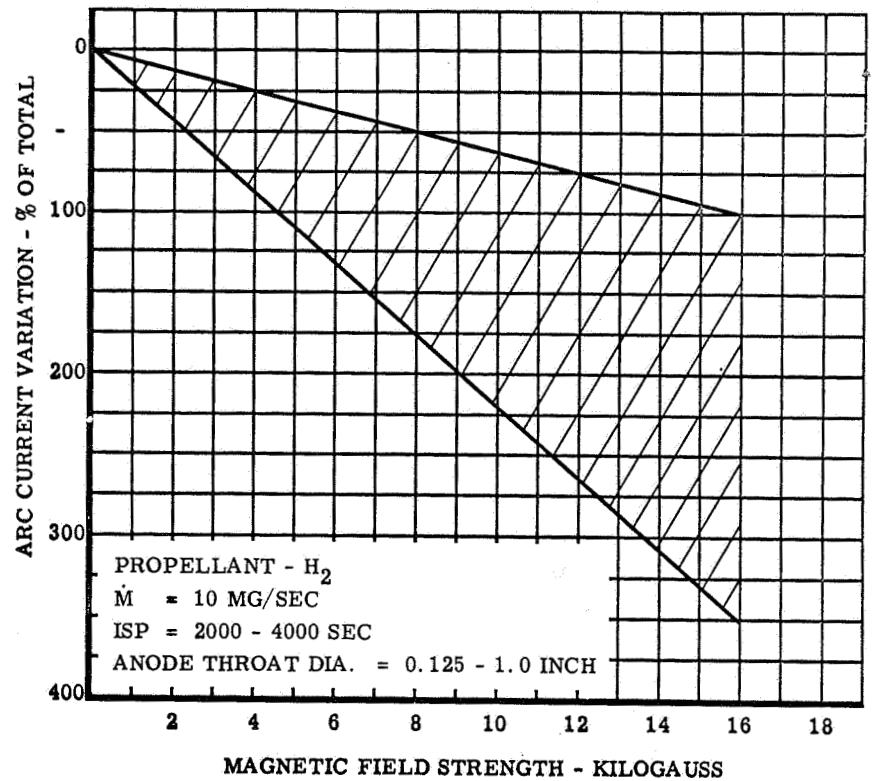

Figure 177. Variation of Arc Current Versus External Magnetic Field Strength at Various Anode Throat Diameters and Constant Propellant Mass Flow Rate

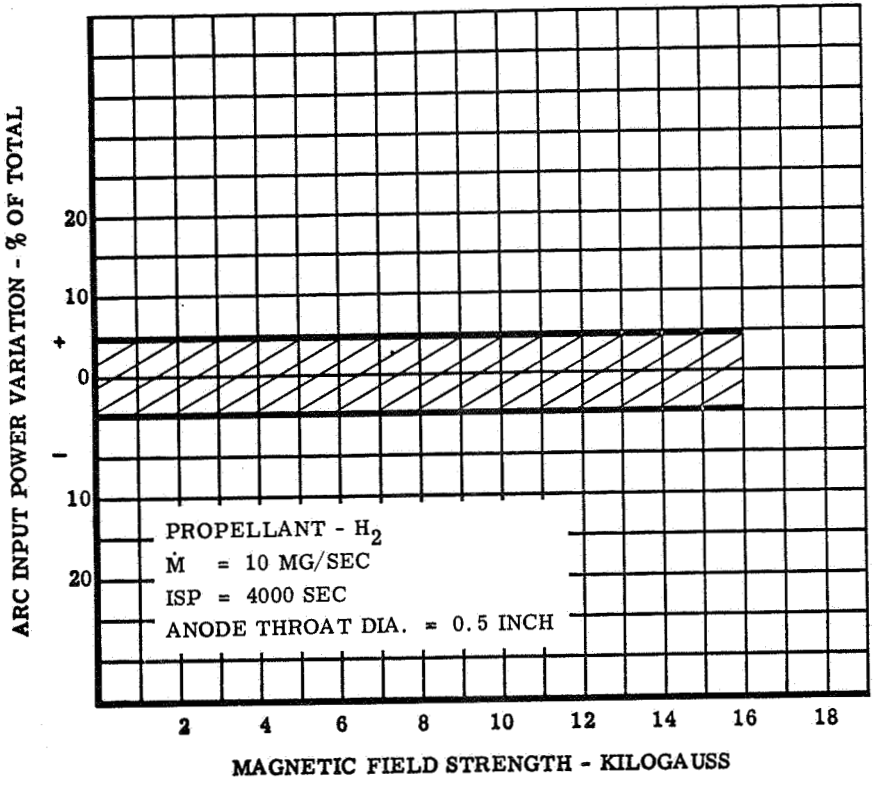

Figure 178. Variation of Arc Input Power Versus External Magnetic Field Strength at Constant Anode Throat Diameter, Specific Impulse and Propellant Mass Flow Rate

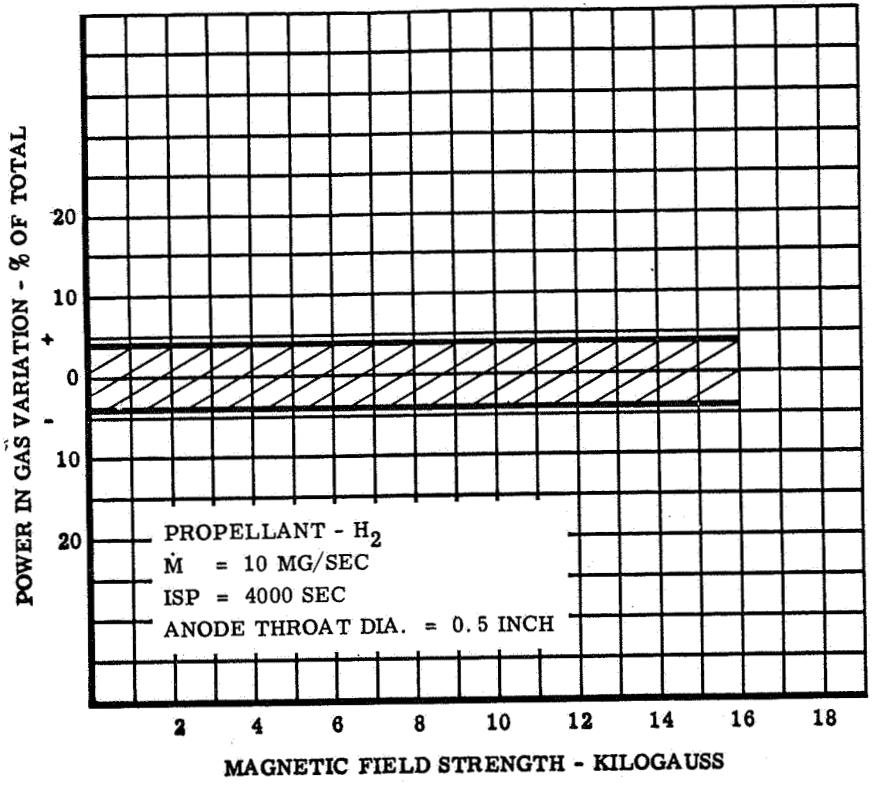

Figure 179. Variation of Power in Gas Versus External Magnetic Field Strength at Constant Anode Throat Diameter, Specific Impulse and Propellant Mass Flow Rate

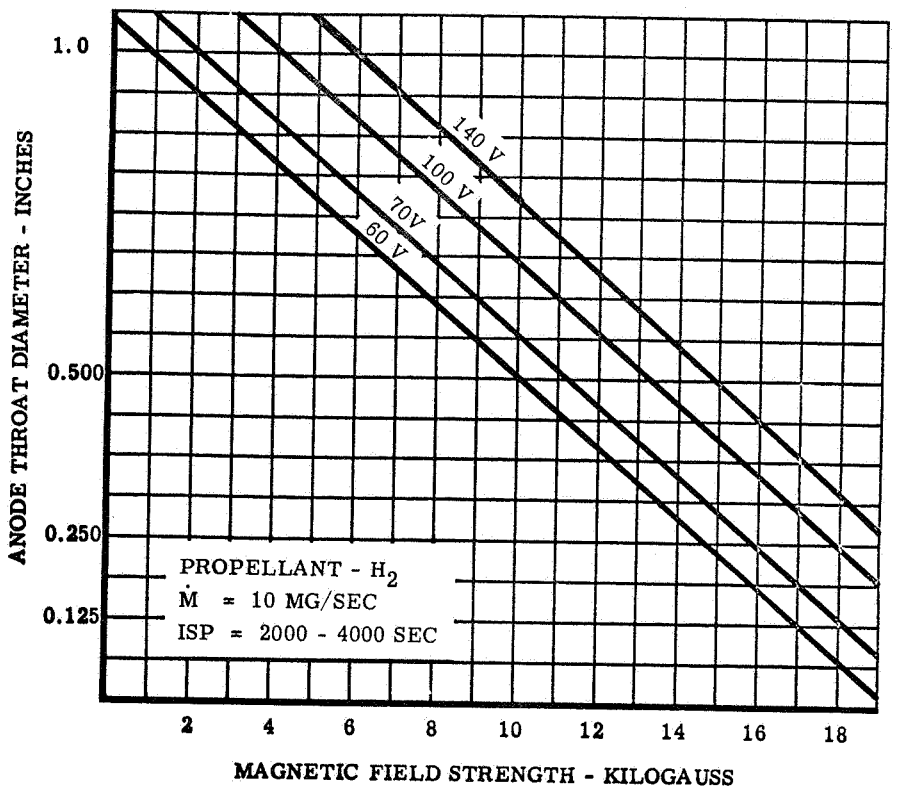

Figure 180. Anode Throat Diameter Versus Magnetic Field Strength for H_2 Propellant at Constant Voltage Operation

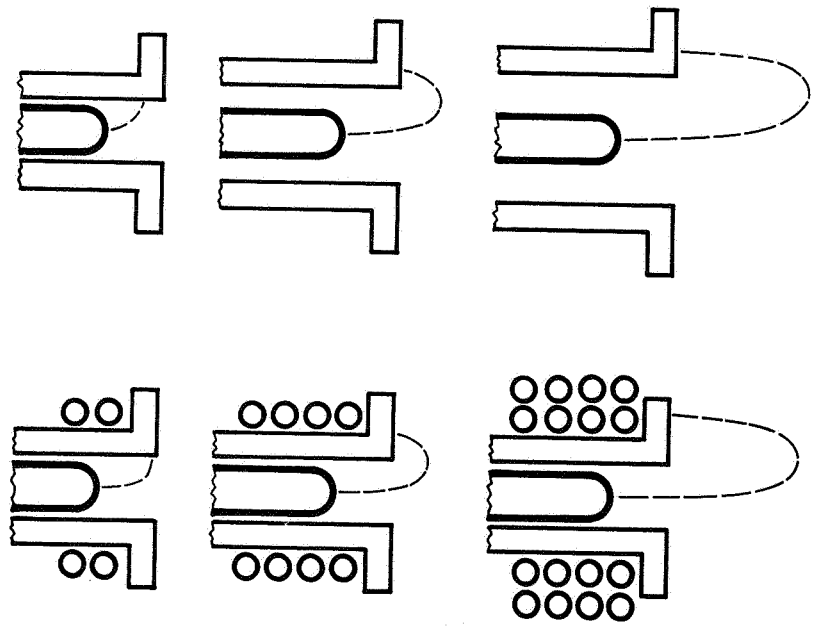

Figure 181. Increased Plasma Plume With Increased External Magnetic Field Strength or Increased Anode Throat Diameter

series of tests that confirm this behavior. During the tests other influences which affect the spreadout of the anodic arc foot have been identified (as for example the pressure in the arc chamber and in the vacuum tank). Other influences, such as the current, the power density of the arc, and the L/D ratio of the throat contribute to the position of the arc foot along the throat of the thrustor, and to the shape of the part of the discharge outside the throat (Figure 182). The information obtained during the tests, especially if augmented by additional experiments (as for example determining performance with various L/D ratios) seems sufficient to permit the design of a "best" geometry for practical operation, and may avoid at the same time conditions which might produce anomalous results. From the results of these tests it appears that the use of an external magnetic field, while sometimes desirable, is not generally worth its high cost in weight and complications and that if its effects are not carefully evaluated, anomalous test results are to be expected.

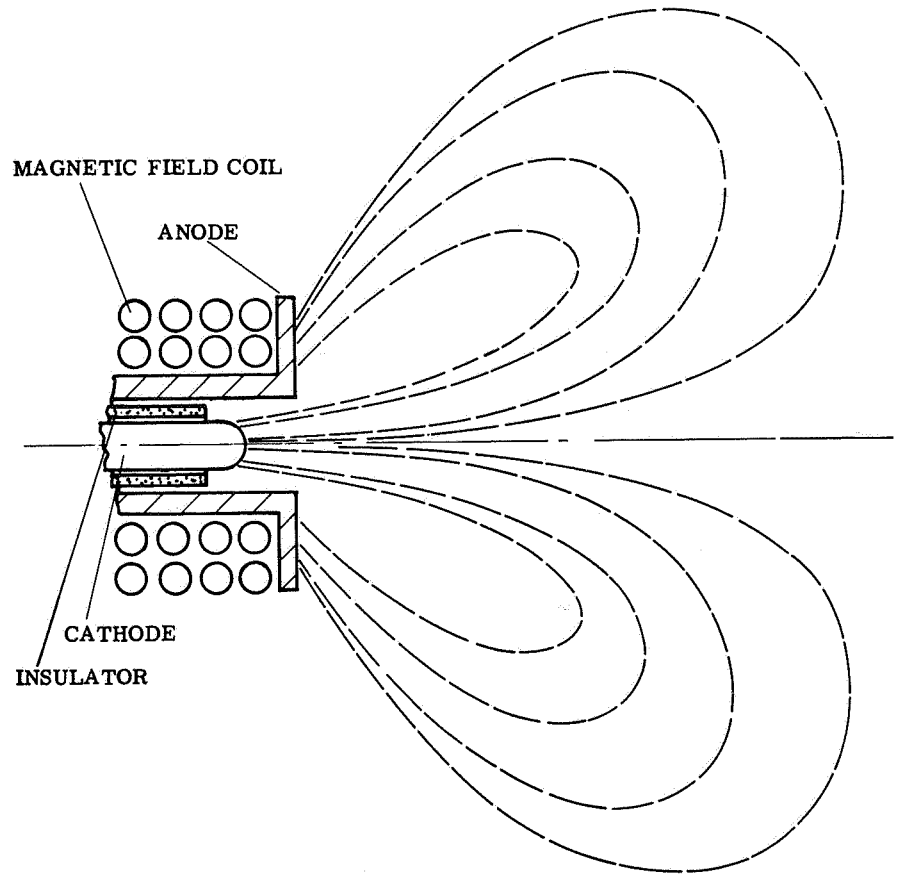

Figure 182. Assumed Typical External Arc Current Path for Various Operating Conditions

2.3.7 Effect of the External Environment on Anomalies

It is believed that a well-designed thermo-ionic thrustor will operate in space without difficulty and without showing up any anomaly in thrust output. But before a real space test is attempted, similar conditions should be reproduced in the laboratory. This space simulation is at the limit of terrestrial capabilities even without a thrustor in operation. But if a continuous flow of propellant (even a minimum quantity) must be pumped out continuously, the simulation of space conditions has to be ruled out. To avoid this huge vacuum problem and at the same time to have the possibility of testing without the anomalous effects caused by an imperfect vacuum, it has been suggested that cryogenically condensable propellants be used with a condensing system ahead of the vacuum pumps. It is our impression that this solution does not eliminate the problem of propellant recirculation (because around the thrustor, before the cryogenic baffles are reached, an appreciable pressure exists). There is also the likelihood that a large quantity of solid propellant will condense around the thrustor and the possibility of re-evaporation (as has been noted by some laboratories) with all the related problems. Aside from the pressure level, the environment of pure space is different because it is unlimited and does not contain conducting or magnetic walls. Our measurements have been done in what can be termed as "average" vacuum tanks. Figure 183 shows the dimensions of the vacuum tank used for testing with gaseous propellants while Figure 184 shows the dimensions of the vacuum tank used for testing with alkali metals and metal vapor testing. Figures 185 and 186 show the tank used to study the vaporization characteristics of lithium and potassium. In this section

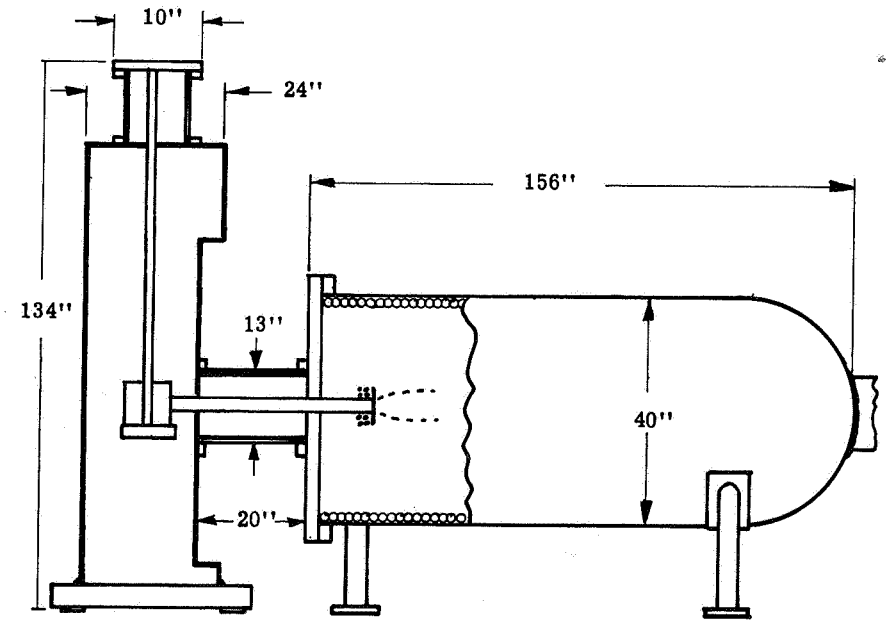

Figure 183. Dimensions of the Vacuum Tank Used for Testing Gaseous Propellants

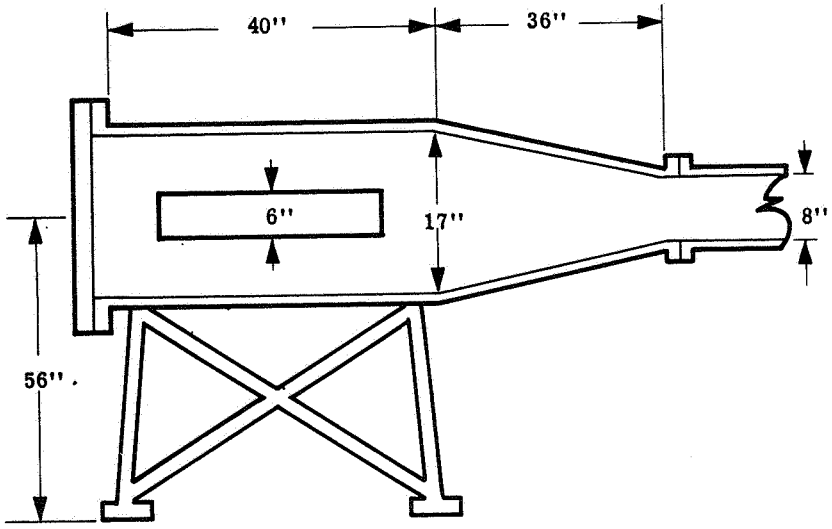

Figure 184. Dimensions of the Vacuum Tank Used to Test Alkali Metal Propellants

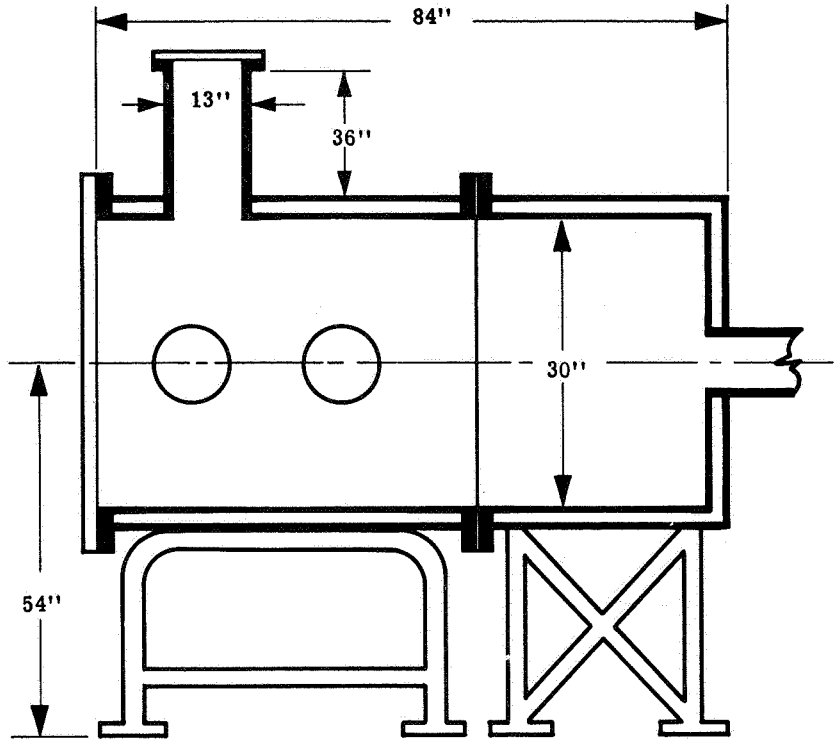

Figure 185. Dimensions of the Vacuum Tank Used to Study Vaporization of Lithium and Potassium

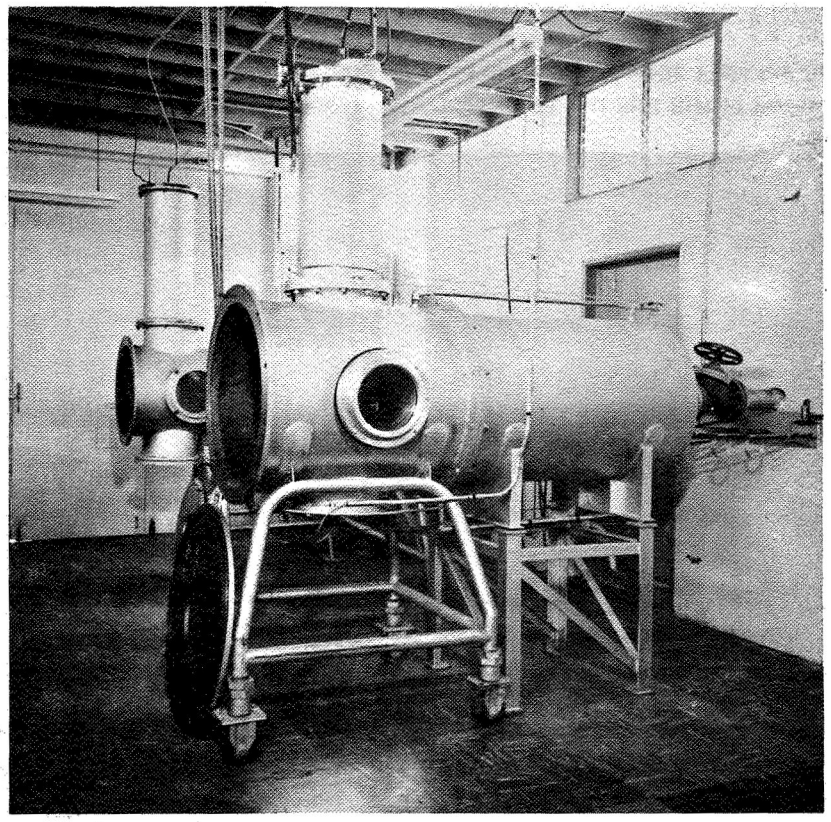

Figure 186. Photograph of Vacuum Tank Used for Studies of Vaporization Characteristics of Lithium and Potassium Propellants

we report on some unusual results obtained during the study of the effect of our external environment on the operation of thermo-ionic thrustors. The standard propellant used was hydrogen. An external magnetic field continuously variable from 500 to 16,000 gauss was available. The d.c. power used during the tests was continuously variable between 5 and 250 kw. As reported elsewhere a portion of the environment testing program has not been completed due to expiration of the contract (effect of various L/D ratios and operation without an external magnetic field). A detailed description and illustration of the environmental conditions might be useful to familiarize the reader with the various effects. During any particular run the mass flow is kept constant and the specific impulse is varied in fixed steps (1000, 2000, 4000, and 8000 seconds). The vacuum level in these tests is kept constant at about 25×10^{-3} Torr. The arc is always started at the minimum power at fixed mass flow and with a value of external magnetic field capable of assuring the maximum stability. The operation is gradually brought to different values of external magnetic field strength and to higher values of specific impulse. Short interruptions for instrument control are intermixed. At very low values of magnetic field and low power (specific impulse less than 1000 seconds) we find a characteristic operative condition illustrated in Figure 187. The explanation of the beam-like jet is not certain. The length (many feet) and the inclination (very stable) suggests the idea of a direct discharge to the end of the vacuum tank. When the intensity of the external magnetic field is increased slightly (always at low power), the long beam disappears and a normal jet is established. Figure 188 shows the effect of increasing the power input without

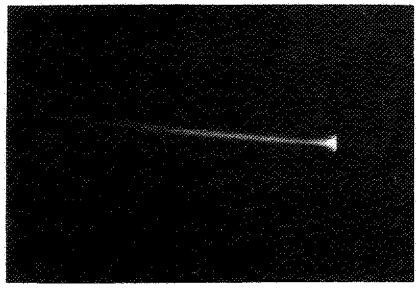

Figure 187. At Very Low Magnetic Field and Low Power, Beam-Like Jet is Formed

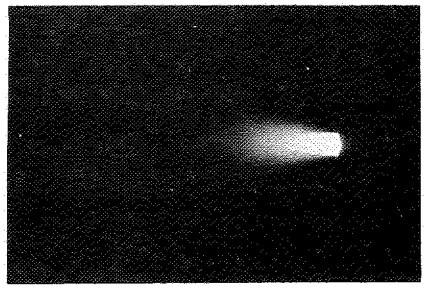

Figure 188. Increasing the Magnetic Field and the Power, a Regular Jet Appears

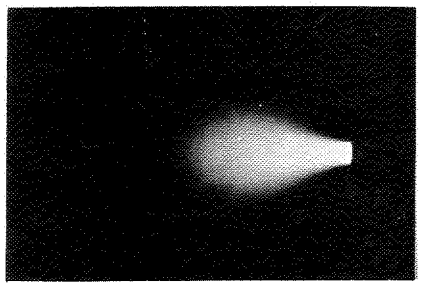

Figure 189. Increasing the Power at Constant Magnetic Field the Jet Remains Regular

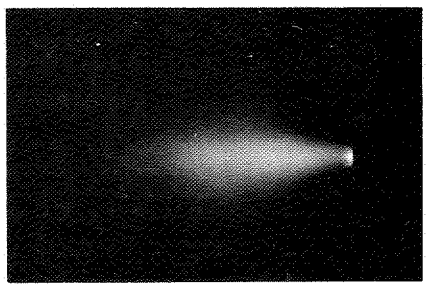

Figure 190. At Still Higher Power and the Same Magnetic Field the Jet is Still Regular

changing the intensity of the magnetic field. The jet expands in all directions maintaining the same regular proportions (Figure 189). With further increase of power but with the same intensity of the magnetic field, the jet expands further but does not change its proportions (Figure 190). If at this point the intensity of the magnetic field is increased the appearance and proportions of the jet begins to change. Around a luminous center jet a sort of a coaxial luminous glow appears that in the opinion of many investigators is indicating the path of the anodic current (Figures 191 and 192). It is to be noted that the increase of the magnetic field intensity produces a rapid increase in the arc voltage. At this point if the power input is increased the jet fattens maintaining its new form (Figures 193 and 194). The general proportions and appearance of the jet remains unvaried. Wher the magnetic field is increased again, the appearance of the jet changes once more. A beam-like central or cathodic part reappears with a strong anodic side lobe (Figure 195). The bending of this anodic lobe, more visible at slightly decreased input power (Figure 196), suggests that it is coming from the tank walls while the central beam discharges at the end of the tank. The separation is more marked when the input power is further decreased (Figure 197) and the central jet remains sharply directed toward the end of the tank, increasing in length if the magnetic field is further increased (Figure 198). During the conditions illustrated in Figures 195 and 198, the back part of the thrustor and its connections are covered by a sort of a glow discharge (using helium instead of hydrogen in analogous conditions the intensity of the glow is increased). Increasing still further the magnetic field and the arc power, a concentrated (arc type) discharge is established

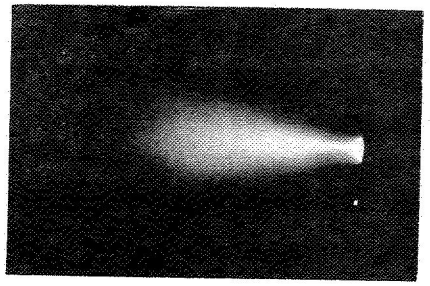

Figure 191. Increasing the Power and the Magnetic Field of Figure 190, an External Coaxial Anodic Path Appears

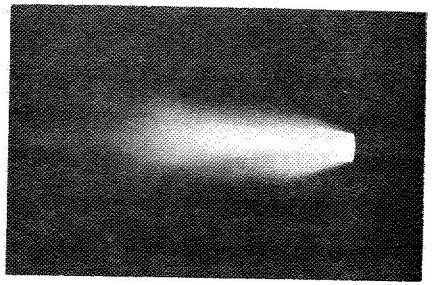

Figure 192. Increasing the Magnetic Field of Figure 191, the Jet Lengthens Conserving Its Shape

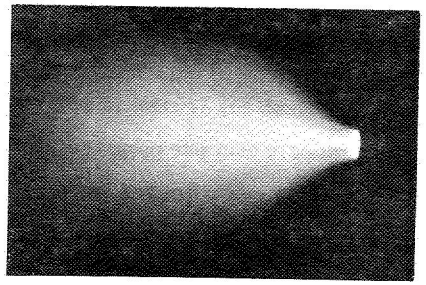

Figure 193. Increasing the Power of Figure 192 the Jet Fattens and the External Anodic Path Increases

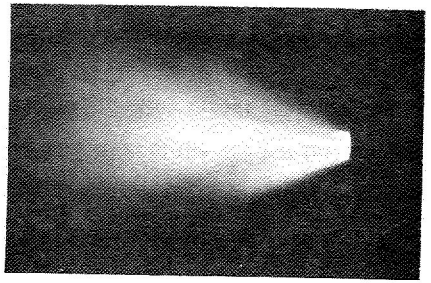

Figure 194. Increasing the Magnetic Field of Figure 193 the Jet Lengthens Conserving Its Shape

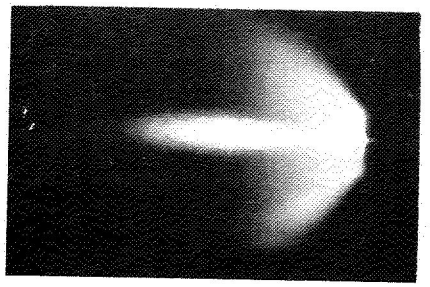

Figure 195. Increasing the Magnetic Field of Figure 194 the Anodic Coaxial Path Separates From the Central Beam

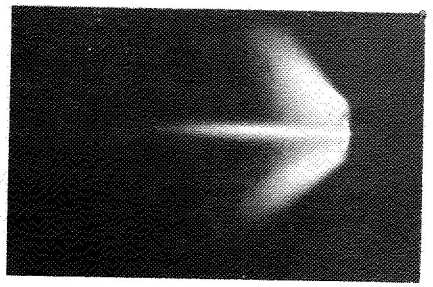

Figure 196. Decreasing the Power of Figure 195 at the Same High Magnetic Field the Separation is Improved

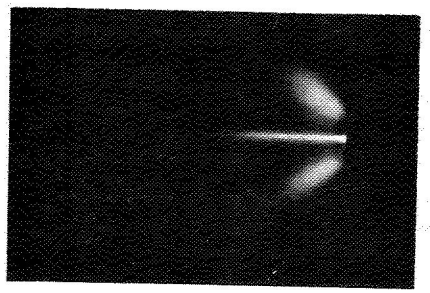

Figure 197. At the Lower Power of Figure 196 and the Same Magnetic Field the Separation is Very Sharp

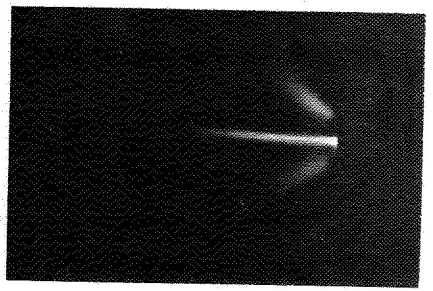

Figure 198. At Still Lower Power of Figure 197 and Higher Magnetic Field the Central Jet Extends Toward the End of the Tank

between the side lobe and the vacuum tank and another appears in the back between tank and electrodes as illustrated in Figure 199. It was noted that in this condition the apparent thrust values increase. To check the validity of the measurement an artificial current of a few hundred amperes was applied between the two points illustrated in Figure 200. An interaction with the external magnetic coil resulted producing a false thrust reading. The same variation was obtained by applying the same current (with a completely separated and insulated circuit) during operation of the arc but further tests are necessary for quantitative results. These false thrust readings can be important during operation at very low mass flow if in these cases the value of the current should be much reduced. As pointed out before, by increasing the throat diameter, similar cases can be repeated at relatively low values of the external magnetic field. We have noticed that this discharge can have an influence in the determination of the thermal efficiency. In other words, if a discharge to the vacuum tank exists, the relative losses are subtracted from the anode losses (measured in the thrustor cooling) making the thermal efficiency appear higher (Figure 201). Further tests are necessary to confirm this behavior, but it is believed that the analysis of these phenomena can improve the precision of these measurements. The need for an insulated tank and completely insulated thrustor components and thrust stand deserves attention (Figure 202). The use of special technology to avoid the spreading of the arc outside the thrustor or the related harmful effects seems also very worthwhile. The study of mass entrainment and other environmental factors influencing the precision of thrust measurements were not completed before expiration of this work.

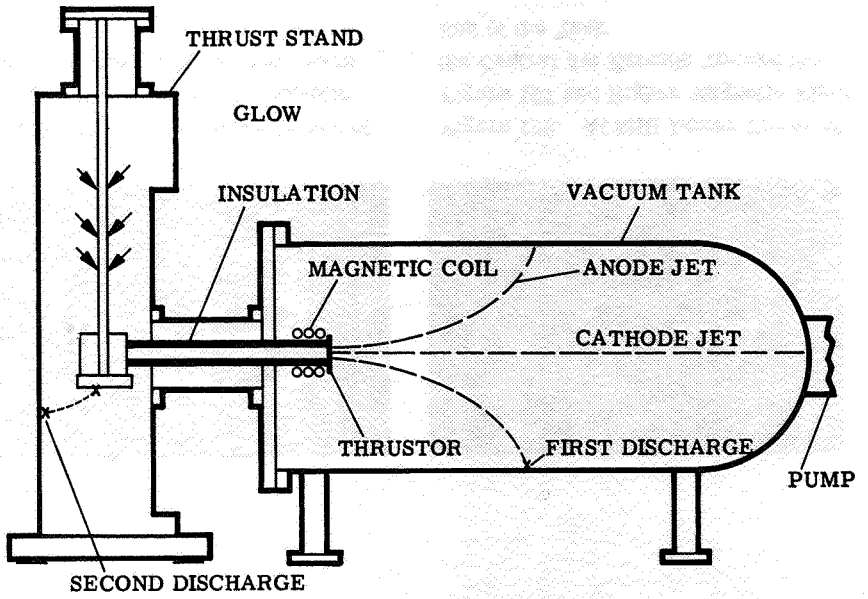

Figure 199. At Very High Magnetic Fields the Jet Discharges to the Vacuum Tank in Two Points

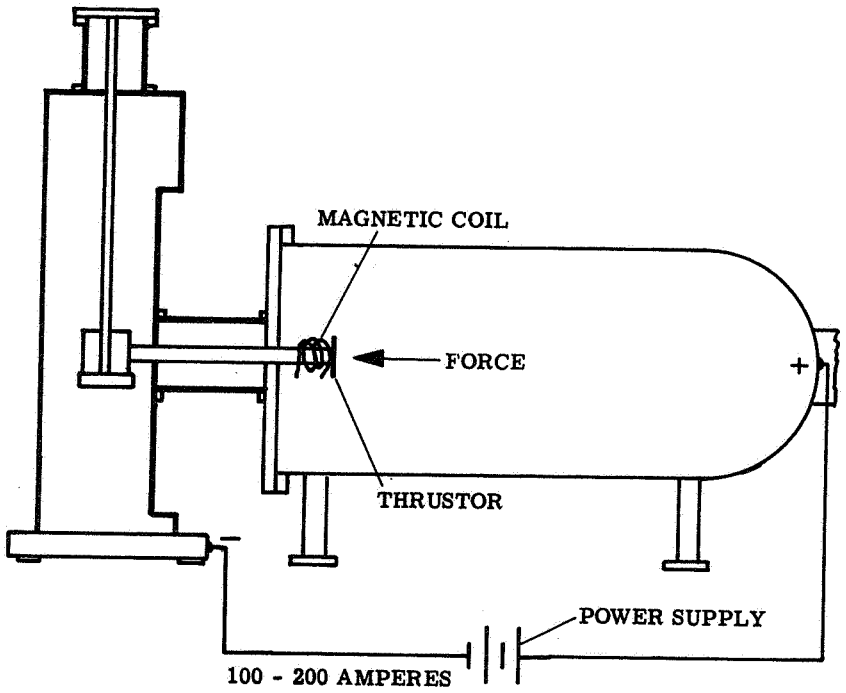

Figure 200. Applying an External Current to the Vacuum Tank Interaction With the Magnetic Coil has Been Detected

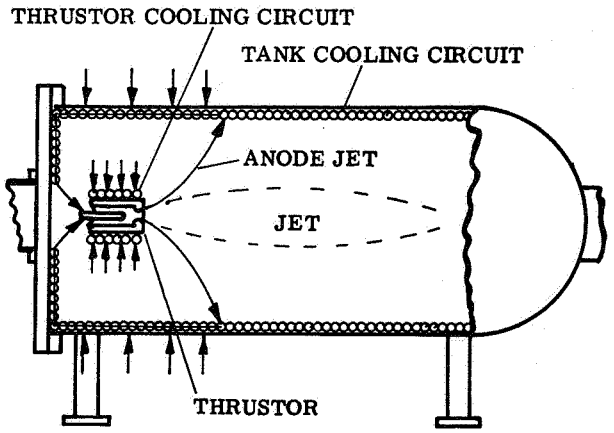

Figure 201. A Partial Discharge to the Tank May Apparently Decrease the Thermal Losses

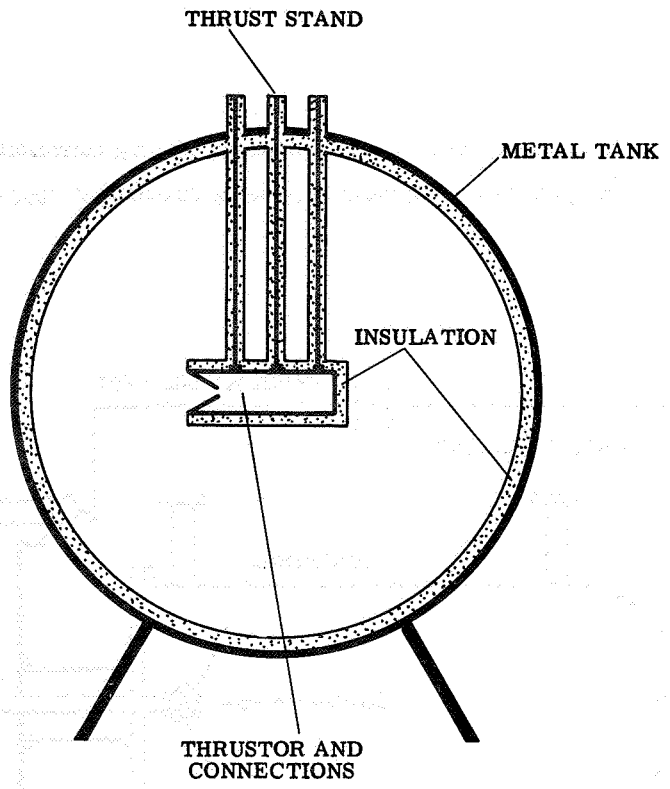

Figure 202. Schematic of Totally Insulated Thrust Stand Facility With Attached Thrustor Suggested for Improved Future Experimentation

3.0 ANALYTICAL INVESTIGATION

The theoretical considerations presented here are of a semi-quantitative nature. Even if one is willing to accept a one-dimensional continuum model of the flow, the analytical problem is still a formidable one and is presently beyond the reach of exact analytical methods. The theoretical work undertaken here has been aimed at understanding some of the more basic aspects of the problem. The effect of the applied and self-induced magnetic field on plasma motion and current distribution has been partially clarified. Energy exchange between electrons and ions has been studied primarily to see if a thermal model of the arc is tenable. An approximate calculation of thrust based upon the momentum equation and displaying explicitly the effect of magnetic compression at the electrode surfaces is discussed. The utility of formulas of this kind is doubtful and it is argued that an approach that makes direct use of the energy equation where the dominant heat transfer and ionization losses can be introduced explicitly is preferable.

The theoretical analysis contained in Section 3.1 is the work of R. G. Jahn.* It is presented in a self-contained form and may be read without reference to other parts of the study. B. Podolsky** has worked on the analytical problems in the early phases of the study but was unable to continue due to illness.

---

*R. G. Jahn, Forrestal Research Center, Princeton University, Princeton, New Jersey.

**B. Podolsky, Physics Dept., Cincinnati University, Cincinnati, Ohio.

3.1 An Electron's View of the MPD Arc Jet

At the present time, the true significance of the magnetoplasmadynamic arc jet for space propulsion is clouded by a certain amount of experimental ambiguity and controversy on the one hand, and by a general theoretical intractibility on the other. For example, one may still argue such fundamental questions as whether the superior performance of these devices is a result of a genuine electromagnetic acceleration process, a la the classical crossed-field accelerators; an enhanced electrothermal process wherein the electrodes are protected, and the exhaust channeled by magnetic confinement; or a totally spurious interaction of the arc pattern with the laboratory environment, such as an entrainment of the background gas in the vacuum tank, or a magnetic or electric interaction between the arc pattern and the tank walls. Likewise, the role of externally imposed magnetic fields in the physical processes and terminal performance of the arc is far from clear, and the relative importance of Lorentz currents, Hall currents, and ion currents throughout the arc pattern has not yet been completely defined by either experiment or theory.

These difficulties in basic understanding clearly stem from the large number of terminal parameters which can control the physical interactions, superimposed upon the essential complexity of the plasma state itself. The experimenter has under his control such inputs as gas type and mass flow, electrode geometry and material, external circuit characteristics and arc power level, exhaust pressure, and external magnetic field strength and configuration. The theorist, on the other hand, ultimately must deal in such

microscopic parameters as electron densities and temperatures, collision frequencies and ionization cross-sections, and internal electric and magnetic field configurations, or in various continuum parameters such as electrical conductivities and diffusion coefficients that are based on the particle properties. The gulf between these experimental and theoretical positions is extreme, and must eventually be bridged by detailed interior diagnostic studies from the one side, and by judiciously cast analytical models from the other, if sound progress in the exploitation of this device is to be made.

It is the purpose of this note to cast one such simplified theoretical model, admittedly crude in many respects, partly for the purpose of discussing a few of the more evident characteristics of MPD arcs, namely, their current configurations, their thrust production mechanisms, and their tendencies in electrode erosion, and partly to outline the need for diagnostic experiments and more sophisticated analyses. The point of view will be microscopic, in the spirit that if one can ascertain how an isolated electron, or ion, will respond to a given environment, he then can make a more intelligent guess about the macroscopic behavior of the plasma. On this basis the dispute between the pure electromagnetic, and the electrothermal plus magnetic nozzle interpretations is deferred until a later stage, in the sense that this distinction relates to the collective motion of the particle swarms, rather than to the individual trajectories.

To narrow the analysis at the outset, we will consider only the conventional coaxial arc jet configuration with negative center electrode, and presume complete azimuthal symmetry in all electric, magnetic and flow velocity fields, in all thermodynamic properties, and in the charge density and current density

distributions. The working gas will be hydrogen, completely dissociated and totally ionized at all points of interest in the field. We will confine our attention to the four permutations of low and high arc currents, with and without externally applied magnetic fields. Notation will be introduced as needed.

We will first express the Hall parameter in terms of the prevailing magnetic field, ion density and electron temperature. The processes of current conduction and thrust production in steady electric and magnetic fields will then be expressed in terms of this parameter. To apply this formulation to the MPD arc configuration, we will next pose a model of the electron density and temperature fields based on experimental data and physical reasoning. The Hall parameter and gyro radii will then be mapped over the flow field for the four cases mentioned above, using the best available estimates for the relevant parameters. From these and the foregoing general discussion, inferences will be drawn about the current pattern and thrust contributions in the arcs. Finally, suggestions for elaboration of the theoretical approach, and for the most critical experimental measurements will be offered.

3.1.1 Hall Parameter and Gyro Radii

With the exception of the electron density and temperature, the most important index controlling the current conduction and thrust production processes is the Hall parameter, relating the gyro frequency of the electrons to their collision frequency with ions:

$$\Omega = \frac{\omega}{\nu} = \frac{e\,B}{m}\, n\, Q\, \bar{v} \qquad (1)$$

Here m is the particle mass, n the number density of ions or electrons, e the electronic charge, B the magnetic induction field, Q the Coulomb cross-section, and $\bar{v}$ the appropriate mean particle velocity. For the gyro frequency we have directly,

$$\omega = 1.76 \times 10^{7}\, B \qquad (\text{sec}^{-1} \text{ for } B \text{ in gauss}) \qquad (2)$$

The Coulomb cross-section may be written[14]

$$Q = \frac{\pi e^4}{(4\pi\epsilon_0)^2\, \xi^2} \ln \Lambda \qquad (\text{m k s system}) \qquad (3)$$

where $\epsilon_0 = 8.85 \times 10^{-12}$, ξ is the relative kinetic energy of the two colliding particles, and $\ln \Lambda = \ln \left[\frac{8\pi\epsilon_0 \xi}{e^2} \cdot r_0 \right]$ where r_0 is an artificial cutoff parameter usually taken as the Debye length, $\lambda_D = \frac{\epsilon_0 k T}{n e^2}$. $\ln \Lambda$ is a very gently varying function over a broad range of electron densities and temperatures, and is tabulated in many references.[14, 15] For our purposes it may be given the value 10. We thus have

$$Q = \frac{6.5 \times 10^{-13}}{\xi^2} \qquad (\text{cm}^2 \text{ for } \xi \text{ in electron volts}) \qquad (4)$$

In most regions of the arc, the electrons may be expected to have a Maxwellian energy distribution, and we can define an average cross-section, evaluated at the mean thermal velocity,

$$\bar{v} = \left(\frac{8\,k\,T}{\pi\,m}\right)^{1/2} = 6.2 \times 10^5\, T^{1/2}, \tag{5}$$

Thus:

$$\bar{Q} = \frac{5.4 \times 10^{-5}}{T^2} \qquad (\text{cm}^2 \text{ for } T \text{ in } ^\circ\text{K}) \tag{6}$$

Using the same mean velocity, the collision frequency may be written

$$\bar{\nu} = n\,\bar{Q}\,\bar{v} = \frac{33.5\,n}{T^{3/2}} \tag{7}$$

and the Hall parameter becomes

$$\Omega = \frac{\omega}{\bar{\nu}} = 5.3 \times 10^5\, \frac{B\,T^{3/2}}{n} \tag{8}$$

One might consider computing a similar parameter for the ions, but within the framework of the chosen model, their collision frequency is ill defined. While an ion indeed experiences collisions with other ions at a rate,

$$\nu^+ = \sqrt{2}\,n\,Q\,\bar{v}^+ \tag{9}$$

these serve primarily to maintain isotropy and equilibrium in the ion random thermal motion, rather than exert any damping on an organized streaming motion such as is involved in an ion current. Ion-electron collisions detract no significant momentum from the ion motion, and ion-neutral collisions, which

could impede the streaming, are excluded by the assumption of complete ionization. Ion current patterns will thus be determined by other factors, including electrode geometry, which will need be examined in each particular case.

The gyro radii of both the ions and electrons can have a bearing on the current conduction, thrust production, and electrode erosion processes when they become comparable with critical dimensions of the arc, such as the inter-electrode spacing, cathode tip diameter, current sheet width, etc. These are given by

$$r_B = \frac{m\,v_\perp}{e\,B} = \frac{v_\perp}{\omega} \tag{10}$$

$$r_B^+ = \frac{m^+\,v_\perp^+}{e\,B} = \frac{v_\perp^+}{\omega^+} \tag{11}$$

where $v_\perp$ denotes the component of the particle's velocity perpendicular to the locally prevailing magnetic field. To obtain an order of magnitude, we can again insert the mean thermal speeds:

$$r_B = 0.035\,\frac{T^{1/2}}{B} \qquad (\text{cm for } B \text{ in gauss}) \tag{12}$$

$$r_B^+ = 1.46\,\frac{(T^+)^{1/2}}{B} \qquad (\text{cm for } B \text{ in gauss}) \tag{13}$$

If the ion has acquired streamwise speed in excess of $(v^+)_{th}$, its gyro radius will be correspondingly larger

$$(r_B^+)_u = \frac{u}{\omega} = 1.04 \times 10^{-4}\,\frac{u}{B} \qquad (\text{cm for } B \text{ in gauss}) \tag{14}$$

3.1.2 Conduction Processes

An isolated charged particle in uniform applied electric and magnetic fields will execute a general spiral motion whose details depend on the magnitude and orientations of the fields and on the initial velocity and charge of the particle.[15] In the special case of orthogonal E and B fields, the particle orbit is a cycloid, advancing in the $\vec{E} \times \vec{B}$ direction at a net drift speed of $\frac{E}{B}$, and of transverse dimension $2\, r_B$. Addition of a component of electric field parallel to B protracts this cycloid, parabolically in time, along the direction of this component, $E_{\parallel}$, while the cross-field drift speed and gyro radius remain determined by $E_{\perp}$. Positive and negative charges spiral in opposite sense, follow $E_{\parallel}$ in opposite sense, but drift in the same direction, $\vec{E}_{\perp} \times \vec{B}$, at a speed, $\frac{E_{\perp}}{B}$, independent of their mass. Such motion continues until interrupted by a collision, at which time the particle begins a new trajectory, displaced on the average about one gyro radius along $E_{\perp}$.

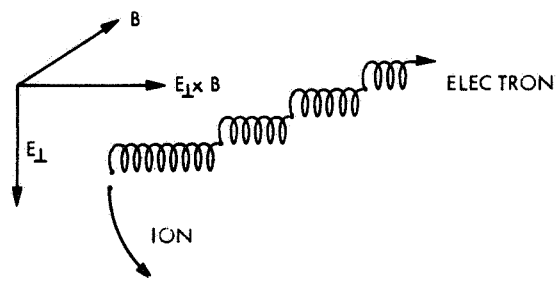

The ratio of cross-field drift motion to motion along $E_{\perp}$ thus is just given by the Hall parameter, Ω.

The current constituted by a swarm of electrons, each executing motions of this sort superimposed on their initial random thermal motions parallel to B, is essentially an algebraic summation, and thus also determined by Ω. For a swarm of ions, the identity of the colliding particles makes the net motion effectively collisionless, i.e., entirely cross-field drift, provided the electrode surfaces are far away in comparison to r_B^+. Near the electrodes, current can be carried parallel to $\vec{E}$ by those ions within one gyro radius of the surface. For electrode separation $d << r_B^+$, all ion current will be essentially along $\vec{E}$ lines:

To illustrate, let us consider a few special cases of conduction between two plane parallel electrodes a distance d apart:

Case 1: $\Omega << 1$; $\vec{E} \perp \vec{B}$; $d << r_B^+$

Let $\vec{B}$ be along $\vec{z}$, $\vec{E}$ along $\vec{y}$

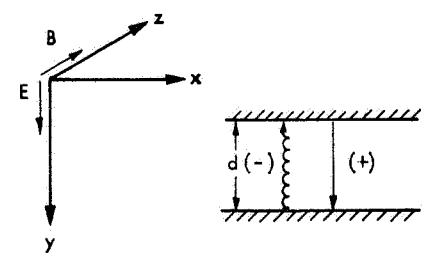

Electron Current	Ion Current
$j_x = \Omega\, j_y \approx 0$	$j_x^+ \approx \frac{d}{r_B^+}\, j_y^+ \approx 0$
$j_y = -n e \bar{v}_y = +\left(\frac{n e^2}{m \nu}\right) E = \sigma_o E$	$j_y^+ = n e \bar{v}_y^+ \approx n e \left(\frac{e E d}{2 m^+}\right)^{1/2}$
$j_z = 0$	$j_z^+ = 0$

The relative importance of the ion current as written can be estimated by rewriting and comparing with $\sigma_o E$:

$$j^+ = n e \bar{v}^+ \approx n e \left(\frac{e E d}{2 m^+}\right)^{1/2} \approx \sigma_o E \left(\frac{m}{m^+}\right) \left\{\frac{\nu d}{v_e}\right\} \qquad (15)$$

where $v_e = \left(\frac{e E d}{m^+}\right)^{1/2}$ is the speed acquired by an ion falling through a potential drop Ed. In problems of our interest, $\nu \approx 10^9 \text{ sec}^{-1}$, $d \approx 1$ cm, $E d \approx 100$ volts, hence j^+ $0.1\, \sigma_o E$. Note that the ion current quoted here requires an adequate supply of ions to be released near the anode and consumed near the cathode, by no means a trivial requirement in practical situations. If this cannot be satisfied, the ion current will be correspondingly reduced.

Case 2: $\Omega >> 1$; $\vec{E} \perp \vec{B}$; $d << r_B^+$

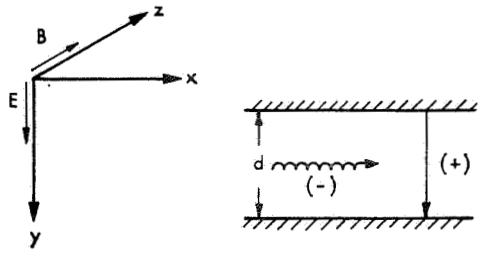

Electron Current	Ion Current
$j_x = -n e \bar{v}_x = -n e \frac{E}{B} = -\sigma_o E/\Omega$	$j_x^+ \approx \frac{d}{r_B^+} j_y^+ \approx 0$
$j_y = j_x/\Omega \approx \sigma_o E/\Omega^2 \approx 0$	$j_y^+ = n e \bar{v}_y^+ \approx n e \left(\frac{e E d}{2 m^+}\right)^{1/2}$
$j_z = 0$	$j_z^+ = 0$

In this situation, the conduction current is carried primarily by the ions; the electrons produce a nearly pure Hall current.

Case 3: $\Omega >> 1$; $\vec{E} \perp \vec{B}$; $d >> r_B^+$

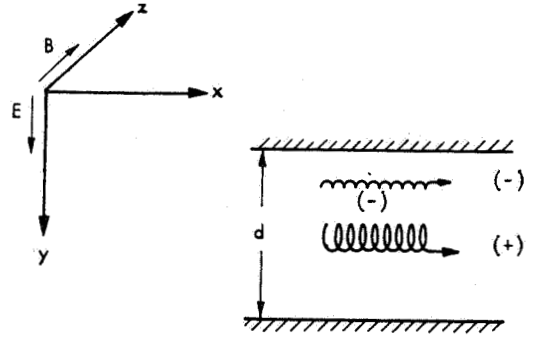

Electron Current	Ion Current
$j_x = -n e \bar{v}_x = -n e \frac{E}{B}$	$j_x^+ = n e \bar{v}_x^+ = n e \frac{E}{B} = -j_x$
$j_y = j_x/\Omega \approx 0$	$j_y^+ \approx \frac{r_B^+}{d} j_y^+ \approx 0$
$j_z = 0$	$j_z^+ = 0$

Here both ions and electrons are constrained to cross-field drift. Little conduction current flows and the drift currents algebraically cancel.

Case 4: $\Omega >> 1$; $\vec{E}$ not $\perp \vec{B}$; $d << r_B^+$

Let $\vec{B}$ lie along $\vec{z}$, $\vec{E} \times \vec{B}$ along $\vec{x}$

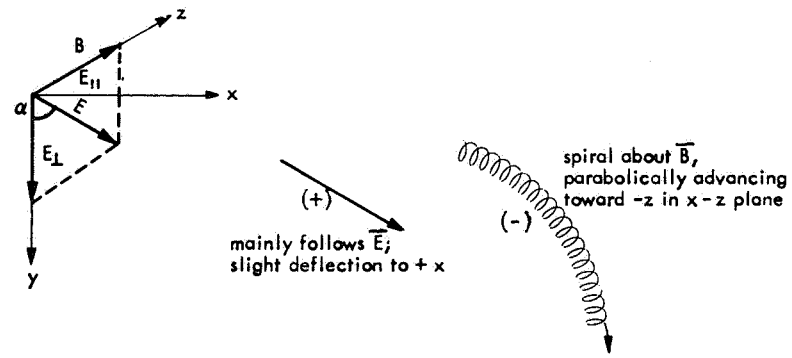

Electron Current	Ion Current
$j_x = -n e \bar{v}_x = -n e \frac{E_\perp}{B} = -\sigma_o \frac{E_\perp}{\Omega}$	$j_x^+ \approx \frac{d}{r_B^+} j_y^+ \approx 0$
$j_y = j_x/\Omega \approx 0$	$j_y^+ = n e \bar{v}_y^+ \approx n e \left(\frac{e E_\perp d}{2 m^+}\right)^{1/2}$
$j_z = n e \bar{v}_z = +\sigma_o E_{\parallel}$	$j_z^+ = n e \bar{v}_z^+ \approx n e \left(\frac{e E_{\parallel} d}{2 m^+}\right)^{1/2}$

In this, the most general configuration of uniform fields, we acquire a component of conduction current along $E_{\parallel}$ that is unimpeded by the $\vec{B}$ field. The total conduction current, i.e., the current parallel to $\vec{E}$ is now

$$j_{\parallel} = j_y \cos\alpha + j_z \sin\alpha \approx \sigma_o E \sin^2\alpha \tag{16}$$

if the ion current is negligible compared to $\sigma_o E_{\parallel}$.

The above concepts can be expressed in a more sophisticated manner for the plasma as a whole via a conductivity tensor relating the current to the effective local field:

$$\vec{j} = \underline{\underline{\sigma}}\, \vec{E}' = \underline{\underline{\sigma}}\, (\vec{E} + \vec{u} \times \vec{B}) \tag{17}$$

where $\vec{u}$ is the center of mass streaming motion of the gas. In the rectangular coordinate system used above, for example, the conductivity tensor may be written

$$\sigma = \sigma_o \begin{pmatrix} \frac{1}{1+\Omega^2} & \frac{-\Omega}{1+\Omega^2} & 0 \\ \frac{\Omega}{1+\Omega^2} & \frac{1}{1+\Omega^2} & 0 \\ 0 & 0 & 1 \end{pmatrix} \tag{18}$$

where again the scalar conductivity coefficient $\sigma_o = \frac{n e^2}{m \nu}$. [More precise calculation adds a coefficient of 1.8 to this definition[2]]. Note that ion motion cannot contribute to the conductivity tensor as defined, since it is indistinguishable from the center of mass motion, $\vec{u}$.

3.1.3 Thrust Mechanisms

At this point we will attempt to identify the components of thrust contributed by the electron and ion motions in the four cases discussed in the previous section. These may be assigned either by establishing the net force exerted on the particles by the fields, or by considering the rate at which their organized drift motion transfers momentum by collision:

Case 1: $\Omega << 1$; $\vec{E} \perp \vec{B}$; $d << r_B^+$ (Refer to earlier sketch)

Electron Contributed Thrust	Ion Contributed Thrust
$F_x = -n(B e \bar{v}_y) = +j_y B$	$F_x^+ = n(B e \bar{v}_y^+) = j_y^+ B$
$F_y = -n(e E) + n(B e \bar{v}_x)$	$F_y^+ = +n(e E) - n e B \bar{v}_x^+$
$= -n e E + j_y B/\Omega \approx -n e E$	$\approx n e E \approx -F_y$
$F_z = 0$	$F_z^+ = 0$

The "electrostatic" thrust components are seen just to balance each other, leaving the familiar Lorentz thrust $(j + j^+)$ B in the $\vec{E} \times \vec{B}$ direction.

Case 2: $\Omega >> 1$; $\vec{E} \perp \vec{B}$; $d << r_B^+$

Electron Thrust	Ion Thrust
$F_x = n(m \bar{v}_x)\nu \approx n m \nu \frac{E}{B}$	$F_x^+ = n(B e \bar{v}_y^+) = j_y^+ B$
$\approx (n e E)/\Omega \approx 0$	
$F_y = -n(e E - B e \bar{v}_x) \approx 0$	$F_y^+ = +n e E - n e B \bar{v}_x^+ \approx n e E$
	$\approx j_x B$
$F_z = 0$	$F_z^+ = 0$

Here the $\vec{B}$ field has restrained the y - migration of the electrons, leaving the ions free to gain momentum in that direction. The relative importance of the x component of ion thrust will depend on the particular electrode spacing and field intensity.

Case 3. $\Omega >> 1$; $\vec{E} \perp \vec{B}$; $d >> r_B^+$

Electron Thrust	Ion Thrust
$F_x \approx 0$ as in Case (2)	$F_x^+ = \dot{n} m^+ \bar{v}_x^+ = \dot{n} m^+ \frac{E}{B}$ (see below)
$F_y \approx 0$ as in Case (2)	$F_y^+ = +n e E - n e B \bar{v}_x^+ \approx 0$
$F_z = 0$ as in Case (2)	$F_z^+ = 0$

In a strictly steady state, and in the absence of collisions, F_x^+ would be zero, since the mean momentum of the ions does not increase once their $\vec{E} \times \vec{B}$ drift has been established. In any finite device, however, ions would need be supplied at a rate $\dot{n}$, and each of these would have a momentum increment added in amount $m^+ E/B$.

<u>Case 4:</u> $\Omega >> 1$; $\vec{E}$ not $\perp \vec{B}$; $d << r_B^+$

Electron Thrust	Ion Thrust
$F_x = n(m\bar{v}_x)\nu \approx n e E_\perp/\Omega \approx 0$	$F_x^+ = n(B e \bar{v}_y^+) = j_y^+ B$
$F_y = -n(e E_\perp - B e \bar{v}_x) \approx 0$	$F_y^+ = n e E_\perp - n e B \bar{v}_x^+$
	$\approx n e E_\perp \approx j_x B$
$F_z = -n e E_{\parallel}$	$F_z^+ = +n e E_{\parallel} = -F_z$

The cancellation of the electron and ion contributions to the z component leaves these results identical to Case 2 above if $E_\perp$ is substituted for E The sole effect of adding a component of $\vec{E}$ parallel to $\vec{B}$ has been to rotate the $\vec{E}$ vector with respect to the total thrust $\vec{F}$ through the angle α If one is specifically interested in the components of thrust parallel and perpendicular to $\vec{E}$, these follow directly from the geometry:

$$F_{\parallel} = F_y \cos\alpha \approx n e E_\perp \cos\alpha \approx n e E \cos^2\alpha \tag{19}$$

$$F_\perp = \left[(F_y \sin\alpha)^2 + (F_x)^2\right]^{1/2} \approx n e E \cos\alpha \sin\alpha \tag{20}$$

again neglecting the ion current. Note that $F_\perp$ is maximized for $\alpha = 45°$

In the following sections we will apply in qualitative form the results of these special problems, in those regions of the arc where they apply.

3.1.4 Density, Temperatures, and Field Patterns in the MPD Arcs

A. Charge Densities

In principle, the relations presented in the two previous sections would permit some determination of the current density patterns in the arc, and thence the thrust densities, if the charge density n, electron and ion temperatures T, T^+, fields $\vec{E}$, $\vec{B}$, and flow velocity $\vec{u}$ were known over the regime of interest. All of these are interrelated in a badly non-linear fashion, however, and gross approximations must be made before the approach can be pursued. $\vec{E}$ and $\vec{B}$ are partially under control of the experimenter and partially derived from the current, charge density, and stream velocity patterns developed in the arc. In following sections, we will consider a few special cases. The stream velocity $\vec{u}$ is determined by the entire complex acceleration process and we will only note that it rises from a negligible value at inlet, monotonically through the arc region to some exhaust value appropriate to the desired specific impulse.

For the charge densities and temperatures we must also use crude models. Consistent with the assumption of full dissociation and ionization, and perfect expansion at the arc nozzle exit, we might assume equal densities of electrons and ions throughout the field, at a value sufficient to balance the ambient gas pressure in the vacuum tank. That is

$$n\,k\,(T + T^+) = p_t \tag{21}$$

This would shift the burden to an estimation of T and T^+ throughout the arc, compounding any error made in those choices. Physically, however, we note

that while decreases in temperature will tend to increase n in (21), some recombination attendant such cooling will tend to lower n, thereby weakening the temperature dependence. Further, radial magnetic pressures developed by the current patterns should be added to p_t in (25), further increasing n in the hotter, current carrying regions.

The only available measurements of electron densities in remotely relevant arc environments support these presumptions. Kelly[16] has found electron densities in argon plasmajets at mass flows from 300 to 500 milligrams/sec, arc currents from 1000 to 1500 amperes, that show surprisingly small axial decay over one meter of jet length. Radial variations in n are found to be larger, but still less than one order of magnitude over the domain of interest. Our ignorance of the detailed situation thus justifies no more elaborate assumption than that of uniform charge densities throughout the field, at some value consistent with the arc dimensions, mass flow rate, and exhaust velocity:

$$n = \frac{\dot{m}}{M\,u\,A} \tag{22}$$

where m is the mass flow, M the atomic weight, and A a characteristic cross-sectional area of the arc. In the MPD devices of interest, n thus is of the order of 10^{14} cm^{-3}

B. Temperatures

Assignment of temperature profiles in the arc plume is also highly presumptive. Kelly[16] has found an exponential decay of electron temperature along the jet axis, with relatively slight radial decay. Jacobs[17] has found electron and ion temperatures remain in equilibrium in argon jets at high pressures,

but T decays less rapidly than T^+ at pressures below 100 mmHg. We will thus presume

$$T = T_o e^{-\frac{z}{\beta}} \tag{23}$$

$$T^+ = T_o^+ e^{-\frac{z}{\beta^+}} \tag{24}$$

where T_o, T^+ are the values at the orifice, z is the axial dimension from the orifice, and β, β^+ are characteristic cooling dimensions. It might be presumed that β is of the order of the luminous dimension of the jet, and β^+ somewhat shorter. Similar radial decay factors could be incorporated, but this algebraic complication will add little to the following semi-quantitative analyses.

C. Self-Induced Magnetic Fields

For coaxial arc of azimuthal symmetry, the self magnetic field readily follows from Maxwell's relations to be entirely azimuthal, and of magnitude dependent only on the radial position and total current enclosed by a circle at that radius:

$$B_\theta' = \frac{\mu_o \hat{I}}{2\pi r} = 0.2\,\frac{\hat{I}}{r} \qquad \text{(gauss for I in amps, r in cm)} \tag{25}$$

at a given radius between the electrodes, the enclosed current $\hat{I}$ will be a monotonically decreasing function of axial position, z, depending on the particular plume pattern. B_θ' (r, z) will mirror this dependence.

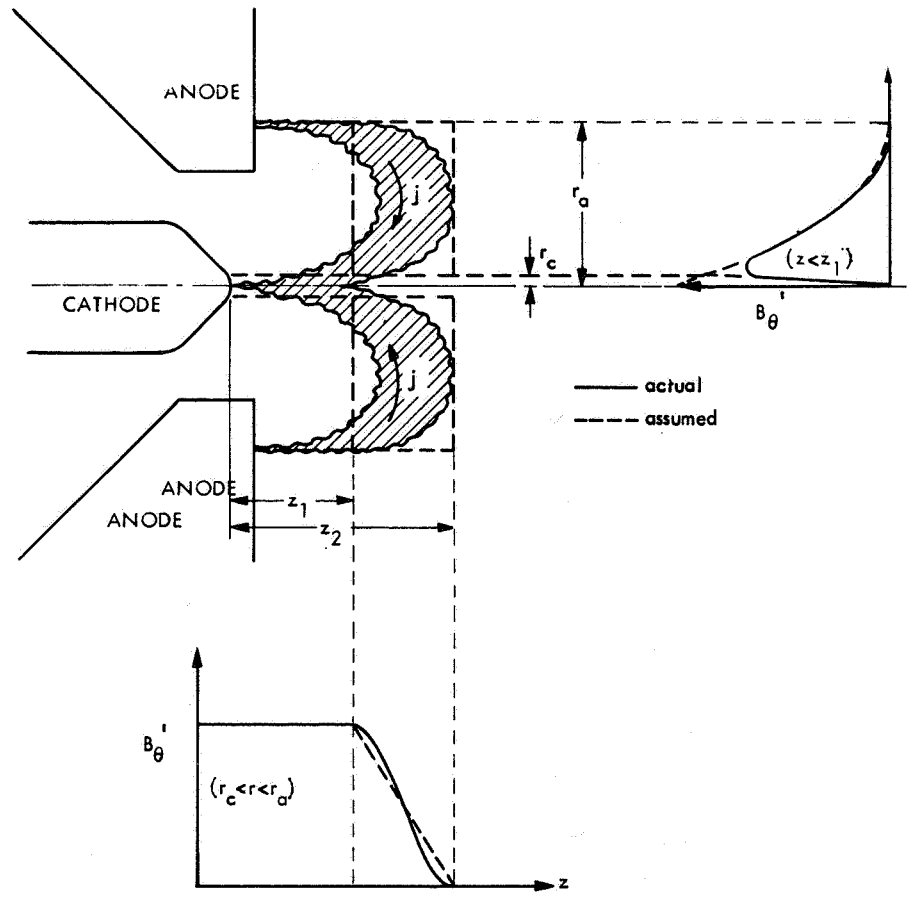

In our subsequent calculations we will simplify the current and induced field distributions drastically. For example, we may use:

$$\hat{I} = \begin{Bmatrix} I\left(\frac{r}{r_c}\right)^2 \\ I \\ 0 \end{Bmatrix} \quad \text{for } z < z_1; \quad \begin{Bmatrix} r < r_c \\ r_c < r < r_a \\ r > r_a \end{Bmatrix}$$

$$\hat{I} = \begin{Bmatrix} I\left(\frac{r}{r_c}\right)^2 \left(\frac{z_2 - z}{z_2 - z_1}\right) \\ I\left(\frac{z_2 - z}{z_2 - z_1}\right) \\ 0 \end{Bmatrix} \quad \text{for } z_1 < z < z_2; \quad \begin{Bmatrix} r < r_c \\ r_c < r < r_a \\ r > r_a \end{Bmatrix} \qquad (26)$$

$$\hat{I} = 0 \quad \text{for } z > z_2$$

a pattern dotted in on the preceding sketch.

D. External Magnetic Field

The field from a many-turn coil of large dimensions is of a very complex functional form.[18] If the coil is very tightly wound so that its cross-section is of negligible extent, the field on its axis is given by

$$B(z, o) = \frac{\mu_o N I}{2} \frac{a^2}{(z^2 + a^2)^{3/2}} = B_o \frac{a^3}{(z^2 + a^2)^{3/2}} \qquad (27)$$

where N is the number of turns, I the coil current, a the mean radius of the coil, and $B_o = \frac{\mu_o N I}{2a}$ is the field at its center. If the coil radius a is comparable with the arc plume width, we expect the radial variation in the magnitude of B will not be large over much of the interaction region, even though the direction of B changes substantially with radial position. This approximation is supported by measurements of such field patterns.[19] In our later calculations, we will thus approximate the external field by relation (27) for all r and z. Note that for $z >> a$, this field falls off as a dipole, $\frac{1}{r^3}$.

3.1.5 Application to Arc Jet Without External B Field

We are finally in a position to estimate the current patterns in various MPD arcs. We will consider first the case of no external field, and begin by calculating maps of the Hall parameter and gyro radii for a relatively low (150 amps) and relatively high (3000 amps) arc current. Referring to the model in Section 3.1.4 C, the self-induced field B_θ' in the region $r_c < r < r_a$, $z < z_1$ is simply $0.2\ I/r$. Assigning $T_o = T_o^+ = 20{,}000°K$; $\beta = \beta^+ = 15$ cm; $n = 10^{14}\ cm^{-3}$, $u = 5 \times 10^6$ cm/sec, relations (8), (23), (26) yield, for $I = 150$ amp and 3000 amps respectively:

$$\Omega = 5.3 \times 10^5 \frac{B\,T^{3/2}}{n} = \begin{Bmatrix} 0.5 \\ 10 \end{Bmatrix} \frac{e^{-z/10}}{r} \tag{28}$$

The corresponding gyro radii for the electrons and thermal ions are given by relations (12) and (13)

$$r_B = 0.35 \frac{T^{1/2}}{B} = \begin{Bmatrix} 0.16 \\ 0.008 \end{Bmatrix} r\, e^{-z/30} \tag{29}$$

$$r_B^+ = 1.46 \frac{(T^+)^{1/2}}{B} = \begin{Bmatrix} 6.8 \\ 0.34 \end{Bmatrix} r\, e^{-z/30} \tag{30}$$

while for fully accelerated ions, (14) gives

$$(r_B^+)_u = 1.04 \times 10^{-4} \frac{u}{B} = \begin{Bmatrix} 17.3 \\ 0.87 \end{Bmatrix} r \tag{31}$$

In Figures 203 and 204 are plotted contours of constant Ω in the r - z plane for these two current levels. From these, certain inferences can already be made about the current patterns. Note first that while the electric field may have both

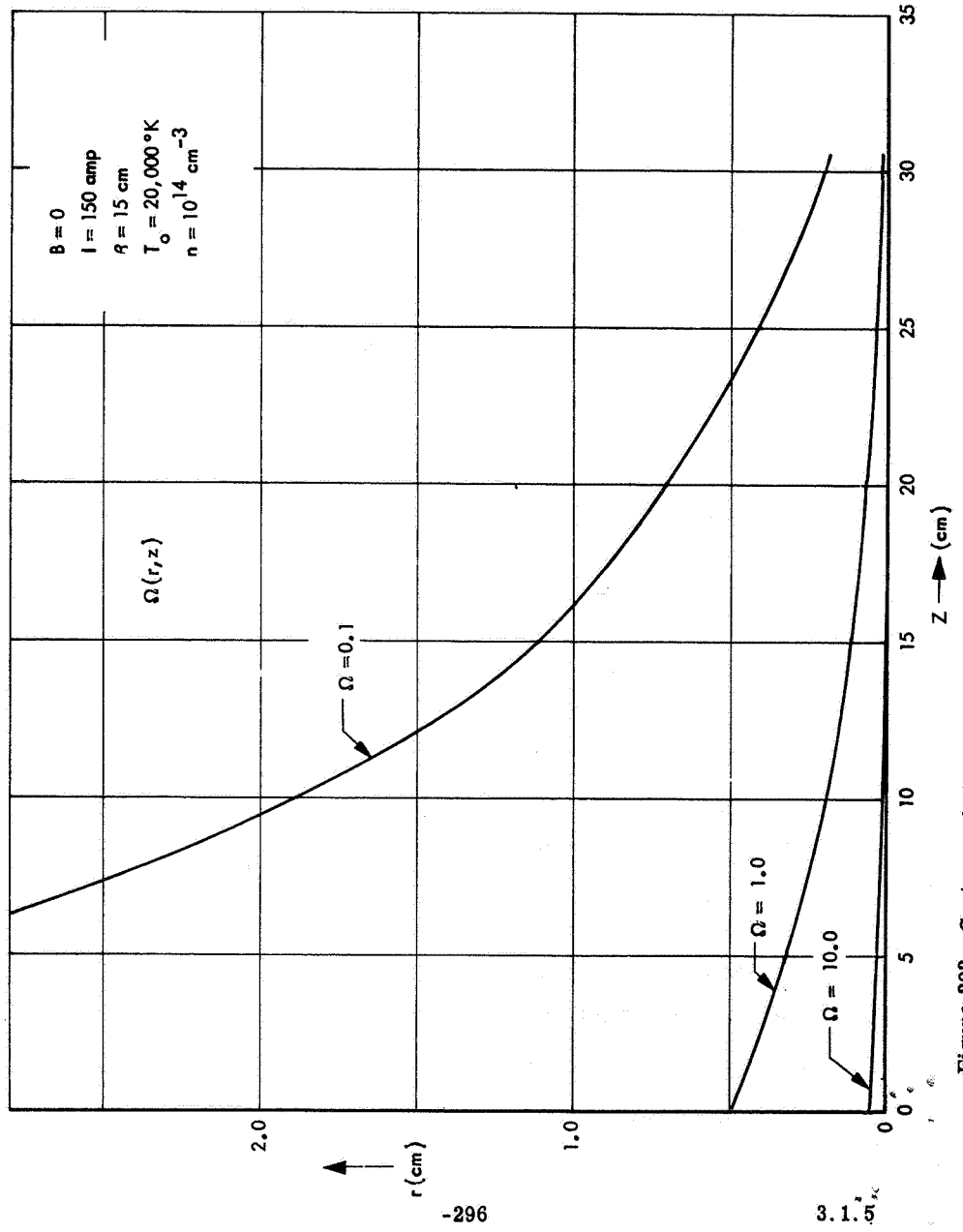

Figure 203. Contours of Constant Hall Parameter in the r - z Plane in the Self-Field of the Arc

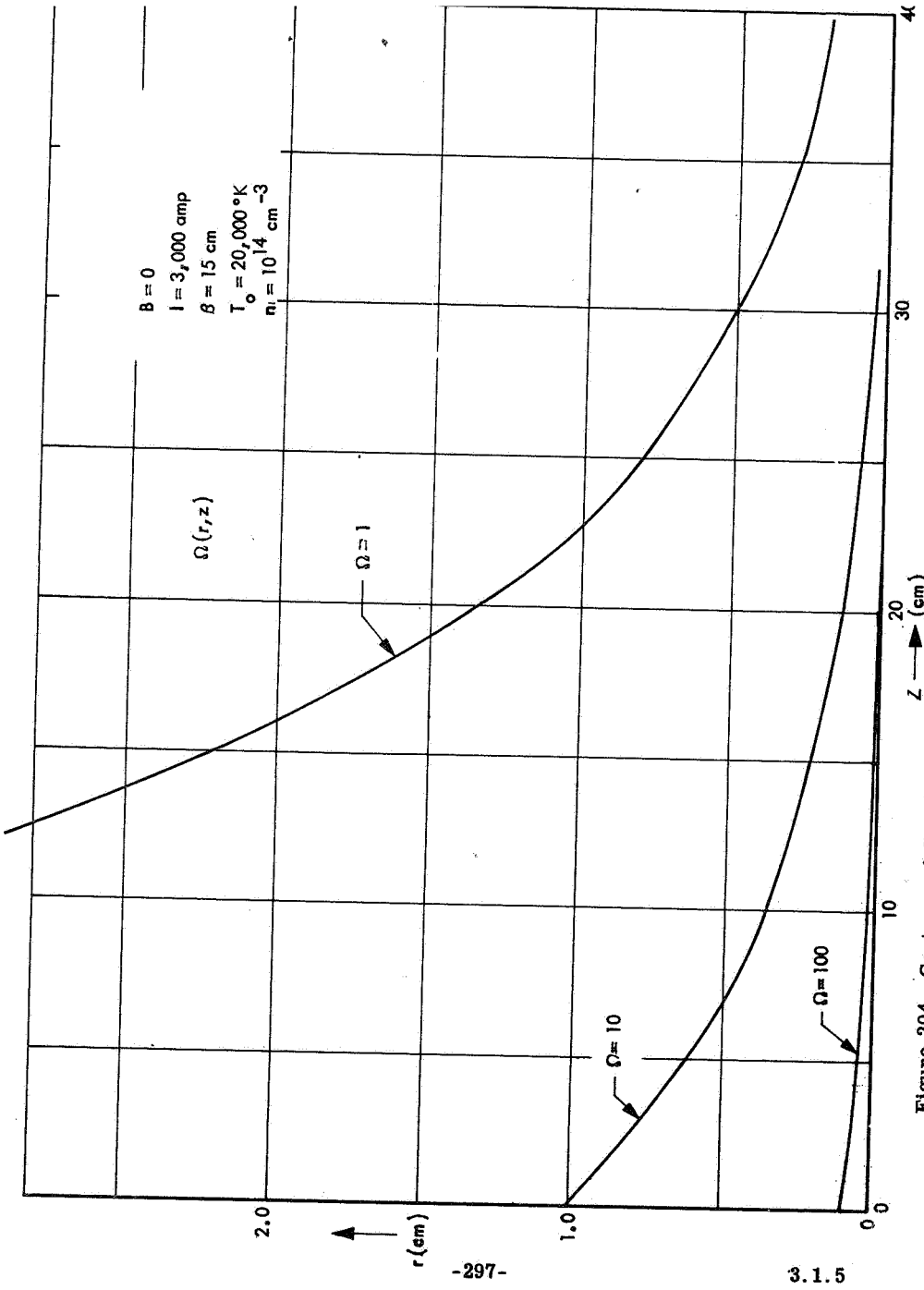

Figure 204. Contours of Constant Hall Parameter in the r - z Plane in the Self-Field of the Arc

radial and axial components in the gap, it is always normal to the induced field, B_θ'. Thus, any parallel field electron conduction must occur by collision. In the light of this, now note that electrons emitted from the cathode tip find themselves in a region of very high Hall parameter, and are thereby constrained to spiral axially outward with little cross-field migration toward the anode. That is, we deal here with a "Case 2" situation. This axial streaming, doubtless related to the classical "cathode jet," will continue until a region of sufficiently

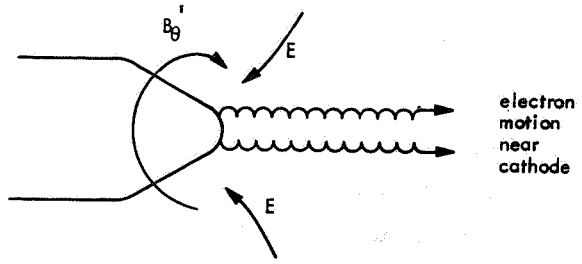

low Ω is reached that significant radial cross-field motion can be developed by collisions. This is one possible assignment of the cross-current leading edge z_1. From this point on, the cross-current will develop rapidly for several reasons. First, Ω will decrease even more rapidly with z than shown in Figures 203 and 204 because the enclosed current, and hence B_θ' are now decreasing with z. The model assumes constant radial current density in this region, for example, which would modulate the Ω curves by the factor $\left(\frac{z_2 - z}{z_2 - z_1}\right)$ over this domain. Second, as the electron migrates radially outward, it further lowers its Ω, thereby again improving the radial component of its motion. At sufficiently large r or z, the conduction becomes collision dominated, as in

our general "Case 1" above. The composite electron conduction picture then is a loop, beginning with an axial Hall current from the cathode, completed to the anode by a collisional conduction zone where current essentially follows the electric field lines.

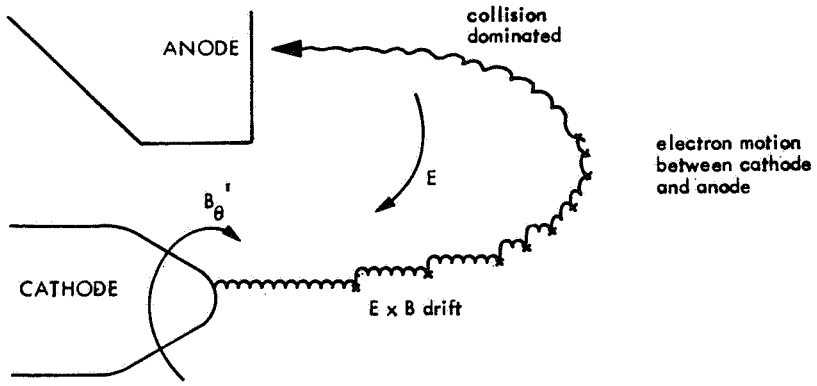

The axial position at which cross-field current develops clearly increases with field strength, B_θ', and thus with arc current. That is, the higher the arc current, the greater the axial protrusion of the electron current pattern.

As in our general "Case 2," above, one should now ask whether, in the absence of radial electron current near the cathode, the ions may conduct current across the electrode gap upstream of the onset of electron cross-current; i.e., does ion current, rather than electron cross-current define z_1. Again, it is difficult to generalize the availability of this process. The model presumes that ions are accelerated to a terminal velocity u, which in the absence of significant inter-species collisions will be given by some

effective potential drop: $u = \left(\frac{2\,e\,V}{m^+}\right)^{1/2}$ Hence, a mean ion current density of the order of $(n\,e\,u)$ should be available. However, there is the obvious integral requirement that the total ion current not be incommensurate with the total mass flow, i.e.,

$$I^+ \leq \frac{\dot{m}\,e}{M} \tag{32}$$

For example, to be consistent with the values chosen for u, β, etc., one should assign mass flows of about 10^{-3} and 25×10^{-3} gm of hydrogen, respectively. Thus ion current is confined to a maximum of about 100 and 2500 amps, respectively, somewhat marginal values considering the idealizations of the model, but perhaps indicative of the importance of the ion conduction process.

If ion conduction is to be taken seriously, one should next examine the ion gyro radii to illuminate the ion current configuration. For the low current case, r_B^+ is clearly much larger than the electrode gap, whether computed on a thermal or stream velocity basis. Thus the ions may be expected to follow closely the local electric field direction. However, there is substantial deviation from this in the high current case. Figure 205 shows a map of r_B^+ and $(r_B^+)_u$ for this situation, which indicates that not only will the ion orbits be bent significantly by B_θ', but that in the immediate neighborhood of the cathode tip, the ions also may lapse into a cross-field drift or Hall motion.

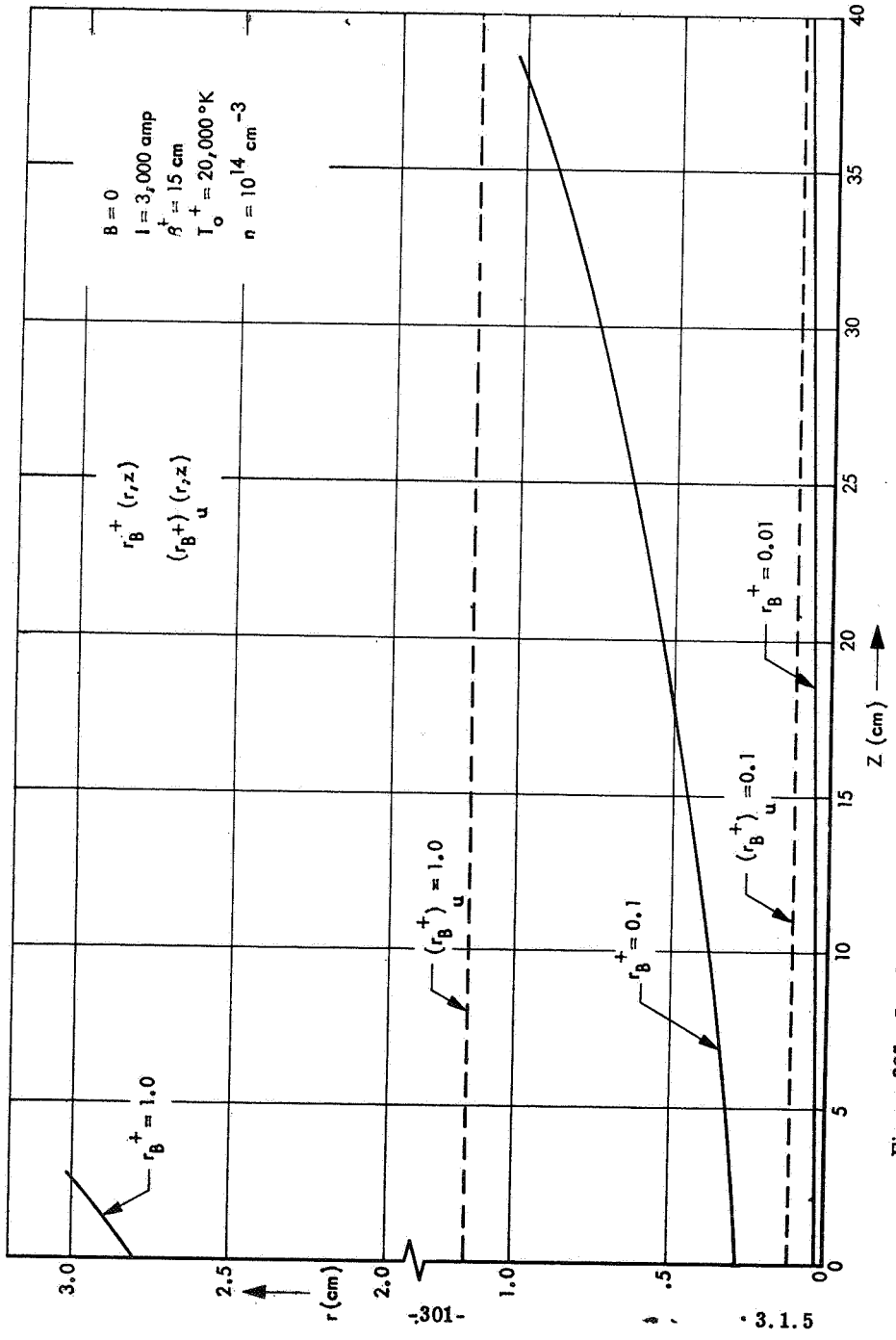

Figure 205. Ion Gyro Radii as a Function of Radial and Axial Position in the Self-Field of the Arc

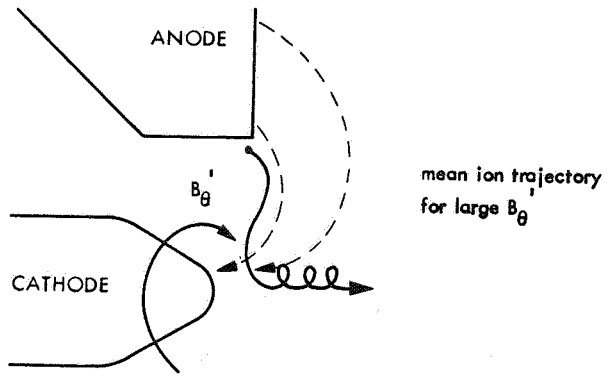

The importance of this axial turning of the ion orbit to the thrust mechanism has been pointed out by Stratton.[20] What may be even more significant is the protection of the cathode from ion bombardment afforded by this process. The small ion gyro radii in this region effectively force the ions to join the cathode jet at a finite separation from the material surface. The cathode tip is thereby magnetically protected in much the same manner as once proposed for magnetic shielding of re-entry bodies. It may well be that it is this magnetic protection of the cathode surface which permits very high currents to be drawn through the electrodes, contrary to the earlier experience with higher pressure electrothermal arc jets, thereby making the magnetoplasmadynamic regime accessible.

It now remains to discuss the thrust production mechanisms of this class of jet. Just as the current pattern is a patchwork of various contributions, we must expect a variety of contributions to the thrust. In the outer regions we have a collision dominated electron current and an ion current that also conforms to electric field lines, hence a predominantly Lorentz

thrust mechanism, normal to the local electric field, in amount $(j + j^+) B_\varsigma'$. The inverse radial variation of the magnitude of B_θ' reduces the relative importance of this region, and the curvature of the electric field lines causes the thrust density vector to diffuse radially outward near the anode.

At intermediate radial and axial positions, depending on the relative importance of ion current, we may find a regime of predominantly electron Hall current and ion conduction current, corresponding to general "Case 2" above. Here there will be an additional component of thrust, predominantly in the radial direction, derived from the unbalanced electric field force on the ions. This must manifest itself in a radial compression or "pinching" of the plasma which will produce a gasdynamic reaction force on the cathode surface.

Finally, very near the centerline, at high current levels, we may enter a domain akin to general "Case 3" above, where the ions also are constrained to an axial drift. This will create a neutral jet of plasma streaming axially outward at a speed given by the local ratio of E/B, contributing a thrust determined by the mass flow concentrated in the jet.

The integrated effect of this pattern of interactions is easily derived in the gross by magnetogasdynamic arguments, or indeed follows as a general consequence of the Maxwell stress tensor[21]

$$\int \vec{F}\, dv = \frac{\mu I^2}{4\pi} \left[\frac{3}{4} + \ln \frac{r_a}{r_c} \right]. \tag{33}$$

However, it is only by more microscopic arguments such as those above that one acquires some insight into the controlling mechanisms and their relative importance.

As an illustration, consider the question of possible ambient gas entrainment at the periphery of the jet which could introduce spurious thrust contributions in vacuum tank testing of the device. If the radial current is carried primarily by electrons, the integrated effect of electron collisions would be to expel gas outward over the entire plume periphery, thereby discouraging gas entrainment. If ion current must be invoked, however, a source of ions must be steadily provided near the anode. This source normally would be the inlet gas flow through the orifice. If this proves inadequate, however, as in very low mass flow operation, the arc may elect to ingest the necessary supply of heavy particles from the ambient gas adjacent to the anode, outside of the plume. This pumping process has indeed been demonstrated visually in an arc jet operating with no external source of mass flow.[22] As another alternative, the arc might elect to consume electrode material for this ion supply, a process which also has been observed in another set of experiments.[6]

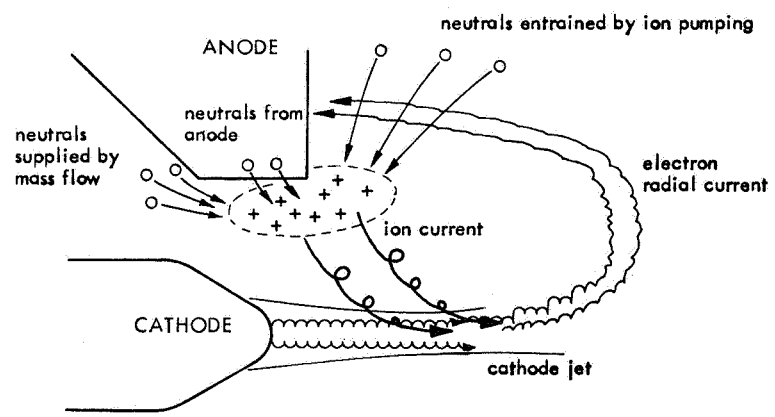

3.1.6 Application With External B Field and Low Current

Let us next consider operation of the arc when an external field of the type described in Section 3.1.4 D is imposed. We will first assume that this field is sufficiently strong, and that the arc current is sufficiently low that the self-induced field from the latter may be neglected. Employing relation (27) to approximate the B field pattern over the region of interest, we again compute a Hall parameter map: From (8), (23), and (27), we form

$$\Omega = 5.3 \times 10^5 \left(\frac{B_o T_o^{3/2}}{n}\right) \frac{a^3}{(z^2 + a^2)^{3/2}} e^{-\frac{3}{2}\frac{z}{\beta}} \tag{34}$$

Inserting the conditions $T_o = T_o^+ = 20,000°K$; $\beta = \beta^+ = 15$ cm; $n = 10^{14}$ cm^{-3}; $a = 5$ cm; $B_o = 10^4$ gauss, this becomes

$$\Omega = 150 \left(\frac{5}{\sqrt{z^2 + 5^2}}\right)^3 e^{-\frac{z}{10}} \tag{35}$$

Fig. 206 is a plot of this Ω as a function of z. As anticipated from the dipole nature of the imposed field, Ω decreases very rapidly with axial distance. It is of course independent of r by assumption. Since Ω is linear in B_o, similar curves for other applied fields follow from simple scale charge of that presented.

For the example chosen, we note that electrons emitted from the cathode tip again find themselves in a region of very high Hall parameter, just as in the self-induced case discussed previously. There are two important distinctions, however. First, in this region the applied electric and magnetic fields are not

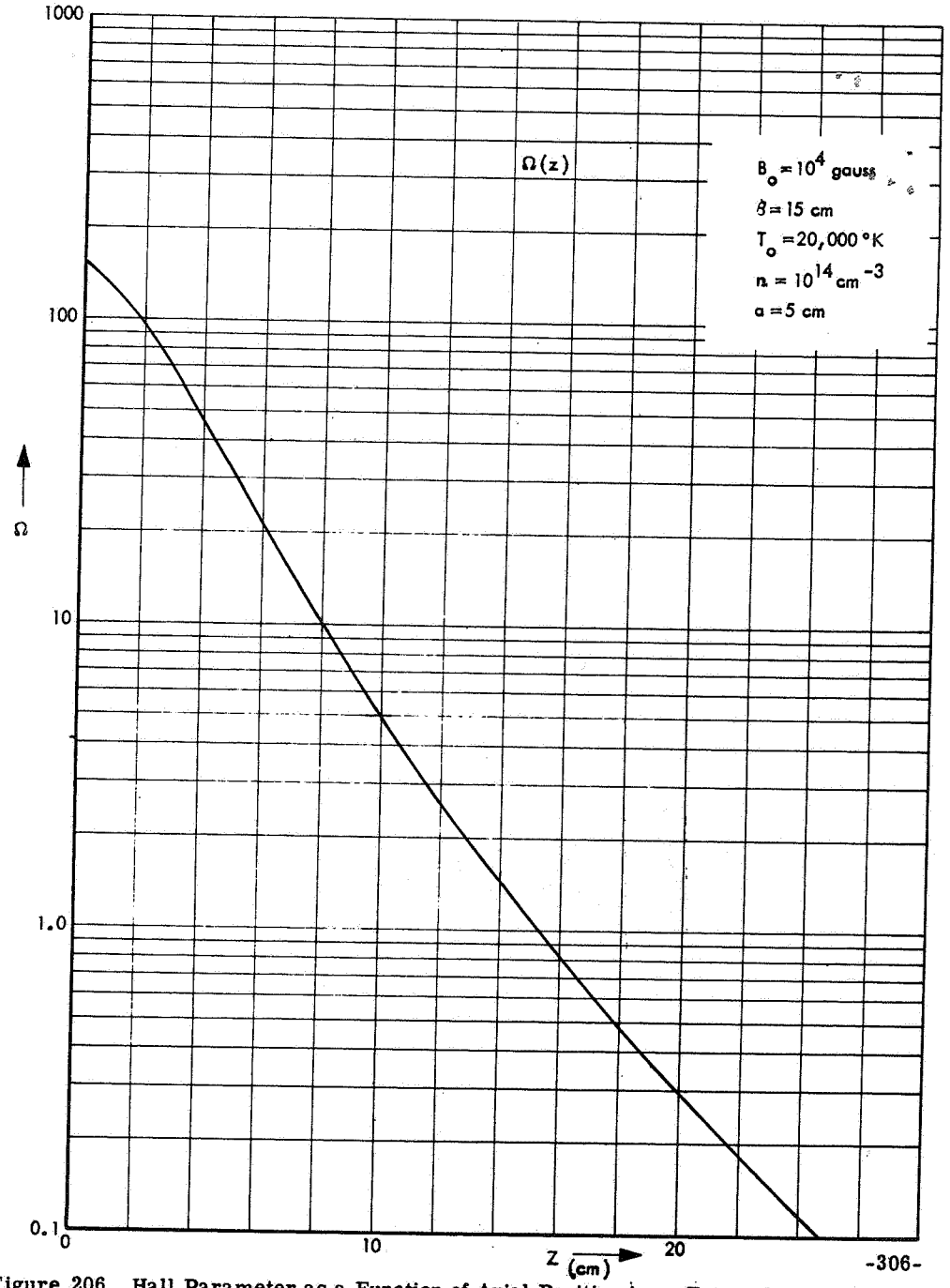

Figure 206. Hall Parameter as a Function of Axial Position in an External Magnetic Field

perpendicular, but have significant components parallel to each other. Therefore we must expect substantial electron conduction along the B-field lines,

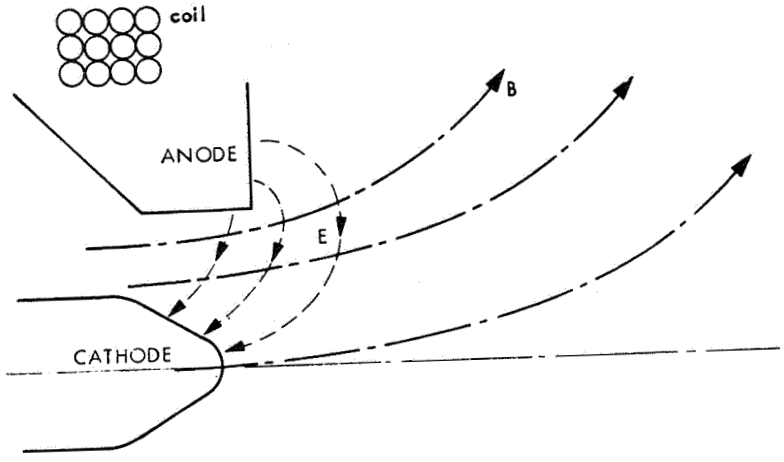

as in general "Case 4" above. Second, the cycloidal electron drift or "Hall current" is now in the azimuthal direction, in the sense of $\vec{E}_\perp \times \vec{B}$. The composite electron motion in this region, therefore, is a cycloidally-embossed spiral about the z axis, emanating from the cathode and confined to the funnel-shaped surface determined by the local B-field lines.

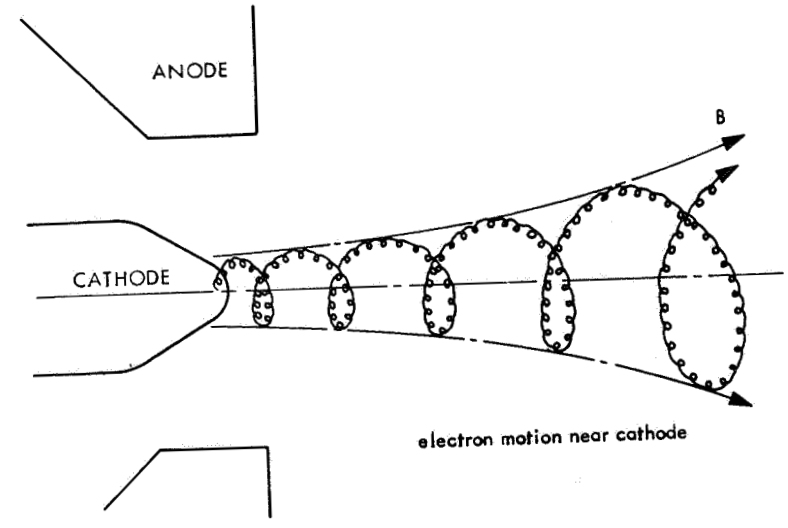

This type of motion will continue until the electron progresses far enough downstream to reach the collisional regime where it can begin to migrate back toward the anode along the local field lines, as in the self-induced field situation discussed previously. Note here, however, that unlike that case, as the electron approaches the anode from downstream, it re-enters a regime of high Hall parameter where it is again tied up by the strong B field. That is, near the anode we find another region of spiralling electron current like that found near the cathode.

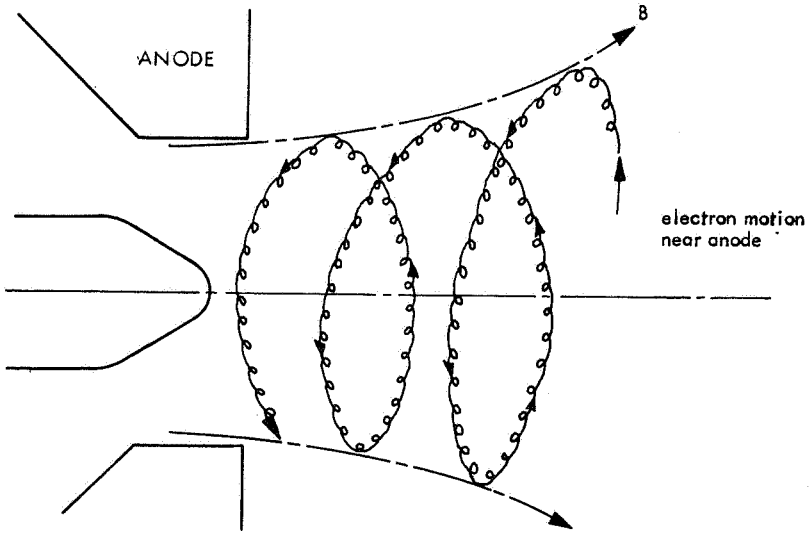

To summarize the electron conduction picture, then, we anticipate two coaxial shells of spiralling electron current, the inner one emanating from the cathode, the outer one returning to the anode, the surfaces of which coincide with the local B field lines. As the magnetic field is intensified, these shells should lengthen and become more paraxial, corresponding to the local increase in the Hall parameter. The radial electron cross-current between these shells must be achieved by collisional conduction, and thus is deferred to a region sufficiently downstream that the Hall parameter has relaxed to a modest value.

Again at this point one should ask whether ion current might bridge the gap between the two electron current shells upstream of the electron collisional zone. In this regard it is essential to compute the ion gyro radii as a function of axial position in this B field. From relations (12) and (13) we have for the chosen case

$$r_B^+ = 1.46 \frac{T^{1/2}}{B} \approx 0.02 \left[\frac{\sqrt{z^2 + 5^2}}{5}\right]^3 e^{-z/30} \tag{36}$$

$$(r_B^+)_u = 1.04 \times 10^{-4} \frac{u}{B} \approx 0.05 \left[\frac{\sqrt{z^2 + 5^2}}{5}\right]^3 \tag{37}$$

These functions are displayed in Fig 207. It is seen that both near the anode, where the thermal value, r_B^+, is probably relevant, and near the cathode, where the streaming value $(r_B^+)_u$ is perhaps more valid, the ion gyro radius is substantially smaller than the electrode gap, and therefore the main ion current components will be an azimuthal $\vec{E}_\perp \times \vec{B}$ drift, and an axial streaming along the $\vec{B}$ lines due to $\vec{E}_\parallel$. Significant radial current will be deferred until a downstream location where the gyro radius has become comparable with the electrode spacing. In the particular case computed, this is seen to be roughly the same axial distance as that for the onset of collisional electron current, and thus it would seem that ion current will not substantially shorten the plume length.

It should also be noted that in the region near the electrodes where r_B^+ and $(r_B^+)_u$ are small, the azimuthal ion drift is in the same sense as that of the electrons, and thus, to the approximations of the model, no net Hall current

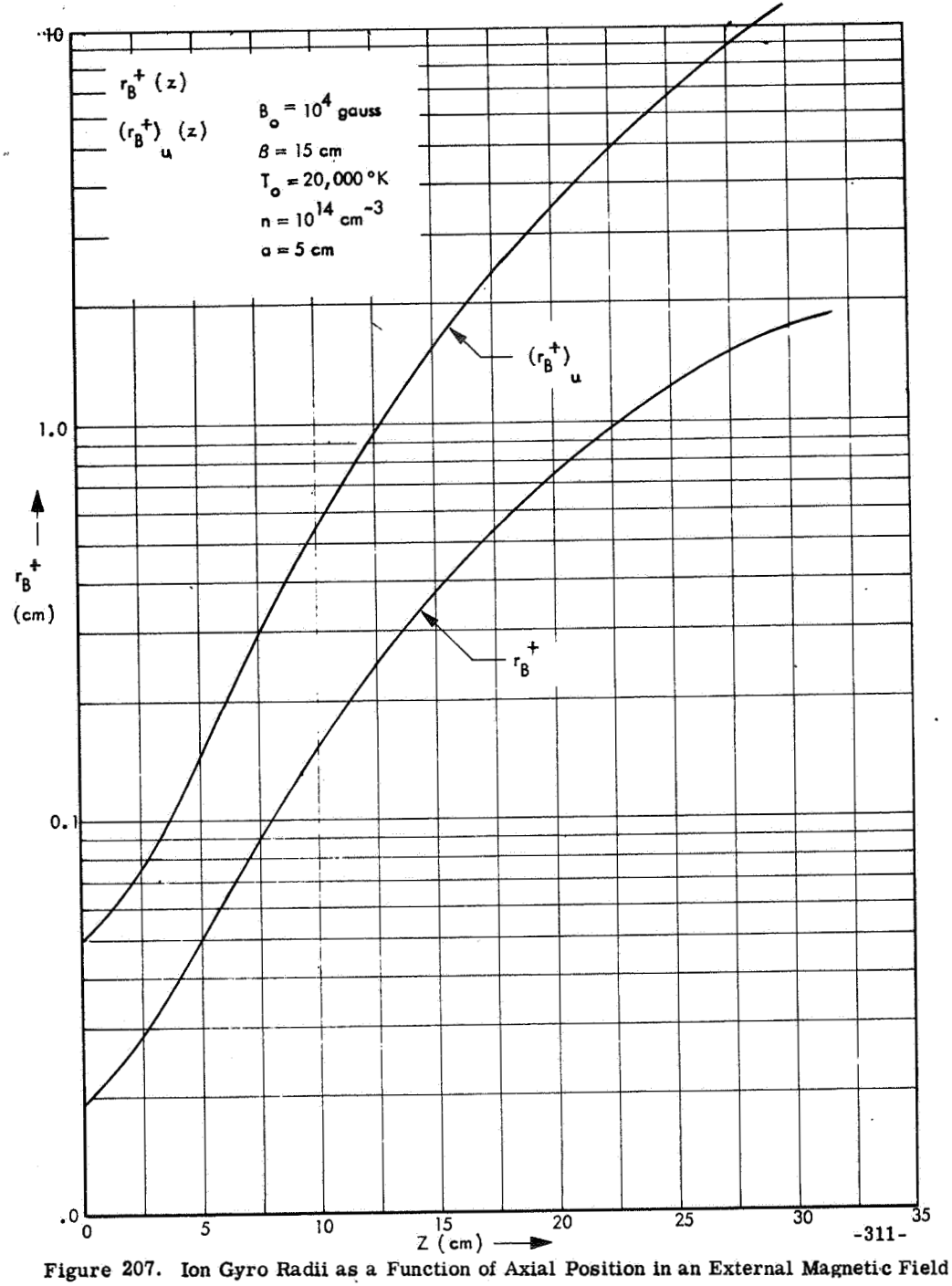

Figure 207. Ion Gyro Radii as a Function of Axial Position in an External Magnetic Field

flows. Rather, since the ions carry the mass of the system, there is a swirling motion of the gas as a whole in a sense determined by $\bar{E}_\perp \times \bar{B}$. These concentric, swirling cylinders of plasma may act more or less as extensions to the material electrodes, protracting them to a downstream location where the magnetic field is weak enough that the arc circuit can be completed across the field lines. Such "electrode extensions" may be helpful in relieving the heat transfer from the dissipative cross conduction region to the metal surfaces, but may also make the arc more vulnerable to ambient gas entrainment.

If one accepts this model of the current pattern, the thrust production mechanisms follow directly from the general cases discussed in Section 3.1.2. In the downstream region of the plume where radial currents are flowing, we have a collision dominated, Lorentz regime akin to "Case 1," yielding a predominantly azimuthal body force on the gas, $\approx j_r B_z$. Along the tubular anode jet and cathode jet we have collisionless regimes like "Case 3," with an additional component of E superimposed parallel to B. The latter can produce no net thrust on a neutral plasma, as shown in "Case 5," leaving again only the azimuthal thrust density, $\dot{n}\, m^+ \frac{E}{B}$ to swirl the gas.

One might now well ask where is the axial body force ultimately required to make this arc a useful accelerator. Not only does our model predict negligible net Hall current, it now predicts negligible streamwise thrust. The former property follows from the assumption of complete ionization; the latter from the neglect of the induced field, of all electrothermal effects, and field gradient drifts. That is to say, the arc with external field as postulated, with complete ionization and negligible self-induced field, does not impart streamwise momentum to the gas. Rather it protracts the current pattern and sets

the gas into rotational motion. In so doing, however, it may provide a better environment for electrothermal or self-induced magnetic acceleration processes to proceed when superimposed on it. For example, we have mentioned that the physical displacement of the radial conduction zone from the metal electrodes may permit higher total arc currents to be drawn than if this zone were in direct contact with the electrodes. Also, the "magnetic nozzle" effected by the external field pattern may improve the exhaust profile and electrothermal recovery efficiency.

The remarks about ambient gas entrainment made in connection with the self-field accelerator are equally appropriate here. The model requires a steady source of ions near the anode, and if it cannot acquire these from the inlet gas supply, it may elect to ingest particles from the surrounding environment, or to consume its electrode material. The greater the axial protraction of the plume, the more convenient external gas ingestion would seem.

3.1.7 Application to Arc Jet with External B Field and High Current

There is little reason to grind through the general case where the self-induced field is comparable with the applied field, since all of the resultant processes have already been examined in one of the above simple situations. Clearly the total $\vec{B}$ field, composed of the vector sum of the induced and externally applied field, will now have all three components, radial, axial, and azimuthal, i.e., the magnetic lines of force will be trumpet-shaped spirals about the centerline. The $\vec{E}$ Field will retain both radial and axial components and thus the charged particle trajectories will be complex three-dimensional superpositions of $\vec{E} \times \vec{B}$ drifts, collisional displacements, and parallel field accelerations determined by the specific details of the field patterns. Radial, axial, and azimuthal thrust density components will arise which may be thought of as superpositions of the mechanisms found in Sections 3.1.5 and 3.1.6 above, i.e., the plasma will simultaneously be pinching, streaming, and swirling in the exhaust plume.

In an environment as complex as this, the distinction between electrothermal and electromagnetic acceleration processes would seem to become rather academic. In principle one could compute the ratio of j^2/σ to $|\vec{j} \times \vec{B}|$ everywhere in the field and draw some inference about the more dominant process, but even in this tedious undertaking, certain interactions, such as those of magnetic containment might be somewhat ambiguous. On an atomic scale, the distinction relates to the ability of the particles to randomize the energy imparted to them by the electromagnetic fields over the dimensions available to them in the device. Efficient randomization of electron motion by their

collisions with ions is evident in the low Ω regimes, but in their free-orbit drifting regimes, and in the "collisionless" motions of the ions, randomization depends on subtler details of their interactions with the fields than have been considered here.

3.1.8 Extension and Improvement of the Analysis

By far the most important assumption of the foregoing analysis is that of complete ionization. In eliminating the neutral species from the problem we have removed the most effective mechanism for damping of organized ion motion, and thereby we project that motion into a prominence it would not enjoy in a partially ionized gas. Ions thus are able to achieve cross-field drift flux equal to that of the electrons, and thus they acquire constant drift velocities in the $\bar{E} \times \bar{B}$ direction. Device size, rather than mean free path becomes the dimension to compare with gyro radius in ascertaining ion current patterns.

It would therefore be of considerable interest to repeat this analysis, under the contrary assumption of significant ion-neutral collision frequency, for the purpose of high-lighting those aspects of the arc behavior which are sensitive to this choice. In that analysis the ion Hall parameter, $\Omega^+ = \frac{e\,B}{m^+}\, n\, Q^+ \bar{v}^+$ where Q^+ is the effective ion-neutral momentum transfer cross-section, will play a corresponding role to the electron Hall parameter in determining the ability of the ion current to follow the local electric fields. Where Ω^+ is very large, the results will approach those derived above. Where Ω^+ is small, ion drift will be impeded, and electron Hall currents will flow unbalanced. The collision-dominated ion trajectories will predicate new components of thrust density which will alter the composite thrust picture derived above.

Closely related to this modification would be the consideration of gases of higher atomic weight. Even if the complete (single) ionization assumption were retained, these gases would display quantitatively different behavior because of the increased gyro radii of the ions. This would manifest itself in

reduction of the domains of ion $\vec{E} \times \vec{B}$ drift, and corresponding shortening of the axial position for onset of radial ion current.

Obvious refinement of the analysis can also be made by the use of less cavalier assumptions regarding the field geometries and intensities, and the electron density and temperature patterns. While it is doubtful that these refinements will alter the qualitative results of the crude model, they may provide a basis for more significant quantitative comparisons with the experiments proposed in the next section.

In the same spirit, it would be well to examine more closely the fringe effects associated with the narrow current regions that arise in the simple model. The particle trajectories discussed in Section 3.1.2 presumed infinite, uniform media except where specifically noted, whereas the arc models postulated confine the current regions rather distinctly. Such delineation can embody local charge separation fields and other fringe effects which may have importance to the acceleration process.

Also, charged particle drifts resulting from non-uniform magnetic fields have been largely ignored. Normally these are important to the order of the fractional change in the field over a gyro radius,[15] and thus, in the light of the large ion gyro radii involved, should be considered more closely. Even more satisfactory would be a process of exact, point-by-point trajectory iteration for the two charged particles in the particular non-uniform field chosen, which would, of course, encompass all such drift processes automatically.

Organized plasma processes such as fluctuations, waves, and boundary instabilities have not been considered, and may well be expected in the postulated environment. Various arc instabilities are encountered experimentally

and may reflect organized plasma motions in the plume. Development of criteria for the possible modes and their comparative importance in this system could shed some light on the serious operational problems of arc localization and consequent electrode destruction.

3.2 Energy Transfer and Acceleration Processes

3.2.1 Electron Energy Gain in the Arc and Thermalization of the Plasma

In the usual arc jet operation* cold gas is fed into an arc chamber and then flows on to become part of a strong electrical discharge. The gas flows through the discharge and is ejected into a vacuum in the form of a hot ionized jet. In the process there is a transfer of electrical power to power in the jet. The primary energy transfer mechanism here is the acceleration of charged particles in the electric field of the arc. From a microscopic point of view, the magnetic field, either self-induced or applied, does not add energy directly to the ions or electrons, since the Lorentz force on a charged particle always acts perpendicular to its motion. Two types of energy addition may be distinguished. The particles can gain energy in the electric field without undergoing many collisions, and a directed flow might be obtained through the interaction of the charged particles with the electric and self-induced or applied magnetic field. Alternatively, the number of collisions suffered by a charged particle in falling through a significant fraction of the arc potential or during the expansion process may be very large. This would be a case of energy addition by ohmic dissipation. That is, electrical energy is converted to plasma energy by first accelerating charged particles in the electric field and then this directed energy is converted to thermal energy by particle - particle collisions. To obtain useful kinetic energy the plasma must then undergo a directed expansion. In the former case (few collisions) the thermal energy would remain relatively

*Arc jets have also been operated without through flowing propellant (see references 1 and 2).

small and one would achieve, to some extent, a direct conversion of electrical energy to directed mass motion.

We shall adopt the point of view that the electrical to plasma energy transfer is primarily an ohmic heating process. To indicate the presumed thermal nature of the energy transfer we shall sometimes speak of a thermal arc jet even though the state of the plasma may be far from thermal equilibrium. In the following we consider some basic aspects of the transfer of energy from electrons to heavy particles.

Let us assume that the gas is fully ionized. Then Coulomb collisions will provide the collision mechanisms between electrons and heavy particles. In addition we suppose that the electrons, because of their small mass, gain energy in the electric field much more rapidly than the heavier ions. When strong magnetic fields are present conditions might arise where the ions would gain energy in the field faster than the electrons, but this possibility is not considered here. An expression for the electron energy relative to the ion energy is derived below for a fully dissociated fully ionized hydrogen plasma. We follow a derivation given by Allis.[23] This reference may be referred to for more details. Consider the motion of an electron under the force of an electric field and forces due to collisions of the electron with other particles. The Langevin equation for the motion of the electron is given by

$$\frac{d\vec{v}_e}{dt} = -\frac{e\vec{E}}{m_e} + \frac{e\vec{B}\times\vec{v}_e}{m_e} + A(t)\,, \tag{38}$$

where

e, m_e, and v_e are the magnitude of the electron charge, mass and velocity, t is time, and $\vec{E}$ and $\vec{B}$ are the electric and magnetic fields. $\vec{A}(t)$ is a random force due to collisions of the electron with other particles. Taking the scalar product of (38) with the electron momentum we obtain an equation for the rate of gain of the electron energy as it moves in the applied electric field while being impeded by collisions:

$$\frac{d u_e}{dt} = - e \vec{E} \cdot \vec{v}_e + m_e \vec{v}_e \cdot \vec{A}(t) .$$

Taking an average over a time Δt such that many collisions take place but that the electron energy u_e does not change appreciably we obtain

$$\frac{d u_e}{dt} = - e \vec{v}_{e,d} \cdot \vec{E} + m_e \left\langle \vec{v}_e \cdot \vec{A}(t) \right\rangle, \tag{39}$$

where $\vec{v}_{e,d}$ is the drift velocity of the electron and

$$\left\langle \vec{v}_e \cdot \vec{A}(t) \right\rangle = \frac{1}{\Delta t} \int_{\Delta t} v_e \cdot A(t)\, dt$$

is the average value of $\vec{v}_e \cdot \vec{A}(t)$ over many collisions. This term gives the average rate at which energy is lost due to collisions. Since excitation and ionization collisions are absent, in accordance with the assumption of full ionization, this term gives the rate at which equipartition is established between two sets of particles with different energies. We take this rate as

$$m_e \left\langle \vec{v}_e \cdot \vec{A}(t) \right\rangle = \frac{u_e - \bar{u}_p}{t_{eq}} \tag{40}$$

where $\bar{u}_p$ is the average proton energy and t_{eq} is the characteristic time of equipartition of energy.* This time is approximated by

$$t_{eq} = \frac{m_e + m_p}{2\, m_e}\, t_D , \tag{41}$$

where $t_D = 1/\nu$ is the deflection time for 90° Coulomb collisions defined by Spitzer[15] and ν is the number of 90° collisions per unit time suffered by an electron and is thus the usual collision frequency. The factor $(m_e + m_p)/2\, m_e$ arises because in a collision of a light particle with a heavy slowly moving particle approximately a fraction $2\, m_e/(m_e + m_p)$ of its energy will be lost in the collision. The characteristic time for energy exchange will thus be about a factor m_p/m_e longer than that for momentum exchange. We have neglected electron - electron collisions which amounts to assuming a micro canonical energy distribution for the electrons.

The drift velocity of an electron in a steady and uniform electric and magnetic field in a stationary plasma (or in a reference frame moving with the mass velocity) is given by

$$\vec{v}_{e,d} = \mu \vec{E}$$

where μ is the mobility tensor which is just the conductivity tensor displayed in equation (18) divided by $- n e$. That is

$$\mu = - \frac{e}{m_e \nu} \begin{pmatrix} \frac{1}{1+\Omega^2} & \frac{-\Omega}{1+\Omega^2} & 0 \\ \frac{\Omega}{1+\Omega^2} & \frac{1}{1+\Omega^2} & 0 \\ 0 & 0 & 1 \end{pmatrix}, \tag{42}$$

*See, for example, pp 135 - 136, reference 15.

where the tensor is represented in a coordinate system where coordinate directions x^1 and x^2 are perpendicular to the magnetic field and x^3 is parallel to the magnetic field. In (39) we thus have the term $\vec{E}\cdot(\mu\,\vec{E})$. Using (42) for μ and using the rules of vector algebra with an electric field $\vec{E} = (E_\perp, 0, E_\parallel)$ we obtain

$$\vec{E}\cdot(\mu\,\vec{E}) = -\frac{e}{m_e\,\nu}\left(\frac{E_\perp^{\,2}}{1+\Omega^2} + E_\parallel^{\,2}\right),$$

and thus

$$\frac{d\,u_e}{dt} = \frac{e^2}{m_e\,\nu}\left(\frac{E_\perp^{\,2}}{1+\Omega^2} + E_\parallel^{\,2}\right) + m_e\left\langle\vec{v}_e\cdot\vec{A}(t)\right\rangle. \tag{43}$$

Using (41), with $t_D = 1/\nu$, in (43) yields

$$\frac{d\,u_e}{dt} = \frac{e^2}{m_e\,\nu}\left(\frac{E_\perp^{\,2}}{1+\Omega^2} + E_\parallel^{\,2}\right) - \frac{2\,m_e\,\nu}{m_e + m_p}\,(u_e - \bar{u}_p)\,. \tag{44}$$

The first term on the right-hand side is the electron gain in energy per unit time from the electric field; the second term is the loss in electron energy due to recoil in collisions with protons. If the energy of the electron is constant in time then we have, after rearranging,

$$u_e - \bar{u}_p = \frac{m_p\,e^2}{2\,m_e^2\,\nu^2}\left(\frac{E_\perp^{\,2}}{1+\Omega^2} + E_\parallel^{\,2}\right) \tag{45}$$

where m_e/m_p has been neglected compared with unity. Define a mean free path for momentum transfer collisions by

$$\lambda = \frac{v_e}{\nu}$$

where v_e is taken to be the mean thermal velocity of electrons with a Maxwellian energy distribution, as given by (5). Using the above expression for λ in (45) gives

$$\frac{u_e - \bar{u}_p}{u_e} = \frac{m_p}{4\,m_e}\left(\frac{e\,\lambda}{u_e}\right)^2\left(\frac{E_\perp^{\,2}}{1+\Omega^2} + E_\parallel^{\,2}\right) \tag{46}$$

where u_e is now interpreted as the energy of an electron with the mean thermal velocity. If the Hall parameter is small compared to unity then it is clear from (46) that the quantity $e\,E\,\lambda/u_e$, where $E = \sqrt{E_\parallel^{\,2} + E_\perp^{\,2}}$, is signigicant for determining the energy difference between electrons and heavy particles under the conditions assumed here. This quantity is the ratio of energy gained by the electron in the field between collisions to its energy. As can be seen from (46), if

$$\left(\frac{e\,E\,\lambda}{u_e}\right)^2\left[\frac{E_\perp^{\,2}}{E^2\,(1+\Omega^2)} + \left(\frac{E_\parallel}{E}\right)^2\right] \tag{47}$$

is much less than unity the electron and proton energies will nearly be equal. In this case the transfer of electrical energy to electrons and then to the heavy particles by collision is immediate and one has a case of ohmic heating with near equipartition of energy. If the quantity in (47) multiplied by m_p/m_e is of the order of unity then equipartition will not be maintained during the energy addition although thermalization may still occur during an expansion process.

Departures from electron-ion energy equipartition will lead to inefficient utilization of the electrical energy. The magnitude of this inefficiency has not been considered here. Nonequipartition in the other direction, i.e., ions hotter than electrons, would probably be a desirable condition if it could be realized.

Although the values of the plasma parameters are not known well enough to calculate accurately the departure from equipartition using equation (46), we will estimate these parameters and then use (46) to obtain a rough idea of possible differences of electron and ion energies in the jet. Consider a region of the arc jet off the axis where the axial component of the electric field is small compared with the radial component divided by the Hall parameter. We take the radial component to be perpendicular to the applied magnetic field. Suppose

$$E_\perp = 20 \text{ volts/cm}, \qquad n_p = n_e = 10^{14} \text{ cm}^{-3}$$
$$T_e = 2 \times 10^4 \text{°K}, \qquad B = 2500 \text{ gauss}. \tag{48}$$

By (45) and (5) and (7) we calculate

$$\lambda = 0.07 \text{ cm}, \qquad \frac{e E_\perp \lambda}{u_e} = 0.7 .$$

For the above values of B, T_e and n_e, the Hall parameter calculated from (8) is $\Omega = 43$. The ratio of the energy difference between electrons and protons to the electron energy as given by (46) is

$$\frac{u_e - \bar{u}_p}{u_e} = 0.2 .$$

On the axis of the jet near the cathode the component of the electric field in the axial direction may be relatively large and the dominant term in (45) or (44) would then be due to $E_{\parallel}$. For example, if $E = 5$ volts/cm and the other values in (48) are the same, then $(u_e - \bar{u}_p)/u_e$ is greater than unity. This means that the "steady state" $d u_e/dt = 0$ will not be attained as assumed above, and the electrons will continue to gain more energy from the parallel component of the electric field than they lose by collisions with the heavy particles until they are out of the region of strong parallel electric field. Since the electrons gain more energy in the field than they transfer to the protons, the electron energy will be higher than the proton energy.

To transfer the excess electron energy to the protons it is then necessary to have thermalization between electrons and protons in a region downstream from the region of electrical energy addition. The rate at which thermalization proceeds is characterized by the equipartition time given in equation (41). From equation (41) and (7) for $T_e = 2 \times 10^4$ °K and $n_p = 10^{14}$ cm^{-3} we obtain

$$t_{eq} = 7.7 \times 10^{-7} \text{ sec}^{-1} \tag{49}$$

Let us suppose the mass velocity is equal to the speed of sound at 10^4 °K. That is

$$v_{mass} = \sqrt{\frac{\gamma R T}{M}} = 1.2 \times 10^6 \ \frac{\text{cm}}{\text{sec}}$$

where M is the molecular weight of the proton gas. A characteristic length for equipartition is defined by

$$d_{eq} = v_{mass} \times t_{eq} = 0.9 \text{ cm}$$

where the values of v_{mass} and t_{eq} computed above have been used. So we see that for these conditions, even if the electrons were to acquire much more energy than the protons in the heating region of the flow, equipartition would be established in a length the order of a few centimeters after the plasma is out of the region of strong parallel electric fields.

Since the collision time $t_D = 1/\nu$ increases as $T^{3/2}$ the equipartition time will increase rapidly with increasing temperature. For very high electron temperatures, say 100,000°K, the equipartition length is of the order of 10 cm if the proton density is 10^{14} cm^{-3}, and longer if the proton density is less (see equation (7)). A nozzle (either magnetic or metal) of the order of 30 cm would then be required to obtain an approximately complete transfer of excess electron energy to the protons.

At very high electron energies conditions for "runaway" electrons[24] may exist in some regions of the flow.[25] The most favorable conditions for runaway are probably on the periphery of the jet where electrons can flow to the anode parallel to magnetic field lines and in the hot core of the jet where acceleration parallel to magnetic field lines may also occur (see sketch on page 292). The parameter

$$\Sigma = 6.61 \times 10^8 \frac{T\,E}{n_e \ln \Lambda}$$

as given in Spitzer[15] determines the conditions for electron runaway in a fully ionized gas. For $\Sigma << 1$ runaway will not be important. For Σ of the order of unity conditions for runaway electrons will exist. Taking

the numerical values of E and n_e used in our previous example, with $T_e = 100,000°K$ and $\ln \Lambda = 10$ (see page 276) then $\Sigma = 0.33$. In this case a significant fraction of electrons will run away during the electron self-collision time, which is about 10^{-10} sec for the conditions taken here. We note that Spitzer's[15] formulas for the collision frequency and resistivity are no longer valid when runaway occurs.

The runaway phenomena is mentioned here since these high-energy electrons could be the cause of damage observed at the anode surface at the periphery of the flow, where it appears that very hot electrons hit the anode and cause localized melting and erosion. Also, in high magnetic field and high temperature operation what appear to be current streamers attach to the end of the vacuum tank many meters from the cathode surface, and this could be a manifestation of runaway conditions.

Let us briefly summarize the contents of this section. We have used the Langevin equation, which describes the motion of a single electron, to obtain an expression for an average electron energy relative to the average proton energy in a fully dissociated and ionized hydrogen plasma in a uniform and constant electric and magnetic field. This equation shows that when the Hall parameter is much less than unity the quantity $e\,E\,\lambda/u_e$ is significant for determining differences of electron and proton energy in the region of electrical energy addition. If the Hall parameter is not negligible compared with unity the significant parameter is given by (47).

The characteristic time for equipartition of energy is the Coulomb collision time multiplied by the ratio of proton to electron mass. Out of the region

of electrical energy addition approximately equipartition of proton and electron energy will be obtained in several equipartition times. For a plasma with a mass velocity v_{mass} and an equipartition time t_{eq} the characteristic length for equipartition is $d_{eq} = v_{mass} \times t_{eq}$. Equipartition of energy will be nearly established in several equipartition lengths after the plasma is out of the heating region.

For an electron density of 10^{14} cm^{-3}, electron temperature of 2×10^4°K and electric field of 20 volts/cm perpendicular to a magnetic field of 2500 gauss, the ratio of the difference between electron and proton energies to the electron energy is found to be 0.2. For the same temperature and an electric field of 5 volts/cm parallel to the magnetic field, a very strong nonequilibrium state will develop. The equipartition length is about 1 cm, so for both these cases equipartition will nearly be obtained in the order of a few centimeters of the flow.

For temperatures of 100,000°K the equipartition length is about 10 cm which is a significant fraction of the visible dimensions of usual plasma jet expansion plumes. This condition is unfavorable for the transfer of electrical energy to the heavy particles in the flow. For $T_e = 100,000$°K and $E_{\parallel} = 5$ volts/cm it is shown that conditions for runaway electrons exist, which would lead to unusually energetic electrons in the jet.

3.2.2 Elementary Aspects of an Axisymmetric Rotational Flow in a Strong Magnetic Field

In this section the magnetogasdynamic equations for an axisymmetric fully ionized arc jet flow are considered. We shall assume that the mass flow is parallel to the applied magnetic field lines. This is a valid assumption if the diffusion velocity perpendicular to the magnetic field is small compared to the axial mass velocity of the flow. The diffusion velocity perpendicular to the magnetic field as given by Spitzer[15] is

$$v_D = - \frac{\eta_\perp (\text{grad } p)_\perp}{B^2}$$

where $\eta_\perp$ is the resistivity perpendicular to the magnetic field and $(\text{grad } p)_\perp$ is the gradient in the pressure perpendicular to $\vec{B}$. For $n = 10^{14}$ cm^{-3}, $T = 2 \times 10^4$°K, $B = 2500$ gauss, and $r = 1$ cm the diffusion velocity is of the order of

$$v_D = 4 \times 10^3 \text{ cm/sec}.$$

Taking v_z equal to the velocity of sound at 2×10^4°K we obtain

$$\frac{v_D}{v_z} = 2 \times 10^{-3}.$$

Hence for these values, which we consider representative of conditions in the exhaust jet, the perpendicular diffusion velocity is more than two orders of magnitude less than the axial mass velocity. Visual observations of the flow for magnetic fields of 2000 gauss and more indicate that the flow

is following the magnetic field lines which is in agreement with the above order of magnitude calculation.

The momentum equation for a time independent, electrically neutral, non-viscous flow is

$$\rho \vec{v} \cdot \text{grad}\, \vec{v} = - \text{grad}\, p + \vec{j} \times \vec{B}, \tag{50}$$

where ρ is the mass per unit volume, $\vec{v}$ is the mass velocity, p the scalar pressure and $\vec{j}$ and $\vec{B}$ are the electric current and magnetic field. To study the effect of the magnetic field on the momentum transfer in the flow we write (50) in curvilinear coordinates where one set of coordinate surfaces coincides with the applied magnetic field and another set of coordinate surfaces is taken perpendicular to the field lines.

This coordinate system is illustrated in the sketch shown below

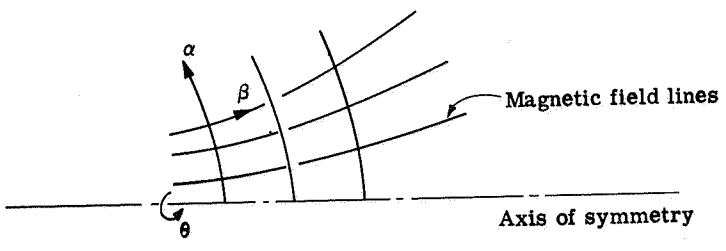

Position measured perpendicular to the field lines is denoted by the coordinate α, and the position along the magnetic field lines is given by β The angular orientation of a plane perpendicular to surfaces of constant α and β is indicated by θ. Thus a point in the flow is labeled by the three coordinates (α, θ, β). Because of the assumed cylindrical symmetry there will be no dependence of the dependent variables on θ although forces and motion in the θ-direction occur.

In this coordinate system the square of a differential distance is given by

$$d s^2 = g_{\alpha\alpha} (d\alpha)^2 + r^2 (\alpha, \beta)\, d\theta^2 + g_{\beta\beta} (d\beta)^2, \tag{51}$$

and so the nonvanishing components of the metric tensor are

$$g_{\alpha\alpha}, \quad g_{\theta\theta} = r^2 (\alpha, \beta), \quad g_{\beta\beta}. \tag{52}$$

With the aid of the metric tensor the momentum equation can be expressed in these curvilinear coordinates.[26] For the simple case where we can neglect the curvature of the magnetic field lines, we obtain the following equations for the α, θ and β components of (50):

$$- \frac{\rho v_\theta^2}{r \sqrt{g_{\alpha\alpha}}} \frac{\partial r}{\partial \alpha} = - \frac{1}{\sqrt{g_{\alpha\alpha}}} \frac{\partial p}{\partial \alpha} + j_\theta B_\beta \tag{53}$$

$$\frac{\rho v_\beta}{r\, g_{\beta\beta}} \frac{\partial r v_\theta}{\partial \beta} = - j_\alpha B_\beta \tag{54}$$

$$v_\beta \frac{\partial v_\beta}{\partial \beta} - \frac{v_\theta^2}{r} \frac{\partial r}{\partial \beta} = - \frac{1}{\rho} \frac{\partial p}{\partial \beta}. \tag{55}$$

In deriving (53), (54), and (55) we have used the fact that in this coordinate system $B_\alpha = 0$ and $v_\alpha = 0$ which is consistent with our assumptions. It has been assumed that the self-field of the current distribution is small compared with the applied field and the pressure terms. In addition, the symmetry condition that derivatives of all quantities with respect to θ vanish has been invoked.

Equation (53) states that the Lorentz force due to azimuthal currents and applied magnetic field just balances the pressure gradient and centrifugal force normal to the magnetic field lines. This is a direct consequence of our assumption of perfect containment of the flow by the applied field; this is the magnetic nozzle effect. That is, the Lorentz force acts perpendicular to the flow velocity and balances the pressure and centrifugal forces normal to the flow which is similar to the effect of a metal nozzle.

Equation (54) gives the rate of change of angular momentum along field lines in the flow. Inspection of the term on the right hand side of equation (54) shows that the magnitude of the angular momentum per unit mass increases along the field lines wherever there is an α-component of the current. Outside the region of "radial" current flow the angular momentum per unit mass along field lines remains constant, and the flux of angular momentum through a surface normal to the flow is independent of β. To see this we use the equation for conservation of mass in a time independent flow field. In these coordinates the continuity equation can be written in the form

$$\frac{\partial \sqrt{g_{\alpha\alpha}}\, r\, \rho\, v_\beta}{\partial \beta} = 0 . \tag{56}$$

Then equation (54) can be written in the form

$$\frac{\partial (\sqrt{g_{\alpha\alpha}}\, \rho\, v_\beta\, r^2\, v_\theta)}{\partial \beta} = - \sqrt{g_{\alpha\alpha}}\, r^2\, j_\alpha\, B_\beta .$$

Integration over α and θ gives the integral relation

$$\frac{\partial}{\partial \beta} \int \rho\, v_\beta\, r\, v_\theta\, r \sqrt{g_{\alpha\alpha}}\, d\alpha\, d\theta = - \int r\, j_\alpha\, B_\beta\, r \sqrt{g_{\alpha\alpha}}\, d\alpha\, d\theta ,$$

where $r\sqrt{g_{\alpha\alpha}}\, d\alpha\, d\theta = dA$ is a differential element of area normal to the magnetic field lines. Then

$$\frac{\partial L}{\partial \beta} = - \int_{A(\beta)} r\, j_\alpha\, B_\beta\, dA , \tag{57}$$

where

$$L(\beta) \equiv \int_{A(\beta)} \rho\, v_\beta\, r\, v_\theta\, dA$$

is the total angular momentum flux at β and $A(\beta)$ is the area of the flow at β normal to the magnetic field lines. The integral on the right hand side of (57) is the torque per unit length acting on the flow. Wherever the currents j_α vanish, then

$$\frac{\partial L}{\partial \beta} = 0 ,$$

which is the conservation of angular momentum flux, which we must have

in a time independent torque free region of the flow field. There is energy in this rotational motion and the conversion of this energy to axial thrust is discussed briefly below.

Consider a region of the flow where the j_α currents vanish. Then according to (54)

$$\frac{\partial r v_\theta}{\partial \beta} = 0, \quad r v_\theta = c \tag{58}$$

along a magnetic field line, where c is a constant. Let us assume that in some expanding region of the flow ohmic heating of the plasma is negligible and the expansion of the flow is isentropic. Then

$$p = k \rho^\gamma \tag{59}$$

where k is a constant and γ is the ratio of specific heats.

We use the isentropic relation (59) to obtain

$$\frac{1}{\rho} \frac{\partial p}{\partial \beta} = \frac{\gamma k}{\gamma - 1} \frac{\partial \rho^{\gamma-1}}{\partial \beta} = \frac{\gamma}{\gamma - 1} \frac{\partial p}{\partial \beta}. \tag{60}$$

For a perfect gas

$$\frac{p}{\rho} = \frac{R T}{M}, \tag{61}$$

where T is the static temperature at a field point (α, θ, β). With the aid of (58), (60) and (61), equation (55) is thrown in the form

$$\frac{1}{2} \frac{\partial v_\beta^2}{\partial \beta} + \frac{1}{2} \frac{\partial v_\theta^2}{\partial \beta} = \frac{\gamma R}{(\gamma - 1) M} \frac{\partial T}{\partial \beta}.$$

Integration along a magnetic field line yields

$$\frac{1}{2} v_\beta^2 + \frac{1}{2} v_\theta^2 + h = h_o \tag{62}$$

where h_o is the specific stagnation enthalpy of the flow, and h is the specific enthalpy at a point (α, β, θ) in the flow. Equation (62) is a statement of energy conservation for a region of the flow where there is no heat addition or chemical reaction. We see that the energy is divided between kinetic energy of motion along field lines, kinetic energy of rotation and thermal energy. To make efficient use of the energy in the gas it is necessary to recover not only the thermal energy in the expansion but also the rotational energy $\frac{1}{2} v_\theta^2$. From (58) we have

$$v_\theta^2 = \frac{c^2}{r^2}$$

and hence the energy in the rotational motion will decrease as the area of the flow increases. We note that the recovery of rotational energy has nothing to do with electromagnetic effects, but depends only on the expansion ratio, providing viscous effects are not considered. Thus, in a rotational flow an incomplete expansion would be felt in two ways: both thermal and rotational energy would remain unused in an under expanded flow.

3.2.3 A Thrust Formula Showing the Effects of Magnetic Compression

In this section we shall derive a formula for the thrust in terms of arc current for a particular choice of electrode geometry and assumed current distribution at the anode. Consider the axisymmetric electrode configuration with external magnetic field as shown below.

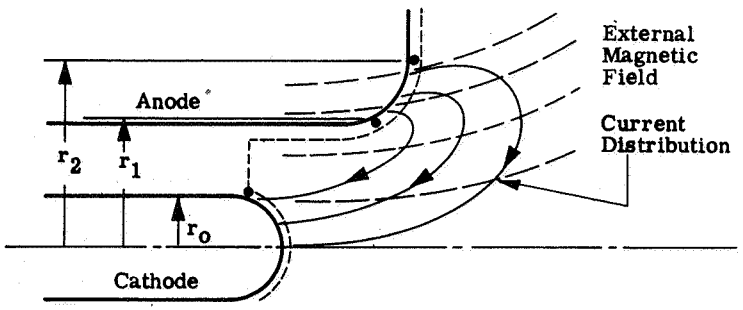

Figure 208. Electrode Configuration Showing Control Surface and Imagined Current Distribution

This configuration is representative of some of the ones that have been used in the tests conducted here. To calculate the thrust produced by the energized flow a control surface is drawn in some convenient way and Newton's law is applied to the mass within the surface and the mass flux through it. The chosen control surface is shown by the dashed line in Figure 208. We will not consider the reaction force on the coil or the thrust due to the blowing term. Then according to Newton's Law the thrust is given by the

sum of the pressure above ambient on the cathode and anode surfaces and entry channel area plus the momentum flux through the control surface. For the above choice of control surface the momentum flux through the surface is probably small and we will neglect this contribution to the thrust. The ambient (tank) pressure is much less than the channel and electrode pressures so for simplicity it will also be neglected in the thrust calculation. The thrust is thus approximated by

$$F = \int_{A_c} p\,dA + \int_{A_{ch}} p\,dA + \int_{A_a} p\,dA,$$

where A_c is the cross-sectional area of the cathode current distribution, A_{ch} is the area of the channel between the cathode radius and the inner radius r_1 of the anode current distribution, and A_a is the area of the current distribution at the anode perpendicular to the axis of symmetry. The pressure just outside the anode current distribution is assumed to be approximately ambient, and consequently the contribution to the pressure thrust on the anode at radii larger than the outer radius of the anode current has been neglected. This should be a fairly good approximation when the applied magnetic field is strong enough to effectively confine the plasma.

A. Momentum and Maxwell's Equations in an Axisymmetric Flow Field

Let us consider the magnetohydrodynamic equations for a time independent, axisymmetric flow field without viscous effects and with a scalar pressure.

The radial and axial components of the momentum equation are

$$\rho v_r \frac{\partial v_r}{\partial r} + \rho v_z \frac{\partial v_r}{\partial z} = - j_z B_\theta + j_\theta B_z - \frac{\partial p}{\partial r} \tag{63}$$

$$\rho v_r \frac{\partial v_z}{\partial r} + \rho v_z \frac{\partial v_z}{\partial z} = j_r B_\theta - j_\theta B_r - \frac{\partial p}{\partial z} \tag{64}$$

where r, θ, and z are radial, azimuthal and axial coordinates measured from the axis of symmetry, ρ is the mass per unit volume, v_r, v_z, and j_r, j_z, j_θ are the indicated components of mass velocity and current density, and B_θ is the azimuthal self-field of the current distribution. B_r and B_z are the components of the external magnetic field. Azimuthal rotational motion of the plasma will not be considered here.

Maxwell's equations in cylindrical coordinates for the magnetic field of an axisymmetric current distribution are

$$\frac{\partial B_\theta}{\partial z} = - \mu_o j_r , \tag{65}$$

$$\frac{\partial B_r}{\partial z} - \frac{\partial B_z}{\partial r} = \mu_o j_\theta , \tag{66}$$

$$\frac{1}{r} \frac{\partial}{\partial r} (r B_\theta) = \mu_o j_z . \tag{67}$$

B. Pressure Forces on the Cathode

We now proceed to derive an expression for the thrust on the cathode. With (66) and (67), equation (63) becomes

$$\rho v_r \frac{\partial v_r}{\partial r} + \rho v_z \frac{\partial v_r}{\partial z} = - \frac{1}{\mu_o} \frac{B_\theta}{r} \frac{\partial (r B_\theta)}{\partial r} - \frac{B_z}{\mu_o} \frac{\partial B_z}{\partial r} + \frac{B_z}{\mu_o} \frac{\partial B_r}{\partial z} - \frac{\partial p}{\partial r} . \tag{68}$$

In the region of the control surface the gradients of the external magnetic field are assumed to be small compared with the radial gradient of the self-induced azimuthal field, and we thus neglect these terms in the above expression. It is customary to neglect the convection terms in equation (68), and we shall do so here, but this approximation is questionable. With these approximations

$$\frac{1}{\mu_o} \frac{B_\theta}{r} \frac{\partial (r B_\theta)}{\partial r} + \frac{\partial p}{\partial r} = 0 . \tag{69}$$

Because of axisymmetry the azimuthal field at a radius r induced by the arc currents will be

$$B_\theta (r) = \frac{\mu_o I (r)}{2 \pi r} , \tag{70}$$

where $I(r)$ is the current flowing through the area of radius r at the cathode. With (70) and the change of variable

$$r \longrightarrow \pi r^2 = A(r)$$

the radial momentum equation reads

$$\frac{\mu_o I}{4\pi} \frac{dI}{dA} + A \frac{dp}{dA} = 0 . \tag{71}$$

Equation (73) can be written in the form

$$\frac{\mu_o}{8\pi} \frac{dI^2}{dA} + \frac{dpA}{dA} - p = 0 . \tag{72}$$

Integrating over the cathode current distribution we have

$$\frac{\mu_o}{8\pi} \int_0^{A_o} \frac{dI^2}{dA} dA + \int_0^{A_o} \frac{d(pA)}{dA} dA - \int_0^{A_o} p\, dA = 0$$

The last term in this equation is just the pressure force on the cathode. The result of this integration is

$$F_c = \frac{\mu_o I_1^2}{8\pi} + p_o A_o \tag{73}$$

where

$$F_c = 2\pi \int_0^{r_o} p(r)\, r\, dr$$

is the axial pressure thrust on the cathode and p_o is the pressure at r_o,

which is the outer boundary of the cathode current distribution. It is clear from the above derivation that the cathode pressure thrust is independent of the current distribution. The first term in equation (73) is due to the magnetic compression of the cylindrical current carrying plasma. The magnetic forces act here to increase the average kinetic pressure in the column above the pressure p_o by the amount $\mu_o I^2/8\pi A_o$.

C. Pressure Forces on the Anode

With an assumption about the current distribution at the anode, equation (72) can also be used to determine the pressure in the anode. Integration of (72) from the inner to the outer radius of the anode current yields

$$-\frac{\mu_o I_1^2}{8\pi} + A_2 p_2 - A_1 p_1 = F_a \tag{74}$$

where

$$F_a = 2\pi \int_{r_1}^{r_2} p(r)\, r\, dr$$

is the force on the anode. p_1 and p_2 are the pressures at r_1 and r_2 and

$$A_1 = \pi r_1^2, \quad A_2 = \pi r_2^2$$

are the areas at r_1 and r_2. To determine the pressure at the outer boundary of the anode current we assume that the current density is

constant. Then the total current flowing through an area of radius r is

$$I = I_1 \left(\frac{A_2 - A(r)}{A_2 - A_1} \right) \tag{75}$$

Substituting (75) in (71) and differentiating gives

$$\frac{dp}{dA} = \frac{\mu_o I_1^2}{4\pi (A_2 - A_1)^2} \left(\frac{A_2}{A} - 1 \right)$$

After integrating from A_1 to A_2 (or r_1 to r_2) we find

$$p_2 = p_1 + \frac{\mu_o I_1^2}{4\pi (A_2 - A_1)} \left[\left(\frac{A_2}{A_2 - A_1} \right) \ln \frac{A_2}{A_1} - 1 \right] \tag{76}$$

With (74) and (76) the force on the anode is

$$F_a = - \frac{\mu_o I_1^2}{8\pi} + \frac{\mu_o I_1^2}{4\pi} \left[\left(\frac{A_2}{A_2 - A_1} \right)^2 \ln \frac{A_2}{A_1} - \left(\frac{A_2}{A_2 - A_1} \right) \right] + p_1 (A_2 - A_1) . \tag{77}$$

The first two terms are due to magnetic compression at the anode and produces an increase in the kinetic pressure above p_1 .

D. Expression for the Total Pressure Thrust

The remaining contribution to the thrust is produced by the pressure in the channel, namely

$$F_{ch} = 2\pi \int_{r_o}^{r_1} p(r)\, r\, dr . \tag{78}$$

Adding the cathode force, the anode force, and the pressure force in the channel, as given by equations (73), (77), and (78) we obtain finally

$$F = \frac{\mu_o I_1^2}{4\pi} \left[\left(\frac{A_2}{A_2 - A_1} \right)^2 \ln \frac{A_2}{A_1} - \left(\frac{A_2}{A_2 - A_1} \right) \right] + p_o A_o + 2\pi \int_{r_o}^{r_1} p(r)\, r\, dr + p_1 (A_2 - A_1) \tag{79}$$

If the pressure across the channel is assumed constant, equation (81) takes the simple form

$$F = \frac{\mu_o I_1^2}{4\pi} \left[\left(\frac{A_2}{A_2 - A_1} \right)^2 \ln \frac{A_2}{A_1} - \frac{A_2}{A_2 - A_1} \right] + p_o A_2 \tag{80}$$

This equation then gives the contribution to the thrust due to pressure forces in terms of the total arc current I_1 , the inner and outer boundaries of the anode current at the anode and the channel pressure p_o We note again that the thrust contributions due to the forces on the coil and the blowing term have not been considered.

3.3 Interpretation of Experimental Results

3.3.1 Efficiency of Operation

For the sake of clarity and convenience we will include in this discussion a description of the efficiencies that are customarily used to characterize the performance of arc jets. The ratio of directed kinetic power in the exhaust flow to the total power into the device is called the overall efficiency and is given by

$$\eta^{ek} \equiv \frac{F^2}{2\,\dot{m}\,P} \tag{81}$$

where F is the total thrust, $\dot{m}$ is the mass flow and P is the electrical power input to the device. We shall take the electrical power as the power into the arc, although there is some expenditure of power in the circuitry connecting the power supply to the arc and also a loss in the coil when an applied magnetic field is utilized.

It is useful to express the overall efficiency as the product of thermal efficiency and thrust - power efficiency. The thermal efficiency is a measure of the effectiveness of the transfer of electrical power to power into the gas and is defined by

$$\eta^{eg} \equiv \frac{\dot{m}\,h_o}{P}\ , \tag{84}$$

where h_o is the stagnation enthalpy of the gas. The thrust - power efficiency measures the recovery of the gas power in the expansion and is defined as the ratio of the directed kinetic power to the total power in the gas. That is

$$\eta^{gk} \equiv \frac{F^2}{2\,\dot{m}^2\,h_o} \tag{83}$$

or

$$\eta^{gk} \equiv \frac{g^2\,I_{sp}^{\ 2}}{2\,h_o}$$

where $I_{sp} \equiv F/g\,\dot{m}$ is the specific impulse and g is the acceleration due to gravity. According to equations (81), (82) and (83) the overall efficiency can be expressed as

$$\eta^{ek} = \eta^{eg}\,\eta^{gk} \tag{84}$$

The loss that determines the thermal efficiency is the heat transfer to the anode and cathode. Extensive testing has shown that the cathode heat transfer is usually a small fraction of the anode power loss. The anode power losses have been observed to be roughly between 40 to 60 percent of the electrical power to the arc in the higher range of specific impulse. It has been suggested[2] that the major part of the power loss to the anode is due to the transport of thermal energy to the anode by the electrons which also carry the arc current. It has also been assumed that the thermal energy the electrons carry is determined by a voltage drop near the anode that is independent of the arc voltage. These assumptions lead to the conclusion that the anode power loss is a linear function of current. These arguments have provided correlation of anode power loss data in some cases but have failed in others.[2] For H_2 in a range of high specific impulse (4000 sec) and strong magnetic fields (~ 3000 gauss) we have observed an approximately constant anode power loss at constant arc power and mass flow when the voltage and current are varied by changing the

applied magnetic field. These data cannot be explained with the assumption of a voltage drop at the anode that is independent of the total arc voltage. Rather it appears that the thermal energy the electrons carry is determined by a voltage that is a constant fraction of the arc voltage.

The thrust - power efficiency is determined by the amount of unrecovered potential energy in the flow (ionization energy and dissociation energy), heat transfer from the expanding flow, and inefficient utilization of kinetic and thermal energy. The ionization and dissociation energy is thought to be unrecoverable because of the slow recombination rates.[27, 28] The concept of frozen flow is then used to describe a flow that expands isentropically with a fixed (or frozen) chemical composition. The frozen flow is thus defined as

$$\eta_f \equiv 1 - \frac{\Delta h}{h_o} \tag{85}$$

where Δh is the energy per unit mass invested in ionization and dissociation of the gas. The frozen flow efficiency is often considered as an upper limit of the thrust - power efficiency since the additional losses due to heat transfer and inefficient expansion will cause the actual η^{gk} to be less than the frozen flow efficiency.

The macroscopic equation for the energy balance on a steady state plasma in an electric and magnetic field can be derived from the Boltzmann equation in the form

$$\text{div}\, \rho\, v\, h = - \text{div}\, \vec{q} + \vec{j}_i \cdot \vec{E} + \vec{j}_e \cdot \vec{E}\,, \tag{86}$$

where h is the stagnation enthalpy per unit mass, $\vec{q}$ is the heat flux and $\vec{j}_i$ and $\vec{j}_e$ are the ion and electron current densities. The term $(\vec{j}_i \cdot \vec{E} + \vec{j}_e \cdot \vec{E})$ is the electrical work done on the plasma per unit volume. The magnetic field does not appear directly in this form of the energy equation which is a consequence of the fact that the Lorentz forces act perpendicular to the motion of charged particles and hence do no work. The magnetic forces of course influence the current distributions $\vec{j}_e$ and $\vec{j}_i$, the charge distribution and hence also the electric field.

The energy equation usually provides the basis for approximate theoretical expressions for the thrust-power efficiency. For example, integration of the energy equation (86) over the entire volume of the flow and assuming the exit flow is fully expanded, uniform and axial in direction yields

$$m\left(\frac{v^2}{2} + \Delta h\right) = - Q + \int (\vec{j}_i + \vec{j}_e) \cdot \vec{E}\, dx\, dy\, dz$$

where Q is the heat loss to the surroundings, Δh is the potential energy of ionization and dissociation and $\dot{m}$ is the mass flow. The last term is the electrical power input to the flow which we may write as $P = I\,V$, where I is arc current and V is the arc voltage. An expression for the thrust-power is then given by

$$\frac{\dot{m}\, v^2}{2} = P - Q - \dot{m}\, \Delta h\,. \tag{87}$$

We take Q to be the heat transfer to the electrodes and neglect the radiation from the expanding flow. Then the electrical power minus the heat

loss to the electrodes is counted as the power in the gas. A formal expression for the thrust-power efficiency thus follows from (87);

$$\frac{v^2}{2\,h_o} = 1 - \frac{\Delta h}{h_o}, \tag{88}$$

where

$$h_o = \frac{P - Q}{\dot{m}} \tag{89}$$

is the stagnation enthalpy per unit mass of what is considered an adiabatically expanding flow. The accurate determination of the potential energy in ionization and dissociation requires a solution of the dynamical equations describing the flow. Even with such assumptions as a one-dimensional flow, thermal equilibrium and that a continuum model of the flow is valid, the equations governing this reacting flow with distributed electrical energy addition and magnetic forces are quite complicated.

Lacking a solution of the flow problem we shall assume that the composition of the gas is determined by the stagnation temperature of the flow corresponding to h_o. The potential energy is then determined from the thermal equilibrium composition of the gas as a function of enthalpy. The potential energy of ionization and dissociation is assumed unrecoverable. This is the usual frozen flow approximation and it is the one we shall use to correlate our experimental data.

There have been attempts to calculate thrust by approximate integration of the momentum equation.[2] This approach, to a certain extent, ignores

the energy equation. An example of this type of thrust calculation is given in Section 3.2.3. Since the dissociation, ionization and electrode power losses are dominant factors in determining thrust we prefer to use an approximation based on the energy equation where we can approximate these losses in the more direct way described above.

Measured thrust-power efficiency is shown in Figure 209. The curve shown is the theoretical frozen flow efficiency discussed above. We note that the frozen flow curve provides an upper bound for the measured efficiency and that the experimental points follow the frozen flow curve rather well at specific impulses greater than 2000 seconds. The relatively low efficiency at 1000 seconds is attributed to a strongly nonequilibrium condition. That is, the degree of ionization is thought to be substantially in excess of the equilibrium value (before expansion) at 1000 seconds. The fact that the measured efficiency follows the frozen flow curve at $I_{sp} > 2000$ seconds suggests that the plasma is not too far from equilibrium when the flow leaves the region that is effective in producing thrust. This is not in disagreement with the order of magnitude calculations of Section 3.2.1, where it was seen that at temperatures of 20,000°K the characteristic length for establishing energy equipartition was about one centimeter.

At specific impulses greater than 2000 seconds the deuterium frozen flow efficiency is significantly better than hydrogen. This is so because the atomic weight of deuterium is twice that of hydrogen while the ionization potential is the same. At equal specific impulses and full ionization deuterium

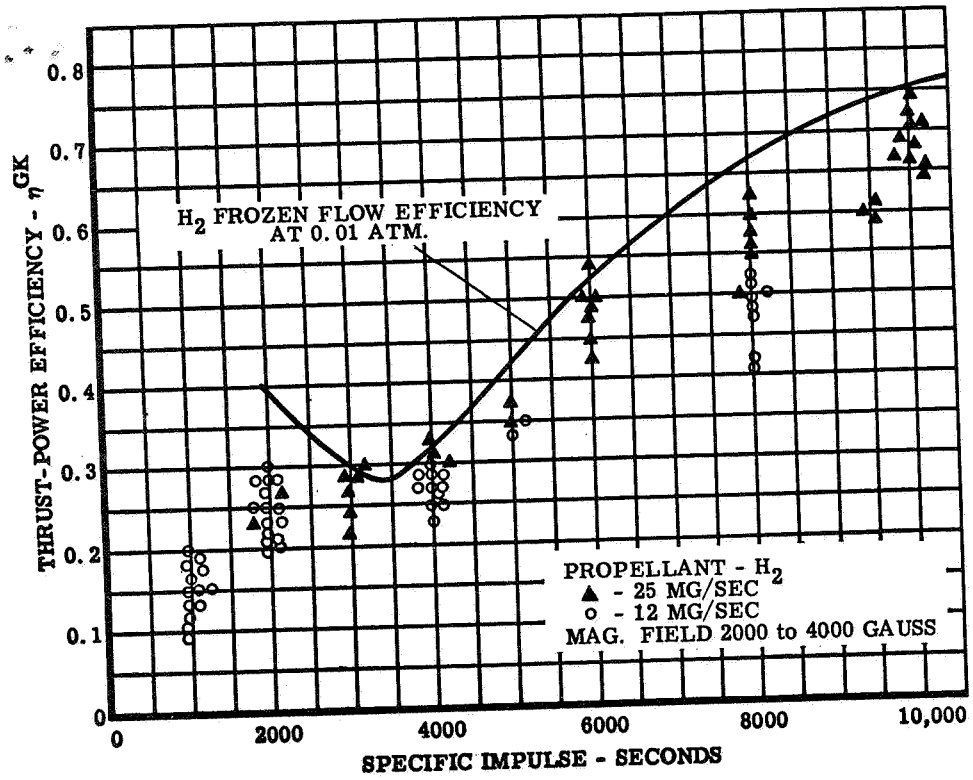

Figure 209. Comparison of Hydrogen Thrust-Power Efficiency With Frozen Flow Efficiency

will thus be hotter than hydrogen by about a factor of two but the thrust-power efficiency should be higher. Measured D_2 thrust-power efficiency is compared with the frozen flow efficiency in Figure 210. We see that the thrust-power efficiency is indeed improved over H_2 by approximately the amount predicted by the frozen flow model. Deuterium is clearly a better propellant than H_2 from the point of view of thrust-power efficiency. Figure 211 shows thrust-power efficiency data for H_2 at various applied magnetic field strengths in a high range of specific impulse. We note that the increase in efficiency is about what one would expect from a good nozzle.

For the purpose of comparison two theoretical curves are shown. The upper one gives the specific impulse for a frozen flow and complete isentropic expansion. The lower curve gives a "frozen flow efficiency" obtained by assuming, as above, that the ionization and dissociation fraction are determined by a static temperature equal to the stagnation temperature of the flow but that there is no expansion (no magnetic or metal nozzle). In this case the specific impulse for a one dimensional flow is given by

$$I^*_{sp} = \frac{1}{g}\sqrt{\frac{\gamma^2 - 1}{\gamma^2}\, 2\, \eta_f\, h_o}\,. \tag{90}$$

γ is the ratio of specific heats corresponding to the frozen composition of the flow, and η_f is the fraction of the gas power used for dissociation and ionization at a specific enthalpy h_o. For no expansion define a "frozen flow efficiency" by

$$\eta^*_f = \frac{g^2\, I_{sp}{}^2}{2\, h_o} \tag{91}$$

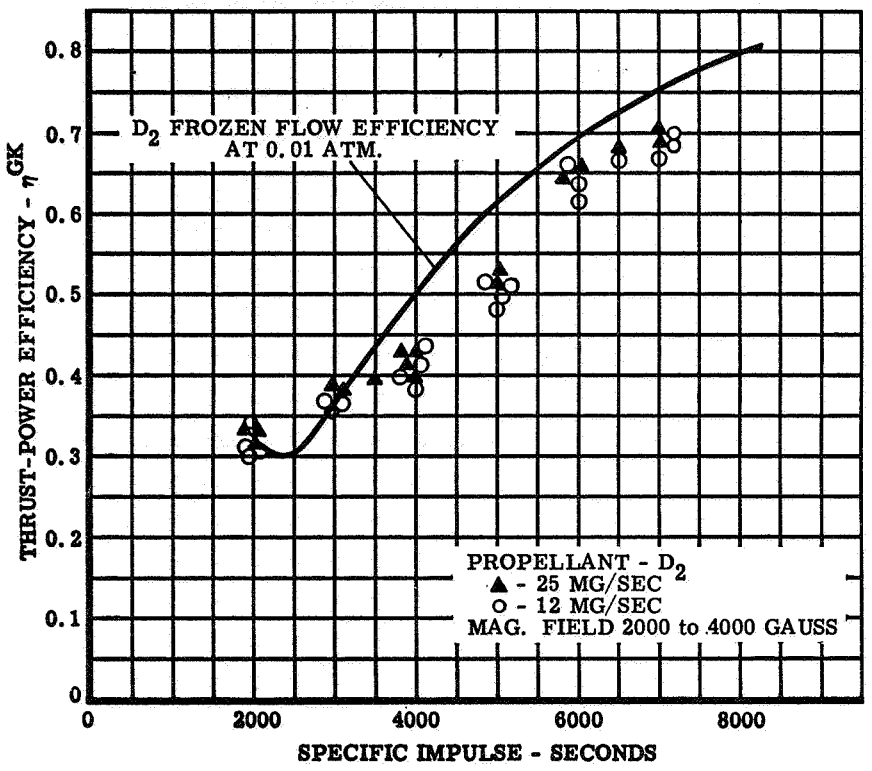

Figure 210. Comparison of Deuterium Thrust-Power Efficiency With Frozen Flow Efficiency

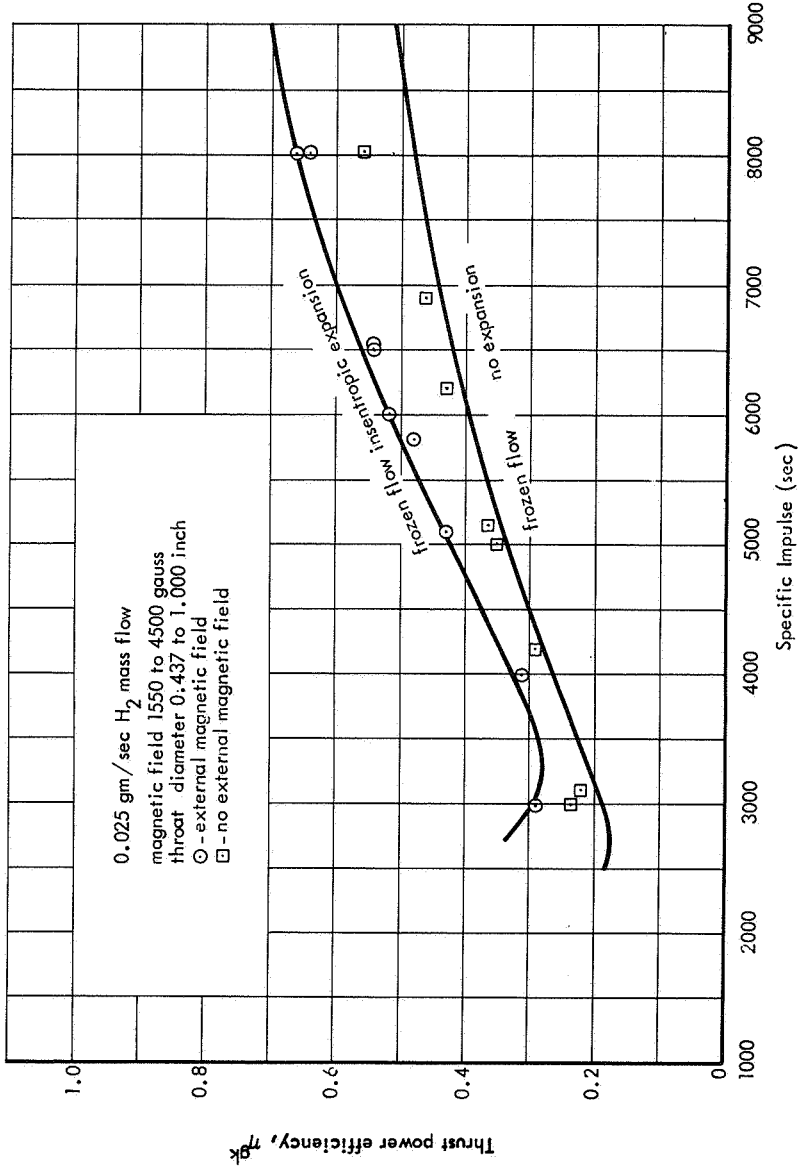

Figure 211. Comparison of Measured Thrust Power Efficiency With Frozen Flow Efficiencies for Operation With and Without an External Magnetic Field

where I_{sp} is given by (90). The difference between the upper and lower curves in Figure 211 is thus an indication of the magnitude of efficiency improvement that can be obtained with a very good nozzle.

There is apparently no way of avoiding the ionization loss at these high specific enthalpy flows. One may conjecture that the ions carry the major part of the current and hence acquire energy directly from the electric field. If the ions were to acquire a large thermal energy, according to the equipartition times we have calculated, the electrons would heat up by collision with the energetic ions. If the plasma comes even approximately near the thermal equilibrium it should be very strongly ionized in the 4000 to 5000 second range of specific impulse. The frozen flow model, which is just an approximate expression of the principle of the conservation of energy, then provides a sensible upper limit on the thrust-power efficiency.

Whenever the magnetic pressure of either the self-induced or applied magnetic field is comparable to the gas pressure in a strongly ionized flow, magnetic effects are likely to be significant. Here the most obvious manifestations of magnetic forces are extended current distributions, rotational motion of the plasma and confinement of the expanding jet. Though these effects are probably important to the operation of the arc jet they do not change the fact that the price of dissociation and ionization apparently must still be paid, and it is this loss that is dominant in determining the thrust-power efficiency. We thus feel that the motivation for employing an applied magnetic field would be to achieve a 10 to 15 percent increase in thrust-power efficiency through nozzle-like effects and to increase arc stability and lifetime by the rotational action of the magnetic field on the plasma.

Further increases in overall efficiency must come from improvement of thermal efficiency and by a choice of propellant with optimum frozen flow efficiency in the desired range of specific impulse.

3.3.2 Discussion of Anomalies in Thrust and Specific Impulse Measurements

It is well-known[1, 2] that at very low mass flow rates the measured thrust-power efficiency can exceed the frozen flow efficiency. This anomaly has cast doubt on the validity of existing measurements over a wide range of conditions. Recirculation or entrainment of part of the ambient gas into the arc and unaccounted-for electromagnetic interactions of the arc with the vacuum tank have been suggested as possible causes of the very high efficiencies. It also appears that under some conditions the tank forms part of the conduction path between cathode and anode which could cause an error in the measurement of thermal efficiency.

The possibility of entrainment affecting arc jet performance arises when the current distribution extends outside the metal surfaces of the thrustor The tendency for arc currents to flow outside is due to the Lorentz force of the self-induced or applied magnetic field acting on the arc currents. The presence of these exterior currents make it possible to create, by ohmic heating and partial confinement of the plasma, a high pressure region outside the thrustor. In such a situation if ambient particles are entrained, heated and contribute to the thrust, they should be counted as propellant flow.

To illustrate the order of magnitude of possible mass entrainment we consider the data shown in Figure 212. We see that at the lower mass flows and higher specific impulses the frozen flow efficiency is exceeded. An addition to the through flowing mass of about 3.5 mg/sec is required to bring the measured efficiency below the frozen flow efficiency.

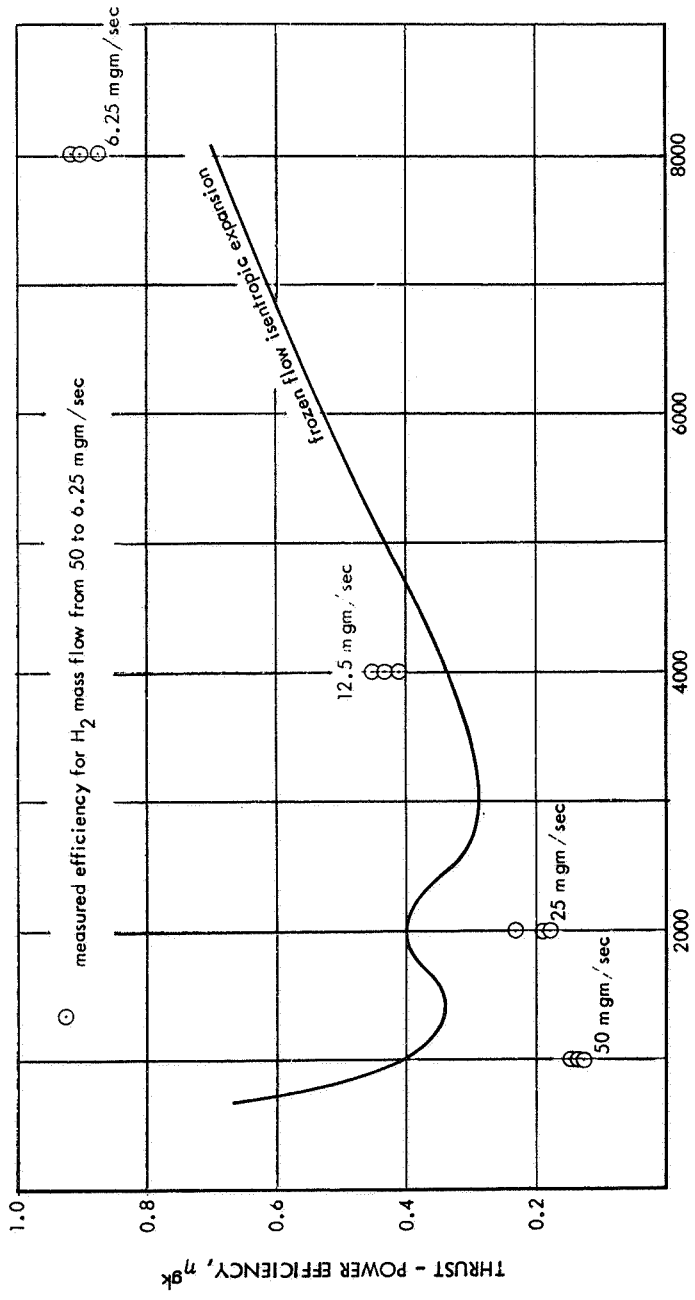

Figure 212. Comparison of Measured Efficiency With Frozen Flow Efficiency

If the tank should acquire a charge distribution, an electrostatic force between the tank and thrustor will be produced. This force is of the order of $4\pi\epsilon V^2$ where ϵ is the inductive capacity of the gas and V is the potential difference between tank and thrustor. For a potential difference of 100 volts this force will be too small to be of any consequence.

The possibility of either induced or conduction currents producing a magnetic interaction between tank and thrustor has not been investigated thoroughly. When an applied magnetic field is utilized it is known that the tank and coil interact to produce a measurable force. When thrust measurements are made, corrections are applied to correct for this force. It is not yet known with certainty that there are no additional magnetic interactions caused by arc currents which produce significant errors in thrust measurements.

Although the uncertainties stemming from an imperfectly controlled testing environment preclude positive conclusions with respect to efficiency of arc operation, certain results are probably independent of the interaction of the arc with the environment. For example, efficiency data at the higher mass flow rates ($\geq$ 25 mg/sec) may be reliable. The characteristic trend of increasing thrust-power efficiency with increasing I_{sp} for H_2 and D_2 propellants will no doubt persist in a more sophisticated testing environment. Relative results such as the superior thrust-power efficiency of D_2 relative to H_2 in the 2000 to 8000 second range can be accepted with confidence.

In addition, thermal efficiency data is probably reliable since entrainment and spurious forces do not affect this measurement. There is the above mentioned possibility that conduction currents in the tank could lead to an error but there is presently no definite evidence that significant errors from this source exist.

4.0 SUMMARY AND CONSLUSIONS

Coaxial thermo-ionic thrustors using hydrogen have been operated continuously for 50 hours at 3000, 6000 and 10,000 seconds without significant changes in performance during the operating period. After cessation of operation, components were examined carefully for wear and changes of any kind. A complete account of the life tests including all performance data has been presented in references 29 and 3. The results of these and many additional tests form the basis of our present knowledge of thrustor life.

The average consumption of cathode material during the 50-hour life tests was about 50 micrograms per hour per kw. The consumption of material was surprisingly uniform over the cathode tip. The rate and uniformity of consumption has been found to be primarily a function of cathode temperature and arc chamber pressure. At high pressure the current is localized at the tip of the cathode, producing a high current density and local erosion and melting of the cathode. As the pressure is decreased (by reducing mass flow or increasing throat diameter), the distribution becomes more diffuse until, at certain pressures, the whole tip of the cathode glows and erosion of the cathode becomes small and uniform. It is natural to conclude that the current is also distributed evenly over the cathode tip and the consequent reduction in current density results in the uniformly small erosion rate. A further decrease in pressure is not beneficial since it causes the discharge to move further back on the cathode and nonuniformities in the current distribution develop.

Erosion at the anode is much more severe than at the cathode. The arc current tends to concentrate in a small area on the anode surface and produce local erosion and melting. When an "axial" magnetic field is applied, the average current is distributed more uniformly on the anode surface with a subsequent reduction in the average current density and erosion. By applying a moderately strong magnetic field the average anode erosion rate was reduced to 5 mg/hr-kw, which is still a factor of 100 greater than the cathode erosion rate.

If the magnetic field is too strong it can have a deleterious effect on the anode. When very strong fields are applied the arc currents tend to flow outside of the thrustor. Part of the electron current appears to enter the anode parallel to the magnetic field lines on the periphery of the plasma jet. These electrons produce excessive damage to the anode which is understandable since they reach the anode by a path of relatively low gas density parallel to the magnetic field lines.

A large part of this program was devoted to the experimental determination of the dependence of efficiency on specific impulse, mass flow, throat diameter, applied magnetic field, arc chamber pressure, voltage-current characteristics and propellant type. These variables, which clearly are not independent, have been varied over a wide range of values. We have found that the measured thrust efficiency for H_2 and D_2 follow the frozen flow efficiency rather closely (except for very low mass flow rates). These results suggest that the frozen flow efficiency sets an approximate upper limit on attainable thrust efficiency. The D_2 frozen flow efficiency is

higher than H_2 and the measured D_2 thrust efficiency has also been consistently higher than H_2. From the criteria of thrust efficiency, without regard to other forces, deuterium is a better propellant than hydrogen.

A significant result of the tests was that the thrust efficiency is relatively insensitive to applied magnetic field strength over a range of 1000 to 16,000 gauss. These results are compatible with a theoretical model of the arc that has the magnetic field acting primarily as a nozzle.

The electrode power loss has been found to be large, with practically all of the loss going to the anode. Electrode losses, or equivalently thermal efficiency, have been measured for a wide range of arc variables. The losses are usually between 40 and 50 percent of the total electrical power input. The thermal efficiency has also been found to be insensitive to magnetic field strength. Changes of η^{eg} are usually less than 10 percent over a range of 1000 to 16,000 gauss. An interesting regularity between arc chamber pressure and thermal efficiency has been uncovered. The pressure can be varied by changing the throat diameter, mass flow, specific impulse and magnetic field strength. The thermal efficiency usually increases with increasing pressure, with an increase sometimes of more than 10 percent over the pressure range studied. However, in this low pressure range the pressure cannot be increased beyond certain limits or one will reach a domain of operation where electrode damage is prohibitive.

There is no reason as yet to believe that a sizable fraction of the large thermal loss cannot be recovered. That is, there is nothing yet in principle that limits the thermal efficiency as is the case with thrust efficiency

when ionization and dissociation energy are unrecoverable. The experimental knowledge of electrode losses is still inadequate and the theoretical understanding is very superficial and we feel that this important problem should be investigated further.

Thermal efficiencies have also been measured with deuterium, helium, ammonia, lithium, argon, potassium, and tungsten vapor (in electrode vapor operation). These data are given in Sections 2.2.3 and 2.2.4. The thermal efficiency of D_2 is usually about 7 percent less than H_2 at equal specific impulse and arc chamber pressure and the pressure dependence is the same as noted above for H_2. The data for the remaining gases are too few to yield firm conclusions, and this should be kept in mind with respect to the following remarks. The thermal efficiencies of NH_3, He, and so forth are all about 20 percent or more less than H_2. There is a weak correlation between increasing molecular weight and decreasing efficiency. Ammonia, with 45 percent, had the highest thermal efficiency of the gases mentioned above and tungsten was the lowest. We note the large difference between the thermal efficiency of lithium measured by Cann[5] and measured here (see Figure 102).

A study of the effect of the test environment on thrustor performance has been initiated. The goal of this investigation is to define and perhaps construct a test environment that would permit a reliable extrapolation of terrestrial tests to deep space conditions.

We have conducted tests with H_2 which show that the thrust variation is slight for a change in ambient pressure from 1 to 10^{-2} Torr. Similar

results over a larger pressure range are reported in reference 10.

Most of the effort here (and at other laboratories) on the problem of the test environment has gone into reconsideration of necessary conditions to impose on the testing environment and seems to be leading to the concept of a big, very high vacuum, insulated tank. It should perhaps be kept in mind that it may also be fruitful to modify thrustor design, if this can be done without sacrificing efficiency, to minimize interaction with the environment. For example, if it is the low mass flow and the protrusion of the currents outside the thrustor that lead to spurious interactions, then, if back pressures can be kept at an acceptable level, requirements on a facility might be relieved by working with mass flows, magnetic field strengths and electrode geometries where the currents are largely confined to the throat.

The processes of current conduction in steady, uniform electric and magnetic fields have been studied. The Hall parameter has been expressed in terms of the prevailing magnetic field, ion density and electron density. A model of the electron density and temperature fields, based on experimental data and physical reasoning, has been posed. The Hall parameter has been mapped over the flow field for the four permutations of low and high arc currents, with and without a strong applied magnetic field, using the best available estimates for the relevant parameters. In the case of high current and strong applied magnetic field, for a fully ionized hydrogen plasma of uniform particle density without radial pressure gradients, one finds an arc with an axially protracted current distribution involving

negligible net Hall currents, with azimuthal swirling, radial pinching and axial streaming of the plasma.

The energy equipartition of electrons and ions in a steady and uniform electric and magnetic field has been studied. The energy gain of an average electron under the influence of electrostatic and Lorentz forces and a stochastic force due to electron collisions with heavy particles has been considered. Expressions are derived which give the electron-ion energy difference in terms of temperature, particle density and electric and magnetic field strengths. For a specific choice of these parameters we find that large energy differences can develop in regions where there is a large component of the electric field parallel to the magnetic field, for example on the periphery or on the axis of the plasma jet. Equipartition times and lengths have been calculated for assumed values of the relevant parameters. If our estimate of these parameters is representative of conditions in the plasma jet the transfer of energy from electric field to electrons and then to heavy particles should be effective.

An axisymmetric, rotational, fully ionized arc jet flow in a strong magnetic field has been studied. We have assumed that there is no mass diffusion perpendicular to the field lines. The flow has been studied using the magnetogasdynamic equations for an electrically neutral, inviscid plasma. We have used coordinate surfaces perpendicular and parallel to the magnetic field lines which is a natural choice for this problem. In these coordinates the nozzle effect of the applied field is clearly seen. An expression for the change of momentum flux along magnetic field lines has been given. As expected, the energy of the flow is divided between thermal energy, kinetic

energy along the field lines, and rotational energy. It has been shown that both thermal and rotational energy can in principle be recovered as thrust in an efficient expansion process.

The effects of magnetic compression at the electrode surfaces has been examined for an assumed current distribution that seems applicable to our electrode geometry when a strong magnetic field is applied. Formulas of the Maecker type[2] have been obtained which express thrust as a quadratic function of current and a logarithmic function of electrode geometry. However, to compare calculated thrust efficiency with our measurements we have used the frozen flow efficiency rather than the thrust formula mentioned above. The frozen flow efficiency is preferred here because it is based on an approximate integration of the energy equation where the dominant dissociation and ionization losses can be included explicitly.

REFERENCES

1. A. C. Ducati, G. M. Giannini and E. Muehlberger, "Recent Progress in High Specific Impulse Thermo-Ionic Acceleration," AIAA Second Aerospace Sciences Meeting, Preprint 65-96 (January 1965).

2. R. R. John, et.al., "Arcjet Technology Research and Development," Final Report, Contract NAS 3-5900 (December 22, 1965).

3. A. C. Ducati and E. Muehlberger, "Design and Development of a Thermo-Ionic Electric Thrustor," Second Quarterly Progress Report, Contract NAS w-968 (November 1964).

4. R. A. Moore, G. L. Cann, L. R. Gallagher, "High Specific Impulse Thermal Arcjet Thrustor Technology," Technical Report AFAPL-TR-65-48 Part I (June 1965).

5. G. L. Cann, Electro-Optical Systems, verbal communication.

6. F. N. Mastrup, "Spectroscopic Investigation of a Hydrogen Arcjet Plume," AIAA Paper, Second Annual Meeting, San Francisco (July 1965).

7. A. C. Ducati and E. Muehlberger, "Design and Development of a Thermo-Ionic Electric Thrustor," Third Quarterly Progress Report, Contract NAS w-968 (February 1965).

8. A. C. Ducati and E. Muehlberger, "Design and Development of a Thermo-Ionic Electric Thrustor," Fourth Quarterly Progress Report, Contract NAS w-968 (May 1965).

9. R. G. Jahn, K. E. Clark, "A Large Dielectric Vacuum Facility," Department of Aerospace and Mechanical Sciences, Princeton University, Princeton, New Jersey.

10. G. L. Cann, R. L. Harder, R. A. Moore and P. D. Lenn, "Hall Current Accelerator," Final Report, EOS Report 5470, Contract NAS 3-5909 (February 1966).

REFERENCES

11. G. R. Seikel, NASA Lewis Research Center, Cleveland, Ohio, verbal communication.

12. AVCO Corporation, "Arcjet Technology Research and Development," Fourth Quarterly Progress Report, NAS 3-5900 (June 1965).

13. A. C. Ducati, "Study of the Factors Affecting the Efficiency in Thermal Acceleration of Propellants," Final Report, Contract AF 49(638)-1161, (August 1965).

14. G. W. Sutton and A. Sherman, Engineering Magnetohydrodynamics, McGraw Hill (1965).

15. L. Spitzer, Jr., Physics of Fully Ionized Gases, Interscience (1962).

16. A. J. Kelly, N. M. Nerheim, J. A. Gardner, "Electron Density and Temperature Measurements in the Exhaust of a MPD Source," AIAA Paper No. 65-298 (July 1965).

17. P. F. Jacobs, "Electron-Heavy Particle Equilibrium in a Dense Argon Plasma," Ph. D. Thesis, Princeton University, Department of Aerospace and Mechanical Sciences (1965).

18. W. R. Smythe, Static and Dynamic Electricity, McGraw Hill (1950).

19. W. Grossman, R. V. Hess, and H. A. Hassan, "Experiments with a Co-axial Hall Current Plasma Accelerator," AIAA Paper No. 64-700 (August 1964).

20. T. F. Stratton, "High Current Steady State Co-axial Plasma Accelerators," Los Alamos Technical Rep. LADC-7021; AIAA Journal, to be published.

21. R. G. Jahn, "Electromagnetic Acceleration in High Current Arcjets," Consultant report to Giannini Scientific Corporation (March 1965).

REFERENCES

22. R. R. John, et. al., "Arc Jet Technology Research and Development," Third Quarterly Progress Report, RAD-SR-65-92 (March 1965).

23. W. P. Allis, Motions of Ions and Electrons, Encyclopedia of Physics, vol. 21, Springer Verlag, Berlin (1956).

24. H. Dreicer, Phys. Rev., pp. 117, 329 (1960).

25. This observation is due to R. G. Jahn, Forrestal Research Center, Princeton University, Princeton, New Jersey.

26. H. G. Loos, "The Streamsurface Characteristics Methods for Supersonic Flow, With Application to Supersonic Compressors," AFOSR-TN-56-367 ASTIA Document No. AD 95803 (May 1956). Appendix A of this report contains a lucid discussion of the transformation of the fluid mechanical equations from cartesian to general curvilinear coordinates.

27. Massey and Burhop, Electronic and Ionic Impact Phenomena, Oxford University Press, New York (1956).

28. Glasstone, Laidler, and Eyring, Theory of Rate Processes, McGraw Hill, New York (1941).

29. A. C. Ducati and E. Muehlberger, "Design and Development of a Thermo-Ionic Electric Thrustor," First Quarterly Progress Report, Contract NAS w-968 (September 1964).

DISTRIBUTION LIST

NASA Lewis Research Center
21000 Brookpark Road
Cleveland, Ohio 44135
Attn: C. C. Conger, MS 54-1 (1)
J. R. Eski, MS 54-2 (1)
H. R. Hunczak, MS 54-3 (5)
G. Seikel, MS 301-1 (1)
D. Connolly, MS 301-1 (1)
Library, MS 60-3 (2)
Reports Control Office MS 5-5 (1)
W. Moeckel, MS 301-1 (1)
S. Domitz, MS 54-3 (1)

National Aeronautics and Space Administration
Washington, D.C. 20546
Attn: J. Lazar, RNT (1)
J. Mullin, RNT (1)
K. Thom, RRP (1)

NASA Scientific and Technical Information Facility
Box 33
College Park, Maryland 20740
Attn: NASA Representative RQT-2448 (6)

NASA Marshall Space Flight Center
Huntsville, Alabama 35812
Attn: Library (1)
G. Heller, R-RP-DIR (1)

NASA Ames Research Center
Moffett Field, California 94035
Attn: Library (1)
H. Stine (1)

NASA Langley Research Center
Hampton, Virginia 23365
Attn: Library (1)
G. Hess, MS 160 (1)
M. Ellis, MS 160 (1)

NASA Goddard Space Flight Center
Greenbelt, Maryland 20771
Attn: Library (1)
W. Isley, Code 623 (1)

Wright-Patterson AFB
Dayton, Ohio 45433
Attn: AFAPL (API)
G. Sherman (1)
FDCL P. Polishuk (1)
AFARL(ARN)
Eric Soehngen (1)

Headquarters, United States Air Force
Office of Scientific Research
Washington, D.C. 20525
Attn: Dr. M. Slawsky (1)

Oak Ridge National Laboratories
P.O. Box Y
Oak Ridge, Tennessee 37831
Attn: Dr. E. Shipley (1)

United States Army Research Office
Box CM Duke Station
Durham, North Caroline 27706
Attn: Dr. P. Kosting (1)

Research Branch, VKF
Arnold Air Force Station, Tennessee 37389
Attn: Library (1)

AFWL
Kirtland AFB, New Mexico 87417
Attn: WLPC/Capt. C. F. Ellis (1)

U.S. Naval Research Lab.
Washington, D.C. 20013
Attn: Dr. A. C. Kolb (1)

Office of Naval Research
Power Branch (Code 429)
Washington, D.C. 20360
Attn: J. A. Satkowski (1)

National Security Agency
Fort George G. Mead, Md. 20755
Attn: Lt. John D. Ryder, Code 188-7250 (1)

AVCO Corporation
Research and Advanced Development
201 Lowell Street
Wilmington, Massachusetts 01887
Attn: Dr. R. John (1)
Dr. S. Bennett (1)

AVCO Corporation
Everett Research Lab.
2385 Revere Beach Pkwy
Everett, Massachusetts 02149
Attn: R. M. Patrick (1)

Electro-Optical Systems, Inc.
125 N. Halstead Ave.
Pasadena, California 91107
Attn: Dr. R. Buhler (1)
Dr. G. Cann (1)

Gianinni Scientific Corporation
3839 South Main Street
Santa Ana, California 92705
Attn: A. Ducati (5)
J. Todd (1)
E. Muehlberger (1)
R. P. Treat (1)

General Electric Company
Electric Space Propulsion Projects
Evendale, Ohio 45202
Attn: Dr. M. L. Bromberg (1)

General Electric Missiles and Space Division
Valley Forge Technical Center
P.O. Box 8555
Philadelphia, Pa. 19101
Attn: Dr. Per Gloersen (1)

Jet Propulsion Laboratory
California Institute of Technology
4800 Oak Grove Drive
Pasadena, California 91103
Attn: John W. Stearns, Jr
MS 125-224 (1)
N. M. Nerheim (1)
Library (1)

Aerospace Corporation
P.O. Box 95085
Los Angeles, California 90045
Attn: Library Technical
Documents Group (1)

LTV Aerospace Corp.
Advanced Systems, Astro.
Division
Box 6267
Dallas, Texas 75222
Attn: F. T. Esenwein (1)

Westinghouse Astronuclear
Laboratories
Electrical Propulsion Laboratory
Pittsburgh, Pa. 15234
Attn: H. W. Szymanowski,
Manager (1)

Aerojet General
San Ramon, California 94583
Attn: Dr. J. S. Luce (1)

General Dynamics/Convair
P.O. Box 1128
San Diego, California 92115
Attn: Dr. A. V. Larson (1)

McDonnell Aircraft Corporation
Box 516
St. Louis, Missouri 63166
Attn: Dr. W. van Camp (2)

Grumman Aircraft Eng. Co.
Thermodynamics and
Propulsion Section
Plant 5
Bethpage, N.Y. 11714
Attn: I. Tobias (1)

Los Alamos Scientific Laboratory
Los Alamos, New Mexico 87544
Attn: Dr. Thomas S. Stratton (1)

Department of Mechanical
Engineering
University of Minnesota
Minneapolis, Minnesota 55455
Attn: Dr. E. Eckert (1)
Dr. E. Pfender (1)

University of California,
San Diego
LaJolla, California 92037
Attn: Dr. R. Loveberg (2)

Princeton University
Department of Aerospace and
Mechanical Sciences
Forrestal Research Center
Princeton, N.J. 08540
Attn: Dr. Robert Jahn (2)

Stevens Institute of Technology
Castle Pt. Station
Hoboken, N.J. 07000
Attn: Dr. W. Bostick (1)

Northwestern University
Gas Dynamics Lab.
Evanston, Illinois 60201
Attn: Prof. Ali Cambel (1)

Cast Institute of Technology
10900 Euclid Avenue
Cleveland, Ohio 44106
Attn: Dr. Eli Reshotko (1)

Department of Space Sciences
and Applied Physics
Catholic University of America
Washington, D.C. 20017
Attn: Prof. C. C. Chang (1)

Colorado State University
Fort Collins, Colorado 80521
Attn: Prof. W. R. Mickelsen (2)

Cornell Aero. Labs., Inc.
Buffalo, N.Y. 14221
Attn: D. Lockwood (1)

Cosmic, Inc.
4847 Cordell Ave.
Bethesda, Md. 20014
Attn: Dominique Gignoux (1)

Space Sciences, Inc.
301 Bearhill Road
Waltham, Massachusetts 02154
Attn: Dr. S. Ziering (1)

E-3016